MULTI-INSTRUMENT STUDIES OF IONOSPHERIC AND MAGNETOSPHERIC PROCESSES

A Thesis Submitted to

the College of Graduate Studies and Research

in Partial Fulfillment of the Requirements

for the Degree of Doctor of Philosophy

in the Department of Physics and Engineering Physics

University of Saskatchewan, Saskatoon

By

Jun Liang

© Copyright Jun Liang, November 2004. All rights reserved.

Permission to Use

In presenting this thesis in partial fulfillment of the requirements for the degree of Doctor of Philosophy in the Department of Physics and Engineering Physics, University of Saskatchewan. I agree that the Libraries of this University may make it freely available for inspection. I further agree that permission for copying of this thesis in any manner, in whole or in part, for scholarly purposes may be granted by the professor or professors who supervised my thesis work or, in their absence, by the Head of the Department or the Dean of the College in which my thesis work was done. It is understood that any copying or publication or use of this thesis or parts thereof for financial gain shall not be allowed without my written permission. It is also understood that due recognition shall be given to me and to the University of Saskatchewan in any scholarly use which may be made of any material in my thesis.

Requests for permission to copy or to make other use of material in this thesis in whole or part should be addressed to:

Head of the Department of Physics and Engineering Physics

University of Saskatchewan

Saskatoon, Saskatchewan, S7N 5E2

Abstract

In this thesis, several aspects of the convection, magnetic, and optical auroral dynamics of the high-latitude ionosphere are investigated from multi-instrument observations.

The spatial and temporal relationships between nightside radar flow enhancements (NRFEs) and auroral intensifications are studied in Chapter 3. The NRFEs on open field lines are usually associated with very little accompanying auroral and magnetic activity. The NRFEs on closed field lines are often accompanied by optical auroral activity, but there is not a definite one-to-one correspondence. Both the statistical investigation and event study showed that the NRFEs may occur nearly simultaneously with the auroral intensifications. Because existing models associating the tail reconnection process and near-geosynchronous onset of substorms do not explain these correlated radar and optical observations very well, we propose a new model to explain the nearly simultaneous onset of the NRFEs and the auroral intensifications.

In Chapter 4 we describe a small postmidnight substorm event on October 9, 2000 during dominantly IMF By+ Bz+ conditions. A sequence of three optical auroral intensifications and Pi2 bursts were found. The first two activations were characteristic of pseudobreakups, while the last and strongest intensification corresponded to a substorm expansive phase (EP). The auroral, magnetic and radar signatures of the event are interpreted as the consequence of three successive drift-Alfven-ballooning (DAB) mode instabilities in the near-geosynchronous orbit plasma sheet (NGOPS). About 10 minutes after the EP onset, there was a second auroral brightening. The convection feature during this second auroral brightening was consistent with the scenario of a Stage-2 EP. We suggest that the first two pseudobreakups, the Stage-1 EP, and the Stage-2 EP are related, respectively, to loading-unloading, directly driven, and internal magnetotail processes.

Finally, in Chapter 5, we make some comparisons between the ionospheric plasma convection vortex structure observed by SuperDARN and the associated equivalent current pattern derived from the magnetometer observations. The discrepancies between the equivalent convection (EQC) and the SuperDARN-observed convection (SDC) pattern are explained in terms of the effect of day-night photoionization conductance gradient, and the coupling between field-aligned currents (FACs) and ionospheric conductances. In particular, we found the agreement between the EQC and SDC patterns is rather poor for a counterclockwise convection vortex. We suggest the discrepancies are probably due to a downward FAC-conductance coupling process.

Acknowledgements

It is difficult to overstate my gratitude to my Ph.D. supervisor, Dr. George. J. Sofko. With his enthusiasm, inspiration, and his great efforts to explain things clearly and simply, he made me feel the study under his supervision a great pleasure. The thesis would not have been possible without him.

I am also grateful to many people in the SuperDARN group at the Institute of Space and Atmospheric Studies at Department of Physics and Engineering Physics, who have assisted me in the course of this work. Among them, Professor Sasha Koustov provided many insightful comments and general advises for my work, and Dr. Dieter Andre instructed me patiently on the data processing software. I got lots of good ideas from many stimulating discussions, even when we drunk beer together, with Donald Danskin, Masakazu Watanabe, Kathryn McWilliams, Roman Makarevitch, and Leo Benkevitch. In particular, Leo Benkevitch collaborated with me in the study presented in Chapter 5 of this thesis.

I would like to acknowledge the help of Dr. Eric Donovan, Trond Trondsen and Brian Jackel in Department of Physics, University of Calgary, who supplied the NORSTAR All Sky Imager data and helped me process the data. Dr. Eric Donovan is also the co-author of my published papers.

Finally, I am forever indebted to my parents and younger sister for their understanding, endless patience and encouragement when it was most required. I have not seen them for four years. I really miss them.

Table of Contents

List of Tables

List of Figures

List of Abbreviations

Terminologies in Space Physics

AACGM:	Altitude-Adjusted Corrected GeoMagnetic
AAF:	Azimuthally-spaced Auroral Form
AIC:	Auroral Ionospheric Cavity
BBF:	Bursty Bulk Flow
BPS:	Boundary plasma sheet
CGM:	Corrected Geomagnetic
CPS:	Central Plasma Sheet
DAB:	Drift-Alfven-Ballooning
DBM:	Drift-Ballooning Mode
DTNL:	Distant Tail Neutral Line
EP:	Expansive Phase
EUV:	Extreme Ultraviolet
FAC:	Field-Aligned Current
GDI:	Gradient-Drift Instability
GSE:	Geocentric Solar Ecliptic
GSM:	Geocentric Solar Magnetospheric
HD:	Harang Discontinuity
IMF:	Interplanetary Magnetic Field
IPS:	Inner Plasma Sheet
LLBL:	Low-Latitude Boundary Layer
MCS:	Meridional Current System
MLAT:	Magnetic Latitude
MLON:	Magnetic Longitude

MLT:	Magnetic Local Time
MTI:	Mid-Tail Initiation
NEI:	Near-Earth Initiation
NENL:	Near-Earth Neutral Line
NGOPS:	Near-Geosynchronous Plasma Sheet
NRFE:	Nightside Radar Flow Enhancement
OCFLB:	Open/Closed Field Line Boundary
OPS:	Outer Plasma Sheet
PBI:	Poleward Boundary Intensification
PSBL:	Plasma Sheet Boundary Layer
SCW:	Substorm Current Wedge
UT:	Universal Time
WTS:	Westward Traveling Surge

Projects and Equipment

ASI:	All-sky Imager
CANOPUS:	Canadian Auroral Network for the OPEN Program Unified Study
CGSM:	Canadian GeoSpace Monitoring
GSC:	Geological Survey of Canada
HF/UHF/VHF	High-Frequency/Ultra High-Frequency/Very High-Frequency
MACCS:	Magnetometer Array for Cusp and Cleft Studies
MARIA:	Magnetometer and Riometer Array
MPA:	Meridian Photometer Array
MSP:	Meridian-Scanning Photometer
NASI:	NORSTAR All-Sky Imager
NORSTAR:	NORthern Solar Terrestrial Array
NRCAN:	Nature Resources Canada
SuperDARN:	Super Dual Auroral Radar Network

Others

ACF:	Autocorrelation Function
EQC:	Equivalent Convection
FOV:	Field Of View
R_E :	Earth's radius
RTP:	Range-Time Plot
SCHA:	Spherical Cap Harmonics Analysis
SDC:	SuperDARN-observed Convection
VLOS:	Line-Of-Sight Velocity

Chapter 1

Introduction

This thesis presents a study of the auroral ionosphere using Super Dual Auroral Radar Network (SuperDARN) observations supplemented by magnetometer and optical measurements. In this chapter we will briefly introduce some of the basic concepts and paradigms of magnetospheric/ionospheric physics which are related to the research work in the thesis. These include descriptions of the solar wind, magnetospheric regions, ionospheric plasma convection and currents, field-aligned currents, auroras and substorms. Finally we outline the research objectives of this thesis.

1.1 Solar wind and magnetosphere

The existence of continuous flow of solar corpuscular radiation was first conjectured from the observed deflection of comet tails as they passed close to the Sun. *Parker* [1959] showed that the continuous flow was due to a steady expansion of the solar corona, and named the outward streaming coronal gas "solar wind". In 1960 and 1962, satellite observations from Explorer 10 and Mariner II found decisive evidence of a continuous supersonic solar wind. The average bulk flow velocity of the solar wind is about 400 km/s. The expanding solar wind also drags the solar magnetic field outward, forming what is called the interplanetary magnetic field (IMF). Although the solar wind moves out almost radially from the Sun, the magnetic field lines are spirals because of the rotation of the Sun. At the orbit of the Earth the angle between the field lines and the radial direction from the Sun is about 45 degrees.

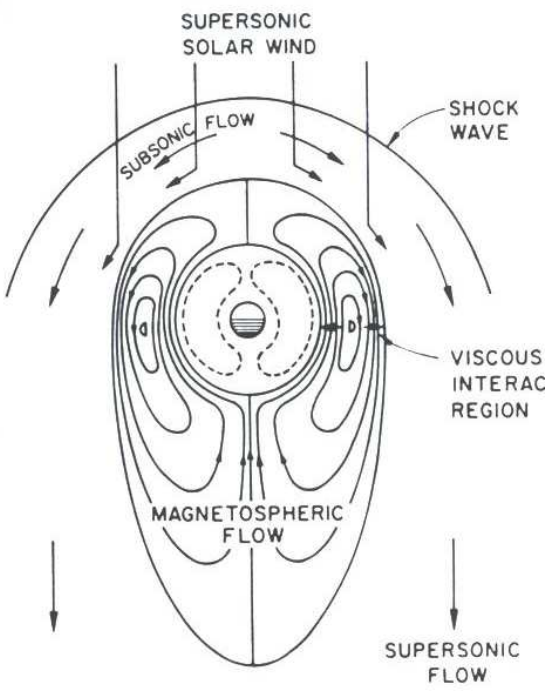

(a)

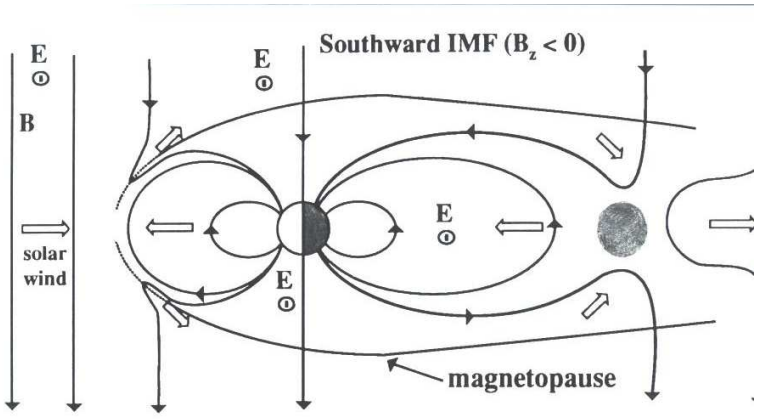

(b)

Figure 1.1 Two types of the solar wind-magnetosphere interaction. (a) Quasi-viscous processes (From *Kelley*, 1989). (b) Reconnection (From *Cravens*, 1997).

The Earth itself has a strong internal magnetic field. In the absence of any external current system, the geomagnetic field can be approximated by a dipole field with an axis tilted about 11º from the spin axis. The solar wind and the accompanying IMF modify the topology of the geomagnetic field lines, creating a cavity called the magnetosphere, the outer boundary of which is called the magnetopause. In front of the dayside magnetopause a boundary called the bow shock is formed due to the change of the solar wind speed from supersonic to subsonic. The region between the bow shock and the magnetopause is called the magnetosheath.

On the dayside, the pressure (mainly the dynamic pressure) of the solar wind leads to a compression of the magnetosphere, such that the magnetopause is typically at a distance between 10 and 12 Earth radii (R_E) from the Earth. Coupling of the IMF with the earth's magnetic field on the dayside by the process of reconnection leads to funnel-shaped areas with near zero magnetic field magnitude, called the polar cusps, through which direct entry of the magnetosheath plasma into the magnetosphere can occur. On the nightside, the magnetic field lines are dragged by the solar wind to great distances (>100 R_E) to form the so-called "magnetotail".

The solar wind couples with magnetosphere mainly in two ways, as shown in Figure 1.1: (1) quasi-viscous interaction [*Axford and Hines*, 1961]; (2) magnetic reconnection or merging [*Dungey*, 1961]. Figure 1.1a illustrates the quasi-viscous interaction in which the plasma inside and near the flanks of the magnetosphere is weakly coupled to the solar wind flow, possibility by waves that propagate across the boundary. Some magnetospheric plasma is then dragged along the antisunward direction, and because of the resulting pressure buildup in the nightside magnetosphere, there must be a flow back toward the sun in the center of the magnetosphere.

Magnetic reconnection is believed to be the major process that transports mass, momentum, and energy from the solar wind into the magnetosphere, and drives the large-scale magnetospheric convection. As shown in Figure 1.1b, reconnection involves the merging of magnetic field lines from the solar wind and the magnetopause to produce two topologically different field lines. In the "antiparallel merging" case, the field lines that undergo reconnection are strictly antiparallel, but in the "component merging" case, there need only be components of the two field line directions that are

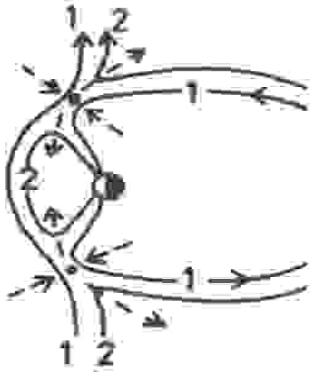

(a)

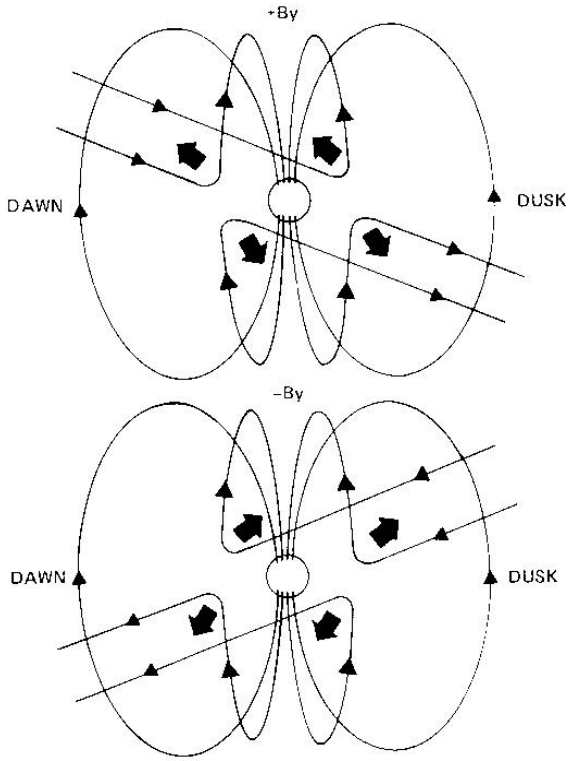

(b)

Figure1.2 (a) Noon-midnight cross section of the magnetospheric topology for northward IMF merging (from *Cowley*, 1983). Heavy dot denotes the neutral line, and the dashed arrow the flow direction in the merging regions. (b) Magnetospheric topology of the reconnection for IMF By-dominated conditions (from *Kivelson and Russel*, 1995), viewed from the Sun. Heavy arrows indicate the direction of magnetic tension force.

antiparallel. Suppose a southward IMF line in the solar wind reaches the magnetopause and merges with a northward Earth magnetic field line, as illustrated in Figure 1.1b. Then, instead of a purely "closed" geomagnetic field line (both ends attached to the Earth) or a purely IMF line, another type of magnetic field line is produced. This new "open" field line has one end attached to the Earth, either near the north magnetic pole or near the south magnetic pole, and the other end in the IMF, stretching out into interplanetary space. The solar wind drags the newly-opened field lines over the polar regions toward the magnetotail, forming the northern and southern "lobe" regions. In the magnetotail, two open lobe field lines, one from the northern lobe and the other from the southern lobe, can reconnect to form a newly closed geomagnetic field line and a new IMF line. The tail reconnection often occurs quite far from the earth (>60 R_E), in which case it is called "distant tail re connection". Interestingly, the quasi-viscous interaction model and the reconnection model produce similar two-cell plasma convection patterns.

During disturbed periods, especially in the late growth phase and expansive phase of the substorm, a so-called "Near-Earth Neutral Line (NENL)" may occur at a distance of 20-30 R_E in the equatorial tail [*Nagai et al*., 1998]. This will be discussed in more detail when we introduce substorm models. Furthermore, dayside reconnection between the field lines poleward of the cusp and the IMF lines may occur in the case of northward IMF Bz, as shown in Figure 1.2a. Finally, reconnection can occur on the magnetopause flanks in the case of strong IMF By as shown in Figure 1.2b.

The concept of "open" and "closed" field lines is essential in distinguishing magnetospheric regions. Regions of open and closed field lines have fundamentally different plasma distributions, so that the particles which flow along the field lines from the magnetosphere to the ionosphere have quite different energies and energy fluxes. Some magnetospheric regions are listed below (see also Figure 1.3).

(i) The **plasmasphere** is a doughnut-shaped region that is located within a few R_E of the Earth, at mid to equatorial latitudes. The plasmasphere contains dense, cold plasma primarily of ionospheric origin and corotates with the Earth. The plasmasphere magnetic field can, with reasonably good accuracy, be described as a dipole field. The plasmapause is the outer boundary of the plasmasphere.

(ii) The **plasma sheet**, also referred to as the "central plasma sheet" by some researchers, normally lies on closed field lines. Plasma densities are typically from 0.4 to 2 cm^{-3} and the particles are hot (keV energies).

(iii) The **neutral sheet** is the current sheet at the middle of the magnetotail, separating the earthward field lines in the northern tail and the tailward field lines in the southern tail. The neutral sheet supports the "cross-tail current' "which flows from dawn to dusk.

(iv) The **northern tail lobe** and the **southern tail lobe** are the regions adjacent to the plasma sheet, containing open field lines in the earthward and tailward directions, respectively. Plasma densities are low (< 0.1 cm^{-3}) in this region and the ion and electron energy spectra are very soft.

(v) The **plasma sheet boundary layer** (PSBL) is a transition region between the almost empty tail lobes and the hot plasma sheet. Counterstreaming field-aligned ion beams are often found in this region and are possibly associated with the distant tail neutral line (DTNL) activation. The PSBL is probably located on closed field lines.

(vi) The **plasma mantle** is a boundary layer several thousand kilometres thick just inside the magnetopause. It lies poleward of the cusp and extends to the tail. It lies on open field lines and is filled by a mixture of plasma of magnetosheath origin and plasma flowing upward from the polar ionosphere. These outflows are called the polar wind.

(vii) The **low-latitude boundary layer** (LLBL) is the low latitude part of the dayside boundary layer and also extends far tailward along the magnetopause flanks. It is partially on open field lines and partially on closed field lines. The LLBL is commonly populated by plasma from both the magnetosphere and the magnetosheath [*Eastman and Hones*, 1979]. Sometimes relatively cold ionospheric components are also present in LLBL [*Fuselier et al.*, 1989].

(viii) The **ring current** and the **radiation belts** are formed by energetic particles moving in the inner portions of the Earth' smagnetosphere, partially in the plasmasphere but extending into the "plasm atrough" region between the plasmasphere and the inner plasma sheet. The ring current plasma is very hot,

with particle energies from tens of keV to MeV range in the "Van Allen" radiation belts. The ring current is westward and carried by energetic electrons and ions whose motion is dominated mainly by their gradient and curvature drifts around the Earth.

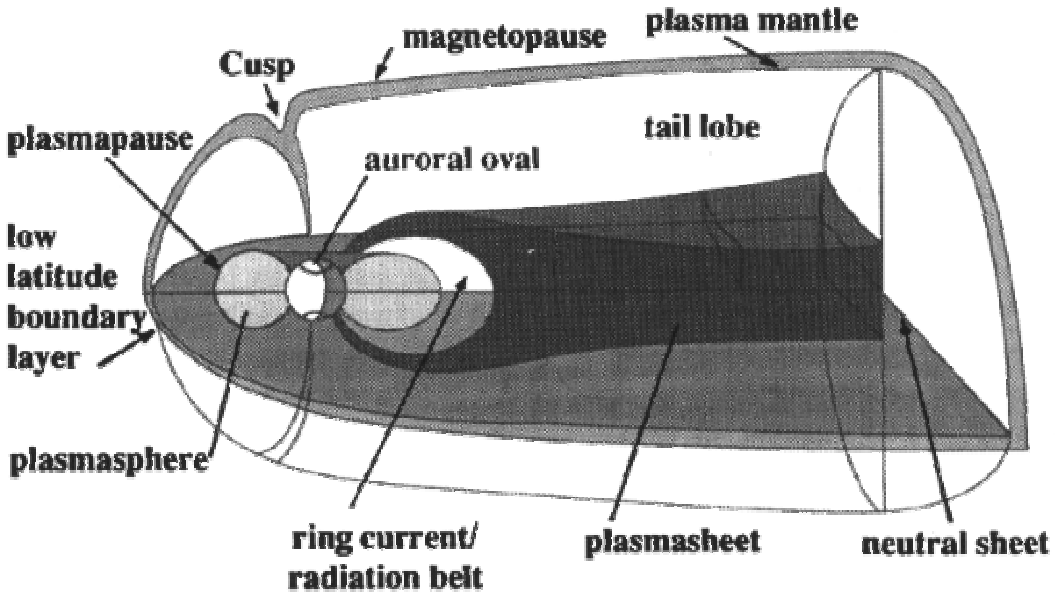

Figure 1.3 Three-dimensional schematic diagram of the Earth's magnetosphere (From *Cravens*, 1997).

To illustrate the effect of IMF on the shape of the magnetosphere we give some examples of magnetospheric field line topology produced by the Tsyganenko-96 model [*Tsyganenko and Stern*, 1996], which is one of the most used and successful empirical global magnetic field models to date. In Figure 1.4, panels (a), (b), and (c) show the magnetic field lines originating from the Earth in the GSM X-Z plane (see Appendix A for the definition of coordinate systems), for different IMF By and Bz conditions. Reconnection between the geomagnetic field lines and the southward IMF is obvious in Figure 1.4b. Also, in the case of southward IMF, the closed field lines in the tail are somewhat "pinched" so that formation of a near-Earth neutral line and reconnection may be expected at ~25 R_E in the tail. In Figure 1.4c, which corresponds to dominantly By+ IMF, some field lines (shown in blue) that just neighbor the northern cusp become

"open". Seen from the GSM X-Y plane (Figure 1.4d), those lines extend to the dawnside flank magnetopause and reconnect to the IMF there. The magnetic field lines in the tail, both open and closed, are also biased to the dawnside, which implies that the neutral sheet is also somewhat tilted under strong IMF By conditions.

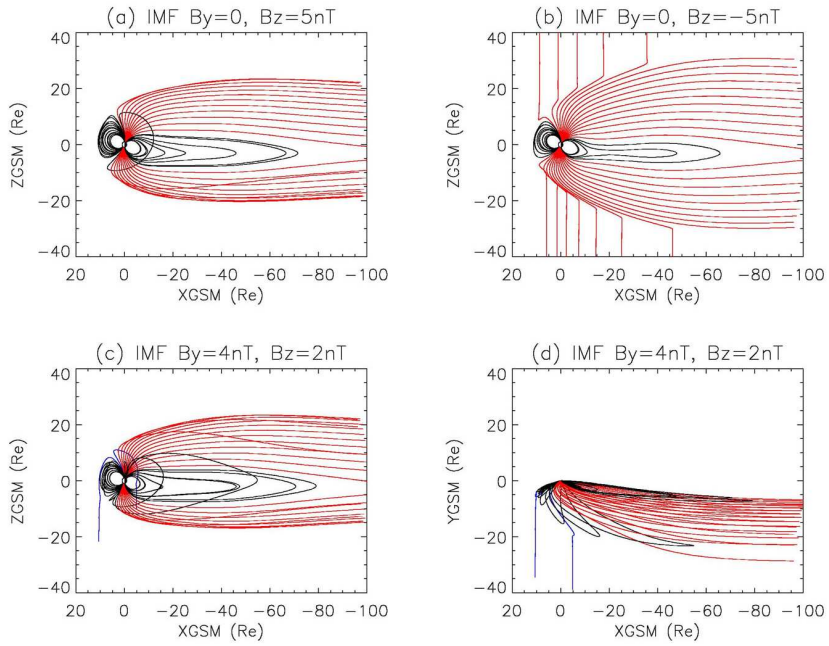

Figure 1.4 Tsyganenko-96 model of magnetic field configuration under different IMF conditions in winter months. The magnetic field lines are projected into the GSM X-Z plane in (a), (b) and (c), but into the GSM X-Y plane in (d). The IMF conditions are as follows: (a) By=0, Bz=5 nT ; (b) By=0, Bz=-5 nT; (c) By=4 nT, Bz=2nT; (d) same as (c).

1.2 Ionosphere

The ionosphere is the ionized component of the Earth' supper atmosphere. Historically, the existence of a "conducting layer", the ionosphere, in the upper atmosphere was first demonstrated because of its prominent effect on radio wave propagation. Even today, ground-based radio wave systems are still very important tools for ionospheric studies. Below we will introduce some basic morphology and dynamic features of the ionosphere.

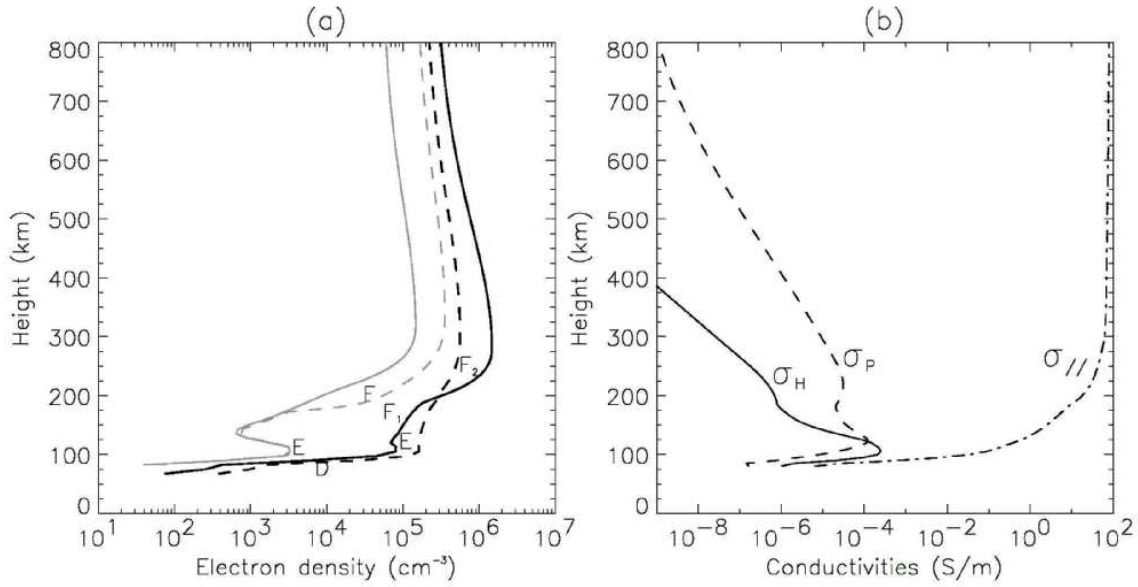

Figure 1.5 (a) Vertical profile of electron density calculated from IRI-2000 model [*Bilitza*, 2001]. Input parameters are Latitude/Longitude=52.5^{0}N/106.5^{0}W (Saskatoon); Date=7-15-2000 (summer, shown in solid lines) and 1-15-2000 (winter, shown in dashed lines); Local time=12 h (shown in darker lines) and 0 h (shown in lighter lines). (b) Vertical profile of Pedersen (solid line), Hall (dashed line) and parallel (dashed dot line) conductivities. The electron density profile is taken from IRI-2000, for latitude 52.5^{0}N, longitude 106.5^{0}W, date 01/15/2000, and local time=12 h. The CIRA neutral atmosphere model [*Rees*, 1988] is used, and calculations of collision frequencies are based on *Banks and Kockarts* [1973].

1.2.1 Ionospheric regions

The ionosphere is divided into several layers or regions according to the electron densities and the dominant ions. These layers are known as the *D*, *E*, and *F* regions, and their locations are shown in Figure 1.5a for different conditions. The first ionospheric layer found was the so-called E region at about 90-150 km altitude. During daytime, one can distinguish a so-called "F_1 ledge" and an F_2 region within the general *F* region. Above the *F* region (> 700 km) is a region of exponentially decreasing density known as the "topside ionosphere". This region extends to altitudes of a few thousand kilometers and, at mid-latitudes and low latitudes, is connected by the magnetic field lines to the plasmasphere. The lowermost region of the ionosphere between 60-90 km altitudes is the D region. The dominant ions in the lower *E* region are NO^+ and O_2^+.

Because O_2 dissociates with increasing height in the *E* region, O^+ dominates in the F region. Above 500 km, lighter ions such as H^+ and He^+ gradually become abundant in the topside ionosphere.

Ionospheric plasma densities differ between daytime and nighttime, and also vary remarkably with season, solar cycle, and level of geomagnetic activity. There are two different ionization processes in the ionosphere. The first is photoionization, caused mainly by solar extreme ultraviolet (EUV) and X-ray photons. The second is impact ionization by precipitating charged particles (including solar and galactic cosmic rays). During the daytime, at subauroral latitudes and even at auroral latitudes during undisturbed magnetic conditions, photoionization is the dominant process, while at high latitudes and at night during magnetic disturbances, impact ionization by precipitating auroral electrons plays an important role in the production of ionospheric plasma.

The particle-impact ionization is of special interest because the precipitating particles not only ionize the atmospheric neutral species but also excite them to higher energy levels. These excited neutral atoms and molecules will generate the optical auroral emissions that will be discussed later. The loss of energy to the atmosphere is different for charged particles and photons, because a precipitating primary particle gradually loses its energy in steps of about 35 eV in the production of each secondary ion-electron pair created by Coulomb collisions as the primary particle travels downward, whereas a photon is absorbed in a single event. A primary precipitating particle can produce secondary electrons that are energetic enough to cause further impact ionization. The stopping altitude of the precipitating particle depends strongly on the initial energy. Electrons and ions with energy less than 1 keV generally deposit their energy above 150 km height, in the ionospheric *F* region, while particles with energies higher than 1 keV can penetrate down to the *E* region and those above about 20 keV to the D region.

1.2.2 Electric currents and plasma convection in the high-latitude ionosphere

The ionosphere is a conducting medium that can support currents flowing both perpendicular and parallel to the magnetic field. Ohm's law for the ionospheric currents is (see Appendix B.1),

$$\mathbf{J} = \sigma_P \mathbf{E}_\perp + \sigma_H \hat{\mathbf{b}} \times \mathbf{E}_\perp + \sigma_{//} \mathbf{E}_{//} \quad , \tag{1.1}$$

where the subscripts '⊥' and '//' denote the components normal and parallel to the magnetic field, respectively, and $\hat{\mathbf{b}}$ is the unit vector along the magnetic field. The derivation of the equations for the Pedersen conductivity σ_P, Hall conductivity σ_H and parallel conductivity $\sigma_{//}$ can be found in Appendix B.1. The three terms on the right side of equation (1.1) are termed Pedersen current, Hall current, and field-aligned current (FAC), respectively.

Typical profiles of the Pedersen, Hall, and parallel conductivities are shown in Figure 1.5b. The Hall conductivity usually peaks at about 110 km and decreases quickly with increasing altitude. The Pedersen conductivity peaks at a slightly greater height and the maximum is smaller than that of the Hall conductivity. The Pedersen conductivity decreases more slowly than the Hall conductivity in the *F* region. Above 200 km altitude, there is virtually no Hall conductivity but still appreciable Pedersen conductivity. The parallel conductivity is very high from the ionosphere up to the magnetosphere; hence the magnetic field lines can be treated as nearly perfect conductors. A small field-aligned potential would generate a large FAC.

In the high-latitude F- region ionosphere, the plasma motion is dominated by Hall drift, given by $\mathbf{V} = \mathbf{E} \times \mathbf{B} / B^2$. Because of the high conductivity along the magnetic field lines, any electric potential that is created between field lines in the magnetosphere will map down to the ionosphere, resulting in ionospheric plasma drift.

Some oversimplified representations of the plasma convection in the high-latitude ionosphere in the northern hemisphere are shown in Figure 1.6. For purely southward IMF the plasma convection pattern consists of two roughly symmetric cells with antisunward flows over the polar cap (on open field lines) and sunward flows within the auroral oval latitudes (on closed field lines). The principal electric fields consist of a dawn-to-dusk electric field $\mathbf{E}_{\mathrm{PC}}$ across the polar cap, which is related to the solar wind-driven reconnection process, and a dusk-dawn field $\mathbf{E}_a$ at the auroral oval latitudes, which is due to the return plasma flow inside the magnetosphere. When the IMF has a duskward component (By>0), the evening convection cell is inflated while the morning

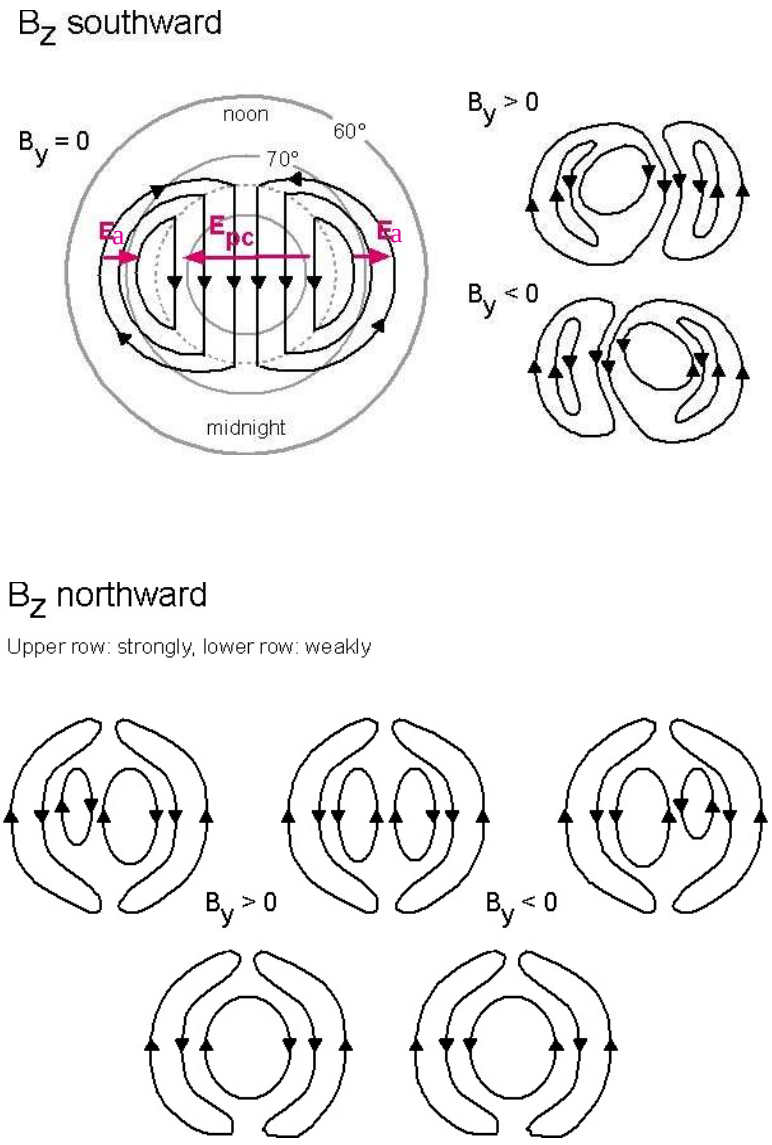

Figure 1.6 Some oversimplified high-latitude ionospheric convection patterns in the northern hemisphere seen from the northern pole. For southward IMF the convection pattern shows a two-cell system with clockwise rotation on the duskside and anticlockwise rotation on the dawnside. The two cells often show dawn-dusk asymmetry due to the effect of IMF By. Some four-cell or three-cell convection patterns may appear for strongly or weakly northward IMF, respectively (from *Reiff and Burch,* 1985).

cell shrinks. The opposite scenario exists when IMF By<0. In case of a northward IMF, the ionospheric convection is usually much more structured and is characterized by velocities of smaller magnitude than in the case of southward IMF. One or two extra "reverse convection cells" may appear at high latitudes for weakly or strongly northward IMF, respectively, resulting in an overall three-cell or four-cell convection pattern. Sometimes the multi-cell structure is not easily recognizable [*Heppner and Maynard*, 1987]; the number of cells is then controversial and is still being investigated.

The field-aligned current is related to convection velocity and electric field by the following equations (see Appendix B.2),

$$J_{//} = B\left(\sum_p \hat{\mathbf{b}} \cdot \nabla \times \mathbf{v} + \nabla \sum_p \cdot \mathbf{v} \times \hat{\mathbf{b}} + \nabla \sum_H \cdot \mathbf{v}\right) \qquad \text{or}$$

$$J_{//} = -\Sigma_P \nabla \cdot \mathbf{E} - \nabla \Sigma_p \cdot \mathbf{E} - \nabla \Sigma_H \cdot \hat{\mathbf{b}} \times \mathbf{E}, \qquad (1.2)$$

where $\sum_P$ and $\sum_H$ are known as the Pedersen and Hall height-integrated (more exactly, field-line-integrated) conductivities, or conductances, respectively. The sign of $J_{//}$ is positive for upward FAC and negative for downward FAC, in accordance with the SuperDARN FAC analysis convention [*Sofko et al*., 1995; *McWilliams*, 1997].

Equation (1.2) shows that the ionospheric FACs can result from: (1) the divergence of the electric field or, equivalently, the curl of the flow (in the northern hemisphere, positive flow vorticity yields a downward FAC while negative curl yields an upward FAC); (2) the product between the electric field and the gradient of Pedersen conductance; (3) the product between the flow and the gradient of Hall conductance. The Hall conductance is generally larger than the Pedersen conductance. Thus the Hall conductance gradient may be larger and hence more effective in producing FACs than the Pedersen conductance gradient.

Statistical FAC distributions obtained from satellite magnetometer observations are shown in Figure 1.7. We see that two FAC bands, similar in size and displacement to the auroral oval, encircle the earth's magnetic poles and that the polarity of the FAC bands reverses across magnetic local noon-midnight meridian [*Zmuda and Amstrong*, 1974; *Ijima and Potemra*, 1978]. The current found furthest equatorward, termed

"Region 2", is directed upward in the morning sector and downward in the evening sector. The adjacent poleward currents, called "Region 1" currents, have the opposite sense to the Region 2 current at any local time. The current density in each region is strongly dependent on the local time and magnetic disturbance level. Typical FAC density, horizontal transverse current density, and total current are of the order of 1 $\mu A/m^2$, 0.1 A/m, and 10^6 A, respectively. The total Region 1 current usually exceeds that of Region 2 by 20-25%. It is interesting to notice that the two systems overlap near local premidnight-midnight region (and extend somewhat into postmidnight sector during geomagnetic disturbed times). Therefore, as shown in Figure 1.7, a downward-upward-downward FAC topology can occur near midnight. According to the general relationship between the FAC, electric fields, and Hall currents (see Appendix B.3), as one proceeds from higher to lower latitudes, a westard Hall current to eastward current reversal, or equivalently, a eastward to westward convection reversal is expected. This current structure was termed the "Harang discontinuity" (HD) in recognization of *Harang*'s [1946] pioneering work.

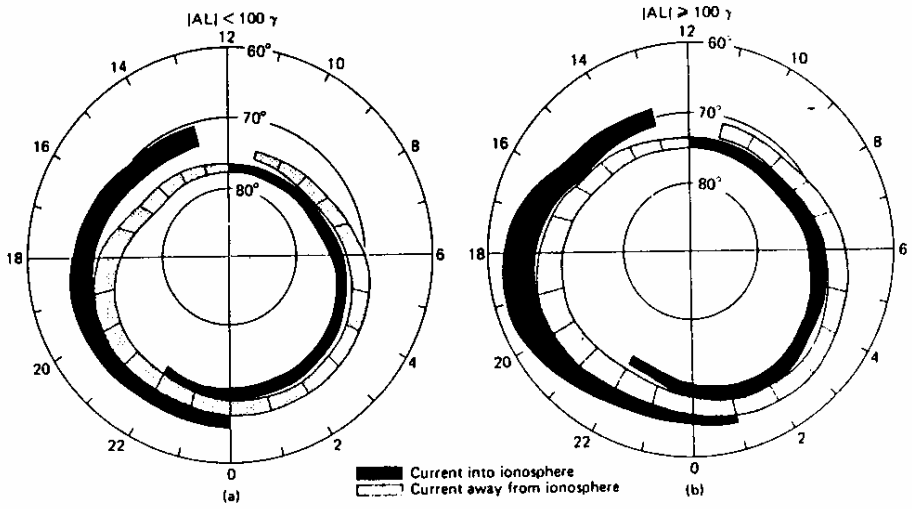

Figure 1.7 Average pattern of FACs in the high-latitude region during (a) weak and (b) disturbances (From *Iijima and Potemra,* 1978).

It is also interesting to notice the correspondence between the two-cell convection pattern and the FAC distribution. The Region 1 current is directly related to the convection cell, that is, there is couterclockwise vorticity or a downward FAC on the

morning side and clockwise vorticy or an upward FAC on the evening side. In the equatorward part of the convection cell, the convection velocity decreases with latitude, and this velocity shear produces a downward vorticity or upward FAC and an upward vorticity or downward FAC on the evening side, corresponding to the Region 2 current system. On the other hand, equatorward of the auroral oval the conductance gradient, which usually points toward the auroral oval, is antiparallel to the dusk-to-dawn electric field $\mathbf{E}_a$ in the morning side and parallel to $\mathbf{E}_a$ in the evening side. Thus acccording to equation (1.2), the Pedersen conductance gradient leads to upward FAC on the morning side and downward FAC on the evening side, again consistent with the Region 2 system.

1.2.3 Equivalent current system

For almost a century, ground-based magnetic field observations have been used to deduce the so-called "equivalent current system". Unlike the satellite magnetometers which make *in situ* measurements of current sheets along the satellite track, the ground-based magnetometers observe magnetic fluctuations arising from the three-dimensional ionospheric currents within about 200 km of the station. Without the knowledge of the ionospheric Hall and Pedersen conductances, one cannot deduce exactly the true ionospheric current pattern from the ground-based magnetometer measurements. Only the equivalent current system, usually assumed to be at ~110 km height and centered vertically above the magnetometer, can be inferred. The equivalent current can be obtained by simply rotating the magnetic field perturbations 90^0 clockwise, or through some complicated upward continuation procedures such as "spherical cap harmonic analysis" (SCHA) technique [*Haines*, 1985; 1988]. Detailed algorithms of SCHA will be given in Chapter 5.2.2.

The basic equation relating the equivalent current to the electric field and ionospheric conductances is given in Appendix B.3. The use of equivalent current in deducing three-dimensional ionospheric electrodynamic parameters has been divided into two approaches. The first approach uses a statistical model of ionospheric conductance to estimate the true three-dimensional ionospheric current system and the convection pattern from the equivalent current, for example, the Kamide-Richmond-

Matsushita (KRM) algorithm [*Kamide, et al*., 1981], and the Assimilative Mapping of Ionospheric Electro-dynamics (AMIE) method [*Richmond and Kamide*, 1988, *Richmond*, 1992]. The second approach uses the two-dimensional electric field measurements from radars and the equivalent current to derive the true ionospheric current system and conductance distribution, for example, the Untiedt algorithm [*Untiedt and Baumjohann*, 1993] and the method of characteristics [*Amm*, 1998].

1.3 Aurora and particle precipitation

The aurora (also known as "Northern Lights" or "Aurora Borealis" in southern hemisphere) is certainly one of the most spectacular phenomena of nature, and has been observed since the dawn of human history. Modern auroral research was founded by the Norwegian pioneer *Kristian Birkeland* [1908], who proposed that the aurora was caused by the particles streaming out of the sun and caught by the Earth's magnetic field. Geomagnetic field lines can guide energetic electrons and protons from the high altitudes in the magnetosphere or magnetosheath to the lower altitudes in the Earth' s ionosphere. Precipitating particles lose their energy via collisions with the neutral particles and ionize them. Some of the atmospheric constituents are excited to higher energy; then they emit auroral light as they return to lower energy states.

The observed auroral spectra are almost all transition lines and bands of neutral or ionized N_2, O, O_2 and N, roughly in the same order of importance. For example, the brightest visible aurora, the "green-line" at 557.7 nm, is due to the transition of an electron from the ^1S excited state to the ^1D state of atomic oxygen, as given below,

$$O(^3P) + e \rightarrow O(^1S) + e' \qquad \text{Excitation from ground state to } O(^1S). \qquad (1.3a)$$

$$O(^1S) \rightarrow O(^1D) + h\nu \qquad 555.7 \text{ nm photon is emitted.} \qquad (1.3b)$$

where *e'* is the secondary electron which normally has considerably less energy than the primary precipitating electron *e*. Another commonly observed line is the "red-line" at 630 nm which occurs when the ^1D state relaxes to the ground state,

$O(^3P) + e \rightarrow O(^1D) + e'$ Excitation from ground state to $O(^1D)$. (1.4a)

$O(^1D) \rightarrow O(^3P) + h\nu$ 630 nm photon is emitted. (1.4b)

The statistical residence time in an excited state before emission is determined by the *Einstein transition probability*. If the atom or molecule in an upper energy state suffers a collision that knocks it out of that state before it has a chance to emit a photon, the emission is "quenched". For example, the $O(^1D)$ state may be deactivated by collisions with N_2 according to,

$$O(^1D) + N_2 \rightarrow O(^3P) + N_2 \quad . \tag{1.5}$$

The importance of the "quenching process" can be revealed by the 630 nm emission. The transition for $O(^1D)$ shown in equation (1.4b) requires about 110 s; this quenching is mostly likely to occur in the lower ionosphere. Thus although the excitation of the $O(^1D)$ state is expected to peak near an altitude of 110 km, the red-line emission generally peaks above 200 km. However, the reaction rates depend heavily on both the thermospheric temperature, which controls the reaction rate coefficients of deactivating collisions such as that in equation (1.5), and the number density of quenching particles (mainly N_2 for 630 nm emissions). Red-line emissions at altitudes as low as 185 km are common in observations [*Jackel et al.*, 2003]. In ground-based optical observations, the ambiguity of the emission height may cause a considerable error in determining the emission height in the case of low-elevation-angle observations. This problem can be partly solved by using a triangulation method in which optical measurements of a given emission region are made from different locations [*Jackel et al.*, 2003]; this will be discussed in Chapter 2.5.3.

The red-line optical emission is of special interest in this thesis because the red-line emissions and the SuperDARN-measured convection velocities are both *F* region features, so it is reasonable to combine them to provide the *F* region ionospheric morphology and dynamics.

The behavior of the protons penetrating the atmosphere is fundamentally different from the behavior of the penetrating electrons. The emissions H_α at 656.3 nm and H_β at

486.1 nm result from excited hydrogen atoms that are produced when energetic protons (H^+) bombard the atmosphere. The excitation mechanism is as follows,

$$X + H^+ \rightarrow X^+ + H^* \tag{1.6a}$$

$$H^* \rightarrow H + h\nu \qquad \text{proton auroral emission} \tag{1.6b}$$

where X denotes atmospheric neutrals, and an asterisk denotes an excited state. The hydrogen atom is free to move along the geomagnetic field line until a new collision occurs, as given by the equation,

$$H + X \rightarrow H^+ + X + e\,. \tag{1.6c}$$

As a result, process (1.6a) can occur again, and the process repeats until there is not enough primary proton energy left to ionize atmospheric neutrals. This proton-hydrogen ion-neutral interchange process leads to a spreading of the proton aurora, so that the emission appears to be quite diffuse. The proton emission is also expected to peak near an altitude of 110 km.

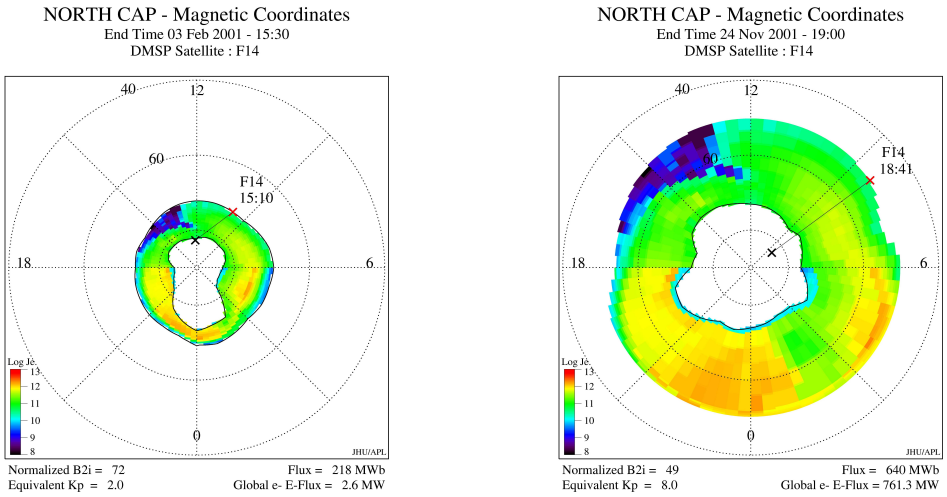

(a) (b)

Figure 1.8 Auroral oval position in northern hemisphere during (a) quiet periods: 2001/02/03 1530 UT, and (b) strongly disturbed periods: 2001/11/24 1900 UT. The plots are taken from http://sd-www.jhuapl.edu/Aurora/ovation/ovation_display.html.

Geographically, most auroras are located within oval shaped regions around the geomagnetic poles of the Earth. The ovals are displaced relative to the magnetic poles such that they extend further towards the equator in the midnight sector. The regions inside the ovals are called the polar caps, in which the magnetic field lines are open. The field lines inside the oval (and at lower latitudes) are closed. The diameter of the ovals depends on the amount of the open flux in the polar cap. During active periods, especially during major geomagnetic storms, the ovals expand to lower latitudes. Figure 1.8 gives the observed auroral oval position during average and extremely disturbed periods. Obviously, the area of polar cap significantly expands and the equatorward border of the auroral oval moves to much lower latitude during such highly disturbed intervals.

The auroral morphology has been associated with different particle precipitation regimes obtained from satellite observations, with the exception of very small scaled "auroral arcs" (tens or hundreds of metres), whose size is beyond the resolution of most satellite measurements. An often-used classification divides the auroras into "diffuse" and "discrete" auroras, as follows. Diffuse aurora are found on the equatorward part of auroral oval, in the region of the so-called "central plasma sheet" (CPS) precipitation, most likely mapping to the inner plasma sheet where the magnetic field is almost dipolar. Discrete auroras tend to be located on the poleward part of the auroral oval, in the region of the so-called "boundary plasma sheet" (BPS) precipitation mapping to outer plasma sheet (OPS) and its boundary layer (PSBL), where the magnetic field is stretched and quite non-dipolar.

Although the terms CPS and BPS were introduced by *Winningham et al*. [1975], it took some time before a clear operational distinction for identifying CPS/BPS precipitation regions was made. This distinction was developed by *Newell et al*. [1996] using DMSP observations. They performed a running average of the correlation coefficient of each electron spectrum (taken during about 1 second) with the 5 previous spectra during an orbital pass. A low correlation coefficient indicates that the satellite is in a region with "structured" electron precipitation, namely the BPS. A high correlation coefficient indicates that the satellite is in an "unstructured" precipitation region, namely the CPS. A boundary denoted as "b4s" and representing the

structured/unstructured (or BPS/CPS, equivalently) electron precipitation boundary was defined as the location at which the correlation coefficient drops from the 0.95-0.6 range to below 0.6. Because the electron precipitation is the major source of the ionization at night in the high-latitude ionosphere, we should expect that, in the ionosphere, the conjugate area to the BPS region is much more structured than the area conjugate to the CPS.

Inside the polar cap there is spatially homogenous precipitation of low energy electrons of only a few hundred eV; this is called the “polar rain” [*Winningham and Heikkila*, 1974]. Polar rain can be used as a diagnostic tool for open field lines [*Shirai et al*., 1998]. It was found that the 630 nm emission caused by polar rain precipitation inside the polar cap is fairly uniform at about 60 R, while in the poleward part of the auroral oval the average 630 nm emission is about 170 R. Therefore it was suggested that the 110 R emission intensity level may be used as a threshold to identify the poleward boundary of 630 nm emission, giving an estimated open-closed field line boundary (OCFLB) with a rms error of ~1º on the basis of the comparison with the DMSP observations [*Blanchard et al*., 1997].

Several characteristics of the SuperDARN HF radar observations have been considered to have the potential for estimating the magnetospheric boundaries. Broad radar spectral width has long been used to identify the dayside cusp region [*Baker et al*., 1995; *Milan and Lester*, 2001]. On the nightside, a sharp spectral width transition from low to high latitudes was also frequently observed but has been given different interpretations. It was related to the CPS/BPS boundary by *Lewis et al*. [1997] and *Dudeney et al*., [1998], while it was also related to the OCFLB by *Lester et al*. [2001]. The equatorward border of the SuperDARN *E* region echoes may act as a tracer of the b2i (ion isotropy boundary), which represents the equatorward boundary of the auroral oval [*Jayachandran et al*., 2002].

1.4 Substorm: Phases and models

The morphology and generation of magnetospheric substorms are long-standing and critical issues of magnetospheric-ionospheric physics. Because of the magnetic disturbances and the accompanying spectacular auroral features, the term "auroral

substorm" was coined by *Akasofu* [1964], who for the first time gave a classical morphological definition of a substorm process. Three phases occur in a typical substorm, namely the growth phase, the expansion phase and the recovery phase [e.g., *Rostoker et al*., 1980].

The growth phase usually begins with a southward turning of the IMF, which enhances the convection electric field as the solar wind energy is transferred to the magnetosphere, most possibly via reconnection. Because of the time delay and difference between the reconnection rate on the dayside magnetopause and on the nightside, there is a net removal of the closed magnetic flux from the dayside magnetosphere, and an increase in open flux in the magnetotail. As a result, the dayside magnetopause moves inward, often in an oscillatory fashion, and the polar cap (the region of open field lines) expands equatorward. The tail lobe field lines are stretched, and the lobe field strength and magnetic pressure increase, which causes a thinning of the plasma sheet. During the substorm growth phase the magnetosphere undergoes a sequence of changes in configuration and an increase in trapped energetic particles in the plasma sheet. This eventually leads to a global instability and the explosive release of the energy stored in the magnetotail; this phase is called the expansive phase (EP).

The substorm EP starts the active part of the substorm process. Energy is dissipated explosively during the substorm EP into magnetosphere and ionosphere. The start of the phase is called the substorm onset. The term “breakup” is typically used in optical auroral observation, because the pre-existing arcs expand poleward rapidly at onset, causing a “breakup” of the original growth phase structures. Part of the near-Earth cross-tail current disappears in what is called the current disruption. A new current system called the substorm current wedge (SCW) is established, which contains a downward FAC on the eastern side of the wedge, a westward electrojet (WEJ) in the auroral ionosphere, and an upward FAC on the western side of the wedge [*McPherron et al*., 1973]. The magnetic field changes to a more dipolar configuration in the near-Earth plasma sheet. Injections of accelerated particles are seen at the inner edge of plasma sheet [*Birn et al*., 1997]. In the ionosphere, auroras suddenly brighten and expand poleward on the nightside, starting from what had been the stable, most equatorward arc in the midnight sector. An auroral bulge with a westward travelling

surge (WTS) forms. Ground based magnetometers show negative magnetic bays of X component associated with the WEJ. Magnetic Pi2 pulsations are observed up to the poleward edge of the auroral electrojet, and can be used as ground-based indicators of the EP onset [*Olsen and Rostoker*, 1975].

At the end of the substorm EP, auroral activity begins to dim at lower latitudes in the oval, and quiet arcs reappear; to the west, the WTS degenerates, and a westward-drifting loop replaces it. Eastward propagating omega bands are seen on the poleward boundary of a diffuse aurora. Pulsating auroras are typical in the morning sector. The magnetosphere slowly recovers to the pre-substorm state over many hours. This phase of a substorm is called the recovery phase.

Magnetospheric substorms encompass a myriad of dynamic disturbances in the magnetosphere, the ionosphere, and even the thermosphere. Many issues related to substorms are still quite controversial. Several substorm models exist, but they may be broadly classified into two categories, the near-Earth initiation (NEI) models and the mid-tail initiation (MTI) models, depending on which region is considered as the location of the onset or major mechanism and which region is the location of the subsequent or secondary effects. An excellent review of the two categories was given by *Lui* [2001].

For about two decades the MTI model was the leading substorm model. It invokes a magnetic reconnection in the mid-tail and the resulting high-speed earthward plasma flow and magnetic flux pileup as the cause of a substorm EP onset. Historically, it is referred as a "Near-earth neutral line" (NENL) model because, in its early version, the reconnection was assumed to occur in the near-Earth region ($|X| \quad 15\ R_E$). A comprehensive description of the model can be found in *Baker et al*. [1996]. However, results of the GEOTAIL mission have indicated that the tail reconnection is usually located beyond 20 R_E downstream [*Nagai et al*., 1998, *Machida et al*., 1999]. In the NENL model, an X-line forms between the oppositely directed closed field lines above and below the current sheet due to the plasma sheet thinning and the highly stretched field configuration during substorm growth phase (see Figure 1.4b). The reconnection proceeds slowly at first. However, as time progresses, the current sheet becomes thinner and the rate of reconnection increases until it becomes explosive. When the

reconnection begins to involve lobe field lines, a portion of the plasma sheet tailward of the X-line is decoupled from the ionosphere and moves antisunward down the tail as a closed field line structure known as a "plasmoid". The recovery phase begins when the plasmoid starts to retreat tailward. Such a plasmoid structure was often observed in the mid- and distant tail regions during the late substorm EP and recovery phase [*Moldwin and Hughes*, 1993; *Nagai et al*., 1994], which constitute the most successful part of the MTI model. An obvious question to the model is how the reconnection in the mid-tail is related to the current disruption and SCW formation in the near-Earth region. To solve this problem, the "flow braking" scenario, a revision of the MTI model, was proposed by *Shiokawa et al*. [1997; 1998]. They postulated that the fast earthward flows ejected from the mid-tail X-line are slowed down and diverted by the rapidly rising magnetic pressure near the transition region from tail-like to dipolar field in the near-Earth tail. This flow braking induces an eastward inertial current opposing the cross-tail current, consequently leading to the current disruption and the SCW formation. However, *in situ* observations have shown that the magnetic dipolarization at the near-geosynchronous-orbit plasma sheet (NGOPS) usually develops in a non-MHD fashion [*Lui et al*., 1999], which cannot be explained under the framework of "flow braking" theory.

The NEI model limits the onset location in the near-Earth region only. A plasma process at the NGOPS, most probably some kind of plasma instability, leads to the cross-tail current disruption and sets up the SCW for a substorm EP onset [*Lui*, 1991; 1996]. Magnetic reconnection might not be the cause but rather a possible consequence of the onset process, that is, the initial current disruption in the near-Earth region can launch a tailward-propagating rarefaction wave, which may set up a favorable condition for an X-line to form farther tailward [*Lui*, 1996; *Erickson et al*., 2000]. Suggestions for the possible NGOPS instability include a cross-field current instability [*Lui et al*, 1991], a drift-Alfven-ballooning (DAB) instability [*Roux et al*., 1991], a shear flow ballooning instability [*Samson et al.*, 1996], or a magnetosphere-ionosphere coupling feedback instability [*Kan*, 1993]. The ballooning instability was initially proposed by *Roux et al*. [1991] and was criticized by *Ohtani and Tamao* [1993a]. They found that, when taking into account the stabilizing effects of plasma compressibility in 19 out of 22 events they studied, a necessary condition for the ballooning instability was not satisfied. However,

Liu [1997] pointed out that *Ohtani and Tamao* [1993a] erred in their handling of the parallel momentum equation. A correction of this error leads to a much increased likelihood of ballooning instability in a realistic plasma sheet. Two-fluid MHD simulations by *Pu et al*. [1997] showed two unstable drift-ballooning mode (DBM) solutions, namely DBM1 (conventional ballooning mode) and DBM2 (drift-Alfven ballooning mode, also known as DAB mode). Using GEOS 2 observations they found that the necessary conditions for DBM2 were fulfilled in 14 out of 16 events. On the other hand, *Elphinstone et al*. [1995] studied the azimuthally spaced auroral forms (AAFs) observed during auroral substorms and suggested that the AAFs are associated with the modified flute/ballooning instability developed by *Ivanov and Pokhotelov* [1987] and *Ivanov et al*. [1992]. The CRRES satellite observation provided clear evidence relating the DAB instability in the NGOPS to the substorm EP onset [*Maynard et al*., 1996; *Erickson et al*., 2000].

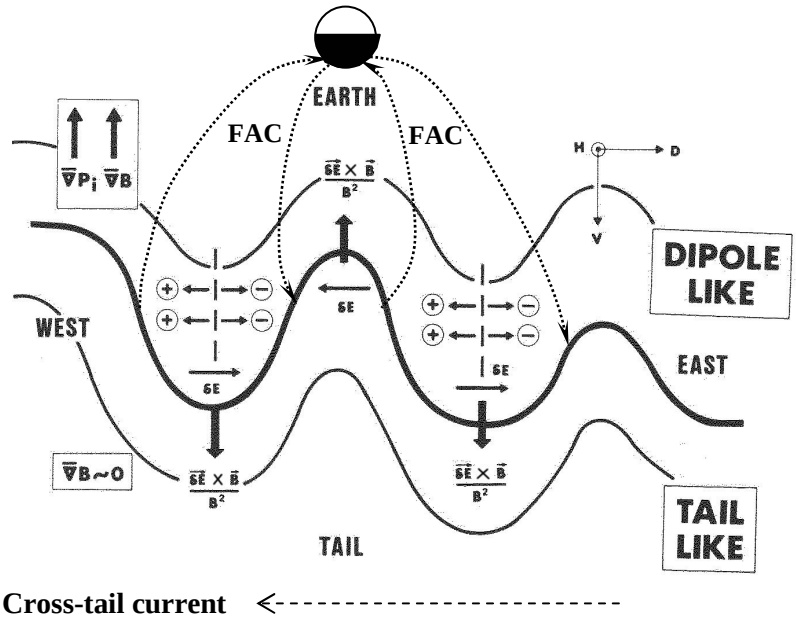

Figure 1.9 Sketch of the drift wave instability at the near-geosynchronous plasma sheet (slightly modified from *Roux et al.* 1991).

A simplified sketch of the DBM instability is shown in Figure 1.9. The gradient of the pressure and magnetic field both point earthward between the boundary of the

dipole-like region and the tail-like region. Assume that there is an initial perturbation moving in the azimuthal direction. Energetic ions and electrons will undergo westward and eastward drifts, respectively. Positive and negative charges accumulate at the edge of the propagating perturbation, generating FACs and producing a polarization electric field $\delta\mathbf{E}$. The resulting $\delta\mathbf{E}\times\mathbf{B}$ force tends to enhance the amplitude of the initial perturbation so that the instability grows. The alternating polarization electric fields that develop in these waves can grow to such a size such that, in a specific half-cycle of the wave, the eastward polarization electric field can reach a sufficient magnitude to overcome the normal westward dawn-dusk electric field. Within that half-cycle the drift wave couples to the Alfven ballooning mode and plasma kinetic energy is converted into the electromagnetic energy which flows toward the ionosphere via Alfven waves. When the energy is released from the plasma during such eastward electric field excursions faster than the background convection energizes it, the cross-tail current is reduced, magnetic field dipolarization begins, and the SCW forms. The incident Alfven wave is partially reflected because of an impedance mismatch between the ionosphere and magnetosphere, and a secondary Alfven wave is launched from the ionosphere due to the disturbance of the ionospheric conductivities and electric fields. The bouncing waves set up the high-latitude Pi2 pulsations (40-150s) which can be seen on the ground up to the poleward limit of the auroral electrojet [*Olson*, 1999; *Olson and Rostoker*, 1975].

Intense debates between the NEI and MTI model proponents have taken place for over a decade. Several attempts have been made to reconcile the conflict. It is possible that the current disruption itself is an independent process, but the reconnection in the mid-tail may set a favorable condition for the current disruption [*Ohtani et al*., 2002]. For example, *Pu et al*. [1999] found that when a fast earthward flow is decelerated inside the NGOPS, the DBM in both equatorial and off-equatorial regions at the NGOPS become unstable and the instabilities grow much faster than without the flow. On the other hand, though enhanced earthward flow is not necessary in the NEI model for a substorm, it was found that following the local onset and SCW establishment, such enhanced earthward flows may play an important role in maintaining the SCW by continually feeding energy into the near-Earth magnetosphere [*Birn et al*., 1999]. Thus

a synthesis of the NEI and MTI models may exist. On the other hand, there is also the possibility one of the models may be correct in some substorms, while the other model is correct for other substorms. For example, *Baumjohann et al*. [1996] suggested a distinction between storm-time and non-storm time substorms. The former behaved more consistently with the MTI model, while the latter usually complied with the NEI scenario. As stated by *Lui* [2001], before the validity of any given model is questioned, the presumption that only one theory is correct may first need to be questioned. In this thesis, we will argue that this is the case for substorm studies. It is not inconceivable that, the future solution to the substorm onset problem will consist of a combination of MTI and NEI scenarios.

An auroral brightening is not always followed by global expansion. Occasionally the brightening lasts only a few minutes and then decays without causing any significant geomagnetic disturbance. Such short-lived and localized auroral activity is called a pseudobreakup or pseudosubstorm. Pseudobreakups can occur either as substorm precursors [*Koskinen et al*., 1993; *Aikio et al*., 1999] or as isolated events during quiet times [*Sergeev et al*., 1986; *Ohtani et al*., 1993b]. Pseudobreakups show most of the signatures found in fully developed substorm onsets, like negative magnetic bays and Pi2 pulsations from ground magnetometer observations (but usually localized in both latitude and longitude), cross-tail current disruption and energetic particle injection at the inner edge of the plasma sheet [*Nakamura et al*., 1994], and plasmoid ejection in the far tail [*Aikio et al*., 1999]. *Rostoker* [1998] suggested that pseudobreakups and substorm EP onsets are associated with almost the same magnetospheric processes but differ only in the magnitude of disturbance, the spatial and temporal scales, and the global consequences. *Ohtani et al*. [1993b] proposed that the major difference between a pseudosubstorm and a major substorm EP onset is that, during a pseudobreakup there is an absence of the tailward expansion of the current disruption. Only the major substorm EP onsets are associated with a significant poleward expansion of auroras and currents in the ionosphere. The pseudobreakups do not grow into real substorms because the amount of energy stored in the tail is not sufficient [*Ohtani et al*., 1993b; *Nakamura et al*. 1994] and/or the ionospheric conditions are not favorable for a full-scale SCW formation [*Koskinen et al*., 1993].

The ionospheric plasma convection flows usually undergo dramatic changes and have fundamentally different features during different stages of a substorm [e.g., *Voronkov et al*., 1999; *Friedrich et al*., 2001; *Kadokura et al*., 2002a; 2002b]. As an efficient tool for direct measurements of two-dimensional ionospheric convection, the SuperDARN program has contributed substantially to substorm studies since its inception [*Lester et al*., 2000]. In the following we will mention some of those contributions during the past five years. The dynamics of global ionospheric plasma convection accompanying substorm evolution were frequently studied for specific events [e.g., *Lyons et al*., 2001; *Lester*, 2002; *Grocott et al*., 2002; *Liang et al*., 2004b; *Hashimoto et al*., 2004]. The flow features were also investigated for a number of specific regions, e.g. the dayside ionosphere [e.g., *Kavanagh et al*., 2002; *Lyons et al*., 2003], inside the polar cap [e.g., *Milan et al*., 2002; *Jayachandran et al*., 2003], inside the nightside main auroral oval [e.g., *Yeoman et al*., 2000a; *Wild et al*., 2000], near the equatorward border of auroral oval [e.g., *Parkinson et al*., 2003], and between conjugate hemispheres [e.g., *Yeoman et al*., 2000b]. The SuperDARN measurements are often made in conjunction with optical auroral observations [e.g., *Liang et al*., 2004a; 2004b; *Bristow et al*., 2001; 2003], global magnetometer observations [e.g., *Saka et al*., 2001; *Kikuchi et al*., 2000, *Boralv* et al., 2000; *Khan et al*., 2001], and satellite *in-situ* observations in the magnetotail [e.g., *Sandholt et al*., 2003]. The effects of substorms on SuperDARN radio propagation and absorption were discussed by *Gauld et al*. [2002].

1.5 Outline of the thesis

The research purpose of this thesis is a multi-instrument joint study of the convection, magnetic and optical auroral dynamics of the high-latitude ionosphere. Chapter 2 gives a brief introduction to all the observation instruments used in this thesis. Chapters 3, 4 and 5 constitute the main work of the thesis. In Chapter 3, we investigate a particular class of enhanced nightside convection events, which we classify as “nightside radar flow enhancements” (NRFEs), in order to study their spatial and temporal relationship with optical auroral activity. We propose a new model to explain the nearly simultaneous onset of the NRFEs and the auroral intensifications.

Some of the results in this chapter were published in *Liang et al*. [2004a]. Chapter 4 presents a study of two-dimensional ionospheric convection and optical auroral dynamics of a small postmidnight substorm event during dominated IMF Bz+ and By+ intervals on October 9, 2000. The whole event sequence is explained in terms of loading-unloading, directly driven, and internal magnetotail processes. These results have been published in *Liang et al*. [2004b] and also form the contents of another paper to be submitted to *Annales Geophysicae*. In Chapter 5, some comparisons between the magnetometer-based equivalent convection and the convection patterns observed by SuperDARN HF radars are made, and the reasons for their discrepancies are discussed. A paper based on the results of this chapter is being drafted. The thesis concludes in Chapter 6 with an overall summary of the work and some proposals for future research.

Chapter 2

Observation instruments

Several sets of observation instruments are involved in the thesis: SuperDARN HF radars, the ground-based magnetometers and riometers, a median-scanning photometer array, high-resolution all-sky imagers, and satellite instruments. In the following we will give a brief introduction to those instruments and their usage in the thesis. Some common data processing procedures, for example, those for the radar and the all-sky imagers, are also introduced in this chapter.

2.1 SuperDARN HF radars

SuperDARN (Super Dual Auroral Radar Network) is an international network of high-frequency (HF) radars used to study the plasma convection, the electric field, and the FACs in the high-latitude ionosphere. Each SuperDARN HF radar is a coherent scatter radar that is sensitive to wave-like plasma irregularities which, for particular directions of the spatial wave vector, cause constructive interference of the scattered signals. Theoretically, the plasma wave irregularities which are favorable for coherent scattering have wave vectors given by [*Kelley*, 1989],

$$\mathbf{k}_{irr} = \mathbf{k}_s - \mathbf{k}_i \quad , \tag{2.1}$$

where $\mathbf{k}_s$ and $\mathbf{k}_i$ are the wave vectors of the scattered and incident waves, respectively. For a monostatic radar equation (2.1) reduces to $\mathbf{k}_{irr} = -2\mathbf{k}_i$. In the ionosphere the

irregularity wavefronts are generally field-aligned, and therefore $\mathbf{k}_i$ must be perpendicular to the geomagnetic field. Since the high latitude magnetic field lines are nearly vertical, it would be impossible for the radio wave to achieve this orthogonality condition above the ionospheric *E* region if the propagation were along a straight line. However, orthogonality may be achieved if there is refraction of the HF waves in the ionosphere. An advantage of HF radar over UHF and VHF radars is that there is more refraction at lower frequencies.

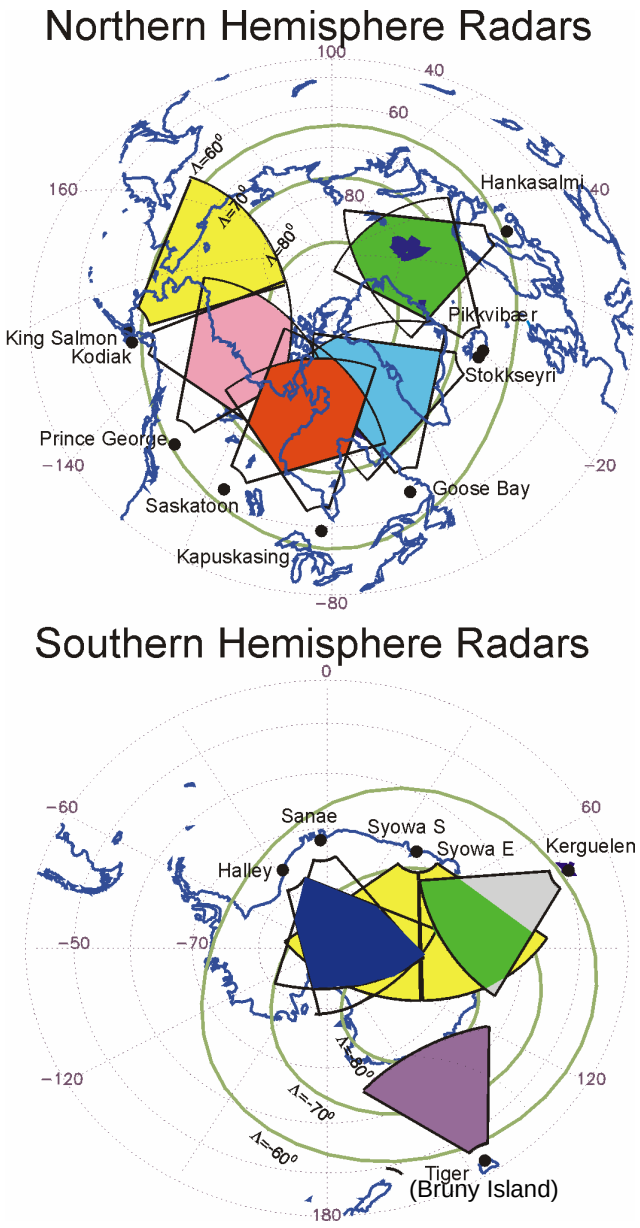

Figure 2.1 Locations of currently operating SuperDARN radars and their field of views (FoVs).

Table 2.1 SuperDARN radar sites and their boresight directions.

Radar Station	Geo. Lat (^oN)	Geo. Lon (^oE)	AACGM Lat (^oN)	AACGM Lon (^oE)	Boresight Direction
Saskatoon	52.16	-106.53	61.34	-45.26	+23.1
Kapuskasing	49.39	-82.32	60.06	-9.22	-12.0
Prince George	53.98	-122.59	59.88	-65.67	-5.0
Goose Bay	53.32	-60.46	61.94	23.02	+5.0
Stokkseyri	63.86	-22.02	65.04	67.33	-59.0
Kodiak	57.60	-152.20	57.17	-96.28	+30.0
King Salmon	58.68	-156.65	57.43	-100.51	-20.0
Þykkvibær	63.86	-19.20	64.59	64.65	+30.0
Hankasalmi	62.32	26.61	59.78	105.53	-12.0
Sanae	-71.68	-2.85	-61.52	43.18	+173.2
Syowa East	-69.01	39.61	-55.25	22.98	+106.5
Syowa South	-69.00	39.58	-55.25	23.00	+165.0
Kergulen	-49.35	70.26	-58.73	122.14	+168.0
Halley	-75.52	-26.63	-61.68	28.92	+165.0
Bruny Island	-43.38	147.23	-55.31	-133.36	+180.0

The present SuperDARN radars are based upon the original radar design used in Goose Bay [*Greenwald et al.*, 1985]. Currently 15 radars are operating, nine of which are in the northern hemisphere and six in the southern hemisphere (see Figure 2.1). Each radar operates at a frequency between 8 and 20 MHz. The main transmitting antenna array of each radar consists of 16 log periodic antennas electronically controlled by a phasing matrix which steers the radar beam through 16 successive azimuthal angles. The azimuthal half power beam width varies between 2.5^o at 20 MHz and 6^o at 8 MHz. Each beam position is sustained for 7 seconds during normal-scan "common mode" operation (or for 3 seconds for fast-scan common mode operation), then is switched by means of a phasing matrix to the next beam position, which is 3.24^0

east or west of the previous one. In common-mode operation, the sequence of 16 beams leads to a field of view (FoV) of nominal azimuthal extent 51.84^0. The complete scan takes about 2 minutes for the normal-scan common mode and 1 minute for fast-scan common mode. The locations of the radars and their FoVs are listed Table 2.1 and shown in Figure 2.1.

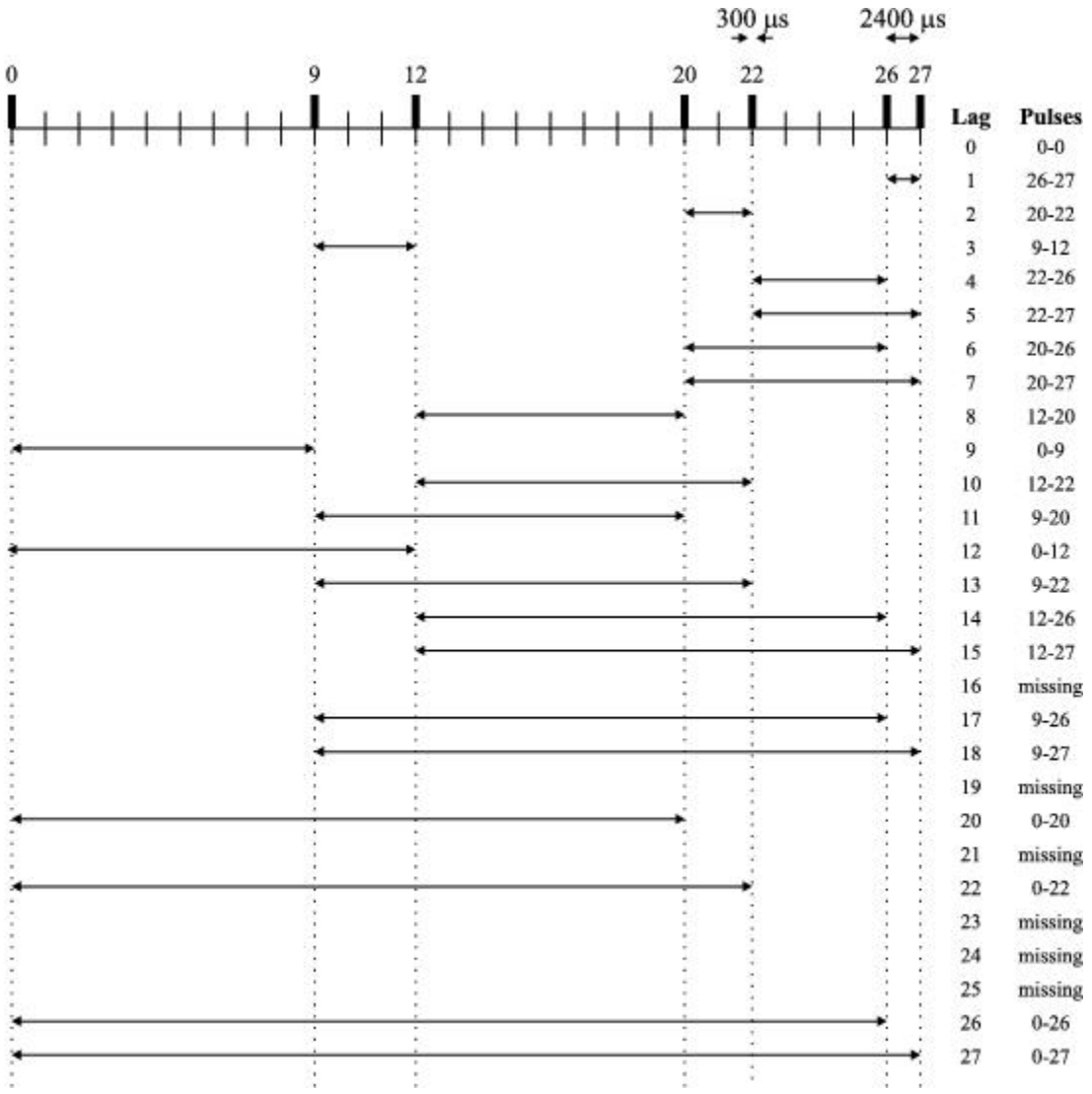

Figure 2.2 The 7-pulse sequence transmitted by the SuperDARN radars. The pulses are 300 µs long and they are separated by integral multiples of the unit separation (lag) time which is normally set to 2.4 ms. A total of 22 usable lags is achieved to calculate the ACF.

The transmitted pulse length, which determines the range resolution, is 300 μs (~45 km) for common mode (normal-scan or fast-scan). However, the pulse length can be decreased to 100 μs (range resolution ~15 km) for the discretionary mode operation. In total 70 range bins are sampled along each beam, the first starting with a delay of 1200 μs after the leading edge of the pulse. This first range bin thus begins at a range of 180 km and the maximum range is 180+70*45=3330 km. The large range coverage makes possible the observation of scattering from near-range meteors in the mesosphere (180-500 km range) to far-range high-latitude ionospheric *F* region scattering out to ranges exceeding 3000 km.

SuperDARN radars measure the complex autocorrelation function (ACF) of the returned signal through the transmission of a sequence of irregularly spaced pulses. The pulses are separated by integral multiples of the unit pulse separation (lag) time (normally set to 2.4 ms). The returned signal is coherently detected so that the in-phase and quadrature components of the signal can be determined, which allows for the real and imaginary parts of the ACF, or alternatively the magnitude and phase of the ACF, to be determined. In terms of ACF determination, a multi-pulse sequence of N pulses is equivalent to $N(N-1)/2$ double-pulse pairs. Fundamentally, when a pulse pair separated by time τ_{lag} is used, one point of the ACF at that lag is determined. A multi-pulse sequence can be carefully devised such that the pulse separations contain most or all of the lags necessary for determining the ACF and such that there is little or no ambiguity in the ranges that contribute to any given lag. Theoretically, for an N-pulse sequence, $N(N-1)/2$ lags of the ACF can be determined, one for the separation of each double-pulse pair. However, due to the monostatic nature of the radars, at some range cells there may be several "bad" lags, because the SuperDARN radar cannot receive when it is transmitting at the same time; therefore, at the time the radar is transmitting new pulses, any returned signal is discarded. In addition, the correlation of a pulse with itself naturally leads to the "zero lag" ACF, which is simply the power of the returned signal. The ACF at each lag is averaged over about 70 multi-pulse sequences for the common scan mode (or about 30 sequences for the fast scan mode). Currently, in normal operation mode each sequence consists of 7 pulses with successive lag intervals of 21.6 ms, 7.2 ms, 19.2 ms, 4.8 ms, 9.6 ms, 2.4 ms (see Figure 2.2), a

maximum of 22 usable lags (including the "zero lag" value) is achieved. For the future, 8-pulse and 9-pulse sequences have been designed and tested [*McWilliams*, 2003].

If the complex ACF has been determined for a sufficient number of lags, several important parameters can be derived by assuming the following ACF models:

$$ACF(\tau) = P_0 \exp(-\lambda\tau + i\,\omega\tau), \text{ or} \tag{2.2a}$$

$$ACF(\tau) = P_0 \exp(-\sigma^2\tau^2 + i\,\omega\tau) \quad . \tag{2.2b}$$

Models (2.2a) and (2.2b) differ only in the assumed pattern of the ACF magnitude decay with time lag, namely an exponential decay in (2.2a) or a Gaussian decay in (2.2b). By making a linear fit to the ACF phase angle variation versus lag, the slope of the line gives the Doppler shift frequency ω_D. The shift ω_D is related to the Doppler line-of-sight velocity (VLOS) V_D of the scatterers by the equation

$$V_D = \frac{c\,\omega_D}{4\pi f_T} \quad , \tag{2.3}$$

where f_T is the radio frequency transmitted by the radar. The line-of-sight velocity (VLOS) is undoubtedly the most important parameter observed by SuperDARN. Theoretically, for a backscatter radar, the measured Doppler VLOS is the phase velocity of the plasma wave irregularity. For the gradient-drift instability (GDI), which is generally believed to be the major candidate that causes the decameter-scale plasma waves in the *F* region ionosphere which coherently backscatter the HF echoes [*Ruohoniemi and Greenwald*, 1997], the phase velocity is always very close to the component of the plasma $\mathbf{E}\times\mathbf{B}$ drift along the direction of incident wave vector at all ionospheric altitude ranges of interest [*Xu*, 2003]. Thus the Doppler velocity measurement of SuperDARN radar yields the line-of-sight component of the $\mathbf{E}\times\mathbf{B}$ drift along the beam direction to good accuracy.

Another important parameter is the backscattered power P_0, which is just the zero-lag ACF value. The spectral width is defined as the full width at half power of the modeled power spectrum deduced from (2.2a) or (2.2b). The parameters λ and σ can be

determined by least-square fitting procedures based upon models (2.2a) and (2.2b), respectively. A Lorentzian spectral width *w_L* and a Gaussian spectral width *w_S* can be derived as follows,

$$\begin{aligned} w\_L &= 2\lambda \quad , \\ w\_S &= 4\sigma\sqrt{\ln 2} \quad . \end{aligned} \tag{2.4}$$

The above procedure is the standard FITACF routine used by the international SuperDARN science team. On the other hand, all the above key parameters may also be obtained from the ACF by using spectral methods such as the Fast Fourier Transform (FFT) or the Burg algorithm for the Maximum Entropy method [*Burg*, 1975]. The Burg algorithm may be used to obtain higher spectral resolution than the FITACF technique and thus has been used to study the double-peak (DP) spectrum of backscattered echoes [*Schiffler*, 1996; *Huber and Sofko*, 2000; *Danskin et al.*, 2004]. However, the underlying physical mechanism for the DP spectrum is still a controversial issue [*Andre et al.*, 2000; *Huber and Sofko*, 2000; *Danskin et al.*, 2004].

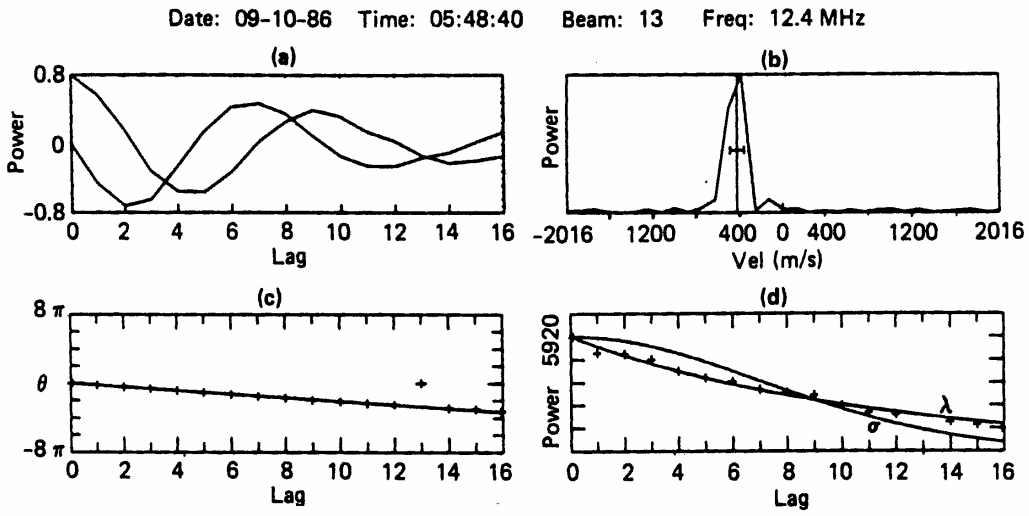

Figure 2.3 An example of the radar signal processing techniques. (a) Real and imaginary part of the ACF. (b) Doppler spectrum obtained through FFT of the ACF. (c) Phase angle as a function of lag and its linear squares fit. (d) Power variation of the ACF as a function of lag with exponential (λ) and Gaussian (σ) least squares fits. (From *Villain et al.* 1987)

Figure 2.3 shows an example of the above-mentioned ACF analysis. Panel (a) gives the real and imaginary part of the ACF. The slope of the best-fit straight line to the graph of the ACF phase angle versus the lag time gives the Doppler frequency shift as shown in panel (c), which is consistent with the result from the Doppler spectrum analysis obtained by FFT technique as shown in panel (b). Two least-square fits to the power variation, the exponential and Gaussian fits, are shown in the panel (d).

Most SuperDARN radars have a second line of antennas which acts as an interferometer array. The elevation angle of returned signals can be determined from the phase difference between the interferometer array and the main antenna array. In this thesis the elevation angle information, if available, is used together with the range information to estimate the scattering height. Since the research interest of this thesis is focused only upon ionospheric *F* region echoes, echoes from scattering heights below 160 km are discarded.

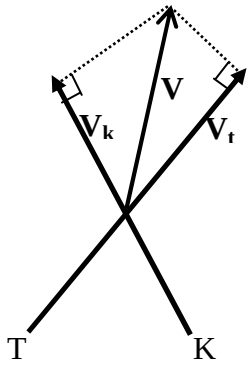

Figure 2.4 Geometry showing the merging technique of plasma convection determination from measurements using two crossing beams.

If at least two radars have overlapping FoVs, it is possible to obtain the two-dimensional convection map within the common FoV in the plane perpendicular to **B** for each scan. This method is known as the merge technique. Assume that, at the intersection of beams from radars 'T' and 'K', the unit vectors along the line-of-sight direction are $\hat{\mathbf{l}}_t, \hat{\mathbf{l}}_k$ and the measured VLOS values are V_t and V_k, respectively. We have,

$$\mathbf{V} \cdot \hat{\mathbf{l}}_t = V_t \quad , \quad \mathbf{V} \cdot \hat{\mathbf{l}}_k = V_k \quad , \tag{2.5}$$

where **V** is the actual two-dimensional convection velocity to be determined. After some vector manipulations, we obtain the equation

$$\mathbf{V} = \frac{[V_t - (\hat{\mathbf{I}}_t \cdot \hat{\mathbf{I}}_k)V_k]\hat{\mathbf{I}}_t + [V_k - (\hat{\mathbf{I}}_t \cdot \hat{\mathbf{I}}_k)V_t]\hat{\mathbf{I}}_k}{1-(\hat{\mathbf{I}}_t \cdot \hat{\mathbf{I}}_k)^2} \quad . \tag{2.6}$$

Another method to obtain the two-dimensional convection velocities is called the FIT technique. The measurements from all data points of all radars are fitted into a mathematical model to obtain the best consistency. A "map_potential" procedure has been developed for this purpose, which uses a combination of the actual data where measurements exist and a statistical global electric potential model [*Ruohoniemi and Greenwald*, 1996; *Ruohoniemi and Baker*, 1998] where no measurements exist.

The map_potential procedure begins with a selection of a data scan for all radars at a specific time. Velocities with error estimates greater than 200 m/s are ignored, as well as ground scatter. A 3×3×3 data sampling method is used in the following way: spatial sampling is performed over a 3×3 beam/gate template centered on the cell of interest, and temporal sampling over 3 successive scans is made by averaging the previous (2 minutes before), current, and next scan (2 minutes after). Thus the sample contains the VLOS data in the 3×3 beam/gate template centered on the target cell and averaged over the three successive scans centered on the time of interest. This sample is then median-filtered to produce a 'best' estimate of the VLOS value for the target cell. Thus the data are filtered both spatially and temporally. This filtering results in a marked improvement in the smoothness of the velocity maps. However, it may smear out some fine structure of the flows. In Chapter 4 we will see that some electric field oscillations are clearly seen from the VLOS observations of beams separated by 7 s, but these oscillations are not shown on the convection map made by the FIT procedure. In other words, the FIT procedure is only suitable for large-scale electric field and flows with variations on time scales greater than 2 minutes.

The next step is to define a global grid for spatial averaging and a time step for temporal averaging period. The time step may be as short as the scan repeat rate, i.e., 2 minutes. The grid is defined with a spatial scale of 1° in latitude, which is about 111 km

projected to the Earth's surface. The number of grid cells distributed in longitude, $n(\theta)$, is set by the requirements that the step in longitude projected to the Earth's surface be as close to 111 km as possible for integer $n(\theta)$. When combining data, the mean velocity and its uncertainty are evaluated at a given grid cell at a given time if at least 25% of the radar samplings for that cell return a velocity value. The filtered VLOS data are converted to the mapping grid, forming a set of N velocity values W_i and their uncertainties σ_i (i =1, 2,…N). These velocities constitute the data base for derivation of the two-dimensional convection pattern.

For the "map potential" method, the electrostatic potential is represented in terms of spherical harmonics,

$$(\theta, \phi) = \sum_{l=0}^{L} \sum_{m=-M}^{M} A_{lm} Y_{lm}(\theta, \phi), \tag{2.7}$$

where the A_{lm} are the coefficients and L and M are the order and the degree of the expansion, respectively, with $M \leq L$. To determine the coefficients A_{lm}, a weighted least-square method is applied to minimize the chi-squared value given by

$$\chi^2 = \sum_{i=1}^{N} \frac{1}{\sigma_i^2} [\mathbf{V}_i \cdot \mathbf{K}_i - W_i]^2 \cdot \tag{2.8}$$

In equation (2.8), $\mathbf{V}_i$ is the fitted velocity vector at the grid cell position associated with i and the dot product provides the projection of this velocity onto the line-of-sight direction, and $\mathbf{K}_i$ is the unit vector along the line-of-sight. The χ^2 value gives an estimate of the goodness-of-fit of the observations to the model.

The fitted convection map gives smoother convection velocities and covers larger areas than the "merged" convection map, because velocity measurements from the overlapping fields-of-view of two radars are needed to obtain the merged values. Owing to this greater coverage, the FIT values are based on the "map potential" technique; this is the standard method used to obtain the large-scale ionospheric convection pattern. However, according to the experience of the author of this thesis, the FIT technique

tends to smooth out some small-scale flow structures due to the filtering process. One must realize that the technique is driven more by the statistical model input rather than actual observations when data points are insufficient. Therefore, in this thesis, we will apply the FIT technique with some caution. Almost all fitted convection maps in this thesis have data points *N* larger than 100 and χ^2/(N-1) less than 1.0, and we have also checked the fitted velocities in each map against the available VLOS measurements from each radar to guarantee that consistency is apparent.

2.2 Magnetometers

The magnetometer data from the CANOPUS (Canadian Auroral Network for the OPEN Program Unified Study) array, the GSC (Geological Survey of Canada) array, and the MACCS (Magnetometer Array for Cusp and Cleft Studies) array are used in this thesis.

Table 2.2 Location of CANOPUS magnetometer stations

Station Name	Code	Geo. Lat (^{o}N)	Geo. Lon. (^{o}E)	AACGM Lat. (^{o}N)	AACGM Lon. (^{o}N)
Contwoyto Lake	CONT	65.75	248.75	73.24	-57.44
Dawson	DAWS	64.05	220.89	65.98	-87.80
Eskimo Point	ESKI	61.11	265.95	71.21	-28.22
Fort Churchill	FCHU	58.76	265.92	69.01	-27.75
Fort McMurray	MCMU	56.66	248.79	64.60	-52.41
Fort Simpson	FSIM	61.76	238.77	67.51	-67.60
Fort Smith	FSMI	60.02	248.05	67.71	-54.90
Gillam	GILL	56.38	265.36	66.71	-28.20
Island Lake	ISLL	53.86	265.34	64.29	-27.83
Pinawa	PINA	50.20	263.96	60.59	-29.41
Rabbit Lake	RABB	58.22	256.32	67.39	-42.48
Rankin Inlet	RANK	62.82	267.89	72.91	-25.34
Taloyoak	TALO	69.54	266.45	78.95	-31.05

CANOPUS was designed as an integral part of the Global Geospace Science Mission (GGS) organized by NASA as part of the International Solar-Terrestrial Physics Program (ISTP). The CANOPUS magnetometer array currently contains 13 stations whose locations are listed in Table 2.2. Their AACGM latitudes and longitudes [*Baker and Wing*, 1989] are also given for reference. It should be noted that, at a fixed geographical position, the AACGM coordinates change slightly every year, and the values listed in the table are calculated for the year 2000. Each station is equipped with a 3-component fluxgate magnetometer of the ring-core type. The data are sampled at a rate of 8 Hz, then are filtered and decimated to a sample rate of one point per 5 seconds.

Table 2.3 Location of NRCAN/GSC magnetometer stations

Station Name	Code	Geo. Lat (^{o}N)	Geo. Lon. (^{o}E)	AACGM Lat. (^{o}N)	AACGM Lon. (^{o}N)
Alert	ALE	82.50	297.65	87.06	99.74
Baker Lake	BLC	64.32	263.99	74.00	-32.54
Cambridge Bay	CBB	69.12	254.97	77.31	-51.27
Fort Churchill	FCC	58.76	265.91	69.01	-27.76
Glenlea	GLN	49.65	262.88	59.93	-30.92
Iqaluit	IQA	63.75	291.48	72.84	14.82
Meanook	MEA	54.62	246.65	62.17	-54.39
Mould Bay	MBC	76.31	240.64	81.03	-86.62
Ottawa	OTT	45.40	284.45	56.08	1.10
P-de-la-Baleine	PBQ	55.28	282.26	65.79	-1.25
Resolute Bay	RES	74.69	265.11	83.37	-40.54
St. John' s	STJ	47.59	307.32	53.75	31.33
Victoria	VIC	48.52	236.58	53.90	-64.01
Yellowknife	YKC	62.48	245.52	69.57	-59.64

The GSC, a branch of Natural Resources Canada (NRCAN), operates a network of 14 Magnetic Observatories across Canada (see Table 2.3 for their locations). Twelve of these observatories are equipped with the modern CANMOS (CANadian Magnetic

Observatory System) instrumentation. Each fluxgate magnetometer samples the magnetic fields at 8 Hz. After filtering and resampling processes, 1-minute data samples are made available to the public.

The MACCS magnetometer array is run cooperatively by Boston University and Augsburg College with assistance from the GSC and CANOPUS. MACCS is a high-latitude array (74^o-84^o AACGM latitude, see Table 2.4 for their locations). As its name suggests, the primary use of MACCS data is for the study of processes mapping down from the magnetospheric cusp and cleft. Four GSC magnetometer stations, as denoted by '*' in Table 2.4, are also included as a part of the MACCS array. The MACCS stations use exactly the same ring-core fluxgate magnetometer used for CANOPUS. The MACCS magnetometers also sample data at 8 Hz, but averaged the sampled data down to a resolution of 1 data point per second (GSC observatories) or 2 points per second (non-GSC sites).

Table 2.4 Location of MACCS magnetometer stations

Station Name	Code	Geo. Lat (^{o}N)	Geo. Lon. (^{o}E)	AACGM Lat. (^{o}N)	AACGM Lon. (^{o}N)
Pangnirtung	PG	66.1	294.2	74.69	19.98
Clyde River	CY	70.5	291.4	79.12	18.50
Iqaluit (*)	IQ	63.8	291.5	72.88	14.86
Cape Dorset	CD	64.2	283.4	74.07	1.65
Iglooik	IG	69.3	278.2	79.01	-7.33
Coral Harbour	CH	64.1	276.8	74.27	-9.91
Repulse Bay	RB	66.5	273.8	76.49	-15.62
Pelly Bay	PB	68.5	270.3	78.23	-22.90
Baker Lake (*)	BK	64.3	264.0	73.99	-32.51
Gjoa Haven	GH	68.6	264.1	77.92	-34.81
Cambridge Bay (*)	CB	69.1	255.0	77.29	-51.19
Resolute Bay (*)	RE	74.7	265.0	83.37	-40.81

Figure 2.5 shows all the above-mentioned magnetometer stations. The fields-of-view (FoVs) of the Saskatoon and Kapuskasing SuperDARN HF radars are also plotted for reference. It can be seen that the CANOPUS magnetometer array, especially the "Manitoba line" at roughly -94º geographic longitude, overlaps the joint Saskatoon-Kapuskasing radar FoVs quite well, and the GSC and MACCS magnetometers provide some support coverage to the east and west of the radars.

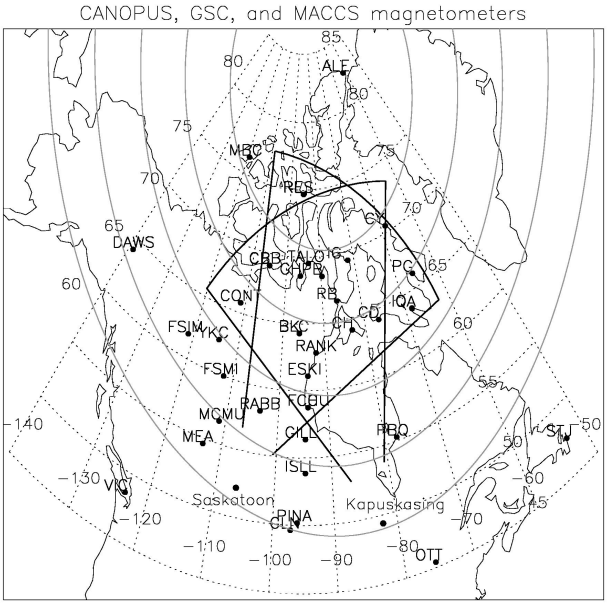

Figure 2.5 CANOPUS, GSC, and MACCS magnetometer stations. AACGM latitudes from 60º to 80º at 5º intervals are shown using solid lines. The FoVs of the Saskatoon and Kapuskasing SuperDARN radars are also plotted for reference.

2.3 Photometers

The CANOPUS meridian-scanning photometer array (MPA) data are also used in the thesis. Currently the MPA array contains 4 meridian scanning photometers (MSPs). A north-south chain of three instruments is located at Rankin Inlet, Gillam, and Pinawa, scanning the meridian close to 330º AACGM longitude. One station at Fort Smith scans the meridian close to 300º AACGM longitude.

The MSP instruments are meridian scanning eight-channel filter wheel photometers. Five of the eight channels measure auroral emissions (470.9 nm, 486.1 nm twice, 557.7 nm and 630.0 nm). The other three measure background intensities near

480 nm, 493.5 nm, and 625 nm to correct for contamination caused by blended auroral emissions, and scattered light of manmade, solar and/or lunar origin. Each instrument scans the meridian at two revolutions per minute with a sampling rate of 510 per scan per channel. Due to the geometry the spatial sampling is dense vertically above the station and becomes less dense on each side of the zenith. After the initial correction for gain nonlinearities, the data are compressed from eight to six channels by averaging the two 486.1 nm channels, and the two associated background channels. Then the sampled data are averaged over 0.5^0 latitude intervals (for an assumed emission height at 110 km) into 17 latitude bins centered on the station. Bin 0 is the most poleward one and bin 16 the most equatorward.

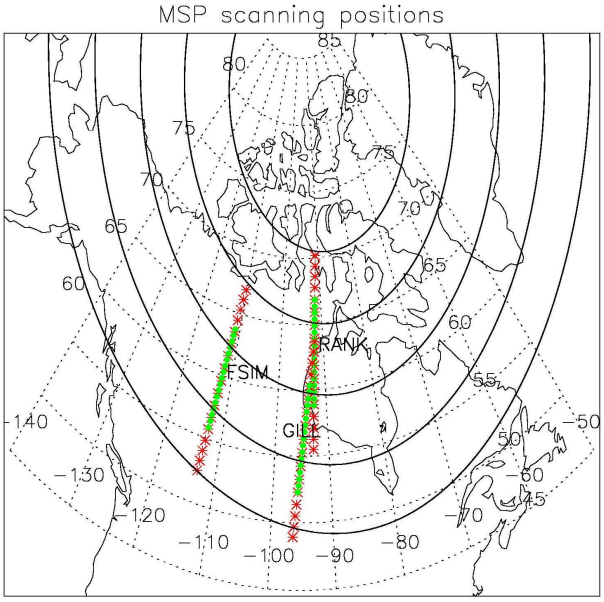

Figure 2.6 The scan lines of the MSP instruments at Gillam, Rankin Inlet, and For Smith. The red asterisks indicate the extent of the scans for the red-line emissions, while the green dots indicate the extent of the scans for the green-line emissions.

In the thesis the 630.0 nm (red-line emission) and 557.7 (green-line emission) observations at Gillam, Rankin Inlet and Fort Smith are of major interest. As we indicated in Chapter 1.3, the 557.7 nm emission is radiated in the atomic oxygen transition O(^1S)->O(^1D), while the 630 nm emission is from the O(^1D)->O(^3P) transition. The excitation to the ^1D state maximizes at about 110 km, so that is the

height assumed for the green-line emission. Due to quenching the red-line emission is usually expected to peak above 200 km. Nominally the assumed emission height is 230 km for the 630.0 nm emission. The scan lines of the photometers at Gillam, Rankin Inlet, and Fort Smith are plotted in Figure 2.6. Red crosses indicate the 17 bin positions at 230 km height and green dots indicate the bin positions at 110 km height.

The poleward bins of the Gillam photometer overlap with, or are close to, several central bins of the Rankin Inlet photometer, for red-line emissions. At times, large discrepancies can be found between the observations from the two photometers. These discrepancies most likely result from an incorrectly assumed emission height (230 km). For bin 17 (the most equatorward bin) of the Rankin Inlet photometer, an assumed emission height of 180 km will cause the bin latitude to be 1.3^0 more poleward than the bin latitude for assumed height of 230 km, but for the bins near the station zenith, the difference will be trivial. A triangulation method [*Jackel et al.*, 2003] which is used to determine the actual emission height will be discussed later in Section 2.5.3.

2.4 Riometers

At each CANOPUS magnetometer station a 30 MHz zenith riometer with a 4-element antenna and a single 150 kHz broadband receiver is also deployed. The riometer measures the cosmic radio noise absorption at 30 MHz. This absorption can occur either in the lower ionospheric *E* region due to the anomalous electron heating by plasma wave instabilities [*Schlegel and St.-Maurice*, 1981], or in the *D* region due to hard electron (>40 keV) precipitation [*Penman et al.*, 1979]. The sample rate and final temporal resolution of the riometer data are the same as the CANOPUS magnetometers.

2.5 NORSTAR all sky imager (NASI)

2.5.1 Equipment description

NORSTAR (NORthern Solar Terrestrial ARray) is a world-class optical and radio facility designed to remote sense auroral precipitation on a continental scale. NORSTAR, whose heritage is CANOPUS, will be the imaging component of the Canadian Geospace Monitoring (CGSM) project. NORSTAR consists of three All-Sky Imagers (ASIs) at Resolute Bay, Rankin Inlet, and Gillam, four MSPs, and 13

riometers. Each ASI is a digital camera equipped with an intensified charge coupled device (CCD). The essential components of the camera are the lens which generates two-dimensional images on the image intensifier' sphotocathode, and a filter which admits only light within a narrow wavelength range centered on a wavelength of interest. There are plans for seven more ASIs. The ASIs and MSPs collect data at four auroral wavelengths (471.3, 557.7, 630.0, 486.1 nm), with an interval of 10-60 seconds per image. The NORSTAR imagers also have a long-wavelength filter that passes all NIR (near-infrared) wavelengths from 650 nm up to the limit of the detector at about 800 nm. The major contribution to luminosity in the 650-800 nm range is from the N2 1PG band [*Jones*, 1974]. In addition to the auroral filters, a background channel operates with a passband at 480.0 nm, where no auroral luminosity is expected. This channel is designed to obtain the so-called "da rk frame" during the first minute of each hour for calibration purposes (see section 2.5.2). Those imagers will provide extensive and unique coverage of the auroral and polar regions over western Canada and Alaska, from roughly 60 degrees invariant up to the geomagnetic pole.

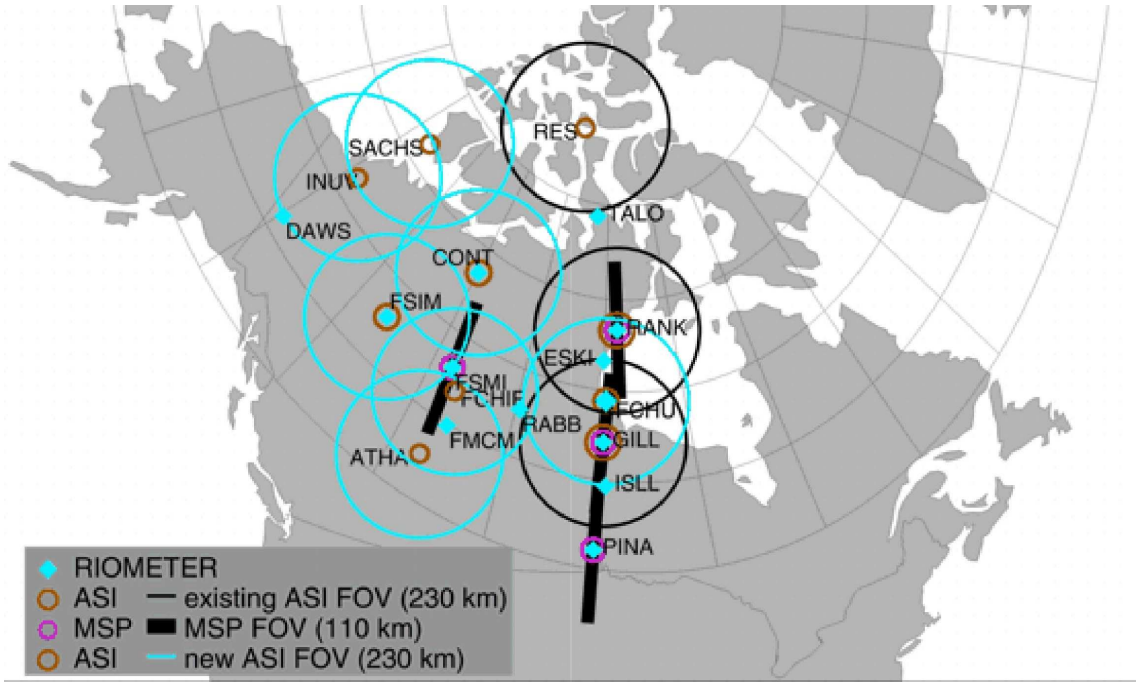

Figure 2.7 Maps of the FoV of three existing ASIs (black circle) and seven ASIs being planned (cyan circle). The positions of the riometers and the MSPs, which were part of the CANOPUS project and now have become part of NORSTAR, are also plotted.

The FoVs of the three existing imagers and seven imagers (assuming a 230 km altitude for the 630 nm emissions and a zenith extent of 75^0) being planned are shown in Figure 2.7. The NORSTAR all-sky imager (NASI) at Rankin Inlet, which provides the best coverage for collaborative studies with the Saskatoon-Kapuskasing radar pair, will be used in this thesis.

2.5.2 Calibration of NASI

So far the NORSTAR data provided by the University of Calgary has not been fully calibrated. The author of this thesis assisted in the raw data processing and calibration work. The raw NASI data is a 256*256 2-bytelength image pixel array. The calibration procedures are detailed in the following (see Figure 2.8).

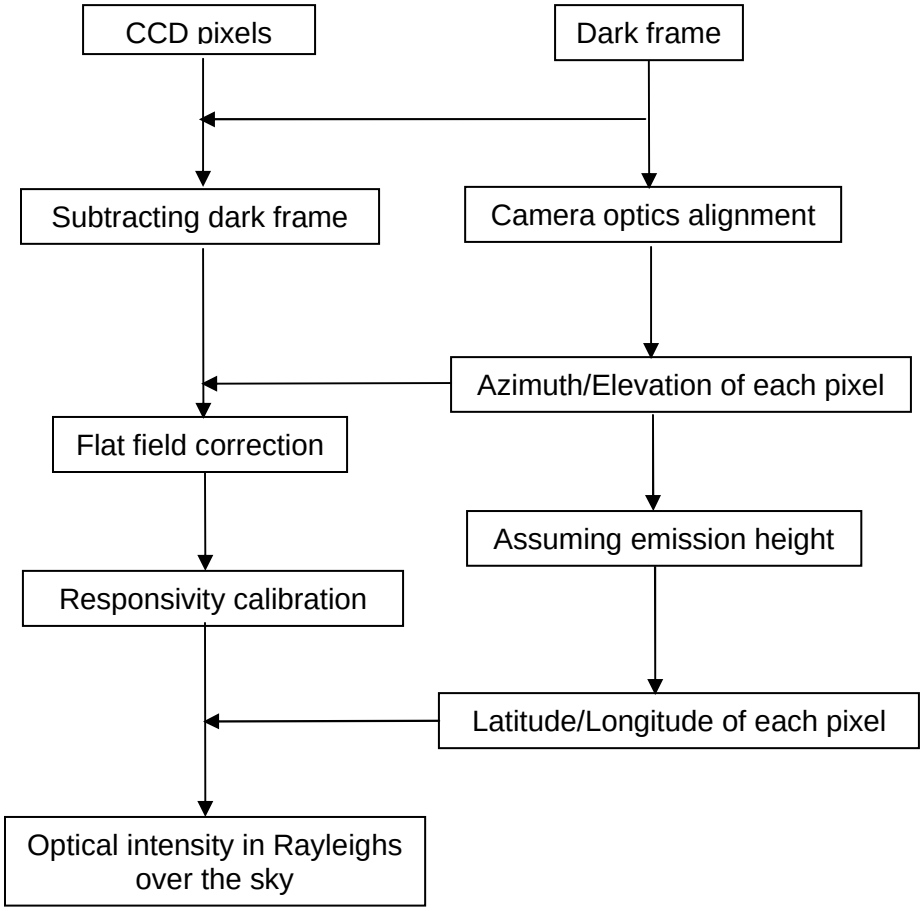

Figure 2.8 Flow chart of the calibration procedures used for NASI data. See the text for detailed descriptions.

The very first procedure is the camera optics alignment. As above-mentioned, the NASI applies a background filter at 480 nm. This background channel is not only essential for accurate photometric work with faint emissions, but also produces useful "star frames" because the major contributors to this channel are celestial sources. Since the star positions are known, the azimuth and elevation angles of each image pixel of the camera can be determined.

The second procedure is the "flat-field" or "zonal scan" correction, which resolves the zenith-dependence of the emission intensity. Analysis of NORSTAR dark-room zonal-scan data yields a flat-field correction frame, which is shown in Figure 2.9. The image array under study should be divided by the flat-field correction frame. However, one should note that the correction does not work well for large zenith angles $>75^0$ (*T. Trondsen*, private communication).

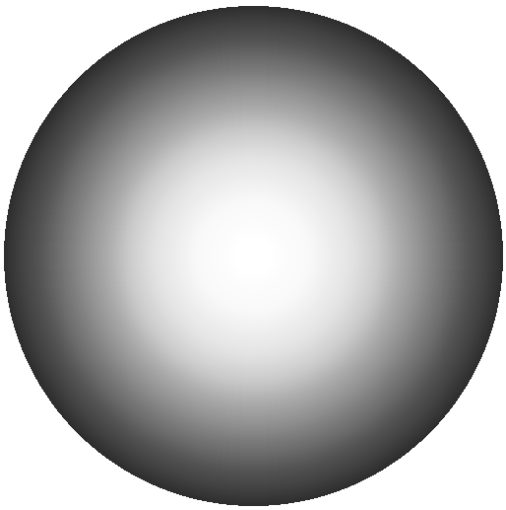

Figure 2.9 Flat-field correction frame of NASI at Rankin Inlet. The value ranges from 0 (darkest) on the edge to 1 (brightest) at the center.

The final but unfinished procedure is the "responsivity" or "sensitivity" calibration. The purpose of the calibration exercise is to produce a conversion factor to allow users of NASI data to convert from raw image pixel "data numbers" to physical units of auroral column emission rate (Rayleighs) for each wavelength employed. The

conversion factor is called the R-Value. The equation relating the NASI data number to the emission intensity in Rayleighs is:

NASI data number= Intensity in Rayleigh * R-value * exposure time . (2.9)

The exposure time of NASI is normally 2 seconds. Experimentally, Low Brightness Source (LBS) measurements were used to calculate the R-values.

2.5.3 Determination of emission heights

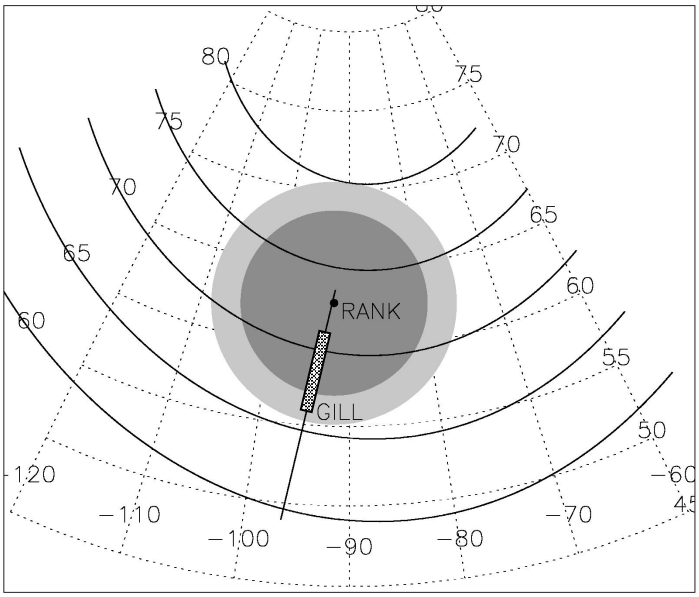

Figure 2.10 Observation geometry for the NASI at Rankin Inlet and the MSP at Gillam. The light gray area is the FoV of the NASI up to 80^0 from the zenith, while the dark gray area is the FoV of NASI up to 75^0 from the zenith. The solid line indicates the scan line of the Gillam MSP. The hatched box denotes the sampling region of NASI pixels chosen for comparison with Gillam MSP data.

As we have mentioned, the assignment of a realistic emission height is a problem for all ground-based optical auroral measurements. *Jackel et al*. [2003] developed a triangulation method to determine the red-line emission height by using the MSP observations at Rankin Inlet, Gillam, and Pinawa. The idea is that if two MSPs have

overlapping scanning areas, a best-fit height for which the highest consistency between the two measurements is achieved can be determined. In this thesis, a similar parallax technique is applied to the use of the NASI data from Rankin Inlet and the MSP data from Gillam. The geometry for this parallax technique is shown in Figure 2.10.

Figure 2.11 shows an example of the application of the technique. The best correlation is achieved for an assumed height of 215 km. Thus, during that observation period, the best-fit emission height is assumed to be 215 km. At lower latitudes ($<68^0$ MLAT), the correlation is poor. This is because, for those latitudes the zenith angle of the NASI is high enough that the flat-field calibration is not very reliable. However, as shown in Figure 2.10, by restricting the zenith angle to values less than 75^0, the coverage extends only down to ~67.5^0 MLAT. The MLAT range 65-67^0 is very important for the auroral substorm studies because this MLAT range is usually where the auroral expansive phase onset and the resulting auroral breakup start. As a compromise, in this thesis we will extend the NASI FoV up to 80^0 zenith angle, but it must be kept in mind that the emission intensity near the edge of FoV might be somewhat overestimated.

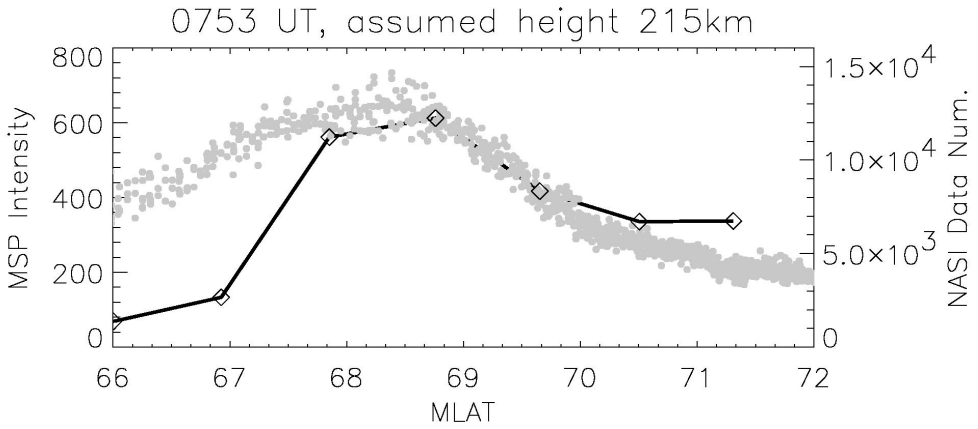

Figure 2.11 Comparison of the MSP emission Intensity in Rayleighs and the NASI data number in the overlapping observation region. Diamonds jointed by a solid line denote the intensities in MSP bins 3 (most poleward) to 9 (most equatorward). The gray dots indicate the NASI observations sampled near the Gillam MSP bins.

On the other hand, the parallax technique can also be applied to estimate the R-value, assuming the MSP data are well calibrated. For example, from Figure 2.11 an R-

value of ~10 can be obtained. However, the R-value estimated based on this technique is found to be significantly different with that based upon the LBS measurements by the NASI data provider [*T. Trondsen*, private communication]. The reason for this discrepancy is still under investigation.

2.6 Satellites

Satellite data from WIND, ACE, GEOTAIL, DMSP and IMP8 are included in this thesis. In the following we give a brief introduction to those satellite projects and their applications in the thesis.

WIND

WIND was launched on November 1, 1994, and is the first of two missions of the Global Geospace Science (GGS) initiative, which is the United States portion of a worldwide collaboration called the International Solar-Terrestrial Physics (ISTP) program. During its first two years of operation, WIND was positioned in a sunward, multiple double-lunar-swing-by orbit with a maximum apogee of 250 R_E. After that, it was put into a halo orbit at the Earth-Sun L1 Lagrangian point — the point where the gravitational and centrifugal pull of the Sun and Earth cancel each other (~230 R_E on the Sun-Earth line). Starting in October 1998, Wind went into a petal orbit that brings it as close as 10 R_E and as far as 80 R_E at an angle of 60^o from the Earth's e cliptic plane.

The Solar Wind Experiment (SWE) and the Magnetic Fields Investigation (MFI) instrument on WIND are used in the thesis to obtain the solar wind parameters, e. g., the IMF, solar wind speed, ion number density. Detailed description of the WIND project and the instruments can be found at web site http://www-istp.gsfc.nasa.gov/istp/wind/ .

ACE

The Advanced Composition Explorer (ACE) satellite was launched on August 25, 1997, and is an Explorer mission that was managed by the Office of Space Science Mission and Payload Development Division of the National Aeronautics and Space

Administration (NASA). It orbits the L1 point and stays at a relatively constant position with respect to the Earth as the Earth revolves around the sun.

The Solar Wind Electron Proton Alpha Monitor (SWEPAM) and the magnetometer (MAG) instrument are used in this thesis to obtain the solar wind parameters. Detailed description of the ACE mission and the on-board instruments can be found at http://www.srl.caltech.edu/ACE/ .

GEOTAIL

The GEOTAIL mission is a collaborative project undertaken by the Institute of Space and Astronautical Science (ISAS) in Japan and NASA in the US. The GEOTAIL spacecraft was designed and built by ISAS and was launched on July 24, 1992. The GEOTAIL mission was divided into two phases. During the initial two-year phase, the orbit apogee was kept on the nightside of the Earth by using the Moon's gravity in a series of double-lunar-swing-by maneuvers that resulted in the spacecraft spending most of its time in the distant magnetotail (maximum apogee about 200 R_E) with a period varying from one to four months. In February 1995, phase two was commenced as the apogee was reduced to 30 R_E so that near-Earth magnetotail processes could be studied.

The Solar Wind Analyzer (SWA) of the Comprehensive Plasma Instrument (CPI) and the Magnetic field (MGF) instrument are used in the thesis to obtain the solar wind parameters. In addition, data from the Low Energy Particle (LEP) experiment and the MGF instrument are used, especially in Chapter 3, to determine the flow velocity and the magnetic field in the mid-tail region. Detailed description of the GEOTAIL project and the instruments can be found at http://www-istp.gsfc.nasa.gov/istp/geotail/ .

GOES

The Geostationary Operational Environmental Satellite (GOES) series of satellites are operated by the National Oceanic and Atmospheric Administration (NOAA) of the US. The GOES satellites circle the Earth in a geosynchronous orbit at about 35,800 km above the Earth. This allows a satellite to remain continuously over a fixed position on the Earth, and obtain important information about the geosynchronous-orbit portion of the magnetosphere.

Two GOES satellites are used in this thesis, namely, GOES-8 and GOES-10. GOES-8 (or GOES-East) is positioned at 75^0 W geographical longitude, while GOES-10 (or GOES-West) is positioned at 135^0 W longitude. The magnetometer instruments on GOES-8 and GOES-10 are used to obtain the magnetic field topology, especially the "stretching" of the magnetic field lines in the geosynchronous-orbit magnetosphere. Detailed description of the GEOTAIL project and the instruments can be found at http://rsd.gsfc.nasa.gov/goes/ .

DMSP

The Defense Meteorological Satellite Program (DMSP) is a US Department of Defense program run by the Air Force Space and Missile System Center. The DMSP satellite series are in circular, 830-840 km sun synchronous orbits at an inclination of 98.3^0. Each satellite crosses any point on the earth up to two times a day and has an orbital period of about 101 minutes.

Each DMSP satellites carries an SSJ-4 Precipitating Electron and Ion Spectrometer which monitors the energy flux of electrons and ions from about 30 eV up to about 40 keV. This precipitation from the earth's magnetosphere is extremely important to space physics research. In this thesis the DMSP satellite series is used to obtain the auroral precipitation boundary, especially the OCFLB. Detailed description of the GEOTAIL project and the instruments can be found at http://dmsp.ngdc.noaa.gov/dmsp.html .

IMP8

IMP8 (IMP J/Explorer 50), the last satellite of the IMP series, was launched by NASA on Oct. 26, 1973. It originally had an elliptical orbit with apogee and perigee distances of about 45 and 25 Earth radii, respectively, but its eccentricity has gradually decreased since it was launched. It now has a near-circular orbit at about 35 Earth Radii and a 12-day period.

The magnetometer instrument on IMP8 is used in the thesis to obtain the upstream solar wind IMF parameters. Detailed description of the GEOTAIL project and the instruments can be found at http://nssdc.gsfc.nasa.gov/space/imp-8.html .

Chapter 3

Nightside radar flow enhancement and its association with auroral intensification

The relationship between fast flows and auroral activity is very important for the understanding of the substorm process. While much research has been done using *in situ* satellite flow observations, joint studies of convection measurements and optical observations in the ionosphere are not common. From the investigation of the Saskatoon-Kapuskasing SuperDARN radar data from 1997-1999, a dataset of nightside radar flow enhancement (NRFE) events has been compiled. From the combined radar, CANOPUS magnetometer and photometer array data, the spatial and temporal relationships between the NRFEs and auroral intensifications has been studied. In this chapter, we will first discuss the statistical behavior of the NRFEs and then we present three case studies. In the first event, two NRFEs on the open field lines were found, but neither was related to any auroral or magnetic activity. In the second event, the NRFEs were found to be related to small negative magnetic bays and high-latitude auroras (possibly auroral streamer structures), which are observed on the west side of the flow enhancement region. The most detailed analysis is made for the third NRFE event which was on closed field lines and was accompanied by a pseudosubstorm. The ionospheric flow enhancements appeared to be at higher latitudes in the BPS region, while the auroral intensifications occurred at lower latitudes inside the CPS region and mapped to the NGOPS. At the intermediate latitudes between the flow enhancements and the auroral intensifications, sheared zonal flows characteristic of the Harang

discontinuity were found. The flow enhancements and auroral intensifications were well correlated and occurred nearly simultaneously. Such a temporal relationship between latitudinally separated regions is not easily explained by the existing models associating the tail reconnection process and the near-geosynchronous onset of substorms. On the basis of the results, we propose a new model to explain the nearly simultaneous onset of the NRFEs and the auroral intensifications [*Liang et al*., 2004a].

3.1 Review of some previous studies

In the late 1970s, high-speed (several hundred km/s) plasma flows were found in the PSBL (e.g., *Lui et al*. [1983]). Later *Baumjohann et al*. [1990] and *Angelopoulos et al*. [1992; 1994] showed that the fast flows also are frequently observed in the plasma sheet. The enhanced plasma sheet flows are generally bursty and localized; they can occur during various stages of substorm development. In the near-Earth region the flows are predominantly earthward. These flows have roughly a 10-minute timescale and are called bursty bulk flow (BBF) events. Imbedded in the BBFs are flow bursts which have velocity peaks of ~1-minute duration. These earthward-moving flow bursts are frequently observed by satellites in the plasma sheet and generally their cause has been associated with magnetotail reconnection processes, including both distant tail reconnection and near-Earth tail reconnection.

The term "flow bursts" also is used to describe ionospheric flow enhancements, but the definition is somewhat arbitrary, varying with observation equipment and the researchers. For example, it was used to describe the fast flows (700-1000 m/s) lasting 5-10 minutes that were observed by the EISCAT incoherent scatter radar [*Lewis et al*., 1992]. The term also was used to describe nightside flows of duration 10-20 minutes and velocities >750 m/s that were observed by SuperDARN HF radars just prior to the substorm onset [*Watanabe et al*., 1998]. These nightside "ionospheric flow bursts" were often attributed to distant tail reconnection [*De la Beaujardière*, 1994; *Watanabe et al*., 1998]. The timescale of the ionospheric flow bursts is comparable to the BBFs but is quite different from the 1-minute timescales of the flow bursts seen in the tail. To avoid confusion, we will use the term "nightside radar flow enhancement" (NRFE) to describe the ionospheric flow enhancements observed by the SuperDARN radars.

During the substorm growth phase, localized auroral brightening is sometimes observed. It is not as intense as the substorm EP onset aurora, and can occur at various latitudes equatorward of the separatrix, whereas the site of substorm onset aurora activation lies near the equatorward edge of the auroral oval. Several types of auroral activation have been associated with the fast flow events observed in the tail, mainly based on measurements from the GEOTAIL satellite [*Nakamura et al.*, 2001a]. First, auroral poleward boundary intensifications (PBIs), which begin just equatorward of the OCFLB, were found to be associated with flow bursts in the plasma sheet and the PSBL [*Lyons et al*., 1999; *Zesta et al*., 2000], and with enhanced equatorward flows in the ionosphere observed by incoherent radar [*De la Beaujardière et al*., 1994]. Second, auroral streamers (N-S aurora) expand equatorward after the initial activation of high-latitude aurora, and the relationship of the streamers to the plasma sheet flow bursts was studied by *Nakamura et al.* [2001b]. Finally, local brightenings and expansions of auroras take place inside the main auroral oval [*Fairfield et al*., 1999; *Nakamura et al*., 2001a]. In a study of joint observations of flow bursts at GEOTAIL and ionospheric auroral intensifications, *Nakamura et al*. [2001a] found that most of the intensifications preceded the flow bursts by a few minutes, which raises a question about the cause-effect relationship between the intensifications and flow bursts.

3.2 Definition of NRFE and some statistical results

From an investigation of the data from the Saskatoon-Kapuskasing SuperDARN radar pair from 1997 to 1999, a data set of NRFEs has been assembled, based on the following criteria for identifying an NRFE event: (1) the observed convection velocity (merged or fitted) must be greater than 600 m/s and directed southward, or, if the data are available from only one radar so that no merged velocity is available, the VLOS of the nearly magnetic northward-pointing beams of the radar must be greater than 500 m/s towards the radar; (2) the fast flows must occur between 2000 and 0400 magnetic local time (MLT); (3) the modified back-scattered power (see equation 3.3 in the section 3.4.2) must be greater than 20 dB. For a well-defined NRFE event, the latitudinal coverage of the flow enhancement structure must be more than two range

bins and the enhancement must last for at least 4 successive scans. The duration of a well-defined NRFE event may range from 10 to 40 minutes.

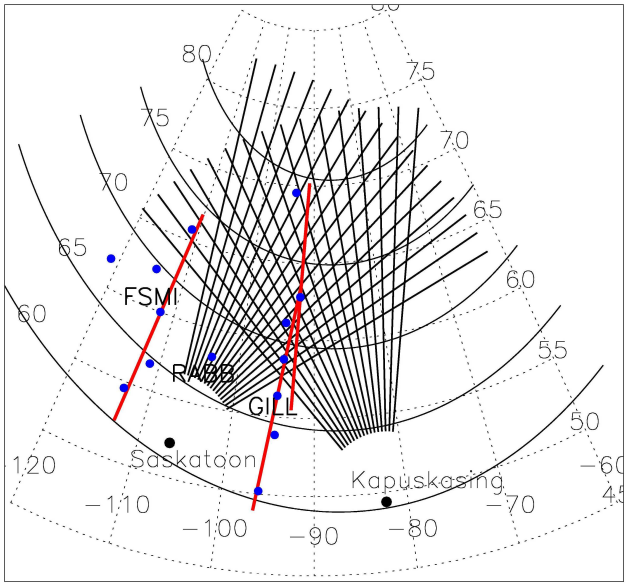

Figure 3.1 FoVs of the Saskatoon-Kapuskasing SuperDARN radar pair, sites of CANOPUS magnetometer stations and scan lines of the MSPs at Gillam, Rankin Inlet, and Fort Smith. AACGM latitudes from 60^0 to 80^0 at 5^0 intervals are shown using solid lines.

The other data for the NRFE studies originated from the CANOPUS MPA and magnetometer array, and from some satellite instruments. The geometry of the beam directions of the Saskatoon and Kapuskasing HF radars, the scanning range of the CANOPUS MSPs at Rankin Inlet, Gillam, and Fort Smith, and the locations of the magnetometers are shown in Figure 3.1. The CANOPUS west-east magnetometer chain (Fort Smith – Rabbit Lake – Gillam) is labelled and is very important in this study because its magnetometer latitude (~67^0 MLAT) roughly maps to the NGOPS where magnetospheric substorms are generally believed to initiate in the NEI model.

To classify the observed NRFE events, we have applied the following procedures which involve the measurements from other instruments:

(a) The NRFEs are classified as occurring either on open field lines or on closed field lines. The OCFLB is determined either from the poleward edge of the 630 nm

optical emission observed by the Rankin Inlet MSP (see Chapter 1.3 and Appendix C.2 for details) or, from a nearby DMSP satellite pass, if one is available. For those NRFE structures which span the OCFLB, if the NRFE has significant portions on both sides of the OCFLB, we identify it as two NRFE events, one on the open field lines side and the other on the closed field lines side; otherwise if the NRFE structure is dominantly on one side of the OCFLB, we classify it according to the side on which its principal part is located.

(b) The CANOPUS local auroral electrojet indices CU and CL are used to infer the geomagnetic disturbance level [*Rostoker et al.,* 1995]. The CU and CL indices are measures of the magnetic effect at the ground of the eastward electrojet and westward electrojet, respectively. Their index determination is similar to that used to obtain the well-known AU and AL indices but is defined only locally within the region observed by the CANOPUS magnetometer array. We define the difference between the CU and CL index as the CE index, the counterpart of the AE index. For each NRFE event, the CE index is averaged during the event interval.

(c) The CANOPUS MSP data at Gillam, Rankin Inlet, and Fort Smith have been checked for each NRFE event interval. If an auroral intensification was found during roughly the same time interval as the NRFE (allowing for a ±10-minute difference), the NRFE is classified as being accompanied by auroral activations. Otherwise the NRFE is classified as being without accompanying auroral activations. Most of the accompanying auroral activations were found to be located inside the main auroral oval, though occasionally intensifications in the poleward portion of the auroral oval were also identified (see event 2 below). In some NRFE events, the auroral emissions were very patchy and with small perturbation magnitude during the event interval, so that it was difficult to determine whether or not there were accompanying auroral activations. We classify those events as NRFEs with uncertain auroral activations. If the quality of the optical data is not good, e.g., highly contaminated by moonlight or clouds, the event is discarded. If an auroral activation was found to accompany an NRFE spanning the OCFLB and having significant parts on both sides of OCFLB, the event is classified only as a NRFE on closed field lines accompanied by auroral activation.

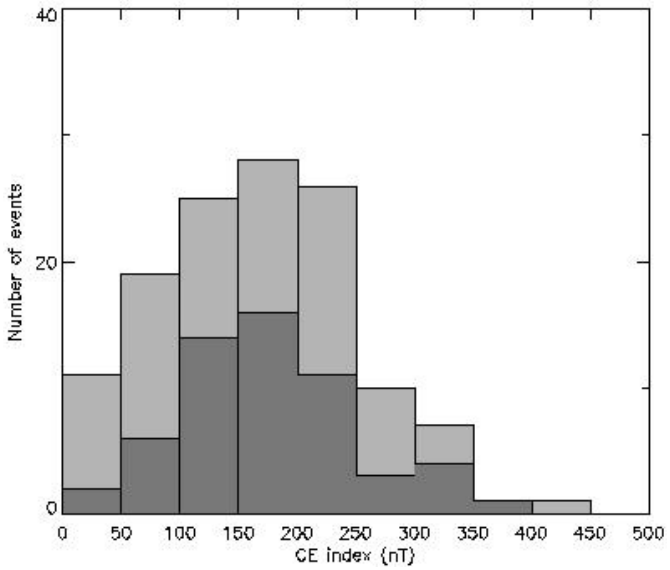

Figiure 3.2 Occurrence of NRFEs on open and closed field lines versus the CE index. Dark bars denote for the NRFE on closed field lines, while the light gray bars denote the NRFEs on open field lines.

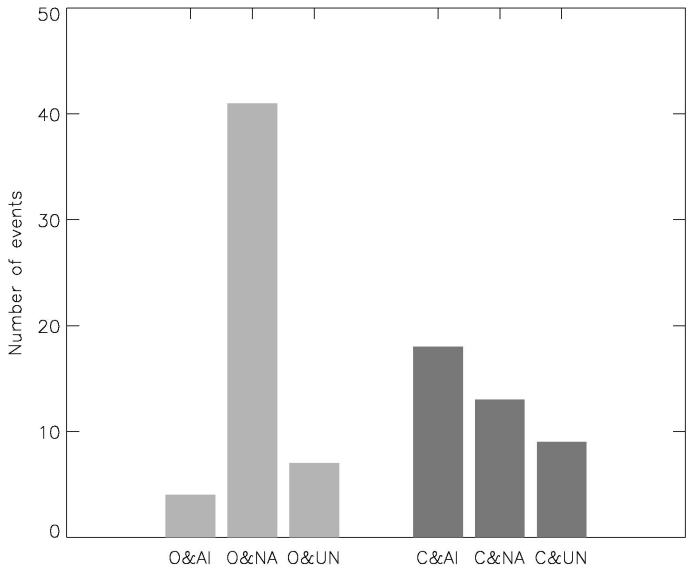

Figiure 3.3 Occurrence of open field lines NRFEs accompanied by auroral intensifications (O&AI), open field lines NRFEs without auroral intensifications (O&NA), open field lines NRFEs with uncertain auroral activations (O&UN), closed field lines NRFEs accompanied by auroral intensifications (C&AI), closed field lines NRFEs without auroral intensifications (C&NA), and closed field lines NRFEs with uncertain auroral activations (C&UN).

It should be noted that the foregoing procedures depend on the availability and the quality of both the magnetic and optical observations, which reduces the number of NRFE events for a statistical study. Figure 3.2 shows the occurrence of the well-defined NRFEs on open and closed field lines versus the CE index. It is very clear that the NRFEs on closed field lines occurred mainly for CE index values from 100 to 250 nT, values typical of the late substorm growth phase, a pseudobreakup or a tiny substorm EP. The number of events drops significantly when the CE index is larger than 250 nT. Care must be taken with the explanation of this drop of occurrence. In case of strong geomagnetic activity, such as a substorm EP, it has been found that the increasing conductances in the auroral oval tend to suppress the electric field and thus decrease the flow velocity, especially the equatorward flow component [*Yeoman et al*., 2000a; *Parkinson*, 2004]. However, it is also true that, during a major substorm EP, the SuperDARN HF radar ionospheric *F* region echoes are often largely absent due to strong absorption in the *E* and *D* regions, or to unfavorable propagation conditions resulting from the enhanced *E* region electron densities. Frequently there is a lack of radar echoes right after the substorm EP onset, in which case the radars would not detect any NRFE events in the *F* region ionosphere. The occurrence of NRFEs on open field lines appears to be less sensitive to magnetic activity, because such events are found for CE index values between 0 and 300 nT. Thus the dependence of open field line NRFEs on the geomagnetic activity level is not as strong as that for the NRFEs on closed field lines. When the CE index is larger than 300 nT, the number of NFRE events on open field lines also drops for the same reasons mentioned above.

Figure 3.3 shows the statistics for the occurrence of NRFEs with and without accompanying auroral intensifications. First we can see clearly that very few NRFEs on open field lines are accompanied by auroral activations. In the following case studies, we will draw the same conclusion repeatedly. This result strongly indicates that the NRFEs on open field lines are not directly related to auroral activity. The relationship between the NRFEs on closed field lines and the auroral intensifications is, however, very complex. We see a slight dominance of NRFEs on closed field lines accompanied by auroral intensifications. Thus it is tempting to suggest that there is a close

relationship between them, but is far from a definite one-to-one correspondence. We will explore the physical implications of this result in section 3.4.

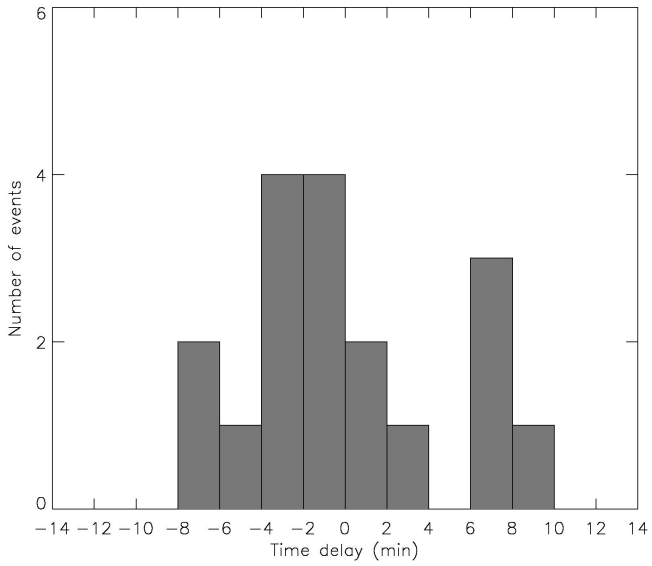

Figure 3.4 Distribution of time delays between the initiation of NRFEs and their accompanying auroral activations.

The timing between the flow enhancements and the auroral intensifications is important for investigating their cause-effect relationship. Figure 3.4 shows the distribution of the time difference between the initiation of the NRFE and the auroral intensifications for all the NRFE events on closed field lines with accompanying auroral activations. The time delays are grouped by intervals of two minutes, which is the temporal resolution of SuperDARN radar observation in normal mode. A positive time delay indicates that the auroral intensification lags the NRFE, while a negative time delay indicates that the auroral intensification precedes the NRFE. We can see that the peak occurrence rate is found at 0 to -4 minutes time delay range, in accordance with the finding of *Nakamura et al.* [2001a] that most of the auroral activations preceded the flow bursts by a few minutes. However, the limited pool of NRFE events with accompanying auroral intensifications here might reduce the reliability of the statistical result. On the other hand, the distribution is widespread, indicating a high variability of the time delays, which in turn implies that the temporal relationship between the flow

enhancements and the auroral intensifications may in fact be very complicated. We suggest that different time delays seen in different events may be caused by significantly different magnetospheric mechanisms, reflecting the high variability and complexity of the substorm process. Several viable models associating tail reconnection, and thus fast flows in the mid-tail, with the near-geosynchronous onset of auroral substorms will be discussed in section 3.4.

3.3 Three case studies: NRFEs on open field lines and closed field lines

3.3.1 March 29, 1999 event

First we will explain the procedures used to identify a NRFE event. There are three approaches. The first and perhaps the most reliable method is the use of merged data, in case there were extensive auroral echoes seen by both the Saskatoon and Kapuskasing radars. Merged convection velocities were available from 0420 to 0510 UT on March 29, 1999. In Figure 3.5 are shown six merged convection maps, each for a two-minute scan. The OCFLB was estimated from the Rankin Inlet MSP 630.0 nm optical emission data (see Figure 3.7a below), and is shown by the '*' symbol in each frame. However, for the scans at 0438-0440 UT and 0456-0458 UT, the poleward border of the 630 nm emission was not well defined (see Appendix C.2), and thus the OCFLB identification is not available.

The first identifiable flow enhancement started at 0438 UT (Figure 3.5a). Fast flows with velocities >1500 m/s first appeared near 78^0 MLAT, and from -40^0 to -28^0 MLON. The flow direction was strongly westward and also somewhat equatorward. The fast flow region expanded to above 80^0 MLAT and west of -50^0 MLON at 0448 UT (Figure 3.5b), and the convection was poleward below 77^0 MLAT, except for some equatorward flows east of -20^0 MLON. The strong westward flow enhancement faded at 0452 UT (Figure 3.5c). After that time the flow pattern changed significantly. At 0456 UT (Figure 3.5d), the flow direction suddenly switched to strongly eastward from 78^0 to 82^0 MLAT and -50^0 to -30^0 MLON. However, the flows were almost purely equatorward at 76^0 to 82^0 MLAT and -30^0 to -15^0 MLON. These fast equatorward flows intensified and extended equatorward to ~74^0 MLAT at 0500 UT (Figure 3.5e). The

velocity peaked above 1000 m/s for both the eastward and equatorward flows. The second flow enhancement lasted about 10 minutes and diminished at ~0506 UT (Figure

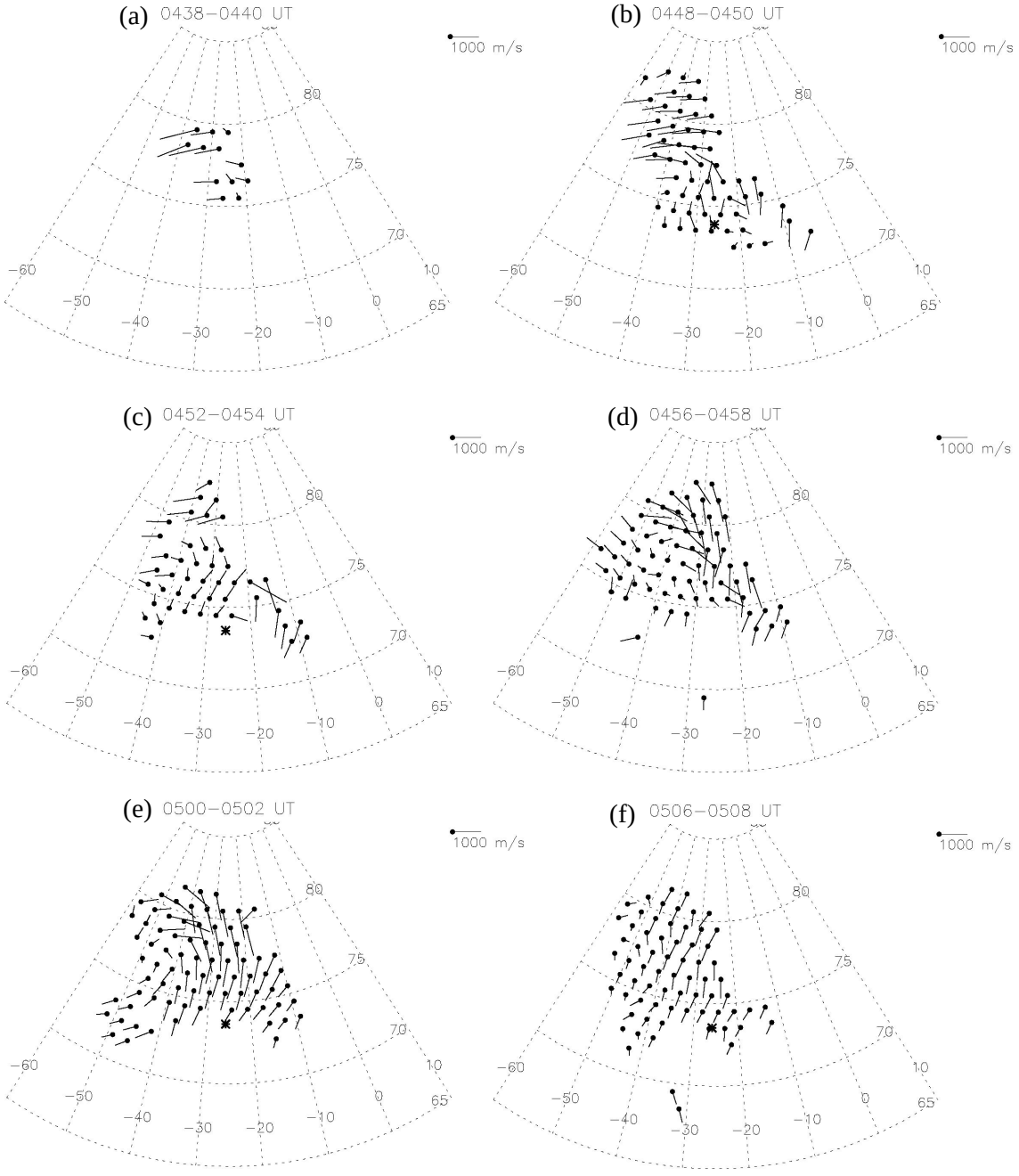

Figure 3.5 Six merged convection map at (a) 0438-0440 UT; (b) 0448-0450 UT; (c) 0452-0454 UT; (d) 0456-0458 UT; (e) 0500-0502 UT; (f) 0506-0508 UT. Asterisks denote the OCFLB estimated from the 630.0 nm optical emission data at Rankin Inlet MSP. The AACGM coordinate system is used.

3.5f). During the whole interval the high-speed flow region was mostly confined to latitudes above 75^0 MLAT and the flow velocity decreased with decreasing latitudes. Below 74^0 MLAT, although the merged data were unavailable in part of the region, the flow velocities that were available were generally small. Relative to the position of the OCFLB inferred from the poleward boundary of the 630 nm emission, it is clear that the flow enhancement regions were located almost purely on open field lines.

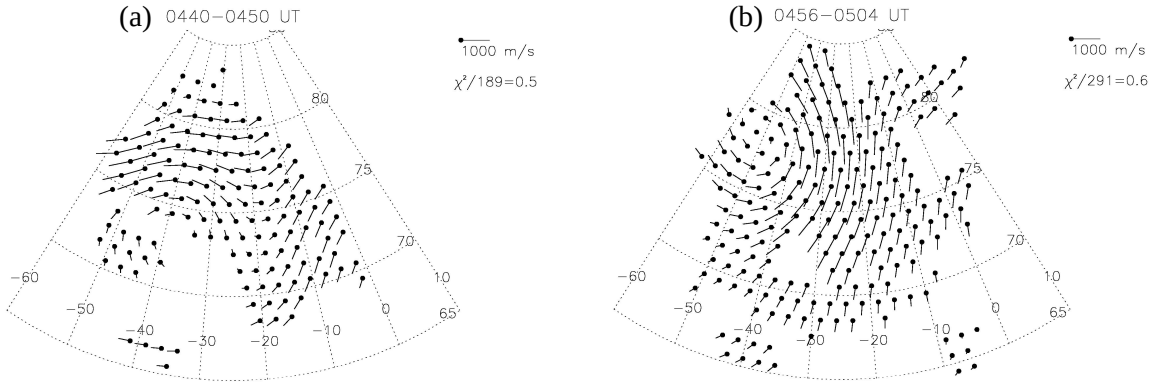

Figure 3.6 FIT convection map during (a) 0440-0450 UT, and (b) 0456-0504 UT. The AACGM coordinate system is applied.

The second approach for NRFE identification is to use the fitted data obtained from the map_potential routine [*Ruohoniemi and Baker*, 1998] (see Chapter 2.1 for a description of the FIT procedure). Figure 3.6 gives two averaged convection maps. The left panel is for 0440-0450 UT, and the right panel is for 0456-0504 UT, roughly corresponding to the two NRFE intervals. It is clear that the fitted convection pattern retains most of the features of the flow enhancement structures at high latitude ($>73^0$ MLAT) that were shown by the merged data in Figure 3.5. During the interval 0440-0450 UT, the fast flows from 75^0 to 80^0 MLAT and -40^0 to -58^0 MLON were strongly southwestward, while during the interval 0456 to 0504 UT, the fast flows were dominantly equatorward. Although the overall convection pattern is consistent with that obtained from the merged data, there are some discrepancies. For example, the strong eastward flows shown by the merged data on the west side of the equatorward flows

during the second flow enhancement period (Figure 3.5d,e) disappears on the FIT convection map. The comparison here validates our previous statement that the FIT procedure tends to smooth out some small-scale flow features, as the result of the averaging processes involved in the FIT procedure.

At times, data were available from only one radar of the Saskatoon-Kapuskasing pair, so that the merged data could not be produced and used as an "absol ute" reference of the convection velocities. Fitted velocities can be derived from one-radar observations but the velocities are then largely influenced by the statistical convection model imbedded in the FIT procedure. For example, for this event, the Kapuskasing data quality was poor after 0510 UT, so the identification of flow enhancements were based only on the VLOS measurements of the Saskatoon radar. Of course, this approach is least effective when the flows approach perpendicularity to the beam direction. Because we are mostly interested in those fast flows which have a strong equatorward component, we used only the beams directed close to magnetic north. The backscattered power and spectral width information from those beams can also be very important in studying the NRFE properties. We will use these two parameters in the study of the third NRFE event.

Figures 3.7a gives the Rankin Inlet MSP 630.0 nm optical emission observations during the interval 0400-0600 UT, March, 29, 1999. Figure 3.7b gives the MLAT-time plots of the VLOS as detected by the Saskatoon radar beam 3, which is directed roughly toward magnetic north. Positive VLOS denotes the towards-radar (roughly equator-ward) velocity component, while negative VLOS denotes the away-from-radar (roughly poleward) component. The dashed line represents the OCFLB estimated from the Rankin Inlet MSP 630 nm emission observations. The two above-mentioned flow enhancement structures from Figure 3.7b can be identified as the two light blue patches at 0438-0448 UT and 0458-0506 UT. They are both located on open field lines. It is interesting to notice that the Saskatoon radar echoes are separated into two regions by the OCFLB, i.e. far-range echoes ($>74^0$) on open field lines, and near-range echoes ($<73^0$) on closed field lines, up to 0510 UT. This spatial separation may indicate that the flows on open field lines and those on closed field lines were associated with different physical process in two topologically distinct magnetospheric regions, and that the

linkage between them, e.g., distant tail reconnection, was not operative from 0428 up to 0510 UT at the MLT sector of Saskatoon radar. There was a hint of flow enhancements on the closed field lines at 71-73^0 MLAT, 0512-0516 UT, when the echoes on open and closed field lines were, for the first time, connected. However, this flow enhancement structure was somewhat "isolated" both in latitudinal coverage and the duration, so little information could be deduced from it.

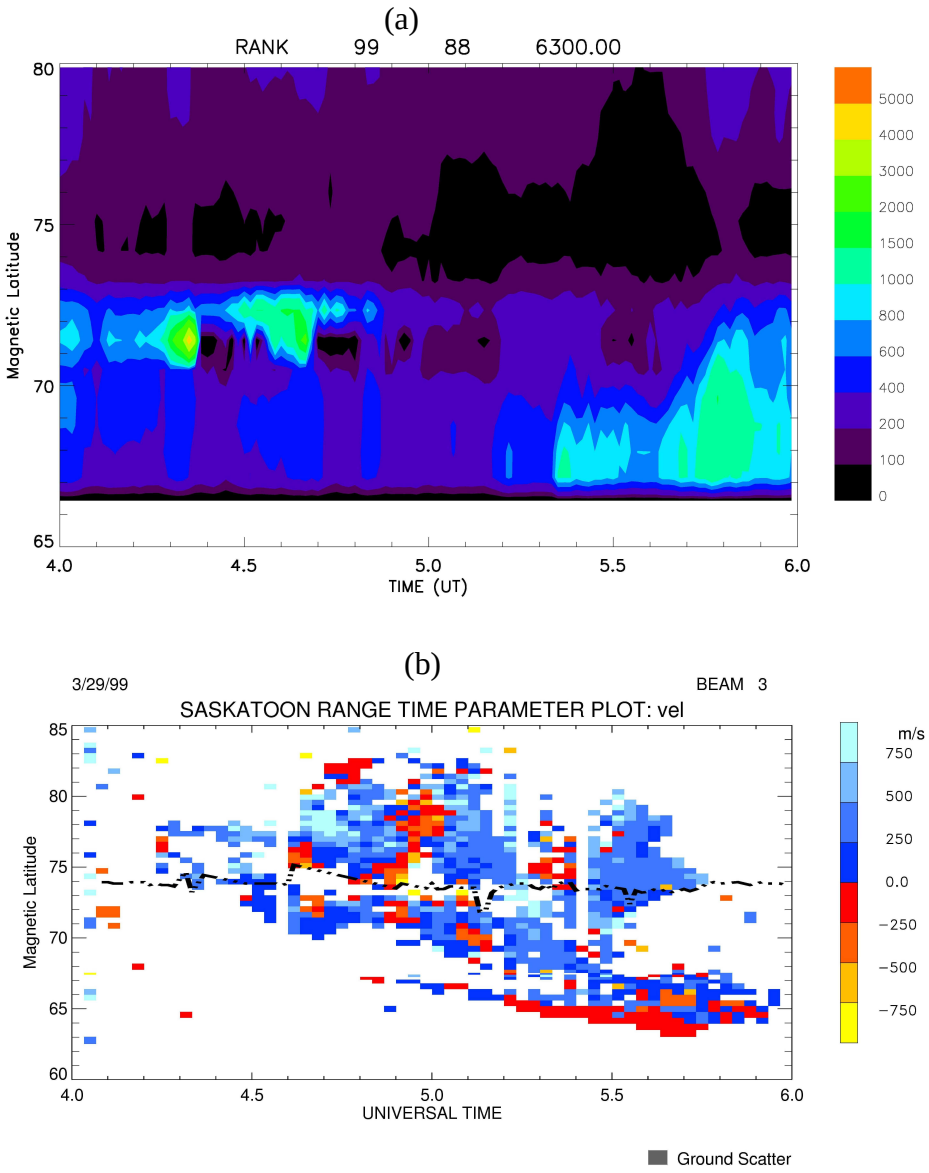

Figure 3.7 (a) Red-line optical emissions observed at Rankin Inlet from 0400 to 0600 UT, March 29, 1999; (b) The VLOS observed on Saskatoon radar beam 3 from 0400 to 0600 UT. The black dashed line indicates the polar cap boundary inferred form the poleward border of observed by Rankin Inlet MSP 630 nm emissions.

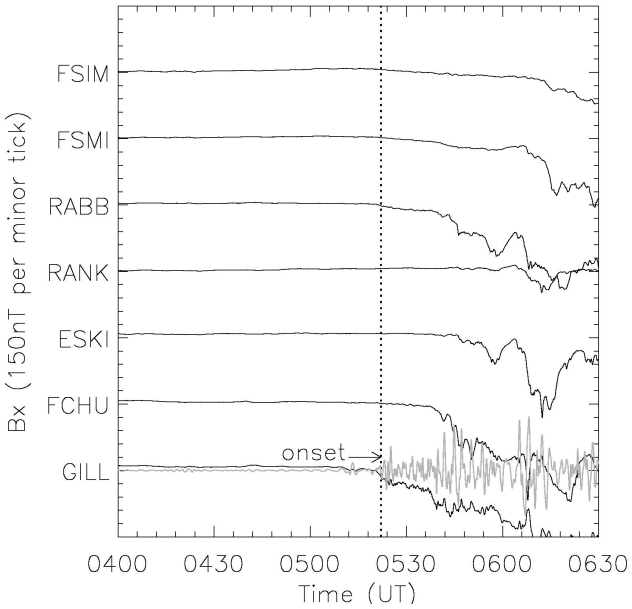

Figure 3.8 X-component (magnetic north) of magnetic fields observed at several CANOPUS stations during the interval 0400-0630 UT. The Pi2 pulsation at Gillam is shown by gray lines and the EP onset time is indicated by a vertical dotted line.

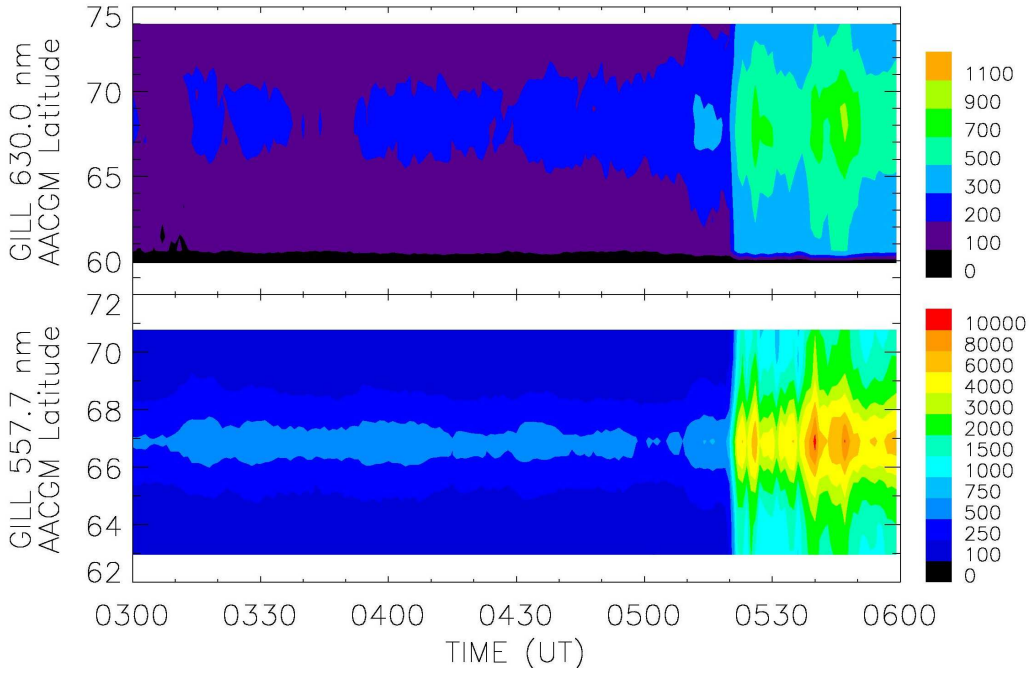

Figure 3.9 MSP observations at Gillam from 0300 to 0600 UT. The upper panel is the 630.0 nm and the bottom panel is the 557.7 nm emission.

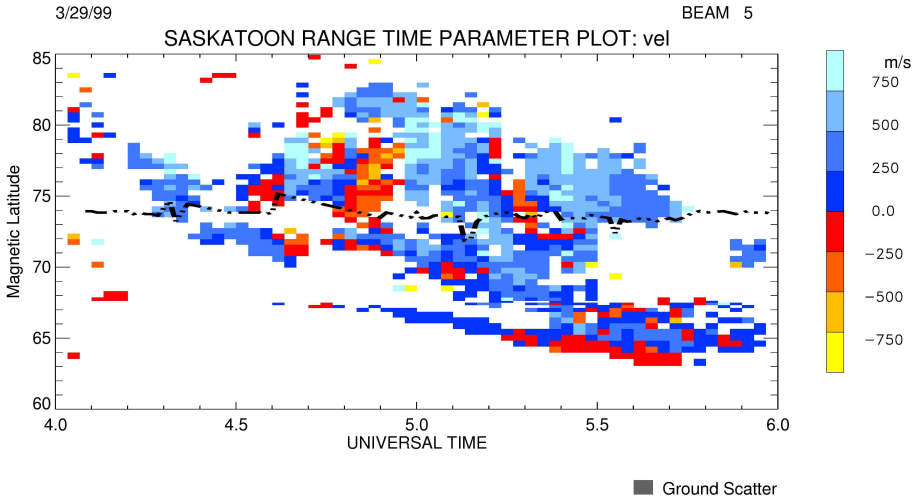

Figure 3.10 The VLOS observations on Saskatoon radar beam 5 during the interval 0400-0600 UT, March 29, 1999. The black dashed line indicates the polar cap boundary inferred form the poleward border of Rankin Inlet MSP 630 nm emission.

The CANOPUS magnetometer data are presented in Figure 3.8, and the MSP observations at Gillam are plotted in Figure 3.9. The negative magnetic bay and Pi2 bursts first started at Gillam at ~0522 UT, which is denoted as the substorm EP onset time. The negative bay was seen at Rabbit Lake at ~0542 UT, and at Fort Smith at 0610 UT. Thus the evolution of SCW was westward, in agreement with the propagation of the WTS. Before the onset there is very little magnetic disturbance at any station. Figure 3.9 also shows that the 630.0 nm and 557.7 nm emissions both revealed an intense breakup at ~0522 UT, but before that breakup there was virtually no auroral activity. We conclude that the flow enhancements on open field lines at 0438-0450 UT and 0456-0504 UT were not accompanied by any auroral and magnetic activity.

There was another equatorward flow structure from 0526 to 0544 UT at 71^0– 80^0 MLAT. This flow structure was found to traverse the OCFLB and has considerable portions on both the north and south sides of the OCFLB. Such an equatorward flow structure can readily be explained in terms of distant tail reconnection. Note that this flow structure occurred in conjunction with the substorm EP onset at ~0522 UT. However, because the majority of the flow structure had relatively small VLOS (<500 m/s), it seems not to fit our criteria for a NRFE. However, a careful inspection reveals

that this structure existed from beams 2 to 5. Figure 3.10 shows the VLOS on beam 5 of Saskatoon radar. A well-defined strong flow enhancement (>500 m/s) interval was visible as early as 0518 UT. Because the enhanced flows appear earlier and have larger VLOS on the eastern beam, it is clear that the flows have a considerable westward component, which is the reason why the magnetic-north directed beam 3 did not observe a strong VLOS for this flow enhancement. Thus we will classify it as a potential NRFE event. We note that the flow enhancement structure starting at 0518 UT seen on beam 5 was dominantly on open field lines. There were some hints of enhanced flows >500 m/s close to and south of the OCFLB after 0524 UT. On the other hand, the equatorward flow structure, though not strong in magnitude, has considerable portions on both open and closed field lines, with both starting at 0526 UT (notice there was an observation gap on beam 3 at 0524 UT).

In conclusion, we have listed three approaches for NRFE identification: (a) from the merged convection data; (b) from the fitted convection data; (c) from the VLOS measurements. The three approaches are generally compatible, but each has its own advantages and deficiencies. In this event we identified three periods of flow enhancements. The first, from 0438 to 0450 UT, was characterized by strong southwestward flows. The second enhancement was during the interval 0456-0504 UT. The convection pattern initially showed strongly eastward flows west of -30^0 MLON and strongly equatorward flows east of -30° MLON. Both of the above flow enhancements were on open field lines, but neither of them were accompanied by auroral and magnetic activity. Finally, there was a third NRFE interval which showed flow enhancements on both open and closed field lines. The enhancement on open field lines began at 0518 UT while that on closed field lines began at 0524-0526 UT; the latter was likely to have been associated with the substorm EP onset (~0522 UT).

During this event, the GEOTAIL satellite was located on the duskside flank magnetosheath. Figure 3.11 gives the magnetic field observed by the GEOTAIL MGF instrument. The position of GEOTAIL at each UT hour is labelled on the top of the plot. There are some spikes in the observation due to the equipment errors. We make the approximation that the magnetic field observations at the position of GEOTAIL are effectively at the subsolar magnetopause. The IMF variations which were assumed to

cause the above-mentioned three flow enhancements are labelled by three gray bands, with time delays between the IMF and flow enhancements of about 43 and 40, and 46 minutes, respectively. The relationship between the NRFEs and the IMF variations, and the expected time delays, will be discussed in section 3.4.1 in this chapter.

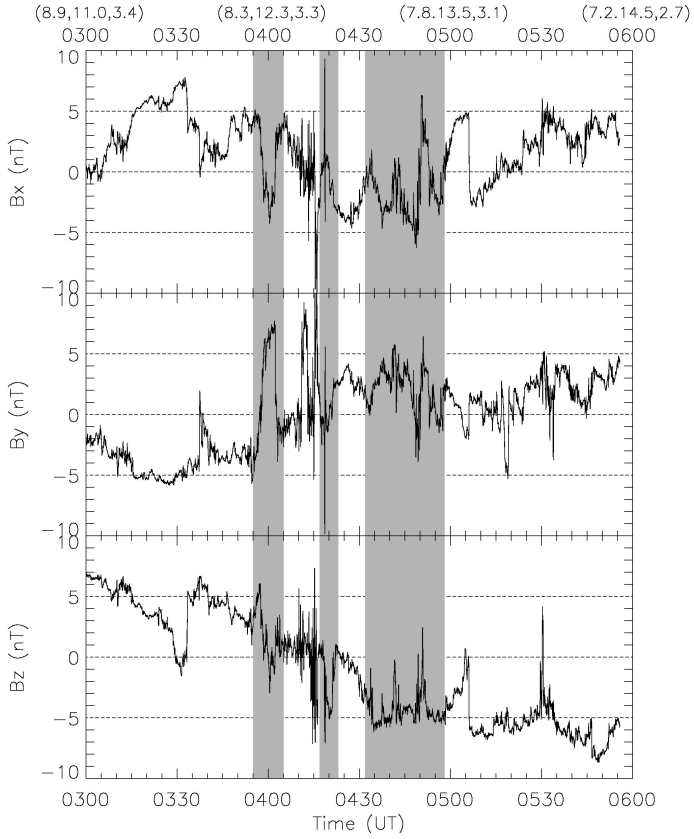

Figure 3.11 IMF observations from GEOTAIL. The GSM position of the satellite at the start of each UT hour is labeled at the top of the plot in units of Earth's radii (R_E). Gray bands indicate the possible IMF fluctuations that caused the NRFEs discussed in the text.

3.3.2 March 21, 1999 event

NRFEs were also found to occur during non-substorm periods. March 21, 1999 was the fourth quietest day in March, and the Kp index was only 1 from 6 to 9 UT on that day. The upper panel of Figure 3.12 gives the VLOS of Saskatoon radar beams 1 to 6 during the interval 0600-0900 UT. Since magnetic north is roughly located between beams 3 and 4, the VLOS values measured on beams 1-6 roughly indicate the equatorward component of ionospheric convection. The color scheme denotes the

latitudes where the echo VLOS values were measured. There were at least three intervals when NRFE structures were found during that period, namely 0630-0710 UT, 0725-0800 UT, and 0836-0850 UT. The lower panel of Figure 3.12 gives the X-component magnetic disturbances at Gillam, Rabbit Lake, Fort Smith, Fort Churchill and Eskimo Point. It is interesting to note that negative magnetic deviations of several tens of nT were observed at Gillam and Rabbit Lake for the first two flow enhancements, and also at Fort Smith for the second flow enhancement. For the third flow enhancement, however, there were some very small negative magnetic deviations at Fort Smith and Fort Churchill but almost no magnetic disturbance at either Gillam or Rabbit Lake. At the latitude of Eskimo Point, there was virtually no magnetic disturbance during the whole event interval.

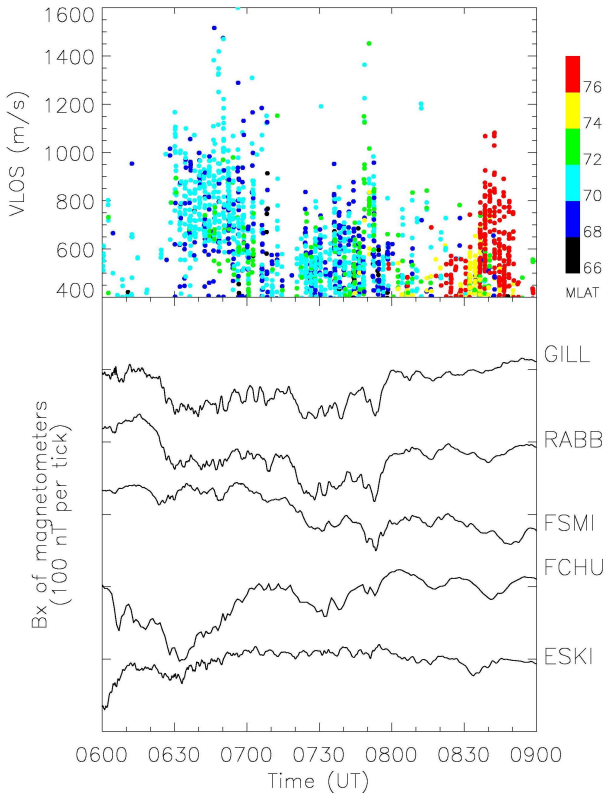

Figure 3.12 The upper panel gives the VLOS observation of beams 1-6. Color scheme denote for the MLAT where the VLOS is measured. The bottom panel gives the X-component (magnetic north) of the magnetic disturbances at several CANOPUS stations.

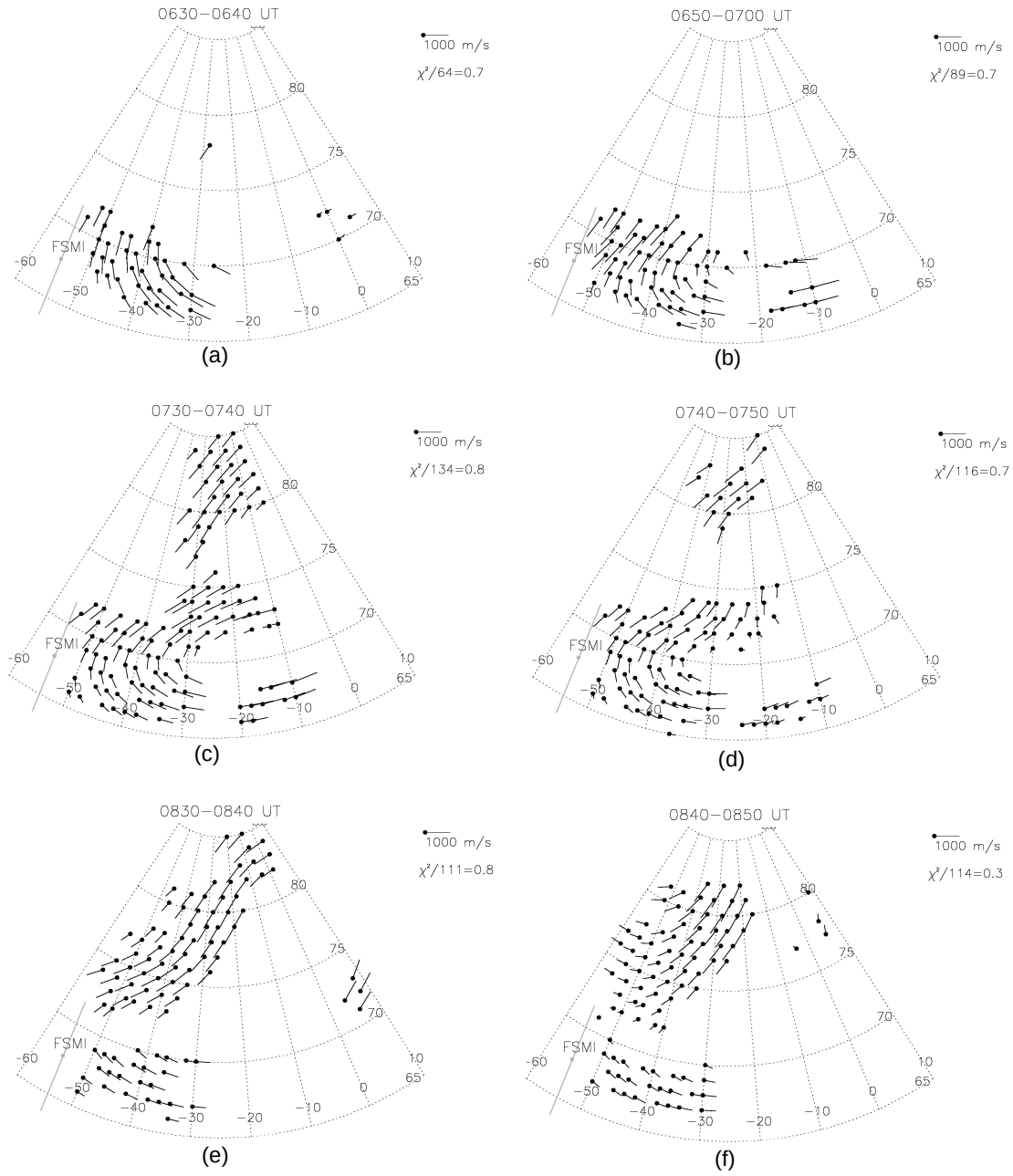

Figure 3.13 FIT convection map during the intervals: (a) 0630-0640 UT, (b) 0650-0650 UT, (c) 0730-0740 UT, (d) 0740-0750 UT, (e) 0830-0840 UT and (f) 0840-0850 UT. The AACGM coordinate system is used.

During the three flow enhancement intervals, the quality of the merged velocity map was mediocre, so we used the FIT convection map instead. Figure 3.13 gives the FIT convection map based on the map_potential procedure during the intervals: (a)

0630-0640 UT, (b) 0650-0650 UT, (c) 0730-0740 UT, (d) 0740-0750 UT, (e) 0830-0840 UT and (f) 0840-0850 UT. We note that, even for these 10-minute averaged maps, the number of data points is still not large. Nevertheless, in those regions containing radar echoes, there are some interesting ionospheric convection features.

The first two panels (a) an (b) correspond to the first NRFE interval. The flow enhancement (800-1000 m/s) was located at latitude $<72^0$ MLAT. The flow direction was dominantly equatorward. Panels (c) and (d) correspond to the second flow enhancement interval. High-speed flows are both seen at high latitudes at about 80^0 MLAT and at latitudes $<75^0$ MLAT. For the latter, the flows with velocity 600-800 m/s were first southwestward and then turned to more southward at $\sim 70^0$ MLAT. Finally, panels (e) and (f) correspond to the third flow enhancement interval. Strong southwestward flows of ~800 m/s were seen at 74^0-82^0 MLAT, while there were only some weak flows at latitudes below 72^0 MLAT.

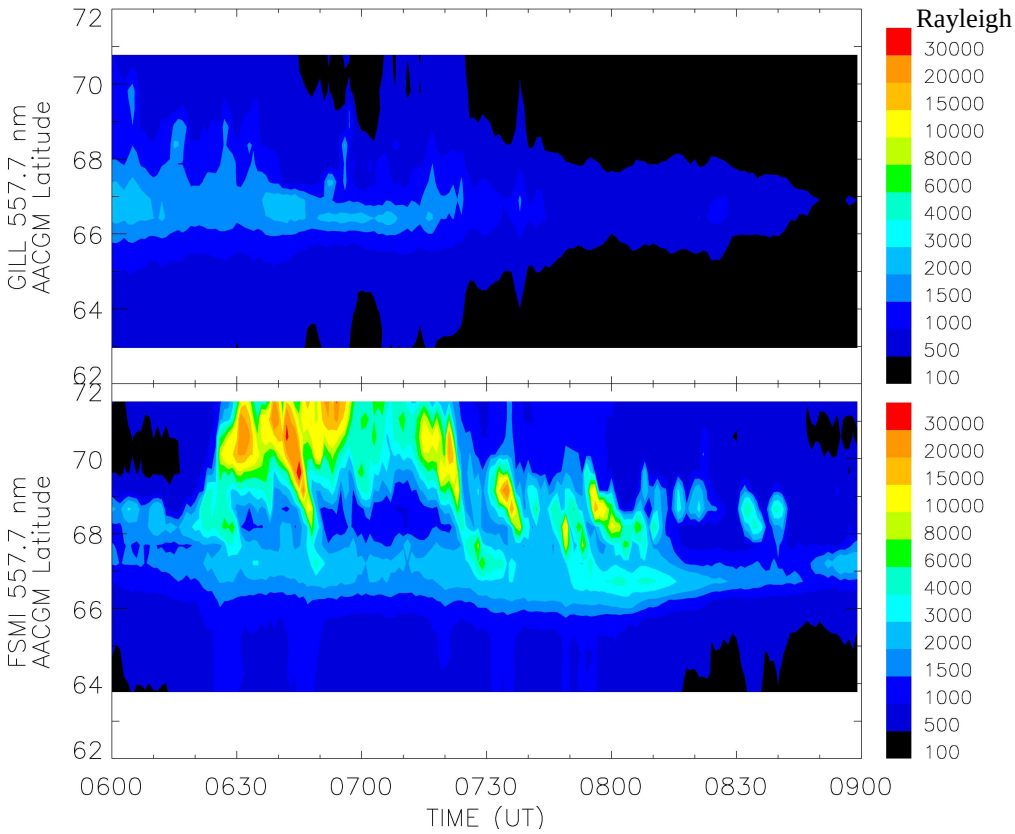

Figure 3.14 557.7 auroral emissions observed by the MSPs at Gillam (upper panel) and Fort Smith (bottom panel) from 0600 to 0900 UT.

Unfortunately the red-line emissions were contaminated by clouds during the event, so the poleward boundary of 630.0 nm emission boundary was not available for the Rankin Inlet MSP. Neither were there any DMSP passes near the radar observation region. Thus the OCFLB information could not be determined for this event. However, an investigation of Figures 3.12 and 3.13 shows that the first flow enhancement started at ~72^0 MLAT and extended equatorward to 68^0 MLAT, while the third flow enhancement started at well above 80^0 MLAT and extended equatorward to 74^0 MLAT. Considering the low geomagnetic activity level throughout the whole event interval, it is not unreasonable to assume that the first and the third NRFE structures, at least the main part of them, were on closed field lines and open field lines, respectively. For the second flow enhancement period, the NRFEs may have occurred on both open and closed field lines.

Figure 3.14 gives the 557.7 nm MSP observations at Gillam and Fort Smith during the interval 0600-0900 UT. The Gillam data in the upper panel reveal virtually no activity during the whole event sequence. On the other hand, the Fort Smith data in the lower panel show quite pronounced sporadic auroral intensification structures in the poleward part of the auroral oval. Those auroral intensifications were separated by about 10 minutes, and either were extended in the north-south direction or showed a slight trend toward decreasing latitude with time. Such slanted traces usually indicate fast equatorward-moving structures. Such signatures are likely indicative of the so-called N-S aurora or "auroral streamers" [*Zesta et al.*, 2000; 2002; *Nakamura et al.*, 2001a; 2001b]. Unlike the auroral brightenings associated with the substorm EP, which usually originate in the NGOPS that maps to the equatorward part of the auroral oval, the auroral streamers are found at much higher latitudes near the auroral poleward boundary. The high-latitude auroras and moderate magnetic disturbances are also the signatures of "convection bays", as discussed by *Sergeev et al.* [1998b; 2001]. However, due to the one-dimensional nature of the photometer observations and the lack of all-sky camera data for this event interval, the two-dimensional structure of the high-latitude auroras observed by the Fort Smith MSP is not known. We cannot say unambiguously whether those high-latitude auroras are north-south aligned structures or east-west arcs propagating equatorward [*Zesta et al.*, 2002].

It is interesting to note that, though somewhat sporadic, the most distinguishable periods for the auroral intensifications are from 0630 to 0658 UT and 0720 to 0800 UT, roughly corresponding to the time intervals of the first and second flow enhancements. In Figure 3.13 we also plot the Fort Smith MSP scanning line (in gray lines). It is clear that the high-latitude auroras observed by the Fort Smith MSP were west of the flow enhancement region, which is consistent with the results of a conjugate study on auroral streamers and flow bursts observed in the tail [*Nakamura et al*., 2001a; 2001b]. For the third period of flow enhancement, which is expected to be on open field lines, there was very little corresponding auroral activity on either the Gillam or the Fort Smith MSP.

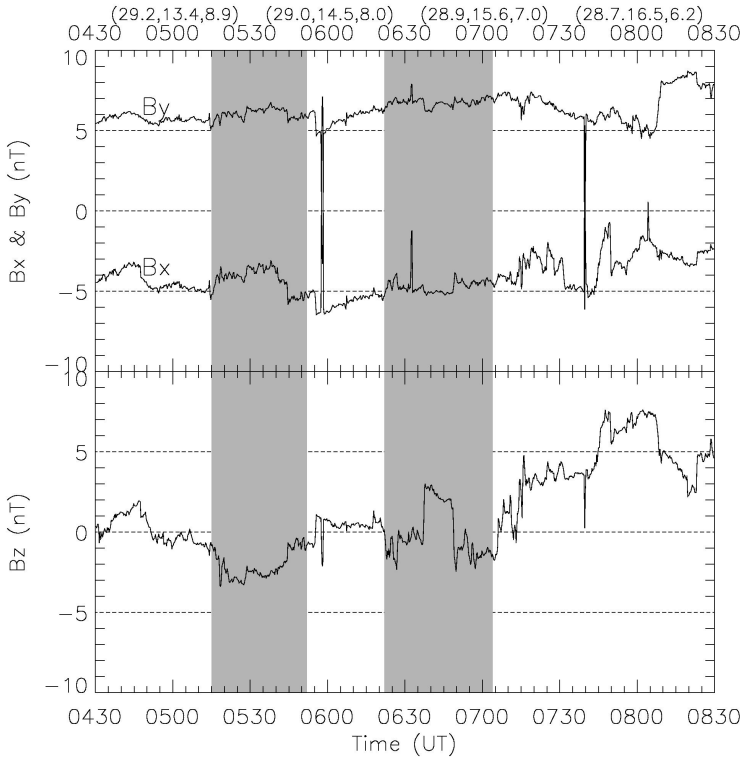

Figure 3.15 IMF observations from the IMP8 satellite. The GSM position of the satellite at the start of each UT hour is labeled at the top of the plot in unit of R_E. Two gray bands indicate the possible IMF events that caused the first two NRFEs discussed in the text.

In conclusion, in this event we identified three NRFE structures. The first and second flow enhancements were found to be related to negative magnetic deviations of several tens of nT but there was very little accompanying auroral intensification at

NGOPS latitude. They were likely to be associated with sporadic auroral structures occurring at the poleward portion of auroral oval. The third flow enhancement, which was probably on open field lines, was found not to be related to any significant magnetic and auroral disturbances.

The IMF parameters from IMP8 are plotted in Figure 3.15. From the two-satellite determination of the solar wind plasma phase fronts by ACE and IMP8 (see Appendix C.1), the solar wind propagation delay between the IMP8 and the subsolar magnetopause is estimated to be ~15 minutes. The IMF activations which were assumed to cause the first two NRFEs are labeled by the two gray bands, with time delays of 75 and 64 minutes, respectively. There is no obvious IMF event that might have caused the third NRFE.

3.3.3 December 26, 1998 event

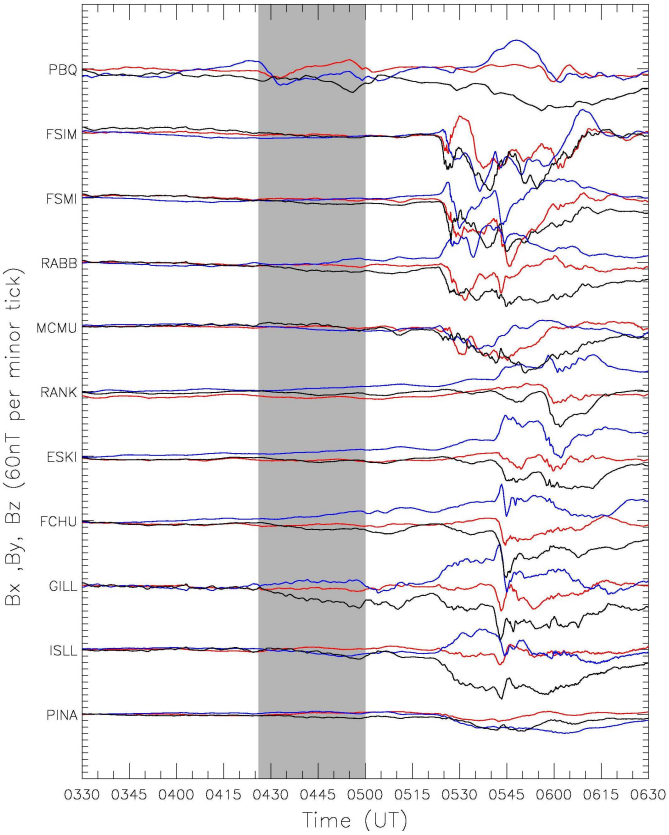

Figure 3.16 CANOPUS magnetometer data from 0330 to 0630 UT on December, 26, 1998. Black, red and blue lines denote the X, Y, and Z components of the magnetic field. The gray band indicates the time interval of interest.

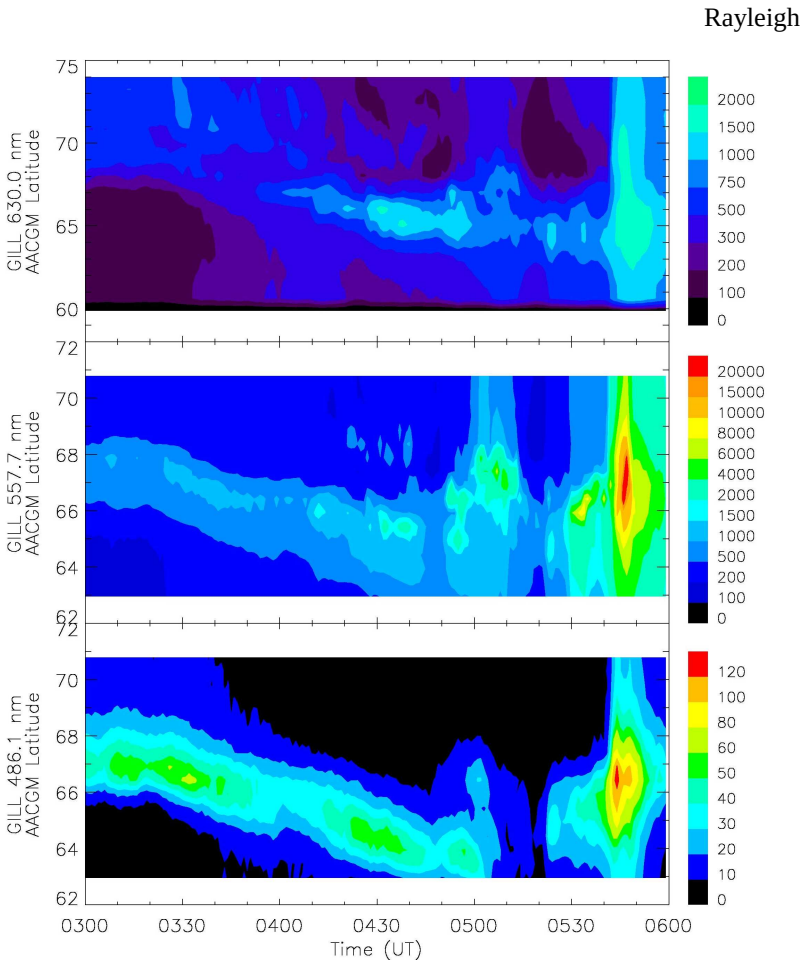

Figure 3.17 The 630.0 nm (upper panel), 557.7 nm (mid panel), and 486.1 nm (bottom panel) auroral emissions observed by the Gillam MSP from 0300 to 0600 UT.

We now focus on a period with concurrent NRFE and pseudosubstorm signatures. The CANOPUS magnetometer data during the interval 0330-0630 UT, December 26, 1998 are presented in Figure 3.16. Figure 3.17 shows the 630.0 nm, 557.7 nm and 486.1 nm emission data of the Gillam MSP from 0330 to 0600 UT.

There was considerable magnetic and auroral activity during this event. For example, there was a definite EP onset at 0524 UT. For this onset, the magnetic disturbances were most intense at Fort Smith and Fort Simpson, west of the "Manitoba line". Negative magnetic deviations were also seen at Gillam and Island Lake but the associated auroral features were weak at the Gillam MSP. A second EP onset occurred at 0541 UT, when the red-line, green-line and H_β emissions at the Gillam MSP all

brightened significantly and expanded poleward abruptly. In addition to these two well-defined onsets, a red-line auroral intensification structure was observed at about 65^0 MLAT by the Gillam MSP from 0426 to 0500 UT. A negative deviation of the magnetic field X component, which began at 0426 UT and reached a peak negative value of ~-200 nT at 0457 UT, was also observed at Gillam. Unlike the major onsets, the magnetic effects seem highly localized near Gillam during this period.

We shall focus on the auroral and magnetic activity from 0426 to 0500 UT in this event study. First we note that it is difficult to classify the activation. There were features similar to a substorm, such as auroral intensifications and a negative magnetic bay, but these were somewhat weak and localized. On the other hand, the equatorward boundary of the H_β (486.1 nm) emission intensification can be used to identify the b2i ion isotropy boundary, and its poleward/equatorward motion can be used to infer the inclination of the magnetic field in the inner magnetosphere [*Donovan et al.*, 2003]. During the period of interest, 0426-0500 UT, the b2i boundary migrated equatorward to ~63^0 MLAT and very little hint of dipolarization was observed, indicating that the current disruption/dipolarization did not occur at the b2i boundary. After 0449 UT there were some small poleward expansions of optical auroras, especially the green-line emissions. However, these expansions are smaller in magnitude than those for a typical substorm EP (see the differences between optical emissions during this period and those after 0541 UT in Figure 3.17). The above signatures are similar to those of a "pseudobreakup" during the substorm growth phase [*Koskinen et al*., 1993; *Nakamura et al.*, 1994; *Aiko et al*., 1999]. However, this event showed a time scale similar to a classical substorm EP but longer than the duration of a typical pseudobreakup, namely <10 minutes. The 0426-0500 activation is not likely to be a "convection bay" either, because convection bays are characterized by magnetic activity from mid-latitudes to latitudes inside the polar cap, but with auroral activation near the poleward boundary, or even without any auroral breakup signature [*Sergeev et al*., 1998b; 2001]. In our event, auroral intensifications occurred at ~65^0 MLAT, with a very localized negative magnetic bay at Gillam. From the Z-component of the Gillam and Island Lake magnetograms, we infer that the WEJ was located slightly south of Gillam. All these observations strongly indicate that the auroral and magnetic activities in this event

began in the near-Earth region as in typical substorms, so the triggering mechanisms might be quite similar. In this paper we will refer to the event as a "pseudosubstorm", which may contain several short-lived "pseudo breakups". This nomenclature is in agreement with that in *Ohtani et al*. [1993b]. We support the view by *Nakamura et al.* [1994] and *Rostoker* [1998] that pseudobreakups and substorm onsets are associated with almost the same magnetospheric processes but differ in the magnitude of the disturbance, the spatial and temporal scales, and the global consequences. For our pseudosubstorm event, we suggest that the initial substorm-like activities, such as cross-tail current disruption and SCW formation, took place in the NGOPS but did not lead to significant tailward expansion to the mid-tail or to earthward progression to the innermost edge of the tail current sheet (b2i). However, the reason for the localization of the activity remains an open question.

Another question relates to the initial position and the extent of the SCW of this pseudosubstorm. The SCW formation usually begins in a restricted time sector and subsequently expands both westward and eastward [*Belehaki et al*., 1998]. The propagation speed and the maximum extension can be quite asymmetric for the westward and eastward expansions. The Rabbit Lake station west of the "Manitoba line" is approximately at the same latitude as Gillam, but the Rabbit Lake data exhibited an X-component bay of only ~-90 nT during the whole pseudosubstorm interval, indicating that the western edge of the WEJ did not reach Rabbit Lake. There is a relative scarcity of magnetometer stations east of the "Manitoba line" at the NGOPS latitude. In the uppermost panel of Figure 3.16 we give the data from Poste-de-la-Baleine (PBQ) station of the NRCAN Geological Survey of Canada (GSC) array, which is similar in MLAT to Gillam but 27^0 east in MLON. At the PBQ station, a ~-220 nT negative X-component bay started at ~0443UT, lagging the beginning of the negative bay observed at Gillam by 17 minutes. A ~1.6^0/min eastward expansion of the SCW thus can be deduced, in accord with the 1-2^0 /min eastward SCW expansion speed estimated by *Kokubun and McPherron* [1981] and *Belehaki et al*. [1998].

We can use the geosynchonous orbit observations of GOES-8 to estimate the eastern limit of the SCW. Figure 3.18 gives the GOES-8 magnetic field measurements from 0300-0630 UT. GOES-8 was located at -75^0 geographic longitude, which is very

close to, and just east of, the PBQ station. The GOES-8 magnetic fields have been converted to the VDH local coordinate system (see Appendix A). The magnetic elevation angle θ_B is defined as:

$$\theta_B = \arctan\left(-B_H / B_V\right) \quad . \tag{3.1}$$

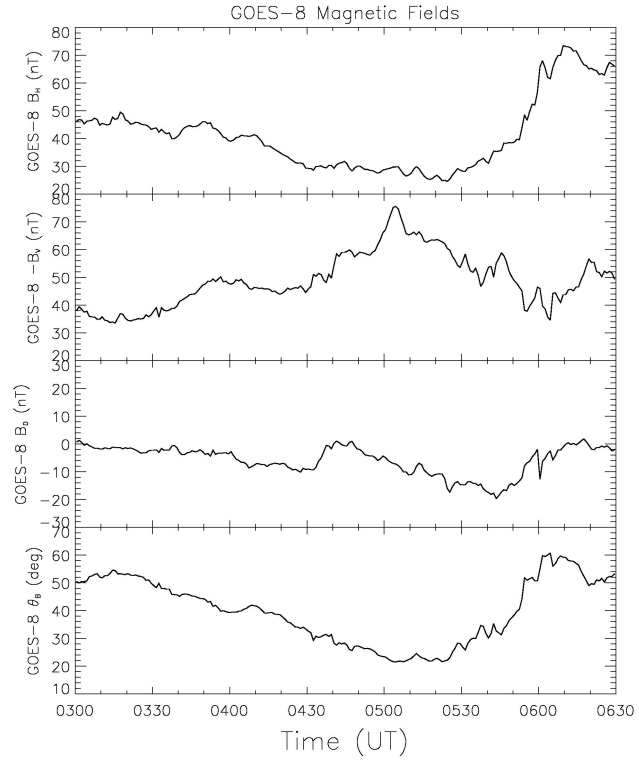

Figure 3.18 GOES-8 magnetic field observations. The magnetic fields are transformed into VDH local coordinates. The first, second, and third panels show the B_H, $-B_V$, and B_D components, respectively. The fourth panel gives the magnetic elevation angle defined by equation (3.1).

It is clear that magnetic field line stretching began at ~0314 UT, as shown by the decrease of θ_B, indicating the start of the substorm growth phase. The magnetic dipolarization effect began at ~0524 UT, which was the first substorm EP onset time shown by the CANOPUS magnetometer data. During the time of interest, namely 0426-0500 UT, no dipolarization was observed at GOES-8, again indicating that the

pseudosubstorm was a localized activation. However, it is interesting that, during the interval 0431-0502 UT, there was a strong decrease of B_V (shown in the plot as an increase of $-B_V$), while the B_H component remained virtually constant. Such a B_V decrease is very likely due to strong downward field-aligned currents (FACs) located west of the GOES-8 position. This downward FAC would mark the eastern edge of the SCW associated with the pseudosubstorm. We can conclude that, after 0431 UT, GOES-8 detected the effect of approaching downward FACs caused by an eastward expansion of the SCW. By 0443 UT the WEJ associated with the SCW had expanded eastward enough to be detected by the PBQ magnetometer. On the other hand, the eastern edge of SCW did not pass the satellite during the pseudosubstorm interval. If it had, a bipolar feature in the B_V component and a magnetic dipolarization effect due to the reduction of cross-tail current would have been detected in the GOES-8 observations. The final eastern limit of the SCW for the pseudosubstorm was longitudinally somewhere between PBQ station and the footprint of GOES-8.

The most interesting feature of this pseudosubstorm event is that, during almost the same time interval, a NRFE event was observed by the Saskatoon SuperDARN radar. Figure 3.19a shows the Range-Time plot (RTP) of the VLOS of Saskatoon beam 4 from 0300 to 0600 UT. The direction of beam 4 is within 15^0 of magnetic north up to 80^0 MLAT. On beam 4 magnetic midnight occurs at about 0726 UT at 70^0 MLAT and at 0707 UT at 80^0 MLAT. The radar observations from 0300 to 0600 UT were confined to the premidnight sector. The dashed line in the plot represents the OCFLB estimated from the 630 nm MSP observations at Rankin Inlet given in Figure 3.19b. Such a 630 nm poleward boundary was identifiable after 0405 UT (~2130 MLT).

Figure 3.19a shows that a very well-defined NRFE structure (VLOS>500 m/s) existed during the pseudosubstorm interval (0426-0500 UT). The NRFE structure first appeared just south of the OCFLB and evolved slowly equatorward. In the vicinity of the OCFLB, the VLOS direction is dominantly toward the radar, indicating flows across the polar cap boundary. This is in accordance with *De la Beaujardière* [1994], who showed that high-speed equatorward flows in the ionosphere are usually seen first near the OCFLB, where they correspond to a localized increase in plasma flow across the separatrix and thus to a localized increase in the nightside reconnection. There were also

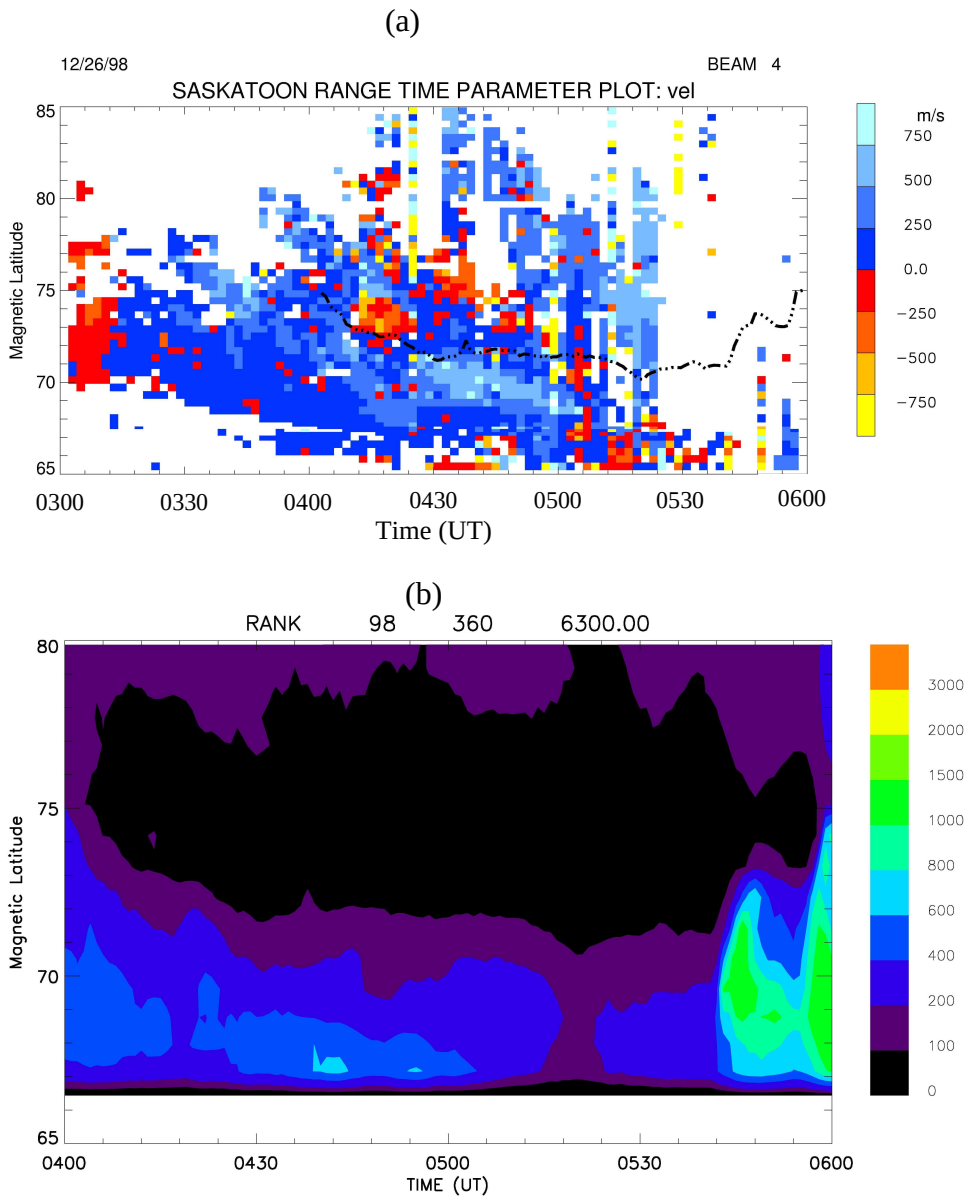

Figure 3.19 (a) The VLOS observations on Saskatoon radar beam 4 from 0300 to 0600 UT, December 26, 1998. The black dashed line denotes the estimated OCFLB from red-line emission observations at Rankin Inlet; (b) Red-line optical auroral emissions observed at Rankin Inlet from 0400 to 0600 UT.

some other identifiable fast flow structures. For example, the first hint of flows with VLOS >500 m/s appeared at ~0336 UT and ~75^0 MLAT, but this flow structure was at ~1940 MLT and mapped to the duskside magnetosphere flank where the dynamic behavior is significantly different from that of the mid- and distant tail regions that are

the major focus of our NRFE study. There is also one "patchy" structure during 0358-0414 UT at 75-78^0 MLAT, which is better seen on beam 5 (not plotted) or later in Figure 3.25, and another well-defined structure during 0510-0524 UT at 74-80^0 MLAT. Those two NRFEs occur on open field lines, and were not associated with auroral activations. Unfortunately, after the substorm onset (~0524 UT in this event), the ionospheric *F* region echoes are mostly absent, probably due to strong absorption in *E* and *D* regions, or to unfavorable propagation conditions resulting from the enhanced *E* region electron densities. This lack of radar echoes prevented us from investigating the association between the optical auroral brightenings and the ionospheric convection signatures during the substorm EP.

The solar wind data from 0200-0600 UT on December, 26, 1998 are plotted in Figure 3.20. Before 0300 UT, IMF Bz was positive for more than 2 hours, with a sudden drop from 10 nT to 0 at 0210 UT and another drop from 8 nT at 0220 UT to 2 nT at 0235 UT. We infer that the magnetosphere was relatively quiet before 0300 UT. The IMF shifted southward at about 0300UT at WIND. After that the IMF was relatively stable and Bz remained negative for more than 3 hours. During the time of interest there was a strong positive By component. The bottom panel gives the solar wind electric field, which was defined as [*Nakamura et al*., 1999]:

$$E_{sw} = -V_x (B_z^2 + B_y^2)^{1/2} \sin^4(\theta/2) \quad , \tag{3.2}$$

where $\theta = \arctan(B_y / B_z)$ is the IMF clock angle. We notice three intervals of enhanced solar wind electric field, i. e., 0300-0325 (SWE1), 0340-0415 (SWE2), and 0430-0440 (SWE3). Interval SWE2 lasted ~35 minutes and showed the strongest electric field, up to 3.8 mV/m. The solar wind was also observed on the ACE satellite (not plotted) located at 224 R_E upstream and ~36 R_E off the Sun-Earth line in the GSM-Y direction. The solar wind observations on WIND agree quite well with those on ACE but with a lag of ~51 minutes. According to the two-satellite determination of the solar wind plasma phase front (see Appendix C.1), the propagation time from WIND to the bow shock (~12 R_E) is estimated as ~2.5 minutes. The slowing of the solar wind through the magnetosheath adds ~3.5 minutes if a thickness of ~2 R_E is assumed. The total solar

wind propagation delay thus is estimated to be about 6 minutes from the WIND satellite to the subsolar magnetopause.

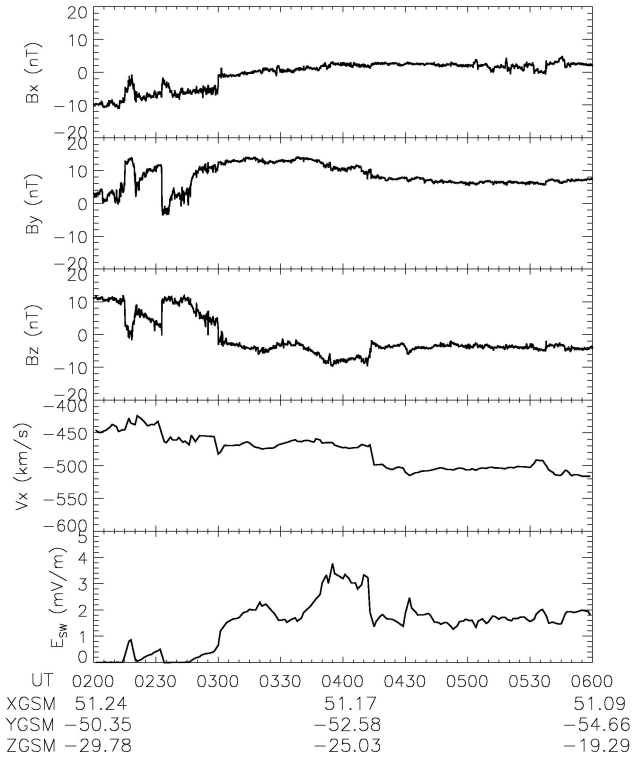

Figure 3.20 Solar wind parameters observed from WIND. The first three panels give magnetic field components in GSM coordinate and the fourth panel shows the X component of the solar wind velocity. The bottom panel shows the solar wind electric field defined by equation (3.2). The GSM coordinate of the WIND is labeled at the bottom of the plot.

The last and weakest solar wind electric field enhancement (SWE3) occurred after 0430 UT and therefore could not have initiated the NRFE under investigation. Both SWE1 and SWE2 are possible candidates for initiating our event. Subtracting the ~6 minutes propagation delay from WIND to subsolar magnetopause, the lags between these two solar wind activations at the dayside magnetopause and the NRFE event would be 80 and 40 minutes, respectively, which are both plausible in terms of the observed delays between the NRFEs and the solar wind activations.

We will use the GEOTAIL observations, which are given in Figure 3.21, to decide whether SWE1 or SWE2 led to the NRFE. To identify the magnetospheric region in which GEOTAIL was located, we define the tail lobes as the region where ion-$\beta < 0.1$ [*Nagai et al*., 1998], the plasma sheet by ion-$\beta > 0.5$, and the PSBL by 0.1<ion-$\beta < 0.5$. These definitions are basically similar to those of Ang*elopoulos et al*. [1994], the difference being that our PSBL classification may in fact include some parts of the outer plasma sheet (OPS). In the seventh panel of Figure 3.21 we show the dawn-dusk component of the convective electric field defined by $\mathbf{E} = -\mathbf{V} \times \mathbf{B}$. We found two large electric field perturbations at 0349-0400 and 0426-0442 UT. It is tempting to associate these two perturbations with the first two major solar wind electric field enhancements, SWE1 and SWE2, with time lags of 49 and 46 minutes, respectively. *Nakamura et al*. [1999] found that the mid-tail plasma sheet electric field responds to the solar wind electric field with a time delay of 45-80 minutes. When GEOTAIL is in the OPS/PSBL or the tail lobe, a shorter time delay is expected. The SWE3 burst might be associated with the small electric field perturbation seen on GEOTAIL at 0500-0505 UT. The last small electric field perturbation right after the first major EP onset (~0524 UT) was likely to be the induced electric field associated with the dipolarization of the magnetic field in the plasma sheet during the substorm EP.

It should be noticed that there was a substantial MLT difference (2.5-3 hours) between the NRFE region seen by the Saskatoon radar and the GEOTAIL position during the event interval. Exact correspondence between the GEOTAIL and SuperDARN observations is not generally expected. However, we notice that the second and strongest dawn-dusk convective electric field enhancement observed on GEOTAIL, which was likely triggered by SWE2, began at almost the same time (0426 UT) as the NRFE observed by SuperDARN. On the other hand, when GEOTAIL was making a sharp transition from plasma sheet to tail lobe, traversing the PSBL at 0427 UT, it observed a very fast and almost purely field-aligned flow. This is a well-known characteristic of the PSBL and is usually related to DTNL activations [*Nakamura et al*., 1999]. In our previous analysis we stated that the NRFE originated just south of the OCFLB and thus was likely associated with a DTNL activation. The DTNL activations shown by GEOTAIL observations and those implied by the NRFE might not be exactly

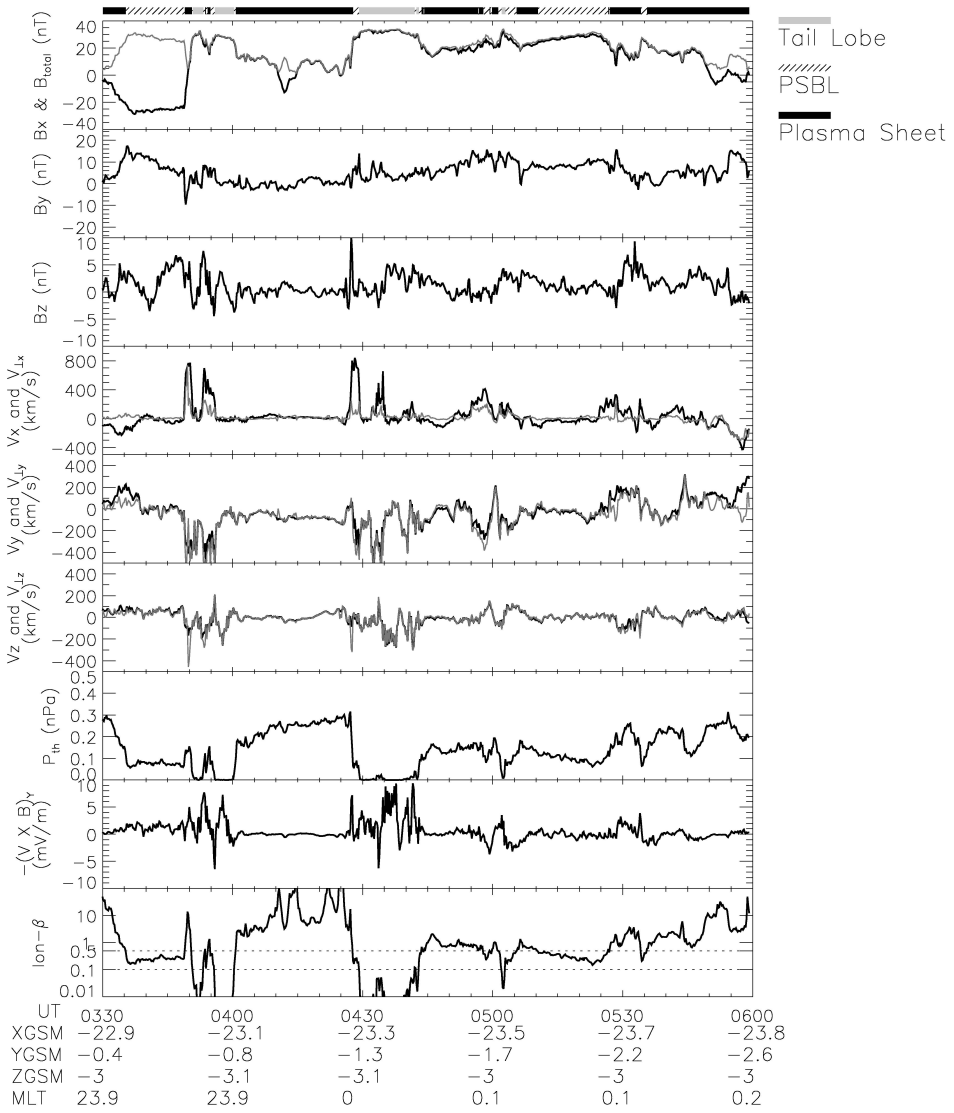

Figure 3.21 GEOTAIL observations of the magnetic field in GSM coordinates, flow velocity, the dawn-dusk component of convective electric field, and the ion-β value during 0330-0600 UT on December 26, 1998. In the first panel the black and gray lines denote Bx and total magnetic field strength B_{total}, respectively. In panels 4/5/6 the black and gray lines represent the GSM-X/Y/Z components of the flow velocity and the convective component of flow velocity which is perpendicular to the local magnetic field, respectively. The GSM coordinate and the MLT of its footprint, which is calculated from the Tsyganenko-96 model [*Tsyganenko and Stern*, 1996] based on the averaged solar wind parameters observed on WIND, are labeled in the bottom of the plot. The estimated magnetospheric regions where GEOTAIL was located are plotted in the top of plot.

the same because the reconnection process in the equatorial tail is usually highly localized. Nevertheless, due to their nearly simultaneous occurrence, it is reasonable to attribute the two DTNL activations to the same solar wind enhancement, namely SWE2. Furthermore, it is also tempting to relate the other two NRFE intervals on open field lines, namely 0358-0414 UT, and 0510-0524 UT, with the solar wind electric field enhancements SWE1 and SWE3 seen on WIND, and with the dawn-dusk electric field perturbations seen on GEOTAIL ~10 minutes before the NRFEs were observed in the ionosphere by radar.

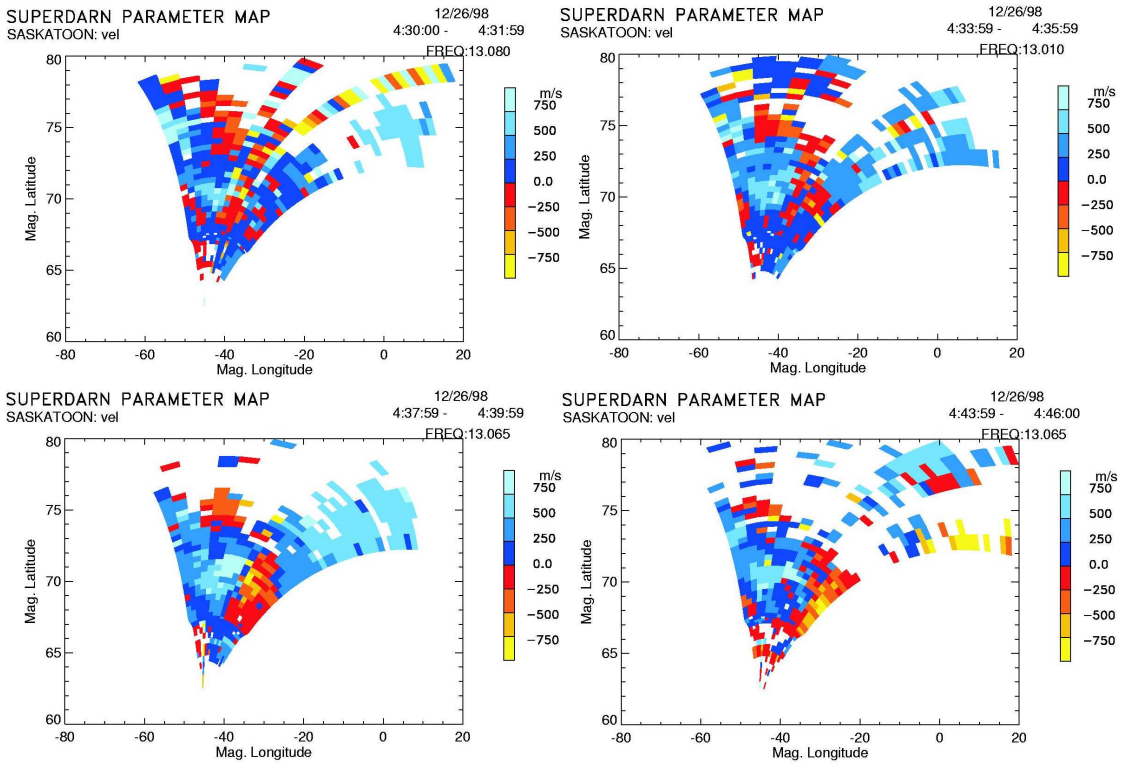

Figure 3.22 Four 2-minute scan maps of the Saskatoon HF radar VLOS observations during the intervals 0430-0432, 0434-0436, 0438-0440, and 0444-0446 UT.

Figure 3.22 gives four scan maps of the Saskatoon radar during the pseudosubstorm interval. The region of flow enhancement between 68.5^0 and 72^0 MLAT was longitudinally localized between beams 3 and 8 during the event and peaked mainly between beams 4 and 7. Interesting information arises from the negative VLOS

structure observed on the eastside beams. Figure 3.23 shows the range-time VLOS plot on beam 15, the easternmost Saskatoon radar beam. The angle between its direction and magnetic north is ~55^0 at the longitude of Gillam. Thus beam 15 measures more of the magnetic zonal flow component than the magnetic meridional component. Eastward flow can produce a negative VLOS (away from the radar), while westward flow can produce a positive VLOS (towards the radar). In Figure 3.23 we notice that there is a well-defined negative VLOS structure from 0428 to 0456 UT, roughly corresponding to the NRFE interval. The negative VLOS structure occupies the latitudinal range 66-70^0 MLAT and reaches a peak negative magnitude of ~-1000 m/s. The negative VLOS structure on beam 15 is also close to Gillam in longitude (see the geometry shown in Figure 3.1).

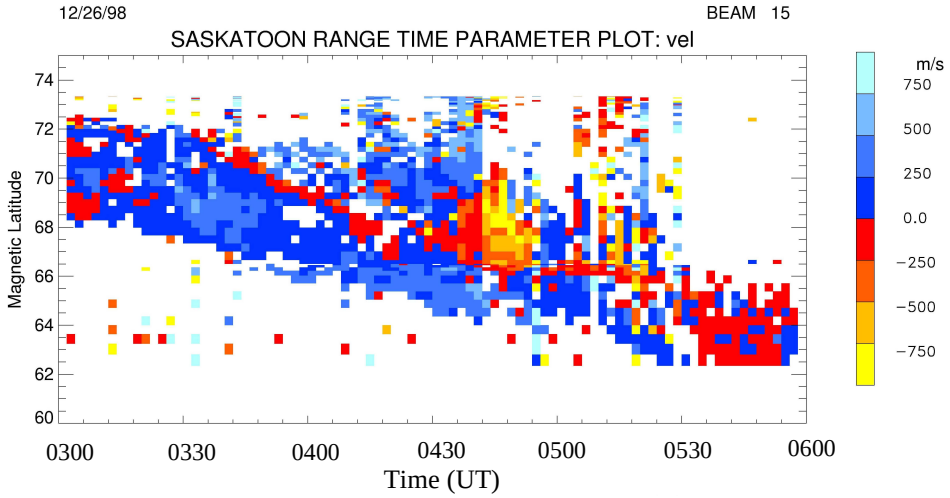

Figure 3.23 The VLOS observations on Saskatoon radar beam 15 from 0300 to 0600 UT on December 26, 1998.

To help in understanding this negative VLOS structure, we give in Figure 3.24 a 10-minute averaged electric potential pattern during 0440-0450 UT (mid-interval of the event) when the largest negative VLOS was found on beam 15. Figure 3.24 is based upon the potential map procedure of *Ruohoniemi and Baker* [1998] for IMF parameters Bz-, By+ and 6<|B|<12, which are the prevailing IMF conditions during the event time (see Figure 3.20). The solid lines are the negative potential contours, on which the convection streamlines are clockwise. The dashed lines indicate the positive potential

contours, on which the convection streamlines are counterclockwise. The gray bar shows the rough latitudinal extent of the auroral intensification observed by the Gillam MSP. During this event interval there was a lack of Kapuskasing radar data, so the fitted convection pattern was determined almost solely from the Saskatoon data and thus was influenced by the statistical convection model. Because the statistical model tends to smear out the localized flow structure, the fitted convection is not appropriate for studying the details of the flow enhancements in our event. However, the fitted convection pattern in Figure 3.24 does show an interesting feature. The equatorward flows between 36-42^0 MLON, where the peak flow enhancement was located as shown in Figure 3.22d, turned strongly eastward at ~68.5^0 MLAT, and reversed to westward at ~66^0 MLAT. A zonal flow shear region, with eastward flows on the poleward side and westward flow on the equatorward side, was easily identified. Such a zonal flow shear region in the midnight-premidnight sector is usually assumed to be a signature of the Harang discontinuity (HD). The HD geometry has a downward vorticity which implies an upward FAC [*Sofko et al.*, 1995] and in turn is closely associated with the optical auroral intensification [*Koskinen and Pulkkinen*, 1995; *Bristow et al.*, 2001].

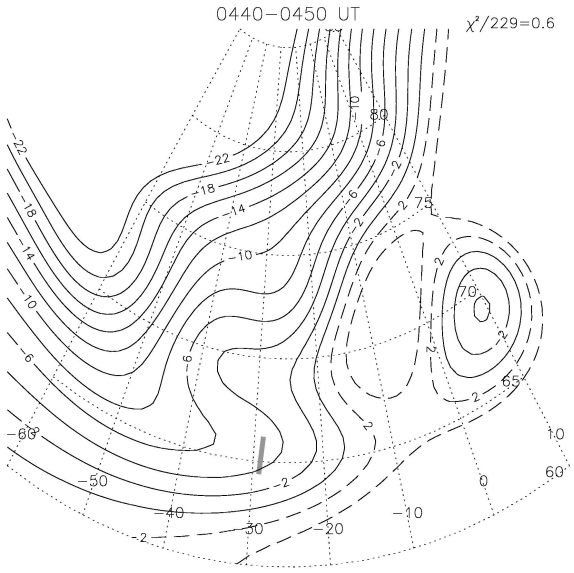

Figure 3.24 The FIT electric potential map averaged over 0440-0450 UT. The gray bar at ~29^0 MLON denotes the latitudinal extension of auroral intensification observed by the Gillam MSP.

Although there were insufficient observations to reveal the azimuthal extension of the auroral intensification structure, the convection pattern is consistent with the suggestion by *Yeoman et al.* [2000a] and *Bristow et al.* [2001] that the ionospheric plasma tends to flow around an auroral intensification region as if the brightened auroras act as an obstacle to the flows. If the transition from negative to positive VLOS values observed on beam 15 is the result of zonally sheared flows, we can infer from Figure 3.23 that such conditions existed at 0332 UT and migrated equatorward until 0424 UT. The implication is that the HD was a consistent feature of the substorm growth phase, but was strongly intensified and expanded during the pseudosubstorm interval.

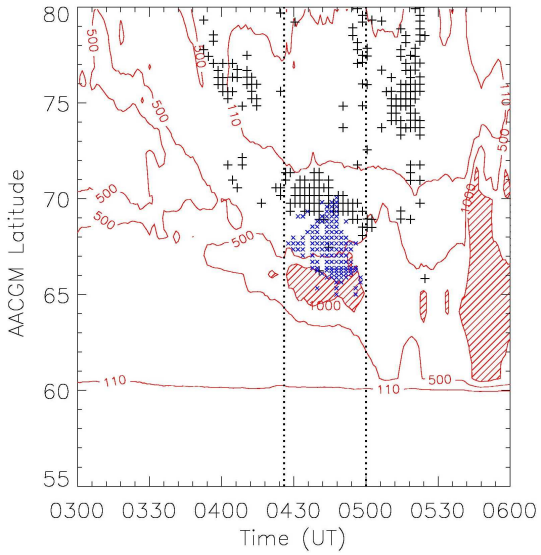

Figure 3.25 The enhancement regions of flow velocity and of optical emissions. The red lines show the 630 nm emission contours. The black '+' symbols denote the region where the VLOS averaged on beam 4 and 5 exceeds 500 m/s. The hatched areas are the regions where the 630 nm emission intensity is larger than 1 kR. The blue crosses denote the region of negative VLOS observed on beam 15 during 0426-0500 UT.

Figure 3.25 illustrates the flow enhancement region based upon the observations on beams 4 and 5, the negative VLOS structure observed on beam 15, and the auroral intensification region. The red lines are the contours of the 630 nm emission. We combined the MSP data from Rankin Inlet and Gillam by simply using the Gillam data

below 70^0 MLAT and Rankin Inlet data above 70^0 MLAT. This minimized the errors arising from low-elevation MSP measurements. The black '+' symbols indicate where the VLOS average of beams 4 and 5 is greater than 500 m/s. As mentioned above, the flow enhancement was mainly detected mainly on radar beams 4 to 7. Beams 4 and 5, within 10^0 of magnetic north at 70^0 MLAT and within 14^0 of magnetic north at 75^0 MLAT, showed the best overall observational data quality during the event. The average VLOS on beams 4 and 5 should represent the equatorward component of the flows to good accuracy. Care was taken to exclude *E* region echoes by using the Saskatoon radar elevation angle observations obtained from the interferometer mode. Again we noticed that the NRFEs at 0358-0414 and 0510-0524 UT, which were on the open field lines, have no accompanying auroral activations. We focus on the concurrent flow enhancement and the 630 nm auroral intensification (>1kR), which were both well-defined both spatially and temporally between 0426 and 0500 UT, as shown between two vertical dotted lines. The poleward border of the flow structure closely matched the 110 R contour, which is assumed to be a proxy for the OCFLB, from 0426 to 0440 UT. An equatorward progression of the flow structure down to ~68.9^0 MLAT can be recognized. After 0440 UT, the structure propagated away from the OCFLB and down to 68.1^0 MLAT. On the other hand, the 630 nm optical intensification region was located at 64.5-66.5^0 MLAT, about 4-5^0 south of the flow structure. This latitude interval should map to the NGOPS. The blue crosses denote the regions of negative VLOS observed on beam 15 during 0426-0500 UT. Although the upper latitudinal limit of the negative VLOS region reaches ~70^0 MLAT, the majority of this structure is between the flow enhancement region and the auroral intensification region. Considering the convection pattern shown in Figure 3.24, the equatorward border of the negative VLOS structure may be used to indicate the zonal flow reversal (east-to-west) boundary. We see that such a boundary first moved equatorward to ~65^0 MLAT from 0426 to 0446 UT, and then poleward to ~66.5^0 MLAT at 0456 UT. These trends exactly match those of the poleward border of the auroral intensification region during the same interval. This coincidence provides strong evidence of the association between the zonal flow shear region (HD) and the auroral intensifications, which is consistent with

the previous finding that the substorm-associated auroral brightening arc is close to but often slightly equatorward of the HD [*Koskinen and Pulkkinen*, 1995].

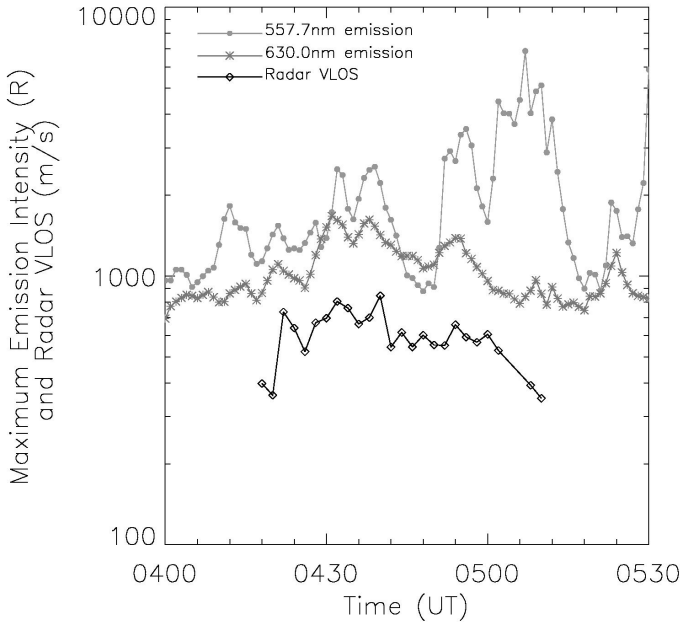

Figure 3.26 The maximum VLOS (diamonds joined by solid line) and the maximum intensities of both 630 nm (asterisks joined by solid line) and 557.7 nm emissions (dots joined by solid line) during the event interval.

To study the correlation between the flow enhancement and the auroral intensification, we selected the maximum optical emission intensity and the maximum VLOS on beams 4 and 5 at each observation time during the event. "Singular" values that are more than 2.5 times higher than values from the neighboring range cells or optical bins are discarded. The maximum values of the emission intensity and VLOS should correspond to observable features of the auroral intensification and the flow enhancement respectively. The results are shown in Figure 3.26. The maximum intensity of the 630.0 nm and 557.7 nm emissions are plotted. During the time interval of the study, the red-line and green-line emissions show fairly good correlation (0.72). The cross-correlation analysis between the red-line emission (1-minute resolution) and the VLOS (2-minute resolution) gives a correlation coefficient of 0.77, with the flow enhancement lagging the auroral intensification by 0-2 minutes.

3.4 Discussion

We have studied three NRFE events and analyzed the different properties of flow enhancements on open and closed field lines. In the following we discuss both the magnetospheric mechanisms which lead to NRFEs on open and closed field lines, and also the spatial and temporal relationships between the NRFEs and the auroral intensifications.

3.4.1 Solar wind activation and magnetospheric dynamics associated with NRFE.

A nightside flow enhancement is usually related to upstream solar wind activation. Some previous studies [*Lewis et al*., 1992; *Blanchard et al*; 1996; *Watanabe et al*., 1998] have shown that the time lags between the solar wind activation at the dayside magnetopause and the nightside flow enhancement were roughly 1 hour. After dayside magnetopause reconnection commences, solar wind plasma enters the magnetosphere and fills the tail lobes. Increased plasma fluxes are carried by the newly opened Earth's magnetic field lines which drape over the polar caps; these plasma flows convect tailward and, at the same time, inward toward the neutral sheet. When mapped to the ionosphere, they are seen as enhanced equatorward flow structures on open field lines. In the case of strong IMF By conditions, the convection of lobe field lines may also have a marked westward component (for positive By) or eastward component (for negative By) [*Nishida et al*., 1998]. Nightside reconnection may occur either at the DTNL between oppositely-directed lobe field lines from the two hemispheres, or at a near-Earth neutral line (NENL), on highly stretched OPS field lines. Both reconnection processes can lead to flow enhancements on closed field lines.

The ionospheric convection change in response to the solar wind activation usually starts near the ionospheric projection of the cusp region and expands towards both the dawn and dusk sectors. The expansion indicates some propagation effects both in magnetosphere and ionosphere [*Saunders et al*., 1992]. However, significantly different timescales of the global ionospheric convection response to IMF variations have been found, which has led to intense debate about their causes (see a debate sequence which begins with *Ridley et al*. [1998], then is followed by a criticism of *Lockwood and Cowley* [1999], and terminates with the reply to that criticism by *Ridley et al*. [1999]).

Those timescales can be distinguished roughly into the "fast" (nearly simultaneously or within a couple of minutes) [*Kikuchi et al*. 1996; *Ruohoniemi and Greenwald*, 1998; *Watanabe et al*., 2000; *Murr and Hughes*, 2001], and the "slow" (a few tens of minutes) [*Cowley and Lockwood*, 1992; *Khan and Cowley*, 1999]. It was found that the entire polar cap ionospheric convection can show a near-simultaneous response to the solar wind activation, but at the onset of the response, the change of nightside flow velocity usually has only a rather small magnitude [*M. Watanabe*, private communication]. According to the above analysis of the magnetospheric dynamics of NRFEs, the time delay between the NRFE and the upstream solar wind activation should belong to the "slow" timescale. The delay required in the slow timescale scenario is roughly the time required for the ionospheric plasma to convect from the dayside to the nightside across the polar cap. If we assume a ~1 km/s antisunward convection velocity, the time delay for the ionospheric plasma to convect from 80^0 MLAT at noon to 75^0 MLAT at midnight is ~46 minutes. From our investigation of the NRFE events, we have found that the NRFEs usually lag the solar wind activations at the subsolar magnetopause by 30-60 minutes. The time delay is usually higher for NRFEs on closed field lines than those on open field lines. One important factor controlling the time delay is found to be the solar wind speed. For example, in the March 21, 1999 event, the first NRFE at 0630-0710 UT on closed field lines was found to lag the IMF Bz negative bay at 0515-0555 UT observed on IMP8 satellite by ~75 minutes. For the third event, the second flow NRFE (0426-0500 UT) lagged the second solar wind electric field enhancement (0340-0415 UT) observed at the WIND satellite by ~46 minutes. After subtracting the respective solar wind propagation delay from each satellite to the subsolar magnetopause, the remaining time delays are about 60 and 40 minutes, respectively. The solar wind speed in these two events was 300 and 480 km/s, respectively. *Watanabe et al*. [1998], on the basis of the assumption that the dayside eroded magnetic flux was conveyed from the dayside magnetopause to the distant tail at half the solar wind speed, were able to estimate the location of the DTNL, which was assumed to be the origin the nightside flow enhancement in their events. Despite its simplicity, the model is instructive in that the time lag between the nightside reconnection and dayside

reconnection was likely dependent on the upstream solar wind speed; higher solar wind speed corresponds to smaller time lag.

We propose that at the onset of the March 29, 1999 event, the first NRFE on open field lines, which is characterized by strong southwestward flows (see Figure 3.5a), was the response to the strong IMF By enhancement observed by GEOTAIL from 0355 to 0455 UT. During the same time interval the IMF Bz component decreased to about 0. It was reported by *Nishida et al.* [1998] that, in the case of strong IMF By conditions (|By| >> |Bz|), the convection of lobe field lines may have a considerable dawn-dusk component, westward under +By and eastward under –By, which is consistent with our radar observations. We also propose that the second flow enhancement was caused by the abrupt IMF southward excursion from 0417 to 0423 UT. The IMF Bz value dropped to -5 nT, while the IMF By became small and negative. The NRFE pattern was then dominantly equatorward (see Figure 3.5b). There was a strong southward IMF interval (Bz ~ -5 nT) at 0430-0500 UT, which might have caused the third equatorward flow structure both on open and closed field lines with the former occurring several minutes earlier than the latter.

In the March 21, 1999 event, the first NRFE (Figure 3.13a,b) is considered to be related to the negative IMF Bz bay at 0515-0555 UT observed by IMP8 satellite. We propose that the second NRFE (Figure 3.13c,d) is related to the IMF conditions during the period 0622-0704 UT, when there were two abrupt IMF southward excursions with an ~11 minute northward IMF period, and when the IMF By component was much stronger than Bz. Thus south-westward flows again dominated for latitude $>72^0$ MLAT in accordance with the model of *Nishida et al*. [1998]. The magnetometer observations, in particular at Gillam, showed that magnetic negative deviations during the second NRFE interval developed in two stages separated by a ~10 minute "recovery" interval, which is very likely to be the consequence of the southward turning- northward turning-southward turning sequence of IMF variations. However, such a feature was not clearly shown in the convection observations. That is probably because the northward IMF turning was very abrupt and the interval was shorter than the inertial response time of ionospheric plasma convection from a "disturbed" state. *Hairston and Heelis* [1995] have found that the ionospheric convection response to an IMF southward-to-northward

turning took much longer time than the response to an IMF northward-to-southward turning of IMF. We could not relate the third flow enhancement (Figure 3.13e,f) to any variations of the IMF. Apparently, that last NRFE was caused by some other mechanism, such as quasi-viscous interaction between the solar wind and the magnetosphere or some internal magnetospheric process.

In the December 26, 1998 event, we have used the GEOTAIL observations near the midnight tail to show that the ~0426 UT NRFE on the closed field lines was most likely to have been associated with the second enhanced solar wind electric field event (SWE2) seen at the WIND satellite. The poleward border of that flow enhancement structure was almost immediately equatorward of the OCFLB from 0426 to 0440 UT; this appears to favor a DTNL origin. After 0440 UT, the NRFE structure gradually departed from the OCFLB and moved equatorward down to 68.1^0 MLAT. The rate of this equatorward progression was ~0.15^0 /min, which is less than half of the flow velocity, so that such a progression cannot simply be due to the earthward migration of enhanced flows generated by the previous DTNL activity. One possible scenario is that, during the persistent solar wind enhancement (SWE2), the initial nightside reconnection occurred at a DTNL. As the outer/distant plasma sheet field lines became increasingly stretched, additional reconnection events might have occurred between those closed field lines. Each new activation would have been located closer to the Earth than the previous existing one, as described by the "ne arer-Earth neutral line" scenario [*Kennel*, 1995]. In this scenario, the OCFLB location would have remained nearly steady but the flow enhancement structure would have gradually moved equatorward.

In conclusion, we have found from case studies that many NRFEs can be attributed to specific upstream solar wind variations, with some degree of confidence. However, due to the large uncertainties in the time lag between the upstream solar wind variations and the NRFEs, and also the uncertainties in the solar wind propagation time from the satellite where the solar wind was measured to the magnetopause (see Appendix C.1), all of the ambiguity in the determination of the cause of the NRFEs cannot be resolved, especially during rapidly changing IMF conditions. We could not provide strong and convincing correlations between the NRFE events and the solar wind variations in every case. Also, within the scope of our observations, we could not predict under what

circumstances a solar wind variation (e.g., a southward IMF turning) would or would not cause an NRFE event.

3.4.2 The spatial separation between NRFEs and auroral intensifications

Flow enhancements on open field lines are not found to have a significant relationship with auroral intensifications and magnetic disturbances. This should not be surprising, because the auroral particle precipitation and its associated current systems, FACs, Pedersen closure currents and auroral electrojets, are all believed to occur on closed field lines. The NRFEs on open field lines undoubtedly reflect some solar wind-magnetosphere interaction processes and thus may play a role in the coupling of energy between the solar wind and the closed magnetosphere, but they appear not to play any direct role in the inner magnetospheric dynamics which control the auroral activity.

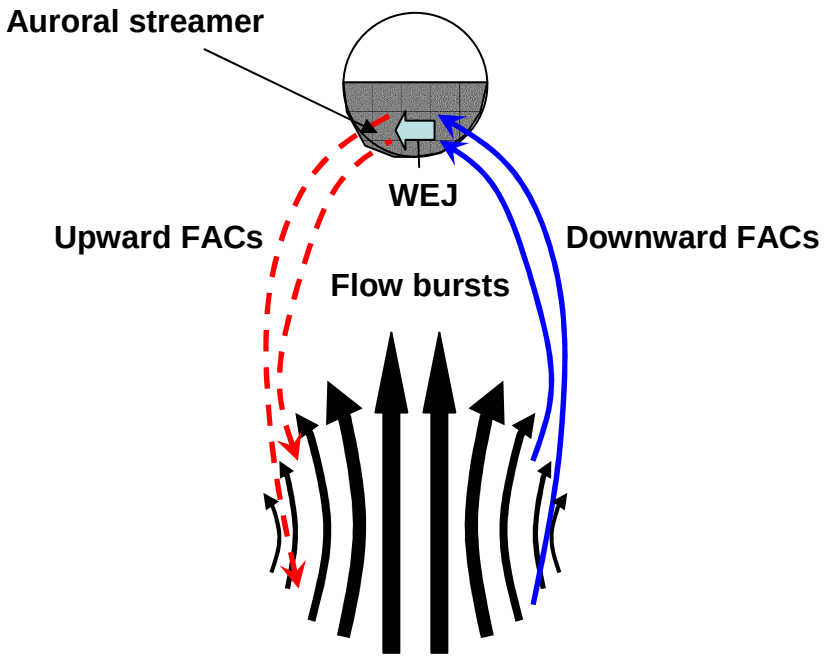

Figure 3.27 A diagram showing the geometric association between the auroral streamers and the high-speed flow bursts. See the text for explanations.

The physics is more complicated for the NRFEs on closed field lines. We have seen two different types of auroral activations accompanying the flow enhancements. In the

March 21, 1999 event, we found that the first and second NRFEs may be associated with the sporadic high-latitude auroral structures observed by the Fort Smith MSP, but those intensifications were located west of the flow enhancement region. Also there were negative magnetic bays corresponding to the occurrence of those two NRFEs. The above-mentioned auroral and magnetic signatures are definitely not substorm-like phenomena because no auroral breakup at NGOPS latitude was observed. A possible explanation for the relationship between the flow enhancement, auroral streamers, and magnetic disturbances is given below, according to *Nakamura et al*. [2001b].

A shown in Figure 3.27, high-speed earthward flow bursts are usually associated with magnetic reconnection somewhere in the tail, either at a DTNL or a NENL. The reconnection process is generally spatially localized, so the resulting fast flow regions are azimuthally confined. On the west side of the fast flow region, a flow shear with positive curl (along the direction of magnetic field) is produced, while on the east side of the fast flow region, a shear with negative curl (opposite to the direction of magnetic field) is produced. These flow shears generate FACs flowing into the ionosphere on the east side of the fast flow region and flowing out from the ionosphere on the west side of the fast flow region [*Sofko et al*., 1995]. A wedge-like current system, which has a geometry similar to that of the SCW, is established. Unfortunately there are no radars in the vicinity of and east of Fort Smith. Therefore we cannot derive the FAC density on the basis of the convection vorticity. The upward FACs on the west side of the flow enhancement region are associated with intensified electron precipitation and optical auroral activities. Since the flow shear and the FACs are tied to the fast flow bursts lying well antisunward of the IPS, the resulting auroral structures are also located at higher latitudes than NGOPS, and presumably are more or less aligned with the fast flow direction. This geometry puts some restriction on our ability to associate our results with the high-latitude auroral structure observed by the meridian-scanning photometer. In the March, 21, 1999 event, for the flow enhancement from 0630 to 0700 UT (Figure 3.13a,b), the convective flows are dominantly equatorward and thus are approximately parallel to the meridian scan line of the Fort Smith photometer, on which the N-S aligned auroral streamers are clearly observed. During the second flow enhancement period 0725-0800 UT (Figure 3.13c,d), however, the fast flows had a

considerable westward component, and presumably so did the resulting auroral streamers. This would explain why auroral streamer structure during this interval is less well observed by the Fort Smith MSP than during the first flow enhancement period.

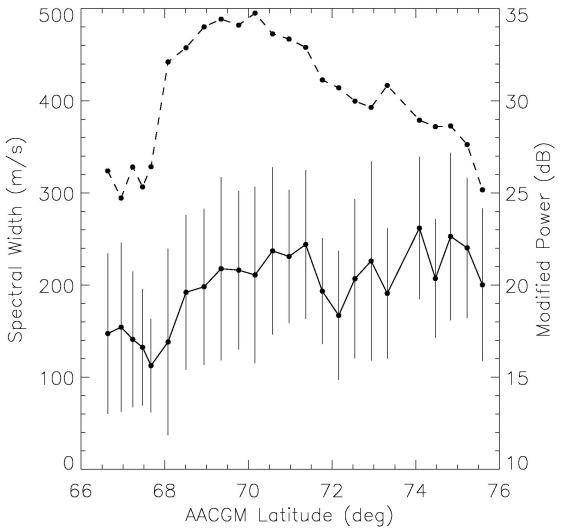

Figure 3.28 The variation of spectral width with latitude. The dots jointed by a solid line denote the average values during the event interval (0426-0500 UT), and the vertical lines indicate the standard deviation. The modified backscattered power (defined by equation 3.3) averaged over the event time is also plotted by the dots joined by a dashed line.

The third event is associated with a totally different set of auroral activity, namely activity that pertains to a pseudosubstorm. We have shown that, in this event, the NRFE and auroral intensification concurred during the interval 0426-0500 UT, but they were clearly latitudinally separated. An understanding of the equatorward cut-off of the NRFE structure can be inferred from the variation of Saskatoon radar Doppler spectral width versus latitude, as shown in Figure 3.28. The observed spectral widths are averaged over those radar range gates which remained at the same latitude during the event interval. The modified backscattered power, which is related to the observed power P_{obs} by (R is the range in km),

$$P_{\text{mod}} = P_{obs} + 30\log_{10}(R/1000) \quad , \tag{3.3}$$

is also averaged over the event interval and plotted. Equation (3.3) accounts for the usual cubic range dependence of the backscattered power (the antenna beam is assumed to be filled with scatterers in the azimuthal direction, but not in the vertical direction).

It is clear from Figure 3.28 that the spectral width increases considerably at 68.1^0 MLAT, and reaches 200 m/s at about 68.9^0. The Doppler spectral width observed by coherent radar is a measure of ionospheric plasma turbulence caused by the spatially structured energetic precipitation or by electric field variations within the radar range-beam cells during the integration period [*Andre et al*., 2000]. The radar spectral width has long been used to identify the dayside cusp region [*Baker et al*., 1995; *Milan and Lester*, 2001]. On the nightside, a sharp gradient between the low (<200 m/s) and high (>200m/s) spectral widths is also frequently observed but has been given different interpretations. It was thought to be the BPS/CPS boundary by *Lewis et al*. [1997] and *Dudeney et al*., [1998], while it was attributed to the OCFLB by *Lester et al*. [2001]. The latter was criticized by *Woodfield et al*. [2002], who found that the regions of high spectral width are observed both on closed and open field lines. *Newell et al*. [1996] have shown that a major difference between the BPS and CPS is that the former is characterized by more structured electron precipitation. *Andre et al*. [2002] made statistical studies of winter HF radar spectra characteristics and found that the broad spectra can be associated with regions of intense and structured low energy electron precipitation in the night sector, which would imply a BPS source. This is in support of the view of *Lewis et al*. [1997] and *Dudeney et al*., [1998].

We suggest that the sharp increase of spectral width occurring at 68.5 ± 0.4^0 MLAT, as shown in Figure 3.28, indicates a CPS to BPS transition. Together with the steep rise of spectral width, there is also a considerable increase of power. The backscattered power is much stronger in the BPS than in the CPS region, a result that is similar to the observation that signals with high spectral width in the dayside cusp also have relatively high backscattered power [*Milan and Lester*, 2001]. It is likely that, when there is structured electron precipitation in the ionosphere, conditions are more favorable for the generation of ionospheric irregularities in the *F* region [*Kelly et al*., 1982], with the result that there is stronger backscattered HF radar power.

We now use the observations to argue that the equatorward border (68.1-68.9^0) of the NRFE structure shown in Figure 3.25 appears to mark an important transition region, namely that between the BPS and CPS. The ionospheric CPS maps to the inner plasma sheet (IPS) (typically <12 R_E in a substorm growth phase), while the BPS maps to the OPS and the PSBL. Although high-speed earthward flows are common in the mid-tail, they are much less frequently observed in the near-earth tail inside 10 R_E [*Nagai et al*., 1998]. On the other hand, ionospheric convection studies show that, when the equatorward flows approach the CPS, they tend to be diverted to eastward by the intensified auroral structures there [*Yeoman et al*., 2000a]. Such an equatorward-to-eastward turning is seen clearly in Figure 3.24 at ~68.5^0 MLAT, so it can be argued that the observed equatorward border of the flow enhancements is roughly consistent with the BPS/CPS boundary. The NRFE structure was located in the BPS, while the auroral intensification was inside the CPS. The observations show that, between those two regions, there is a transition region in which the fast equatorward flows were diverted to eastward in conjunction with the enhanced conductivity in this region of brightened auroras. The flows reversed to westward at ~66^0 MLAT forming a zonal flow shear region which is the characteristic of the HD. The auroral intensification structure is just slightly south of the HD, as inferred from Figure 3.25.

The above analysis also explains the longitudinal difference between the NRFE and the auroral intensifications. Although the azimuthal distribution of the auroral intensifications was not known, the strongest magnetic disturbances were not found at Rabbit Lake, which is closest in longitude to the observed NRFE (see Figure 3.1), but nearer to Gillam, some 10^0-15^0 to the east. Based upon the convection geometry as in Figure 3.24, the HD is expected to form east of the equatorward flows from higher latitudes. Therefore, the most intense upward FACs and auroral intensifications are also likely to be located east of the NRFE structure, in agreement with the observations.

3.4.3 Temporal relationship between NRFEs and auroral intensifications

The statistics of the time differences between NRFEs and the accompanying auroral activations in Figure 3.4 show many events for which the NRFEs slightly lag the accompanying auroral intensifications. In particular, in the third event a temporal

correlation study revealed that the auroral intensification slightly preceded the flow enhancements by 0-2 minutes. However, as we already noted in the discussion of Figure 3.3, for the NRFEs on closed field lines, there is only a slight dominance of those accompanied by auroral activations over those without auroral activation. Thus the actual relation between the flow enhancements and the auroral intensifications is far from a definite one-to-one correspondence. *Watanabe et al*. [1998] suggested that the enhancement of the distant tail reconnection is indirectly coupled with the substorm onset by the rapid nonlinear stretching of the magnetic field; in this scenario, there would be only a weak link between the tail reconnection and the auroral substorm process. However, the fairly good temporal correlation between the NRFE and the auroral intensification as shown in Figure 3.26 still leads us to postulate that there is a more direct physical relationship between them. As shown in Figure 3.4, there is a fairly large spread in the time differences between the NRFEs and the associated auroral intensifications. Therefore the underlying physical mechanisms relating the NRFEs and the auroral activations must be flexible enough to allow for the NRFEs to either precede or follow the auroral activations.

There are two principal candidate models associating tail reconnection, and thus fast flows in the mid-tail, with the near-geosynchonous onset of substorms [*Ohtani et al*., 2002]. Below we give a brief introduction to these two models and comment upon their applicability to our events.

1. In the first model, the substorm occurs first at NGOPS as the result of the onset of a nearby instability and the disruption of cross-tail current. The initial current disruption would produce a tailward-propagating rarefaction wave which may set up favorable conditions for an X-line to form further tailward, leading to the reconnection activation which then generates the high-speed earthward flows [*Lui*, 1996; *Erickson et al*., 2000]. This mechanism was used to explain the observation that there is often a Stage-2 expansion of a substorm [*Erickson et al*., 2000]. Whether the tailward-propagating rarefaction wave is fast mode or slow mode has been a controversial issue [*Ohtani*, 1993c]. We will assume it to be a fast mode because a slow mode would severely increase the time delay between the pseudosubstorm onset and the reconnection. For a fast mode rarefaction wave such a delay depends on the

downstream distance where the reconnection is triggered, but may on average take a few minutes [*Liou et al*., 2002]. In our observations, it should be noted that the electric field enhancement associated with the flow bursts in the tail maps down to the ionosphere to drive the radar-observed NRFE with a delay corresponding to the Alfven wave propagation time along the geomagnetic field lines. The Alfven travel time from the equatorial mid-tail to the ionosphere is typically ranges between 3-8 minutes, depending upon the field line topology and the Alfven velocity. The total time delay is the sum of the required time for the tailward-propagating rarefaction wave to induce a reconnection and the Alfvenic travel time for the enhanced magnetospheric electric field to be conveyed to the ionosphere. Therefore, for this model the auroral intensification should significantly precede the flow enhancement, contrary to many of our observations.

2. When the fast earthward flows generated by tail reconnection reach the IPS, they are decelerated (which is referred to as "flow braking"). Flow braking can induce an eastward inertia current [*Shiokawa et al*., 1997; 1998] or change the pressure distribution and magnetic configuration [*Birn et al*., 1999] in the near-Earth region, subsequently leading to cross-tail current disruption and SCW formation. However, this mechanism does not seem to be plausible in our case. The earthward flow is slowed down mainly between 10 and 18 R_E [*Birn et al*., 1999]. Let us assume the flow velocity is 500 km/s at X = -18 R_E and is uniformly decelerated to 0 at X = -10 R_E. The required time for this flow braking would be 3.4 minutes. *Birn et al*. [1999] numerically simulated the process and found that the maximum effect of cross-tail current reduction occurs about 4 minutes after the rapid increase in flow speed induced by a NENL reconnection at X = -23 R_E. However, in the third event the observation indicates that the initiation of the fast flows might be at a much greater distance down the tail. During the first 14 minutes of the NRFE interval they were likely to originate at a DTNL. If the fast flows started at X = -60 R_E and then traveled at an average speed of 600 km/s, they would require 7.4 minutes to reach X = -18 R_E, so the total time delay to X = -10 R_E would be ~11 minutes. Some additional time (1-2 minutes) is required for the "flow braking" to induce the current disruption, SCW formation, and finally lead to the auroral activation in the ionosphere. Even when we subtract the Alfven travel time

delay required for the flow enhancement to reach the ionosphere, the flow enhancements should still significantly precede the auroral intensifications. This is also in conflict with our observations.

Since both of these existing models lead to significant timing problems with respect to our observations, we suggest a new mechanism. When magnetotail reconnection occurs, it is expected that there will be subsequent earthward flow. That flow would be seen as the ionospheric NRFE after a relatively long Alfven travel time delay because of the substantial length of the OPS field lines. On the other hand, the particle outflow from the X-line compresses the plasma on its earthward side and launches a fast mode wave which subsequently propagates sunward into the IPS [*Yumoto et al*., 1989; *Kepko and Kivelson*, 1999; *Kepko et al*., 2001]. This fast mode wave in the IPS can then assist in the activation of substorm-related processes. For example, *Kepko et al*. [2001] suggested that when the fast compressional wave penetrates to the IPS, it perturbs the field lines and produces Pi2 bursts on the ground. *Sergeev et al*. [1998a] proposed that fast wave modes in the IPS could lead to dawn-dusk electric field (E_y) pulses and correlated impulsive particle injections deep inside the inner magnetosphere. Those E_y pulses drive inward convection within the IPS which can significantly increase the growth rate of NGOPS instabilities such as the DAB mode [*Pu et al*., 1999]. As simulated by *Pu et al*. [1999], the growth time for the DAB instability can be as small as ~10 seconds when there is a convection velocity of ~80 km/s inside the IPS. The NGOPS instabilities in turn can cause cross-tail current disruption and lead to SCW formation, finally resulting in the auroral breakup in the ionosphere. The fast mode wave propagation time from the reconnection site into the IPS, plus the time required for the fast wave to induce NGOPS instabilities and lead to auroral activations, is roughly comparable to the Alfven travel time delay between the distant tail reconnection and the resulting observations of NRFEs in the ionosphere. Consider the rough numerical estimate that follows. The Alfven velocity in the distant plasma sheet and PSBL is much larger than that in the near-Earth region due to the combination of highly stretched magnetic field lines and low densities. Let us assume that the average Alfven velocity is 1400 km/s for the OPS/PSBL, and that the magnetic field line is inclined at an elevation angle of 15^0 above the magnetic equatorial plane beyond 10 R_E.

On this basis we can calculate that the Alfven travel time is ~3.8 minutes from X = -60 R_E to X = -10 R_E. Within 10 R_E the field line is quasi-dipolar so that the Alfven travel time is roughly the same magnitude as the time delay (~1 min) between the ground-observed optical auroral intensification and the NGOPS instabilities. We further assume that fast magnetosonic waves also are generated at the same origin (X = -60 R_E) and travel earthward in the equatorial plane, perpendicular to the magnetic field. Their velocity V_F is given by

$$V_F^2 = V_A^2 + V_S^2 \quad , \tag{3.4}$$

where V_A and V_S denote the Alfven speed and the sound speed, respectively. The adiabatic sound speed in the plasma is related to Alfven speed by

$$V_S^2 = \frac{\gamma\beta}{2} V_A^2 \quad , \tag{3.5}$$

where γ is the adiabaticity index and β is the plasma β value. We use an average β value of 0.5 for the OPS/PSBL, and take $\gamma = 5/3$. The travel time for the fast mode wave to reach the IPS at X= -10 R_E would then be 3 minutes, approximately 0.8 minutes shorter than the Alfven travel time along the stretched magnetic field lines. It should be noted that, in this scenario, the time delay does not depend significantly on the actual site of the tail reconnection. For example, if we consider a NENL at X= -25 R_E, V_A and V_F would be somewhat smaller, but the time delay is still estimated to be ~0.5 minutes, with the fast mode waves reaching the IPS first.

In our model, the flow bursts in the tail would occur first but would take a longer time to impact upon the ionospheric convection and be revealed as NRFEs; the NGOPS instabilities would occur later but then a much shorter time delay would occur for the resulting Alfven waves to induce the optical auroral intensification. As a result, these two time delay routes would lead to the nearly simultaneous occurrence, or even a slight precedence, of the auroral intensifications with respect to the flow enhancements, as seen in Figure 3.26. We have indicated in Figure 3.4 that a majority of the NRFE

events occurred within +2 to -4 minutes of the accompanying auroral activations. Our new model accommodates this range of time delays/advances. On the other hand, those events for which the NRFE significantly lags or significantly precedes the auroral activity, as shown in Figure 3.4, could be explained on the basis of the above-mentioned model 1 and model 2 scenarios, respectively.

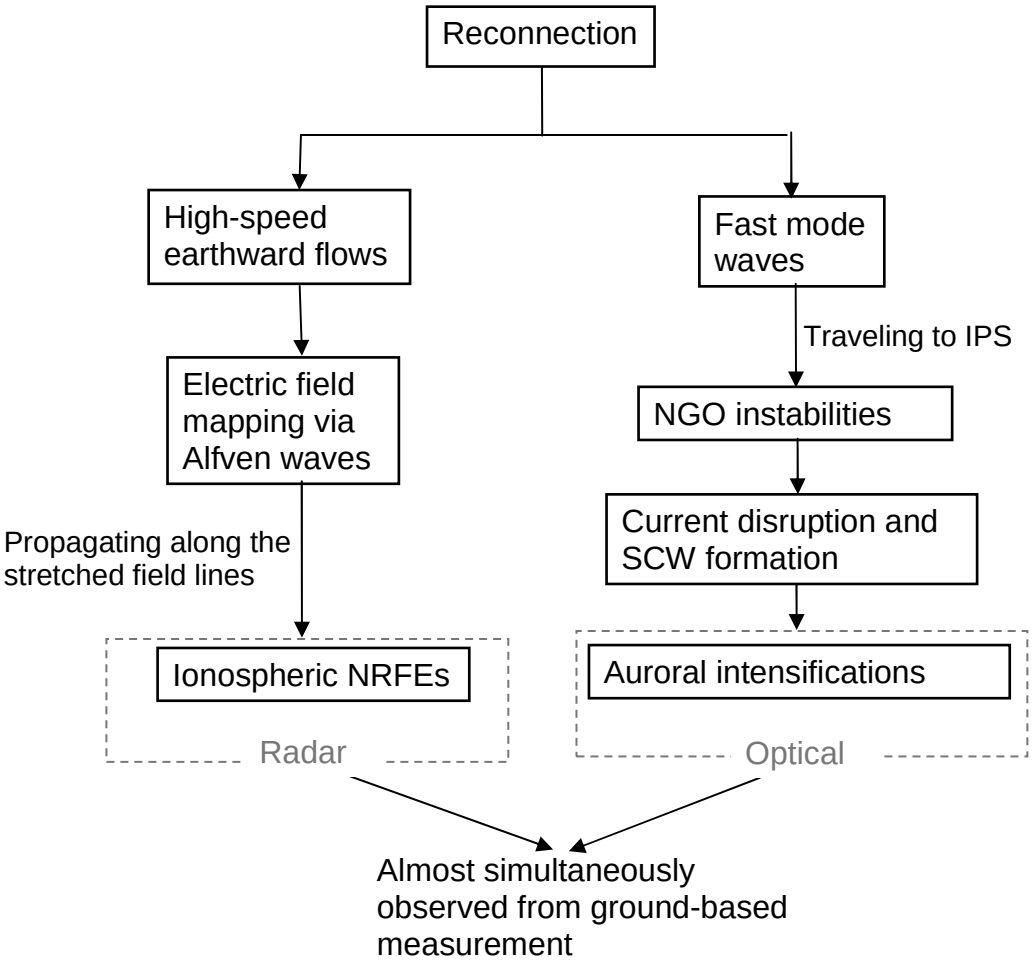

Figure 3.29 Schematic diagram of the new model explaining the almost simultaneous observation of ionospheric flow enhancements and auroral intensifications.

The schematic diagram illustrating our model is given in Figure 3.29. The model can also be used to interpret the observation of *Nakamura et al*. [2001a] that auroral activations related to small poleward expansions/pseudobreakups usually slightly precede the flow bursts seen by GEOTAIL in the tail. Our model shows that this is

expected, because for those events, the assumed reconnection site was located a long distance antisunward of GEOTAIL. Since the fast mode wave travels much faster than the flow itself, our model shows that it is quite possible that the onset of the near-geosynchronous instability and thus of the auroral intensification can occur a few minutes before the fast flows reach the location of GEOTAIL.

As a final remark, we should point out that the two existing models and our new model may all be viable mechanisms relating the reconnection and fast flows in the mid-tail with substorms/pesudosubstorms. Model 1 belongs to a NEI substorm scenario, while Model 2 belongs to a MTI scenario (see Chapter 1.4). Our model is actually a synthesis of the NEI and MTI scenarios. Any one of the three models may be the dominant scenario for an individual substorm development, but none of the models will guarantee a one-to-one correspondence between the flow enhancement and the auroral intensification. For example, both the "flow braking" model (referred above as model 2) and our new model embody earthward energy transport from the mid- or distant-tail into the inner magnetosphere, either carried by fast flows or fast mode waves. However, the amount of energy transported may be not sufficient to induce an auroral activation in the ionosphere or the substorm-associated processes at NGOPS such as DAB instabilities, the cross-tail current disruption, and the SCW formation. Such processes may be prevented because of the status of the inner magnetosphere and/or the magnetosphere-ionosphere coupling system. Therefore, we strongly agree with the view suggested by *Ohtani et al*. [2002] that, because the substorm-associated process at NGOPS and the fast flows at mid-tail occur at quite different radial distance ranges, it is reasonable to regard them as two distinct processes. Our new model shows that they can appear to be physically related because the energy from the tail reconnection site leads subsequently to, on the one hand, earthward flows and their signature as NRFEs and, on the other hand, fast waves to the NGOPS, current disruption, SCW formation and auroral activations. These two quite separate scenarios take about the same time, leading to the near-simultaneous onset of the NRFE and auroral intensification observed in the ionosphere. However, the latter scenario – the NGOPS current disruption and subsequent auroral activation – may not occur at all, in which case there would be an NRFE with no auroral activation. Clearly, the state of the magnetosphere must be such

that the latter can occur in response to the fast waves if auroral activity is to result. The three models above allow for the broad range of possibilities that are observed, and in that sense, our new model fills a gap that the other two models did not explain, namely the near-simultaneous occurrence of the NRFEs and the auroral activations.

3.5 Conclusion

The main purpose of this study is to elucidate the relationship between NRFEs and auroral activations. The NRFEs are classified in two categories, namely those on open field lines and those on closed field lines. The NRFEs on open field lines usually are associated with very little accompanying auroral and magnetic activity. The NRFEs on closed field lines tend to appear during moderate geomagnetic disturbance level and may be associated with two types of auroral activations. The first is high-latitude auroras, such as auroral streamers, located or initiated near the poleward boundary of the auroral oval. In the study of the March 21, 1999, event, we found that the auroral intensifications were located on the west side of the NRFE region, but no auroral activation was found on the east side of the NRFE region or at the NGOPS latitudes. The other is the auroral intensification inside the main auroral oval, which is generally associated with the substorm/pseudosubstorm process. We have concentrated on a December 26, 1998 event in which the growth phase culminated in a pseudosubstorm. An NRFE structure was observed by HF radar from just equatorward of the OCFLB determined from the poleward edge of 630 nm emissions down to 68.5 ± 0.4^0 magnetic latitude, which is roughly estimated to be the BPS/CPS boundary (based upon the Doppler spectral width transition observed by the radar during the event time). The ionospheric optical auroral intensifications were located at $64.5\text{-}66.5^0$ MLAT, inside the CPS. Both the radar beam 15 observations and the fitted convection pattern show that the equatorward flows were diverted eastward and, at lower latitudes, reversed their direction to westward. The result was a zonally sheared flow region characteristic of the Harang discontinuity, and the shear flow region was closely associated with FACs and auroral intensifications. A detailed temporal correlation study between the NRFEs and the auroral intensifications showed that they were well correlated and that the flow enhancements were nearly simultaneous with, or slightly lagged, the auroral

intensifications. Such a temporal relationship could not easily be explained by the existing models that associated the tail reconnection process and the near-geosynchronous onset of substorms. A new model was proposed as follows. A fast mode wave is generated at the tail reconnection site and propagates earthward. When the wave penetrates into the IPS, it assists in the activation of NGOPS instabilities and the onset of the pseudosubstorm. On the other hand, the electric fields associated with the reconnection first lead to earthward flows, and the signature of these is conveyed from the equatorial tail to the ionosphere with a time delay equal to the Alfvenic travel time along the rather long OPS field lines. The result is the NRFE signature in the ionosphere. Although there are two distinct sets of processes that lead to the auroral activation and the NRFE, the time delays between the reconnection and the appearance of the auroral intensifications and NRFEs is about the same, so they would appear in the ionosphere almost simultaneously. Though the applicability of our model to the case of major substorms requires further investigation, the model does provide new insight into the links between reconnection, high-speed flows in the mid-tail, and the near-geosynchronous onset of substorms and pseudosubstorms.

Chapter 4

Convection and auroral dynamics of a small substorm during dominantly IMF B_y+ B_z+ conditions

In this study we present multi-instrument measurements of a small substorm event on October 9, 2000. The substorm was small in magnitude and fairly localized in the postmidnight sector, but showed very well-defined optical auroral, magnetic and radar signatures as observed by the CANOPUS magnetometer array, the MSP at Gillam and Fort Smith, the NASI at Rankin Inlet, and the SuperDARN radar network, respectively. There were initially two weak auroral and magnetic activations starting at 0732 UT and 0743 UT which were pseudobreakups, while the EP onset occurred at 0752 UT. The optical, magnetic and HF radar signatures of the event are interpreted as three successive DAB instabilities. Starting at 0802 UT there was a second auroral brightening with the expected characteristics of a "Stage-2 expansion" [*Erickson et al.*, 2000]. In examining the solar wind parameters observed by the GEOTAIL, the polar cap magnetic activity index, and the global ionospheric convection measurements from eight SuperDARN radars in the northern hemisphere, we find that the first two pseudobreakups, the EP onset and the Stage-2 expansion are related to loading-unloading, directly driven, and internal magnetotail processes, respectively.

4.1 Review of some previous studies

The energies of substorms usually originate from the solar wind. The physical processes involved in dissipating the energy have been divided into "loading-unloading" and "directly driven" [*Baker et al.*, 1997]. The "loading-unloading" process

is widely accepted to be the classical scenario of a substorm, in which the growth phase is a prolonged period (> 30 minutes) of energy storage in the magnetotail, and the EP marks the abrupt release of that stored energy into the nightside auroral ionosphere. The "directly driven" process is manifested by cross-correlation studies that the auroral electrojet indices AE/AL correlate well with the solar wind energy input, with the strongest correlation after a short time lag of ~20 minutes [*Bargatze et al*., 1985]. Sometimes a substorm EP onset [*Liang et al*., 2004b] or pseudobreakup [*Koskinen et al*., 1993] was found to respond to the solar wind energy input after a time lag ≤20 minutes and thus in a "directly driven" fashion. The "loading-unloading" and "directly driven" processes have different time scales, but both may play important roles in substorm dynamics. Their relative importance may vary in different substorm phases and also differ from case to case [*Rostoker*, 1987].

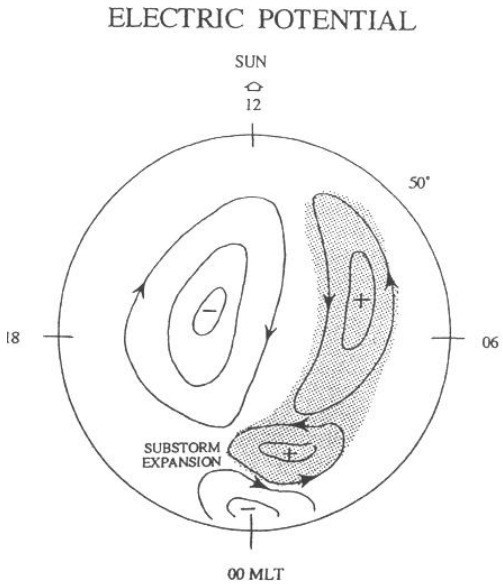

Figure 4.1 Schematic diagram showing two pairs of electric potential cells, representing the effects of enhanced plasma convection and of the substorm EP. The '+' and '-' symbols denote positive and negative potentials, for which the FACs are downward and upward, respectively. The large convection cells centered on the dawn and dusk flank sides are the usual solar wind-driven cells. The small near-midnight convection cell is related to the "unloading" process during the substorm EP (from *Kamide et al*., 1994).

The substorm current patterns at high-latitudes also contain two components, the first related to the 2-cell global convection pattern which is usually directly driven by the solar wind, and the second related to the WEJ, which is associated with the release of previously stored energy in the tail [*Kamide and Kokubun*, 1996]. The latter is usually accompanied by the emergence and enhancement of a small near-midnight counterclockwise convection vortex in addition to the pre-existing 2-cell pattern during the substorm EP [*Kamide et al.*, 1994]. A schematic diagram of their model is shown in Figure 4.1. The current pattern associated with the new pair of convection cells is thus more of a meridional current system (MCS) than the azimuthally-aligned system usually associated with SCW geometry. The existence of the MCS signature during substorms was experimentally observed by *Lopez et al*. [1990] and *Nagai* [1987]. *Kamide* [1996] first suggested that the east-west ionospheric closure of the substorm current was overemphasized by most substorm researchers. *Lui* and *Kamide* [2003] provide further evidence for the dominance of a MCS in substorms. *Akasofu* [2003] re-examined three well-established substorm onset phenomena, namely, the sudden brightening of an auroral arc, the sudden growth of the WEJ, and dipolarization. He concluded that the actual substorm current system is predominantly of MCS form.

One other very important work closely related to the study in this chapter is *Erickson et al*. [2000], who provide clear evidence associating the substorm EP onset with DAB instabilities at the NGOPS, based upon CRRES satellite observations. *Erickson et al*. [2000] also noted that the substorm expansion often occurs in two stages, and that the second stage of expansion (called “Stage-2” EP) occurs ~10 minutes after the initial EP onset. They proposed that this Stage-2 EP is likely to result from the earthward flow enhancements that are expected from the mid-tail reconnection activated by a tailward-moving rarefaction wave generated in the Stage-1 EP.

4.2 Multi-instrument observations

Figure 4.2 shows the location of the magnetometer and riometer sites (black dots), the circular FoV of the Rankin Inlet NASI for the 630 nm oxygen red line (assuming a 215 km emission height), the thick lines along the meridian scan lines of the MSPs at Gillam, Rankin Inlet, and Fort Smith, and the centerlines of the 16 SuperDARN beams

of the Saskatoon and Kapuskasing radars. The magnetic latitudes defined by AACGM coordinates [*Baker and Wing*, 1989] are shown on the background geographic map.

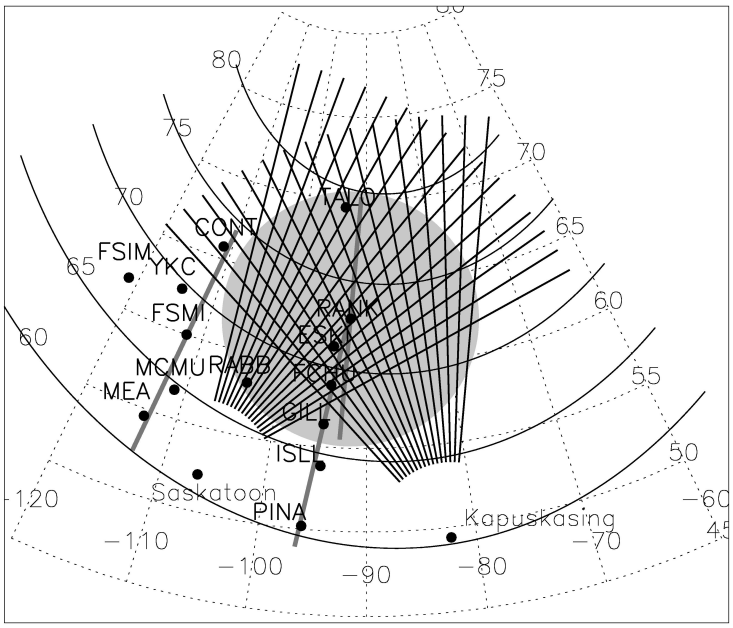

Figure 4.2 Map of the FoVs of the SuperDARN radars at Saskatoon and Kapuskasing, and of the NORSTAR imager at Rankin Inlet (for red-line emission at 215 km height and 80º nadir). CANOPUS magnetometers are shown in black dots. The scan lines of Gillam, Fort Smith, and Rankin Inlet MSPs are also shown in gray lines.

A. Solar wind data from GEOTAIL

Solar wind parameters were available from GEOTAIL for this event. The data are plotted in Figure 4.3. The satellite positions are labelled on top of each plot in GSM coordinates in R_E. First of all, it should be noted that October 9, 2000 was a rather quiet day, dominated by northward IMF. The GEOTAIL satellite measured a positive IMF Bz component during almost the entire UT time interval 0045 to 0800 UT, with only three excursions to negative Bz values, during the intervals 0345 - 0415 UT, 0447 - 0513 UT and 0645 - 0655 UT. The ion number density and solar wind speed at GEOTAIL were rather steady at about 10 cm^{-3} and 320 km/s, respectively. There was also an unusual and structured IMF "square-wave" in the GSM X-Y plane, which was the other likely initiator of the magnetospheric activity. The data for GEOTAIL in Figure 4.3 show that the "square-wave" burst occurred from about 0727 to 0735 UT, with Bx going from an

initial value of about -4.7 nT to about -2.3 nT during the square wave, then falling almost instantaneously back to -4.6 nT at 0735 UT. On the other hand, By rises in about a minute from an initial value of about + 1 nT to about +4.8 nT, and then falls to +1 nT at 0735 UT, only to rise dramatically to about +3.2 nT a minute later at 0736 UT, after which it remains relatively constant. The duration of the square wave is ~7 minutes in these two components, but the Bz component is small during this time. We also checked the IMF data from the ACE satellite (not plotted) to validate the seemly dramatic "square-wave" variation seen on GEOTAIL, and found that ACE showed a very similar Bx-By structure, which differed only slightly in shape from the GEOTAIL event. It is well known that, in By-dominated cases where |By|>Bz, even for northward IMF, there can be strong solar wind-magnetosphere coupling [*Nishida et al.*, 1998]. The "square-wave" change, in which Bx became less negative while By increased, caused a +By-dominated solar wind, which would have facilitated the conditions for "component merging" in the dawn flank magnetopause south of the ecliptic plane.

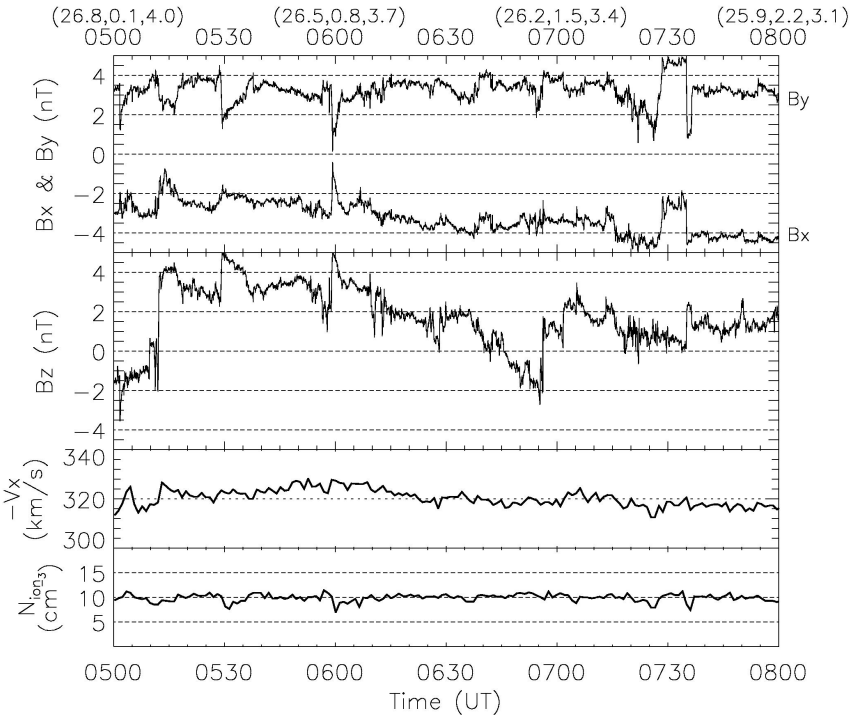

Figure 4.3 From top to bottom panel are the IMF in GSM coordinate, solar wind velocity, and ion number density from GEOTAIL observation, respectively, from 0500 to 0800 UT, October 9, 2000.

In conclusion, we have examined the solar wind observations from GEOTAIL, and found that there are two candidates possibly responsible for the small substorm event on October 9, 2000, namely, the southward IMF excursion seen at 0645-0655 UT, and the subsequent Bx-By structure seen as a "square-wave" at 0727-0735 UT.

B. CANOPUS magnetometer, riometer and photometer observations

In terms of magnetic activity, October 9 was in fact the fourth quietest day (Q4) of the month. The Kp index values during the first three 3-h UT intervals were 1-, 0+ and 0+. We will concentrate on the localized activity over the Canadian territories during the 3-h interval from 0600-0900 UT. Figure 4.4 shows the magnetometer reco rds from some CANOPUS stations and the Yellowknife (YKC) observatory of the NRCAN/GSC magnetometer array. Their geographical and geomagnetic locations can be found in Chapter 2.2. The bottom trace of Figure 4.4 shows the Pi2 pulsations at Pinawa, on an expanded 1 nT/div scale. All other magnetometer traces have a scale of 20 nT/div. Figure 4.4 shows that in the interval 0600 UT to 0732 UT leading up to the first Pi2 event at 0732 UT, there is very little activity at any of the magnetometer sites, as would be expected under such predominantly B_z+ IMF conditions. After 0732 UT there are three obvious Pi2 bursts, which are emphasized by three vertical gray bands. The magnetic bay indicates that the substorm onset began at 0752 UT at both Fort Churchill, where the B_X deflection reached -100 nT, and at Eskimo Point, where B_X decreased to about -50 nT. Very little deflection occurred at Rankin Inlet, so it can be inferred that the electrojet expansion was confined to magnetic latitudes below 72.9°. There was an initial period of increasingly negative B_x deflection at Fort Churchill during the first two Pi2 bursts, showing the pattern similar to a substorm growth phase.

The top panel of Figure 4.4 shows Gillam MSP data that have been processed so as to choose only the value of the brightest pixel in the MSP scan, for the oxygen red (630.0 nm) and green (557.7 nm) lines, where the colors used for the curves match the red and green colors of the emission lines. Arbitrary intensity units are used for each individual line, and the curves are plotted together in Figure 4.4 only so that their time variations can be compared. It is very clear that each of the three Pi2 bursts was closely

associated with the activation of optical auroras, and that the third Pi2 burst was accompanied by the strongest auroral brightening.

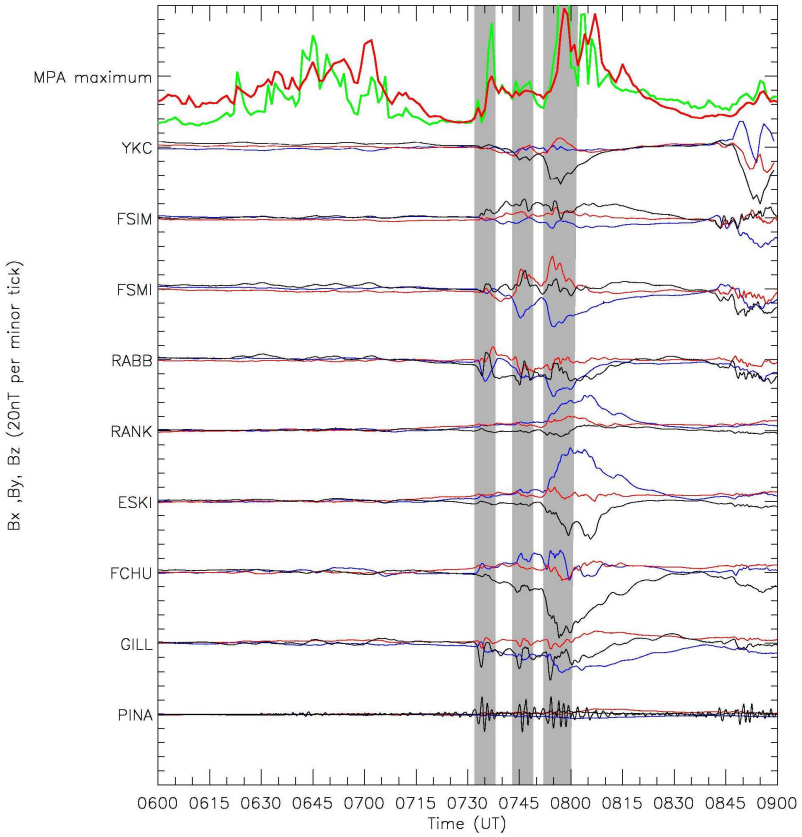

Figure 4.4 Magnetometer records for 9 western Canadian stations from 0600 to 0900 UT. Black, red and blue lines denote the X, Y, and Z components of the magnetic field. The bottom trace shows the Pi2 bursts observed at Pinawa, with scale 1 nT/div. All other magnetometer records are 20 nT/div. The top panel shows the maximum intensities on the Gillam MSP line for the red-line (630.0 nm) and green-line (557.7 nm) emissions, each with its own arbitrary intensity scale.

It is instructive to examine the Pi2 burst behavior as a function of latitude and time. The Pi2 oscillations result from passing the Bx component through a bandpass filter for periods from 40 to 150 s. The results are shown in Figure 4.5, for which the ordinate tick marks are 3 nT apart. The first two Pi2 bursts were observed only at the stations equatorward of Fort Churchill (69.0° MLAT), in keeping with the results of *Olsen and*

Rostoker [1975] that the Pi2 activity is monitored on the ground only up to the poleward border of the auroral electrojet. Only after 0752 UT did the poleward edge of the emission zone go beyond Eskimo Point (71.2° MLAT). We show below that the NASI 630 nm images agree quite well with the magnetic Pi2 observations with respect to the location of the auroral electrojet. On the other hand, there are some differences between start times of the Pi2 bursts at different stations. In particular, we see that the second Pi2 burst appeared at Fort Smith first at ~0740 UT and then later at Rabbit Lake and the "Manitoba line" stations, which strongly implies a west to east propagation delay.

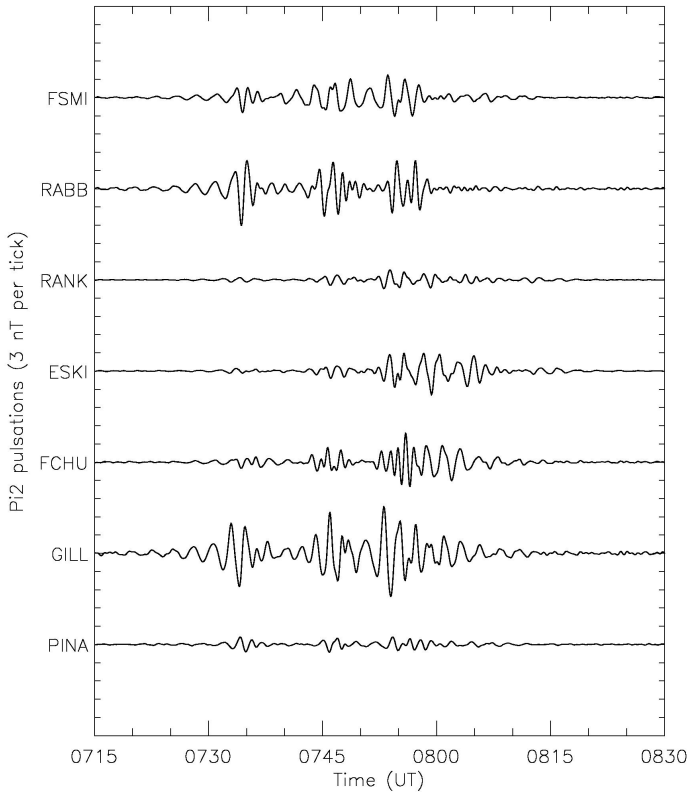

Figure 4.5 Pi2 oscillations of the Bx component as seen on the CANOPUS magnetometers from 0700 to 0830 UT, for a common scale of 3 nT/div.

Figure 4.6 shows the MLAT versus time plot of the 630.0 nm emissions observed by the CANOPUS MSPs at Gillam (top panel) and Fort Smith (bottom panel). Both plots show that the optical emissions intensified from about 0735 UT on the MSP lines. At ~0740 UT, a strong auroral intensification was detected by the Fort Smith MSP. The

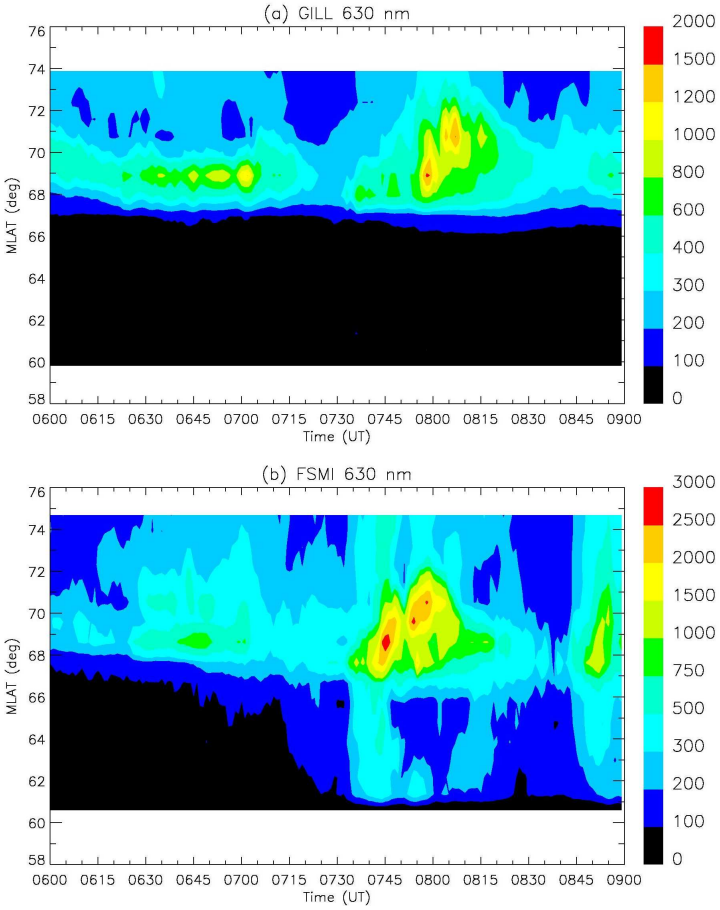

Figure 4.6 MSP 630 nm emission data from 0600 to 0900 UT observed at (a) Gillam and (b) Fort Smith.

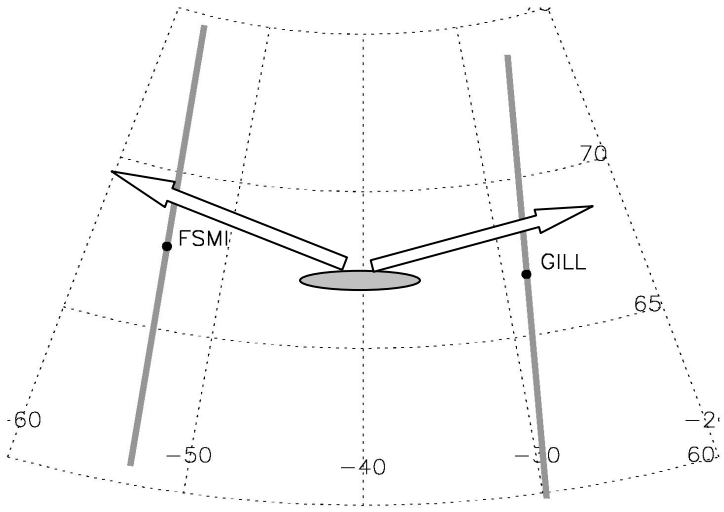

Figure 4.7 Schematic diagram showing the latitudinal offset of an auroral brightening structure observed by MSP instrument due to the propagation effect. See the text for explanations.

intensification structure was slightly slanted, showing an increase of latitude with time, which would imply a poleward motion of the auroral structure. However, the Gillam MSP observations showed no strong intensification at that time but only a relatively weak enhancement starting at 0743 UT. At ~0754 UT, both the Gillam and Fort Smith MSP plots showed strong auroral brightenings which extended well beyond 71^0 MLAT. It should be noted that, when the strong auroral breakup occurred, the intensification structure was seen best by the Fort Smith MSP at latitudes above 69^0 MLAT, which seems to contradict the classical scenario that the substorm-associated auroral brightening usually begins at the equatorward-most arc in the auroral oval [*Akasofu*, 1964]. The Gillam MSP observations also showed that the intensification region extended poleward from ~68^0 MLAT, again at latitudes somewhat higher than the equatorward border of the auroral oval. However, we will argue that such a discrepancy is a local effect due to the one-dimensional nature of the MSP measurements. As we will show later from the two-dimensional NASI observations, significant auroral brightening was found at the southwestern edge (~67.5^0 MLAT) of the NASI FoV.

At the very beginning of an EP onset, the initial activation is usually localized in azimuthal extent, especially for a small substorm such as this October 9 event. Let us consider the geometry shown in Figure 4.7. The initial auroral brightening occurred in the equatorward part of the auroral oval at a longitudinal position somewhere between Gillam and Fort Smith. Subsequently the brightening propagated both westward and eastward as well as poleward. Therefore the auroral brightening observed on the MSP scan line would be located at latitudes greater than the initiation site latitude.

In conclusion, there were three Pi2 burst intervals during the event sequence. The first two Pi2 bursts were associated with relatively weak and/or localized magnetic and auroral activities, and thus be classified as two pseudobreakups. The third Pi2 burst and the accompanying magnetic and auroral activation differed from the previous two not only in the disturbance magnitude but also in the subsequent spatial extent. The magnetometer record at Fort Churchill showed the classical growth-expansive phase signature, with the strongest magnetic bay (~-100 nT) starting at 0752 UT in conjunction with the third Pi2 burst. The coverage of third auroral activation expanded significantly poleward to >71^0 MLAT and also was broad in longitudinal extent, such

that it was almost simultaneously observed by the MSPs at Fort Smith and Gillam. Thus the third magnetic and auroral activation can be defined as a substorm EP (hereafter it is also called a "Stage-1" EP so as to distinguish it from the subsequent "Stage-2" EP discussed below), rather than as a third pseudobreakup.

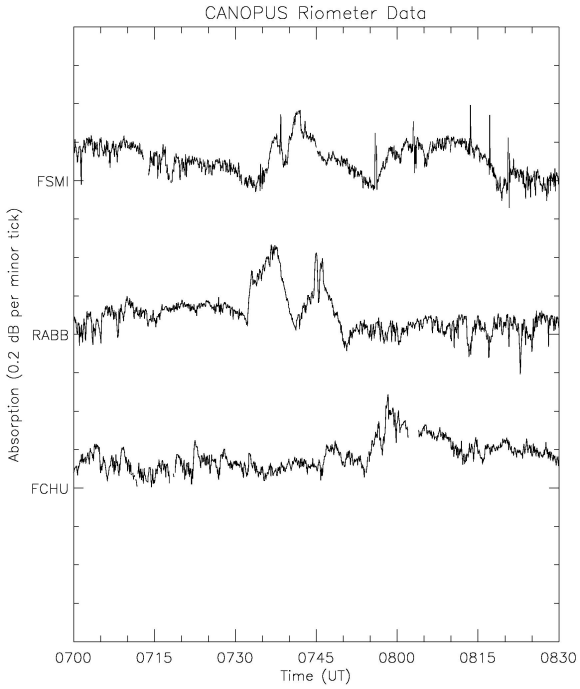

Figure 4.8 Riometer observations from 0700 to 0830 UT at several CANOPUS stations.

Figure 4.8 shows the riometer observations at several CANOPUS stations. At 0732 UT, when the first Pi2 and auroral intensification began, there was a very steep rise in the 30 MHz cosmic radio wave absorption. About 2 minutes later a rise in absorption was also seen at Fort Smith. If we assume that the absorption enhancement are caused by high-energy (>40 keV) electron precipitation, it is clear that the intense precipitation region moved westward. Unfortunately the riometer data at Gillam were not available so we cannot study the eastward propagation effect further east. The riometer data at Fort Churchill did not show any rise of absorption corresponding to the first pseudobreakup because the first auroral activation never reached that latitude. A second rise of absorption was first seen at Fort Smith at ~0739 UT, and subsequently seen at Rabbit Lake at ~0742 UT, and also at Fort Churchill (albeit a very small rise) at ~0744 UT, clearly showing an eastward propagation effect. This is also consistent with the

magnetic observations which showed that the second Pi2 burst appeared at For Smith ~3 minutes before it was recorded by the "Mani toba line" stations. Starting at ~0754 UT, another large increase of the absorption, which accompanied the substorm EP, was seen almost simultaneously at Fort Churchill and Fort Smith. No noticeable propagation effect could be determined at that time. The timing can be interpreted according to Figure 4.7 (note that Fort Churchill is almost at the same longitude as Gillam). If the initiation were located somewhere longitudinally about midway between Gillam and Fort Smith, the required time for the eastward propagation and the westward propagation would be roughly the same. Thus, the riometer observations are consistent with the magnetic and optical auroral observations in that the riometers confirms the existence of three successive activations, namely, two pseudobreakups and a substorm EP. Furthermore, the riometer observations provide important information about the origin and the subsequent propagation of the three activations.

There is another very important feature in Figure 4.4, namely the Eskimo Point magnetometer observations showing a second X-component magnetic bay which began at ~0802 UT. This second magnetic bay was even stronger than the ~0752 UT bay which corresponded to the Stage-1 substorm EP onset. Also another Pi2 burst was seen at Eskimo Point in Figure 4.5 during the second magnetic bay interval. Figure 4.6 shows that a second strong auroral brightening (hereafter referred as the Stage-2 auroral brightening) was seen at about 0804 UT in the Gillam MSP observations after the first brightening at ~0754 UT. However, the Stage-2 auroral brightening was located above ~70^0 MLAT and was not seen at Fort Smith MSP. *Rostoker* [1968] found that during a substorm the magnetic bay disturbances often occurred in a two-stage fashion. *Erickson et al*. [2000] also found that the initial substorm expansion immediately after the onset is usually short-lived (is followed by a "Sta ge-2 expansion". The second auroral brightening, which occurred at 0802 UT, is consistent with such a feature.

C. The NASI 630 nm and SuperDARN convection observations

Now we will focus on the most important parts of the observations in this event, the two-dimensional maps of auroral emission and ionospheric convection. The NASI data shown up to this point were not absolutely calibrated; the actual emission intensity

values in Rayleighs were not available. The data used in this paper are the raw data numbers after the flat-field calibration, which resolved the zenith angle dependence of the emission intensity. The flat-field calibration is usually only accurate at zenith angles less than 75^0. Beyond that, the calibration tends to overamplify the emission intensity. However, to have a full view of the auroral region, especially because for this event the initiation was close to Rabbit Lake, and hence was at about 80^0 zenith angle for the red-line emission seen by the NASI at Rankin Inlet, we were forced to compromise and use an upper limit of 80^0 zenith angle. One should keep in mind that the absolute emission intensities near the edge of the FoV are likely to be somewhat amplified. The assumed emission height was determined from a best-fit parallax technique based on the NASI and Gillam MSP observations (see Chapter 2.5.3).

Figure 4.9 gives the combined NASI 630 nm image and the SuperDARN convection velocities obtained from the Saskatoon and Kapuskasing radar data from 0730 to 0738 UT. The NASI 630 nm images are acquired once every 20 seconds, so the figure is an average of up to 6 such images. The convection velocity maps are based on the global potential mapping procedure of *Ruohoniemi and Baker* [1998]. It should be noted that the SuperDARN convection velocities and the red-line emissions are both ionospheric *F* region features, so combining them on one plot provides a reasonable picture of *F* region ionospheric activity.

Figure 4.9 shows that, for 0730-0732 UT, there was diffuse weak aurora in the eastern half of the FoV, extending longitudinally from 0230 to 0300 MLT, but there was almost no activity near midnight. There are several possible causes of that diffuse weak aurora. The first is that it could have been due to excitation of oxygen by secondary electrons which had energies of about 5-10 eV and which resulted from proton precipitation. However, it is more likely that the diffuse aurora was caused by electron precipitation associated with electrons that had curvature-gradient drifted in the magnetotail from the midnight sector toward the morning sector, where there is evidence of a partial ring current. This region remained relatively unchanged in the eastward portion of the FoV during the more dynamic auroral activities which originated from the southwestern portion of the NASI FoV. It was in the latter region that the original patch subsequently brightened and spread slowly eastward.

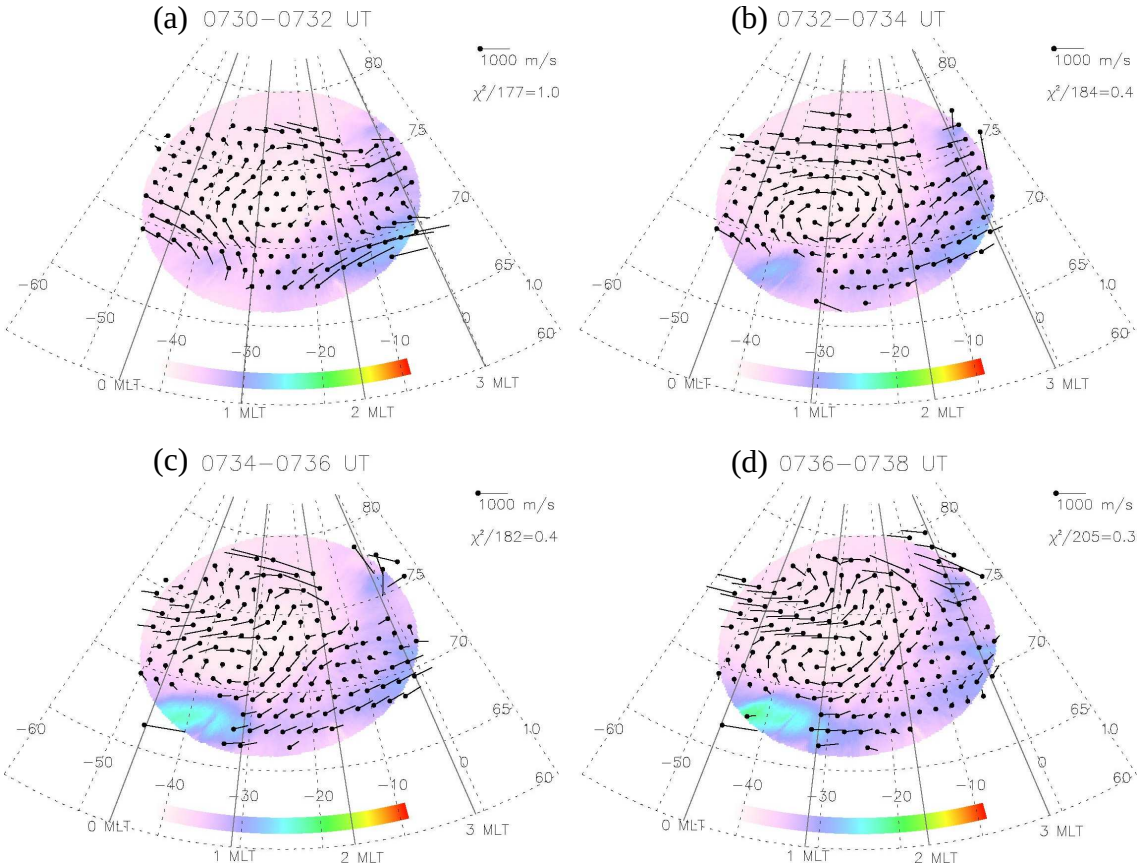

Figure 4.9 Maps showing the NASI 630.0 nm emissions and the SuperDARN convection velocities (arrows) obtained from the FIT procedure (*Ruohoniemi and Baker* [1998]) for the period 0730-0738 UT. The radar data are for standard 2-minute scan, and the NASI data is averaged over that same 2-minute interval. The chi-squared value and the number of actual data points are labeled in the upper right corner of each frame.

Clearly, by 0732-0734 UT, a midnight auroral patch appeared at about 67-68^0 MLAT and 36-40^0 MLON. The patch was just east of Rabbit Lake (-42.48^0 MLON). This intensification occurred in conjunction with both the first Pi2 burst and also the first cosmic radio absorption enhancement starting at 0732 UT at Rabbit Lake; thus we identify this site to be the origin of the first auroral activation. *Stoker et al*. [1996; 1997] found that the cosmic radio waves of decameter wavelength appeared to be absorbed more strongly in regions adjacent to discrete auroral arcs than inside the arc regions themselves. In this regard, we notice that there is a void in the radar echoes within and

nearby the intensified patch. That void was most likely due to the increasing absorption. The subsequent image at 0734-0736 UT shows that the auroras of interest in the southwest part of FoV had considerably brightened and completely dominated the diffuse weak aurora in the eastern half of the FoV. It is interesting to notice that the auroral evolution was led by a series of discrete patches. While the initial patch brightened and broadened, another distinct patch appeared at ~ -35^0, east of the initial patch. By 0736-0738 UT those two patches almost merged together, while a third "detached" patch appeared again at ~ -32^0 MLON.

In terms of the ionospheric convection, one very noticeable feature is that, accompanying the start of auroral activation at 0732 UT, a well-defined counterclockwise convection flow vortex centered at ~1 MLT and ~72^0 MLAT emerged, northeast of the growing auroral patch. The appearance of such a small near-midnight counterclockwise cell after substorm onset has been previously reported by *Lu et al*. [1998] and *Kamide et al*. [1994], who postulated that such cells are signatures of the magnetotail energy release process. Furthermore, the intensified auroral patch was caused by enhanced electron precipitation and thus should be associated with upward FAC, while the counterclockwise convection vortex implied downward FAC. Therefore, it can be concluded that for the first pseudobreakup starting at 0732 UT, the current pattern was more of a MCS, in which the ionospheric Pedersen current flowed equatorward. This is in contrast to the traditional zonal SCW concept, in which the ionospheric closure current is westward. The existence and physical importance of a MCS during a substorm evolution were first noticed by *Kamide and Kokubun* [1996], and further addressed by *Lui and Kamide* [2003] and *Akasofu* [2003]. In particular, *Akasofu* [2003] proposed a new model synthesizing the MCS and eastward plasma flow with three well-established substorm-associated phenomena, namely, the sudden auroral brightening, sudden growth of the WEJ, and cross-tail current disruption/dipolarization. Though there is unfortunately a void in the radar coverage inside the intensified aurora regions in Figure 4.9, we could infer from the overall convection pattern that the flow had a marked eastward component there. In *Akasofu*'s model, eastward flow corresponds to a southward electric field and thus a southward Pedersen current, which is the required closure current sense for the north-south FAC system. The WEJ is the

enhanced westward Hall current which produced the observed magnetic negative bay. The convection pattern and optical observations of the first pseudobreakup are thus consistent with *Akasofu*'s model [2003].

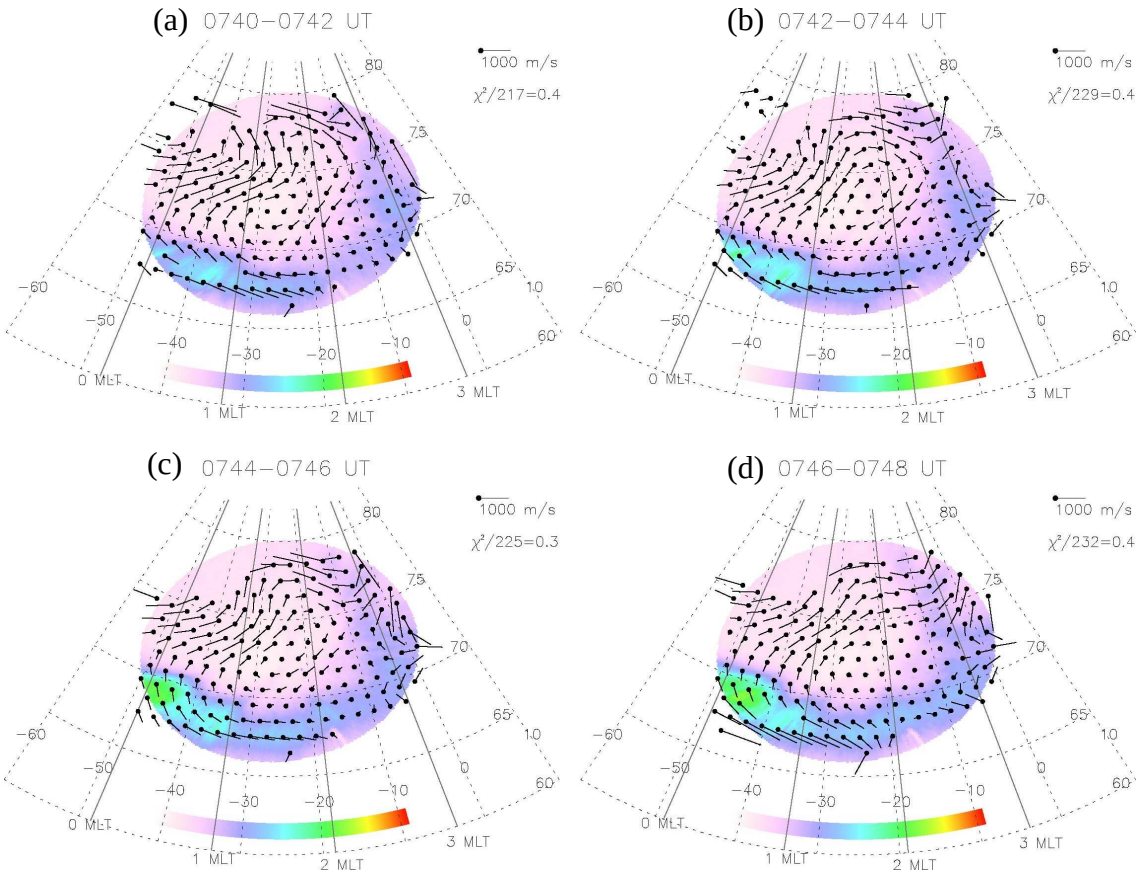

Figure 4.10 Maps similar to Figure 4.9, but for the period 0740-0748 UT.

Figure 4.10 shows the image from 0740 to 0748 UT, which is the interval of the second auroral intensification and the associated Pi2 bursts. At 0740-0742 UT, the overall emission intensity was lower than in the previous frame at 0736-0738 UT, but a new set of discrete patches had emerged in the longitudinal sector from local midnight to ~0100 MLT. Those patches were found to align approximately perpendicular to the flow direction, and thus roughly parallel to the electric field. Those discrete patches intensified considerably by 0742-0744 UT. During the next two frames, those patches not only significantly brightened but also broadened and tended to merge. On the west

side of NASI image, the poleward border of the bright aurora region had slightly expanded to ~70^0 MLAT. In terms of convection, the counterclockwise convection vortex persisted and kept moving eastward but its "focus" was still located at higher latitudes than the intensified auroras. The associated current system thus had become more northeast-southwest aligned. One can conclude that a gradual transition from the initial MCS towards a more zonal SCW was taking place. Within the regions of intensified aurora, the convection flow was generally southeast with a strong eastward component. Figure 4.10d shows that, by 0746-0748 UT, the counterclockwise convection vortex was somewhat deformed on its eastern edge. The reason for such a deformation will be explained later in the analysis of the global northern-hemisphere convection observations.

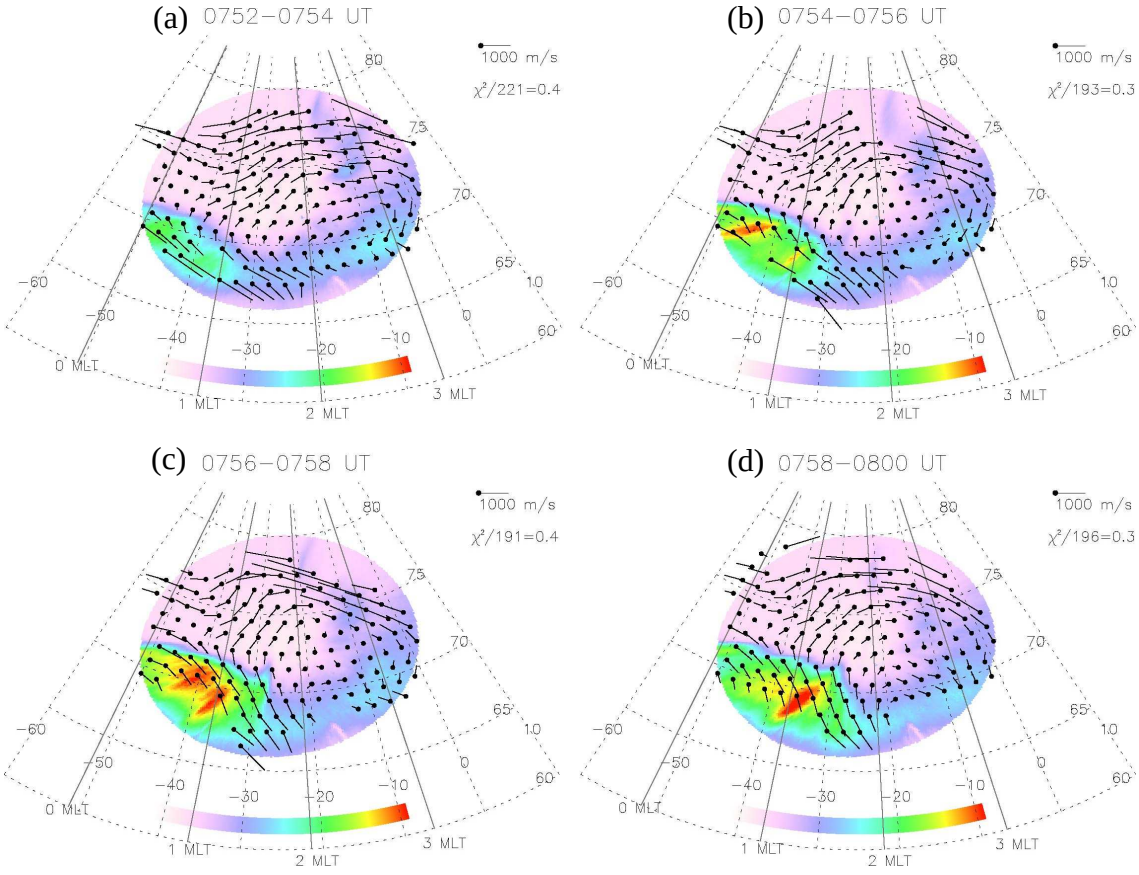

Figure 4.11 Maps similar to Figure 4.9, but for the period 0752-0800 UT.

Figure 4.11 shows four images from 0752 to 0800 UT, which correspond to the substorm EP interval. The auroral luminosity started to increase and expanded poleward following the onset at 0752 UT. At 0754-0756 UT, significant auroral brightening and poleward expansion to ~71.5^0 MLAT were clearly seen. Embedded in the diffusive bright auroras are two clear discrete patches which are separated by ~9^0 in MLON. Again we notice these two patches were aligned nearly perpendicular to the flow direction. By 0756-0758 UT, both of these discrete patches had significantly broadened to bridge the gap between the two patches, but some fine structures seen as "split arcs" developed. By 0758-0800 UT, one of the patches to the west had faded but the other continued to grow. An undulation in the auroral poleward border at ~72^0 MLAT can also be identified. In addition to the drastic auroral brightening and poleward expansion, an overall eastward evolution of auroral brightening up to 1.8 MLT is also clear from the plot sequence. In terms of convection, we see that the downward-FAC counterclockwise vortex had enlarged in spatial scale and had moved eastward, while at the same time its focus had dropped to lower latitudes at 0752 UT (EP onset time), such that the bright auroral region was located more or less directly west of the convection cell. At that stage, the current pattern is entirely consistent with the common SCW alignment. Another very important feature is that the flow direction across the bright auroral region had switched from the original strongly eastward flow at the onset time to a more southward flow at the later time of the Stage-1 EP.

Figure 4.12 shows four images from 0800 to 0808 UT. There was some decay of the auroral emissions from the Stage-1 EP at 0800-0802 UT. Starting at 0802 UT a second (Stage-2) auroral brightening occurred, consistent with that inferred from the Gillam MSP observations. At 0804-0806 UT, an intensified patch was seen at ~-33^0 MLON and ~70^0 MLAT, and the eastward evolution of enhanced auroral luminosity had reached ~2.7 MLT, which is the eastern limit of activity for the whole event. At 0806-0808 UT, though the intensified patch was still visible it obviously had faded. The activity gradually declined afterwards.

The most distinguishing convection feature shown in Figure 4.12 before and during the Stage-2 auroral brightening is that the flow through the bright region of aurora had become dominantly southward. The southward flow extends well poleward of the bright

patch. The morphology and underlying mechanism of this Stage-2 auroral brightening was found to be significantly different from the previous three auroral intensifications, and will discussed in detail later in section 4.3.3 of this chapter.

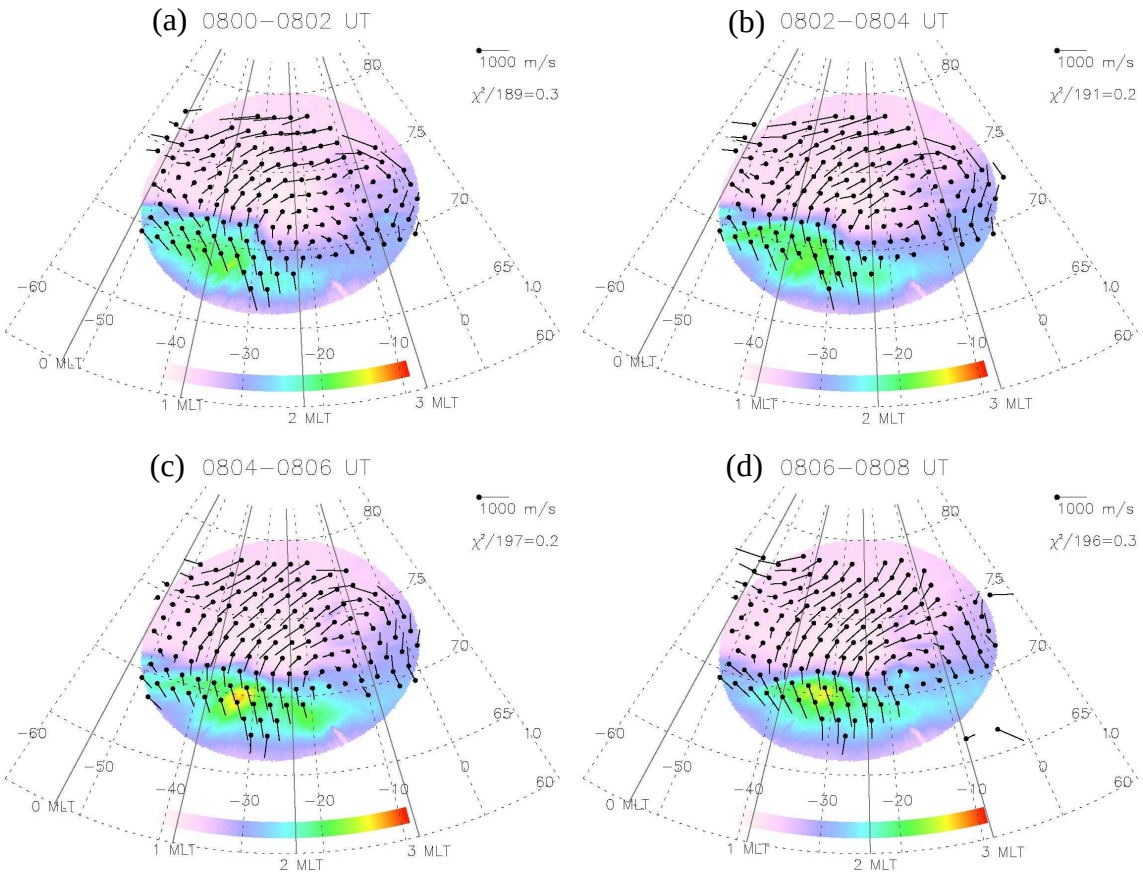

Figure 4.12 Maps similar to Figure 4.9, but for the period 0800-0808 UT.

The high temporal resolution (20 second) of the NASI observations enables a detailed study to be made of the evolution of auroral emission structures during the whole event sequence. The NASI image pixel locations of the band of maximum intensity were plotted as a function of time. The resulting plot, Figure 4.13, shows the latitude band of maximum intensity versus time, the longitude band of maximum intensity versus time, the maximum intensity versus time and the Gillam Pi2 structure versus time, from top to bottom, respectively. The intensity bands correspond to intensities within 5% of the maximum intensity. To reduce the error caused by the flat-

field calibration for large zenith angle observations, we will use the radially-integrated emission intensity to investigate the azimuthal auroral structure. That is, we integrate the raw data number (after the flat-field calibration) between zenith angles 58 and 78^0, which fully covers the bright aurora region, and within every 1^0-wide NASI azimuthal channel (the NASI azimuth is 0 for geographical north and increases in the clockwise sense). The results are shown in Figure 4.14 to Figure 4.16. From Figure 4.13 to Figure 4.16 we can obtain detailed information about the evolution of auroral activities.

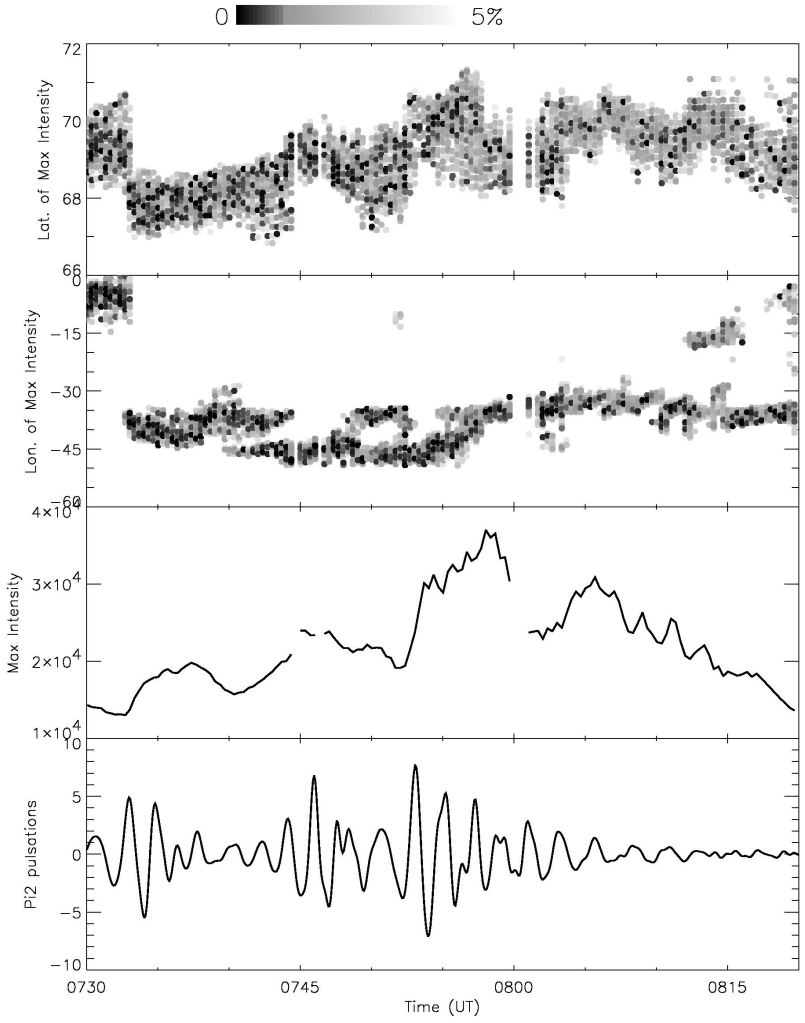

Figure 4.13 The top two panels show the time plots of the latitude and longitude of the NORSTAR image pixels where the 630.0 nm intensity is within 5% band about the maximum. The third panel shows the maximum intensity versus time in unit of raw data number, and the bottom panel shows the Pi2 pulsations in unit of nT at Gillam versus time.

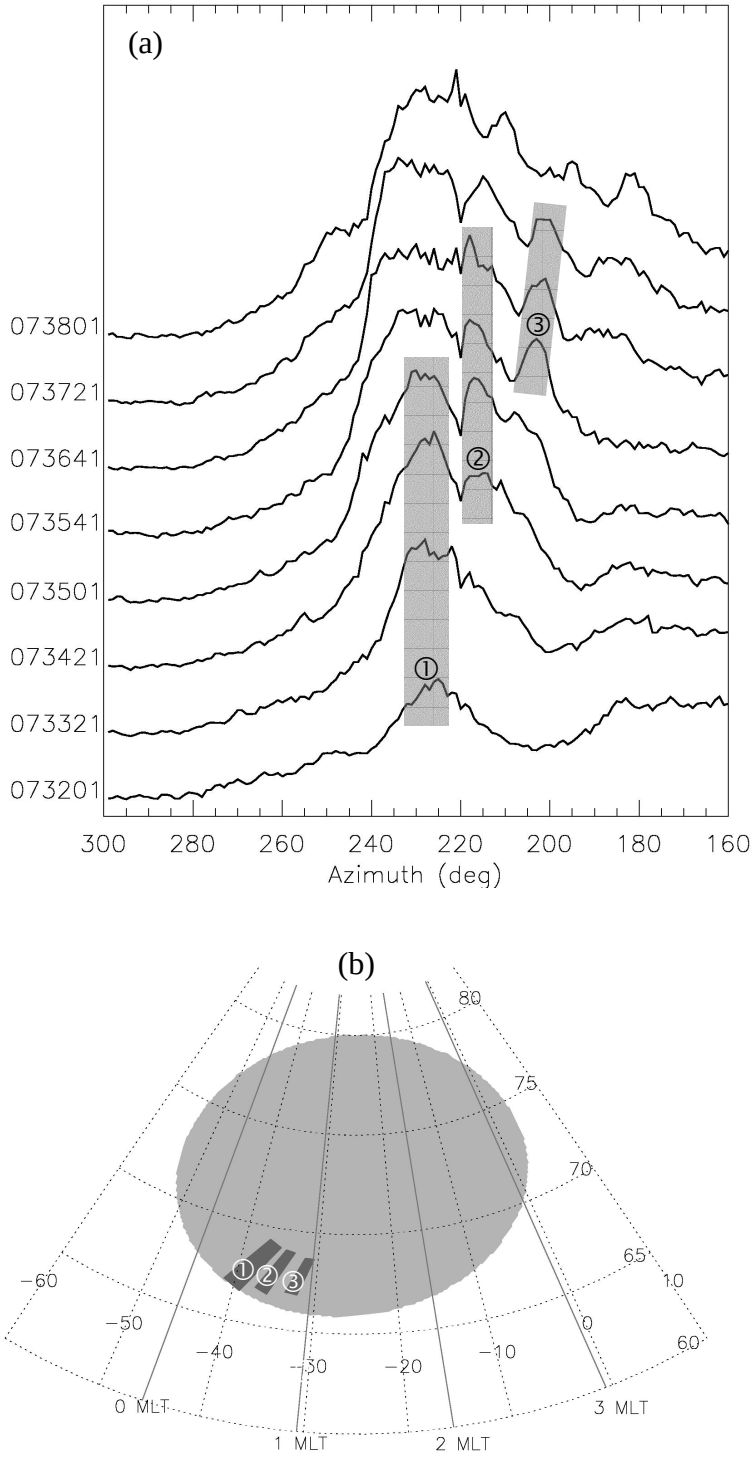

Figure 4.14 (a) The radially-integrated 630 nm emission intensity versus azimuth angle observed by NSAI during the first pseudobreakup interval. The observation time in UT is labeled on the left of each curve. Numbered gray bands indicate several intensified patches. (b) The approximate geomagnetic position of the discrete patches (dark boxes). The gray circle indicates the FoV of the NASI at Rankin Inlet.

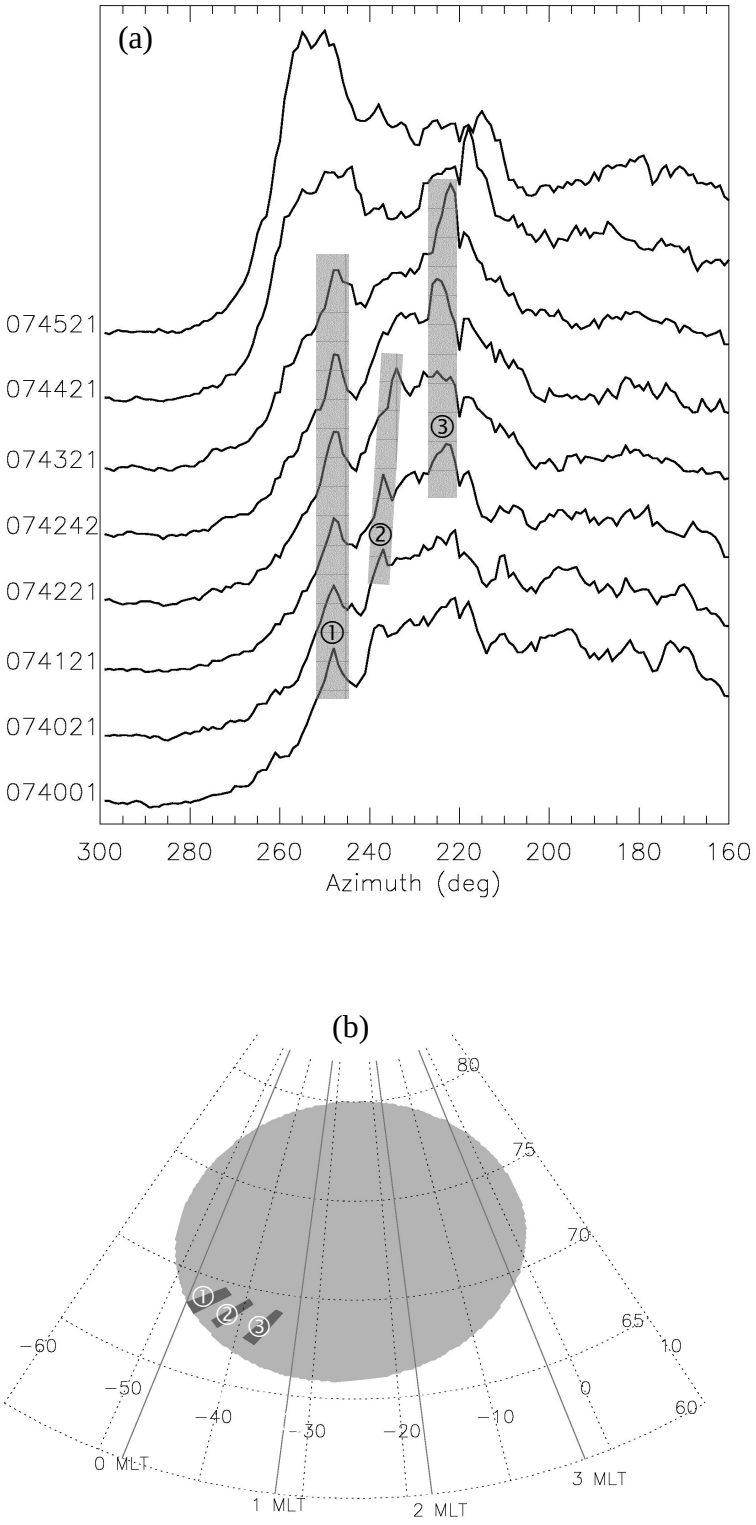

Figure 4.15 Same as Figure 4.14, but for the second pseudobreakup interval.

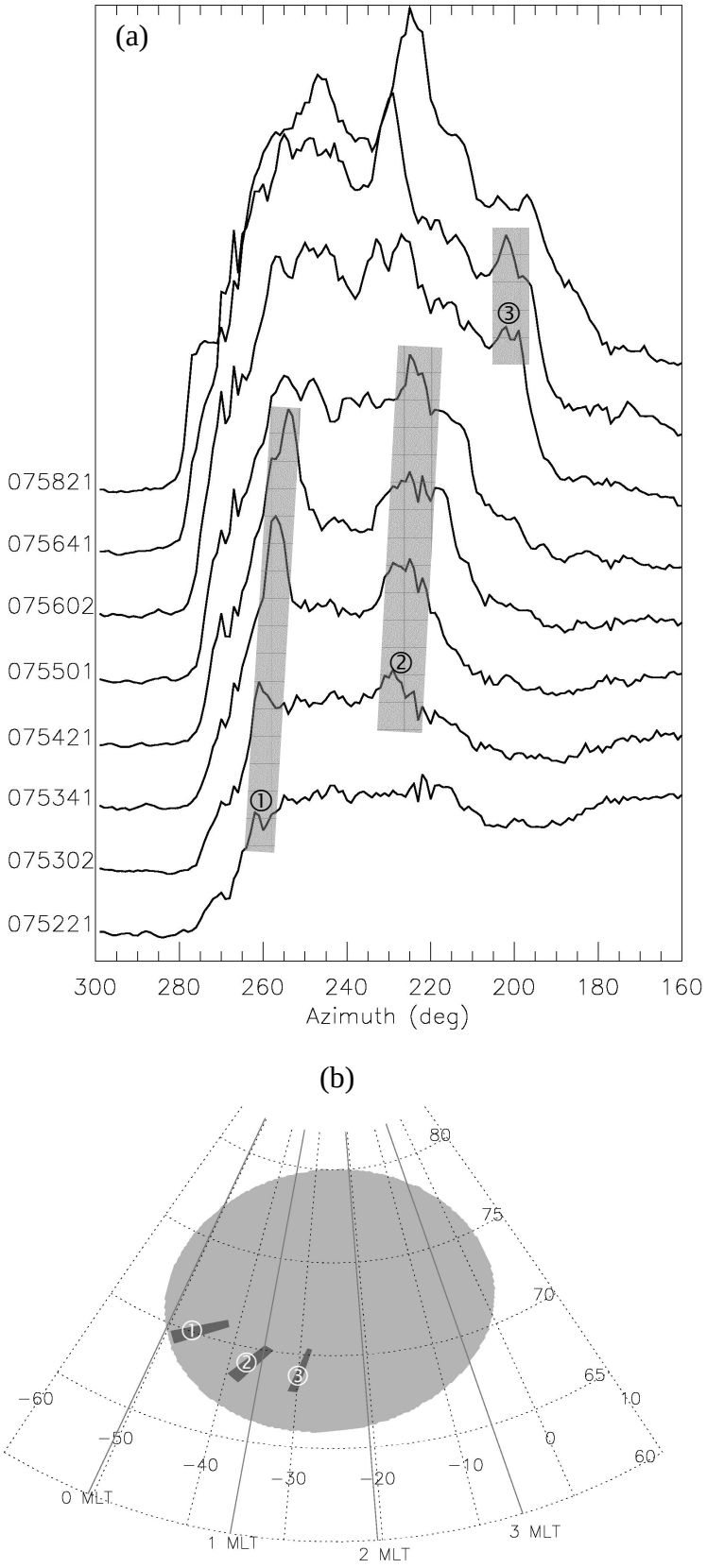

Figure 4.16 Same as Figure 4.14, but for the substorm EP interval.

As noted earlier, there was diffuse weak aurora present in the eastern part of the FoV before 0732 UT. This is seen in Figure 4.13 as the region of diffuse intensity north of 68.5° MLAT and east of -15^0 MLON just before 0732 UT. However, the growth of the first Pi2-associated patch of aurora began at about 0732 UT, and the region of maximum intensity underwent a dramatic shift to the southwest part of the NASI at about -40^0 MLON, as shown in Figure 4.13. This first pseudobreakup was rather stable in latitude (67-68^0 MLAT) after its initiation and showed no significant poleward propagation. Figure 4.14a gives the radially-integrated emission intensity versus the NASI azimuth angle during the first Pi2 burst and auroral intensification interval. In Figure 4.14a, the first patch was located at ~225^0 azimuth at 0732:01UT. By 0733:21 UT, the patch had expanded both westward and eastward, while a small "bump" appeared at ~217^0 azimuth. This small "bump" grew in magnitude and also broadened to evolve into another intensified patch seen clearly from at 0734:21 UT to 0735:41 UT, while another small "bump" at ~207^0 azimuth in turn appeared at 0735:01 and developed into a third intensified patch seen clearly from 0735:41 UT to 0737:21 UT. The third patch showed a tendency toward decreasing azimuth with time, which implied an eastward motion of the patch. In Figure 4.14b we show the approximate geomagnetic positions of the above three successive discrete patches, based on Figure 4.14a. The expansion of the originally azimuthally separated patches 1 and 2 gradually bridged the gap between them. By 0736:41 UT those two patches had basically merged and formed an overall enhancement of luminosity over a broad region, though much fine structure still existed. At the same time a new patch on the east, though initially weak and diffuse, began to develop at ~190^0 azimuth. Afterwards, several wave-like patches were discernible but all clearly showed eastward motion.

The second epoch of auroral intensification started at ~0740 UT, as seen from the second rise of maximum emission intensity shown in the third panel of Figure 4.13. At the same time, a new high intensity structure emerged at about -45^0 MLON and 67-68^0 MLAT, near the southwestern edge of the NASI FoV. During the second auroral activation interval the intensification structure moved poleward to 69.5^0 MLAT until 0745 UT, but then retreated equatorward to ~67.5^0 MLAT. In Figure 4.15a, some structures still existed as remnants of the first pseudobreakup activity. However, a new

patch at ~250^0 azimuth led a new series of discrete intensified patches and thus a second epoch of auroral activity. Another patch at ~237^0 azimuth started to form at 0740:21 UT and showed a slight eastward motion afterwards. The third patch at ~225^0 azimuth appeared at 0742:21 UT. The approximate geomagnetic position of the three discrete patches was plotted in Figure 4.15b. It should be noted that, because the first midnight patch appeared at near the southwest edge of the NASI FoV, there is a strong possibility that the actual initiation site was event further west and/or south of the FoV of NASI. We notice that the patch 3 was "quenched" at 0742:21 UT, and reappeared at 0742:42 UT, whereas patch 2 disappeared at that time. Afterward patch 3 showed a clear eastward motion, and original patch 1 significantly intensified and broadened at 0744:21 UT and 0745:21 UT. An overall enhancement of auroral luminosity over a broad region was seen.

The interval of special interest is from 0752 to 0800 UT, during which the auroral emission enhancement was much stronger than the previous two activations. Notice in Figure 4.13 that, at the start of this activation, the brightening pixels within the NSAI FoV were initially found at as far equatorward as ~67.5^0 MLAT and as far east as -50^0 MLON. It should be noted that, since the brightening was seen to the very southwestern edge of the NASI FoV, the actual origin of the activation might have been even further south and/or west. After its initiation the bright regions moved significantly poleward to >71^0 MLAT and eastward to ~-30^0 MLON. A north-east propagation of the auroral brightening is thus easily identified. After 0758 UT the activation decayed, and the regions of maximum intensity retreated in latitude to 68.5-69^0 MLAT but remained relatively stable in longitude.

Figure 4.16a shows that the very first hint of the appearance of the westernmost patch was at ~260^0 at 0752:21 UT. At 0753:02 UT that initial patch grew and another patch at ~230^0 azimuth appeared. Those two patches strongly intensified and broadened up to 0754:21 UT, and showed a slight eastward trend in their motion. As in the two previous activations, the two separated patches merged. The gap between them became filled by an auroral luminosity enhancement until there was virtually no gap by 0755:01 UT. However, a considerable amount of fine structure in the intensity remained. A new weaker patch at ~200^0 azimuth appeared at 0756:02 UT. After 0756:41 UT, the ~230^0

patch intensity increased significantly, and there was an obvious eastward motion for all patches. The approximate geomagnetic position of the three discrete patches is plotted in Figure 4.16b.

In summary, the NASI observations with 20-second resolution behaved such that, during each auroral activation interval, several discrete intensified auroral patches could be identified. These patches have exactly the same signature as the AAFs reported by *Elphinstone et al*. [1995]. The patches appeared in a sequence such that each new patch formed a little to the east of the previous one. In agreement with *Elphinstone et al.* [1995], the patches behaved exactly as did the AAFs in that they tended to propagate eastward in the postmidnight sector. After their initial appearance, the patches usually intensified and also expanded. The gaps between the patches were gradually filled by diffusive auroral luminosity enhancement, although discrete auroral structures still persisted and usually showed an obvious eastward motion after the diffusive auroral luminosity enhancement.

Figures 4.14b to 4.16b reveal another interesting feature, namely that the azimuthal separation between the patches tended to increase during the event sequence. For example, at the start of the first pseudobreakup interval, the first 2 patches were separated by only $2\text{-}3^0$ MLON, while during the second pseudobreakup, the separation between adjacent patches was $4\text{-}5^0$ MLON. By the time of the Stage-1 substorm EP, the separation had increased to $8\text{-}9^0$ MLON.

In addition to Saskatoon, there was also good scatter from the other six northern SuperDARN radars (Kodiak, Prince George, Goose Bay, Stokkseyri, Thykkvibaer and Hankasalmi), with 2-minute resolution, during the whole event sequence. The general northern hemisphere convection pattern from about 20 MLT through midnight, dawn and noon to about 15 MLT was quite well defined. The cross-polar cap potential drop could be determined from the global SuperDARN observations [*Shepherd et al*., 2001; 2003]. Figure 4.17 shows six frames of combined NASI 630 nm image and global SuperDARN convection velocities during the following intervals: (a) 0718-0720 UT, (b) 0728-0830 UT, (c) 0732-0734 UT, (d) 0748-0750 UT, (e) 0754-0756 UT, and (f) 0804-0806 UT. The cross-polar cap (PC) potential shown in the upper-left corner of

each frame was estimated from the difference between the peak positive and negative potentials. Note that in these six frames the NASI images are shown in gray scale.

Figure 4.17a shows that, at 0716-0718 UT when the cross-PC potential reached a maximum (48 kV), strong flows (~1 km/s) were seen on the dayside at $\geq 80^0$ MLAT, implying enhanced reconnection at the dayside magnetopause. We see a contracted morning counter-clockwise cell on the dawnside flank, as expected from the 2-cell convection pattern under IMF By+ conditions, but near midnight both the convection and the optical emissions were very weak. In the interval 0728-0730 UT, the cross-PC potential decreased to a minimum value (30 kV). The dayside convection diminished but the near-midnight flows at high-latitude ($\geq 75^0$ MLAT, presumed to be on open field lines because of the lack of 630 nm emissions), were somewhat intensified.

The first pseudobreakup began at 0732 UT, which also marked the start of the optical and magnetic activities for the whole event. As we have mentioned before (see Figure 4.9b), an initial auroral patch appeared at ~0.4 MLT and 67-68^0 MLAT, accompanied by a well-defined counterclockwise convection flow vortex centered at ~1 MLT, 72^0 MLAT. The flows at lower latitude (^{0} MLAT) had become noticeably stronger, indicating an increase of convection in the near-Earth plasma sheet. The near-midnight counterclockwise convection vortex kept moving eastward after its emergence, as we have shown in the series of plots in Figures 4.9 and 4.10. By 0746-0748 UT this eastward-moving convection vortex had "collided" with the original morning cell on the flank side and became somewhat deformed on its eastern edge (a hint of another counterclockwise cell on the eastern edge of the map can be seen in Figure 4.10d). By 0748-0750 UT, the initial auroral patch had intensified and expanded both westward and eastward. The nightside flows continued to grow and a single large postmidnight convection cell with a "focus" around 2.3 MLT, 71^0 MLAT became well-established. At 0754-0756 UT, just after the Stage-1 EP onset and the poleward expansion to ~71.5^0 MLAT, the cross-PC potential also reached a peak value (50 kV) and strong flows were seen again on the dayside, while the nightside convection cell was relatively unchanged in position from that in the previous frame but was strongly intensified. At 0804-0806 UT, during the Stage-2 EP, the cross-PC potential reached its maximum value (54 kV) for the whole event.

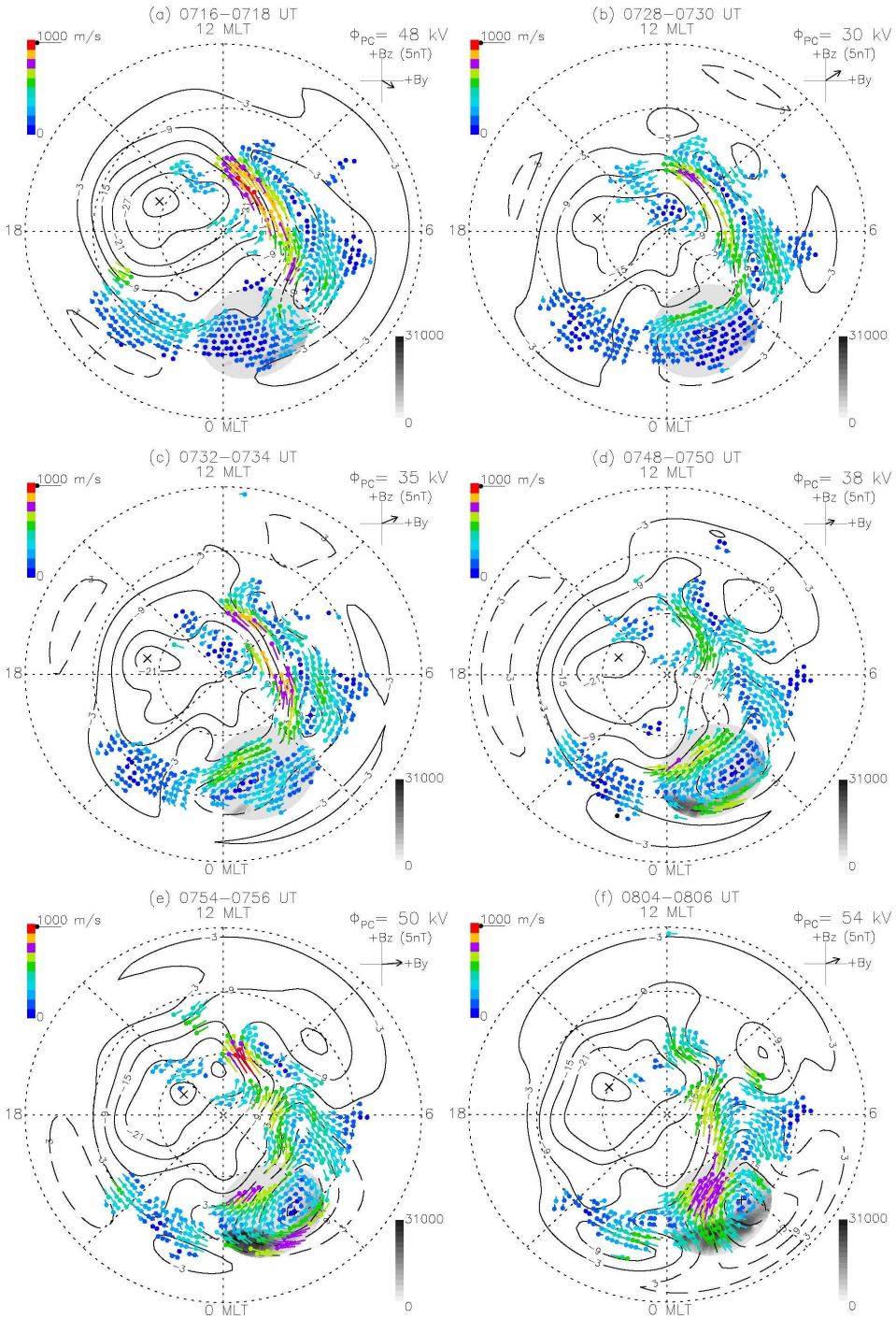

Figure 4.17 Six frames of the global SuperDARN convection (with electrical potential contours overlaid) and NASI 630.0 nm emissions. Dotted circles from outside towards the center represent 60^0, 70^0 and 80^0 MLAT respectively. The colorscale for the convection velocity, the cross-PC potential and IMF parameters, and the grayscale for the NASI emission intensity, are shown at the upper-left, upper-right, and lower-right corners of each frame, respectively.

However, the dayside convection at this time was rather weak and the enhanced flows were mostly on the nightside. The premidnight convection was always very weak during the whole event, implying that the most dynamic substorm-associated processes were restricted to the postmidnight sector.

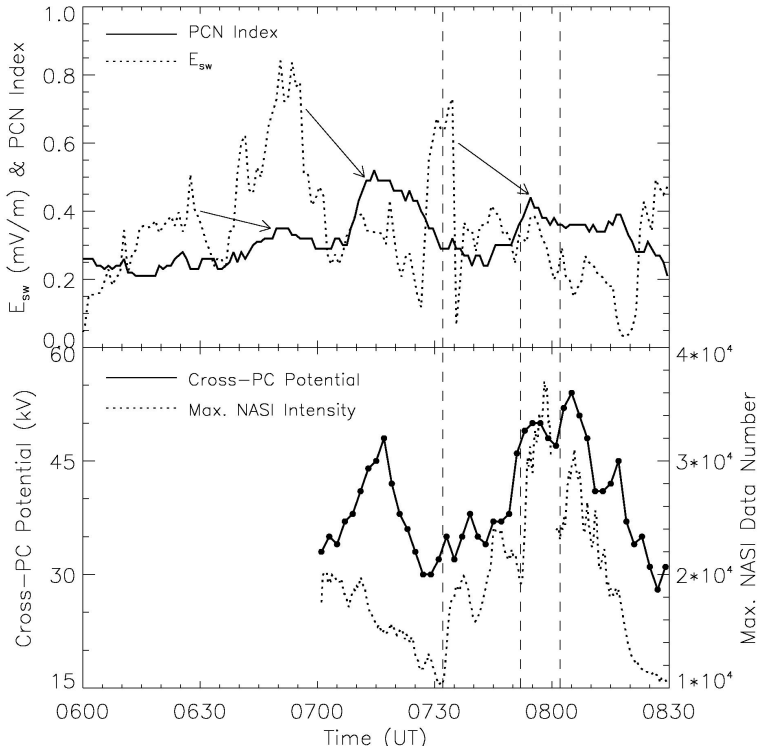

Figure 4.18 The upper panel gives the merging solar wind electric field (dotted line) and the PC index (solid line) from 0600 to 0830 UT. Arrows show the peak-to-peak correspondences between two data sets. The bottom panel gives the cross-polar cap potential (solid line with dots representing the mid-time of each scan) derived from SuperDARN convection measurements and the NASI maximum optical intensity (dotted line) from 0700 to 0830 UT. The start times for the first pseudobreakup, the Stage-1 EP and the Stage-2 EP are marked with dash lines.

To help understand the high-latitude ionospheric response to the solar wind, we use the northern polar cap (PCN) magnetic activity index, which is obtained from the near-pole magnetometer stations at Thule in Greenland (85.4^0 MLAT) [*Troshichev et al.*, 1988]. There was a high correlation between the PC magnetic index and the "merging solar wind electric field" [*Kan and Lee*, 1979], given by

$$E_{sw} = -V_x \cdot \sqrt{B_y^2 + B_z^2} \sin^2(\theta/2), \tag{4.1}$$

where V_x, B_y and B_z are the solar wind velocity, GSM Y and Z components of the IMF, respectively, and $\theta = \arctan(B_y / B_z)$. The merging solar wind electric field and the PCN index are plotted in the upper panel of Figure 4.18. The cross-correlation between them peaks at a lag of 21-23 minutes, as indicated by the arrows between "mat ching peaks". The propagation time of the solar wind from GEOTAIL to the subsolar magnetopause may take ~9 minutes, and a further lag of 12-14 minutes between the solar wind interaction with the magnetopause and the subsequent ionospheric response is not unreasonable (e.g., *Ruohoniemi and Greenwald*, [1998]). In the bottom panel of Figure 4.18 is plotted the SuperDARN-derived cross-PC potential from 0700-0830 UT. The NASI raw data numbers of the brightest pixels within the FoV at each exposure time are also plotted for reference. From the comparison between Figure 4.18 and Figure 4.3, one can readily infer that the cross-PC potential peak at 0708-0722 UT was the consequence of the 0645–0655 UT IMF southward excursion, while the other peak at 0750-0800 UT was associated with the IMF Bx-By structure at 0727-0735 UT.

During the 0802-0806 UT intervals there was a second strong enhancement of cross-PC potential but no counterpart was seen in the PCN index. Also, no major peak which might contribute to this enhancement could be found in the solar wind electric field data. As shown in Figure 4.18 the cross-PC potential also shows a remarkably good correlation with the optical auroral emission intensity, with the former slightly preceding the latter. For the Stage-1 EP, the enhancement of cross-PC potential led the nightside auroral emission by 2-4 minutes, similar to the day-to-nightside convection transition time in response to solar wind variations [*Ruohoniemi and Greenwald*, 1998], while for the Stage-2 EP, the lead time was less than 2 minutes.

D. Observations at geosynchronous orbit

Two geosynchronous satellite observations were available during the event. Unfortunately, they were not at positions that map to the radar and optical observations areas. GOES-10 (~-135^0 geographic longitude) is to the west of our ground-observation area, and GOES-8 (~-75^0 geographic longitude) to the east. However, they still provided

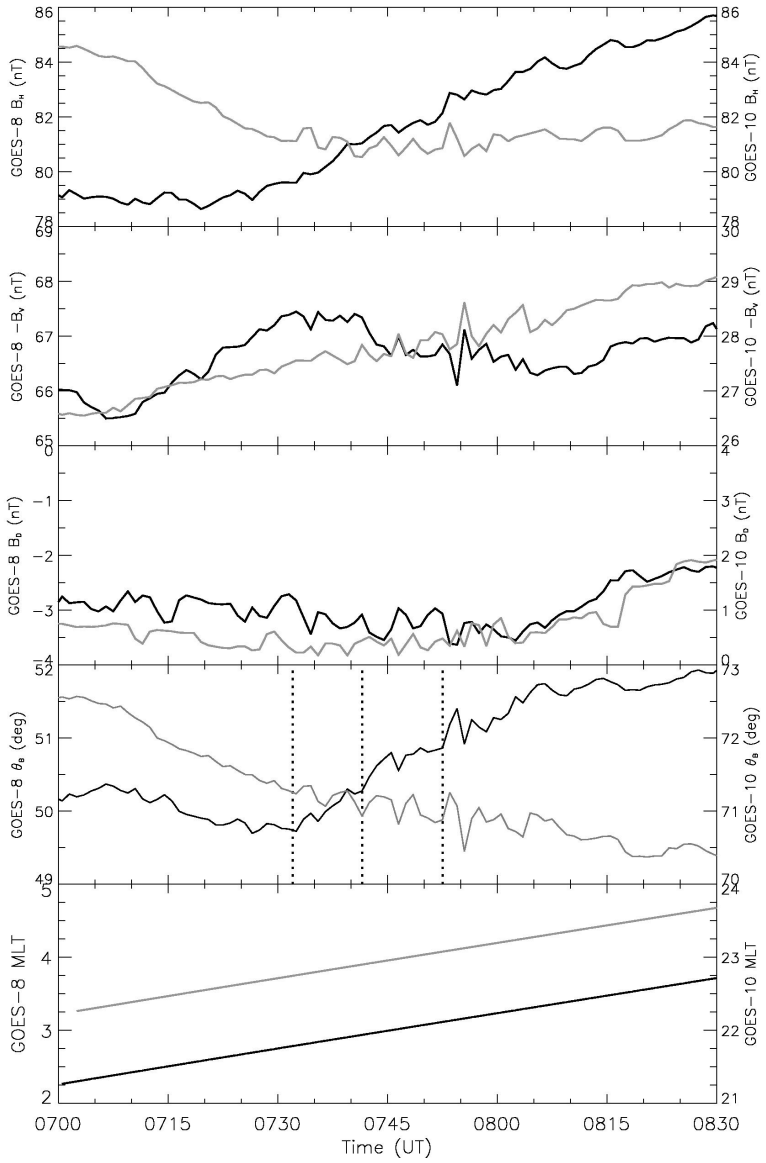

Figure 4.19 Magnetic fields observed at geosynchronous orbit by GOES-8 (black line) and GOES-10 (gray line). The left tick marks are for GOES-8, and the right tick marks are for GOES-10. The final panel gives the MLT at the footprint of GOES-8 and GOES-10.

very important information about the magnetic fields at geosynchronous orbit. Figure 4.19 gives the magnetic fields measured by two satellites and their MLT sectors from 0700-0900 UT. During the event GOES-10 is at 23±0.25 MLT and GOES-8 at 3±0.25 MLT. The GOES magnetic fields are converted to the VDH coordinate system (see Appendix A.1). The magnetic elevation angle θ_B which is defined by the equation,

$$\theta_B = \arctan\left(-B_H / B_V\right) \ , \tag{4.2}$$

is used to identify the dipolarization. On GOES-8 the θ_B value increases from 49.6^0 to 52^0 during the interval 0730-0815 UT. This change is much smaller than that seen in a typical substorm dipolarization event (~10^0 change within 10 minutes was reported by *Liou et al.* [2002]) but it nevertheless indicated a slight magnetic dipolarization at geosynchronous orbit. Considering that the substorm event studied in this chapter is a very minor and localized one and that, as shown by the NASI data, the auroral brightening never reached 03 MLT during the whole event, the small magnitude of the dipolarization observed on GOES-8 is reasonable. We also see that the dipolarization progressed in a multi-step way. The start times of each stepwise increase (shown in dotted lines) were found to be in accord with the start times of the three Pi2s and associated auroral activities. On the other hand, on GOES-10 the overall trend of θ_B was decreasing, so no magnetic dipolarization effect was seen.

On the basis of the geosynchronous measurements and the convection, optical, magnetometer and riometer observations, some final remarks on the initiation and the spatial extent of the three auroral intensifications may be made. The site of the first activation at 0732 UT was unambiguously determined from the NASI observation, i. e., at ~-39^0 MLON, as seen from Figure 4.9b. At the same time, there was an abrupt rise in the 30 MHz cosmic radio wave absorption at Rabbit Lake, which is near (just west of) the initiation site. However, the original sites for the second and third auroral intensifications are not as clear. The NASI observations show that, for those two activations, the initial intensification occurred at the western edge of the FoV at midnight, indicating that the origin of that activation likely was located west of the NASI FoV, in the premidnight sector. For the second auroral activation, the MSP observations at Fort Smith showed a much stronger emission enhancement than that at Gillam. The riometer data also showed that the increase in absorption first occurred at Fort Smith at ~0739 UT, and was subsequently seen at Rabbit Lake at ~0742 UT, and then at Fort Churchill at ~0745 UT, clearly indicating an eastward propagation effect. It is likely that the initiation site for the second activation may have been located close to Fort Smith. The same problem also exists for the third activation, i. e., the substorm EP.

As we have sketched in Figure 4.7, the actual initiation site was probably about midway between Fort Smith and Gillam and outside the NASI FoV. We know of no other observation sets that could have been used to determine the exact initiation sites for the second and the third activations. However, important clues can be found from the magnetic records at Fort Smith, which showed some positive excursions of the X and Y components corresponding to the second pseudobreakup and the substorm EP onset. Such positive excursions are usually the signature of a westward traveling surge (WTS) passing over the station. Therefore we may conclude that the initiation sites of the second and third activations were east of Fort Smith. The geosynchronous GOES data clearly shows that the western limit of all three activations never reached ~23 MLT because no dipolarization effect was ever seen at GOES-10, but for each activation there was a small but clearly identifiable dipolarization effect seen on GOES-8 at ~3 MLT. Furthermore, the ionospheric convection in the postmidnight sector observed by the Saskatoon-Kapuskasing SuperDARN radar pair underwent dramatic changes during the whole event, but the premidnight convection observed by the Prince George-Kodiak radar pair was always small in magnitude and showed only slight changes in the pattern.

Considering all the facts above, the whole event is fundamentally different with those "traditional" substorms which have an initiation site in the premidnight sector and normally show a well-defined westward propagation effect. In our event, the initial activation occurred at ~0.4 MLT. The initiation sites of the second and third activations might have been located longitudinally a few tens of minutes prior to midnight, but they underwent quite asymmetric longitudinal expansions subsequently. The eastward expansion was prevalent and was detected by NASI, the CANOPUS magnetometers and the MSPs in the postmidnight sector. Despite the lack of optical observations in the premidnight sector, the other evidence still shows that the small substorm on October 9, 2000 is a postmidnight event.

Another interesting issue is that, although no dipolarization effect was seen on GOES-10, there were some small wave-like perturbations of magnetic fields with period of ~5 minutes from 0732 to 0805 UT, which indicates the existence of ULF Pc5 waves at geosynchronous orbit in the premidnight sector during the event interval. Large-scale Pc5 pulsations inside the magnetosphere are generally thought to be driven

by mechanisms such as the Kelvin-Helmholtz instability (KHI) at the magnetopause, solar wind pressure pulses or intermittent reconnection processes such as flux transfer events (FTEs). However, in the October 9 event those external mechanisms are somewhat unlikely. As we indicated in the GEOTAIL solar wind data analysis (see Figure 4.3), the ion number density and the velocity of the solar wind were very stable. The duration of the IMF Bz southward excursion was only 10 minutes and the Bx-By structure lasted only 7 minutes, and the timing is either too early or too late for these to be responsible for the observed Pc5 pulsations. Magnetic perturbations of similar periods were also frequently observed at the CRESS satellite during substorms [*Erickson et al*., 2000] and were interpreted as a field line resonance (FLR) signature arising from the passage of the WTS over the satellite. In our event, the WTS did not pass GOES-10 because, if it had, magnetic dipolarization would have been seen on GOES-10. However, we have indicated that the WTS was detected by the magnetometer at Fort Smith, which is only ~0.6 MLT east of GOES-10. We suggest that when the head of the WTS was approaching GOES-10, a FLR was excited and led to the magnetic field Pc5 perturbations seen on GOES-10. Another possibility is that the ULF Pc5 waves were driven by drifting energetic particle fluxes via the drift and drift-bounce resonances [*Southwood and Kivelson*, 1982; *Yeoman and Wright*, 2001]. The source of the westward-drifting energized protons is likely to have been the substorm in the midnight sector. Energetic ions which were accelerated at the inner edge of the plasma sheet would have drifted westward and could have produced the Pc5 pulsations on the GOES-10 via the drift resonance interactions.

4.3 Discussion

A small substorm event has been described in detail, using optical, magnetic and radar observations. Most of the dynamic auroral and convection signatures occurred in the postmidnight sector. The associated convection pattern was quite different from that of substorms that begin in the dusk sector (e.g., *Bristow et al*. [2001]). In this section, we will discuss this event from three aspects, the energy budget of the substorm and the energy dissipation processes, the interpretation of the auroral observations in terms of DAB instabilities, and the Stage-2 EP.

4.3.1 "Loading-unloading" versus "directly driven" processes

First we will concentrate on the convection pattern changes and solar wind control of the substorm activity. The global convection pattern during a substorm usually contains two components: one is directly driven by the solar wind energy input and controls the overall large-scale convection reconfiguration, while the other is caused by the release of stored energy and contributes to the smaller-scale changes in the convection, usually limited to the nightside [*Kamide et al*., 1994]. As we have described above, the GEOTAIL observations revealed a prolonged dominant Bz+ and steady By+ IMF prior to the substorm onset, except for a southward excursion at 0645-0655 UT, and a "square-wave" IMF Bx-By structure at 0727-0735 UT. The IMF southward excursion led to enhanced coupling between the solar wind and magnetosphere, as indicated by the strong increases of the PCN index and cross-PC potential after 0706 UT. When the solar wind-magnetosphere coupling diminished, as shown by the significant drops in both the PCN index and cross-PC potential from 0718 UT to 0730 UT, there were some increases of nightside polar cap convection shown in Figure 4.17b which hint at energy buildup in the tail lobe, but the low plasma sheet convection and lack of auroral activity indicated that no significant energy had penetrated the near-Earth plasma sheet and been diverted into the auroral ionosphere at that stage. The reduction of the solar wind activation and dayside convection could have been favorable for the substorm EP onset triggering as suggested in the "convection reduction substorm model" [*Lyons et al*., 2003].

After the first pseudobreakup at 0732 UT, the nightside flows were enhanced. A small counterclockwise convection vortex appeared with a center around 72^0 MLAT and ~1 MLT, while the previous 2-cell pattern persisted in the dawn and dusk sectors. The increase of nightside convection and the appearance of the small near-midnight counterclockwise cell after a substorm EP onset have been previously reported by *Lu et al*. [1998] and *Kamide et al*. [1994], who postulated that they were signatures of the magnetotail energy release process. *Kamide and Kokubun* [1996] proposed that, during the substorm EP, such a near-midnight cell is added to the pre-existing 2-cell global convection pattern, representing an "unloading" versus a "directly driven" component of the auroral electrojet. These signatures were clearly shown by the SuperDARN

measurements in Figure 4.17c. However, this "unloading" process, which began at 0732 UT, did not evolve into a full-scale EP but instead led to two successive pseudobreakups, likely due to an insufficiency of stored energy in the tail and/or unfavorable ionospheric conditions [*Koskinen et al*., 1993].

As mentioned earlier, after the emergence of the near-midnight convection vortex, it progressed eastward. Surprisingly, by 0748 UT it had merged with the morning cell on the flank to form a large single postmidnight cell centered at ~2.3 MLT, as shown in Figure 4.17d. The distinction between the two components of the auroral electrojet then became vague. This combined convection cell had also expanded to lower latitude, implying that energy could readily penetrate into the near-Earth plasma sheet, and its "focus" was located more or less directly east of the intensified auroras. Thus an azimuthal SCW-like current system appears to have already begun to form by 0748-0750 UT, just before the effect of the IMF Bx-By structure began to impact the ionosphere and cause sharp rises of the cross-PC potential and PCN index after 0750 UT. This current system tended to divert the cross-tail current, paving the way for the expensive phase current disruption process in the near-Earth plasma sheet. Furthermore, the first two auroral activations had resulted in a considerable increase of the nightside ionospheric conductance. The third magnetospheric disturbance would thus have been greatly aided by the new energy input from the enhanced solar wind activation because the magnetotail/ionosphere system had been preconditioned so that the incoming energy could be readily coupled to and dissipated in the nightside auroral ionosphere. Therefore this preconditioned state led the system to respond to the following IMF Bx-By "square-wave" structure in "directly driven" fashion, causing the substorm EP onset at 0752 UT. Comparing Figure 4.17e to Figure 4.17d, we see that the postmidnight convection cell did not change much in shape but strongly intensified in magnitude, indicating there was no extra "unloading" component contributing to this particular substorm EP onset. After 0754 UT, Figure 4.11 shows that there was a change from southeast convection to more southward convection within the bright aurora region. The southward convection maps to the equatorial tail as an earthward flow. Though enhanced earthward flow is not necessary in the near-Earth initiation model for a substorm, it was found that following the local onset and establishment of the SCW,

such enhanced earthward flows may play an important role in maintaining the SCW, as described by global MHD simulations [e.g., *Birn et al*., 1999], which would help the onset to develop into a full-scale substorm EP in our event.

Evidence for "directly driven" substorm EP onsets has been uncommon. *Koskinen et al*. [1993] reported a pseudobreakup which lagged an IMF southward turning at the subsolar magnetopause by ~20 min. In our event, the delay between the EP onset and the IMF Bx-By structure at the magnetopause was only ~16 min. This is almost the least time required for the near-Earth tail to respond to the upstream solar wind variations [*Bargatze et al*., 1985]. We suggest that such a short time delay would not have been possible without the preconditioning of the magnetosphere/ionosphere system. This preconditioning would have facilitated SCW formation, as in our event.

4.3.2 Auroral intensification and DAB instability

In this section we will try to interpret the observed Pi2s and auroral intensifications in terms of successive "drift" waves in the near-geosynchronous-orbit plasma sheet (NGOPS) and the DAB instability. The DAB instability has long been considered to be one of the principal candidates for triggering the near-geosynchronous onset of substorms. In particular, the CRRES satellite observations [*Maynard et al*., 1996; *Erickson et al*., 2000] provided decisive evidence relating the DAB instability at NGOPS to the substorm EP onset. A brief introduction to the mechanism of DAB instability can be found in Chapter 1.4 (see Figure 1.9).

The evolution of azimuthally-spaced intensified patches during each Pi2 burst and auroral activation, as shown in Figures 4.14 to 4.16, provides evidence for the existence of such a drift wave instability in the NGOPS. In terms of the DAB theory, charge separation in the high-pressure region of the wave structure leads to an eastward polarization electric field, while in the low-pressure region, a westward electric field is produced. With the development of the instability and thus the alternating polarization electric fields, the drift wave may couple to the Alfven ballooning mode. Within a specific half-cycle of the drift wave which contains net eastward electric field (thus $\mathbf{J} \cdot \mathbf{E} < 0$, so this region is acting like a "generator"), the plasma kinetic energy is converted into the electromagnetic energy which flows toward ionosphere via Alfven

waves. Such a specific half-cycle of the drift wave is called a "trigger wave" [*Erickson et al.*, 2000].

We believe that the azimuthally-spaced structures observed by NASI were the ionospheric manifestation of such "trigger waves" and the energy deposition processes in the NGOPS. The energy is dissipated in the ionosphere mainly by Joule heating in the horizontal Pedersen currents. As we have mentioned above, the intensified patches were almost aligned with the electric field direction and thus with the Pedersen currents. When energy is released from the plasma during the eastward electric field excursion faster than the background convection energizes it, the cross-tail drift current is disrupted, and depolarization begins. The current disruption/dipolarization rapidly expands azimuthually, spanning several wavelengths in azimuth as compared to the initial "trigger wave" [*Lopez and Lui*, 1990; *Erickson et al.*, 2000]. The particle injection process associated with the dipolarization leads to enhanced precipitation at the inner edge of the plasma sheet within the longitudinal extent of the dipolarization region, which explains the overall expansion and diffusive enhancement of the auroral luminosity after several intensifications of an initially narrow patch. While the dipolarization proceeded, the ballooning waves and thus the discrete patches continued to grow and obviously propagated eastward. This is because that the drift wave is expected to exist near the boundary between the dipole-like field and tail-like field regions. Therefore, as a result of the progressive dipolarization, the waves move in the same sense as the dipolarization expansion, which was eastward in the postmidnight sector. During the substorm EP, the dipolarization and the drift wave also moved tailward, leading to the significant poleward expansion of the auroral brightening.

The initial pressure perturbation and thus the origin of the drift wave were in the midnight sector, as shown in Figure 4.20a. Then the perturbation expanded both eastward and westward but would have suffered increasing damping with longitudinal distance [*Roux et al.*, 1991; *Vetoulis and Chen*, 1994]. As the instability grew in the midnight sector, it reached the "trigger wave" threshold (Figure 4.20b), leading to the coupling of energy into the ionosphere, and the formation of the initial auroral patch in the midnight sector. Away from the midnight sector, the drift waves might have also grown into "trigger waves", but not until some time later (Figure 4.20c,d). According to

this scenario, the discrete auroral patches are expected to appear successively in the midnight sector and expand toward both the evening and morning sectors, until at some azimuthal extent the growing instability is canceled by damping. Such behavior is consistent with the *Elphinstone et al*. [1995] observations of the azimuthal evolution of AAFs. However, it should be noticed that in our NASI observations, only the postmidnight portion and the eastward expansion effect were observed.

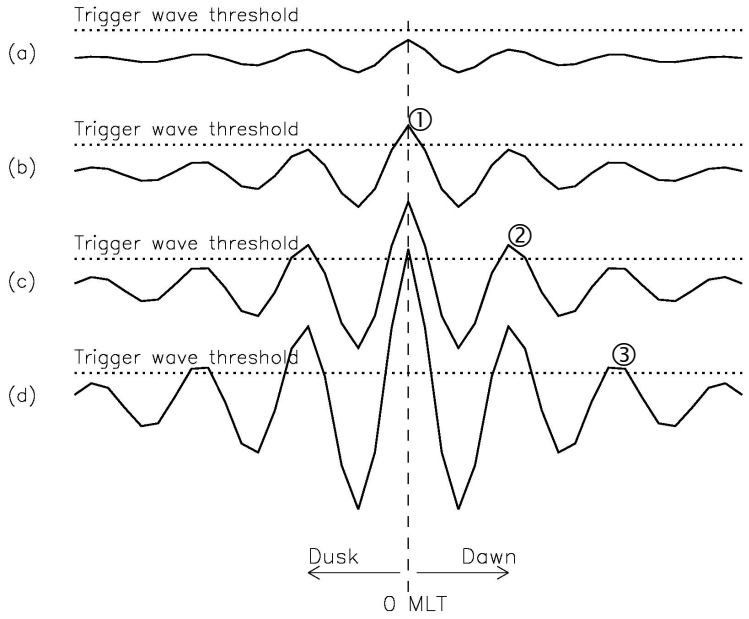

Figure 4.20 A schematic diagram explaining the successive appearance of discrete auroral patches, which correspond as a series of "trigger waves" at the NGOPS.

An important point is that the "trig ger wave" releases power toward the ionosphere during its eastward electric excursion, via incident Alfven waves. The Alfven waves incident upon the ionosphere are partially reflected because of an impedance mismatch between the ionosphere and magnetosphere, effectively causing a secondary Alfven wave to be launched from the ionosphere due to the disturbance of the ionospheric conductivities and electric fields. Such reflected secondary Alfven waves carry return power from the ionosphere to the magnetosphere. These bouncing Alfven waves establish the high-latitude Pi2 magnetic pulsations (40-150s) [*Olson*, 1999]. On the other hand, the electric field within the drift waves keeps oscillating at periods of 60-90

seconds [*Erickson et al*., 2000]. Such electric field oscillations may not be completely in phase with the bouncing Alfven waves (in phase means that there is only an incident wave into the ionosphere during a half cycle of the eastward electric field excursion and only a reflected Alfven wave from the ionosphere during the westward electric field excursion). In the actual situation, interference between the incident and the reflected Alfven waves may occur [*Maynard et al*., 1996]. Such interference may modify the waveform of the initial "trigger wave" and thus cause fine structure in the auroral patch. *Maynard et al*. [1996] reported that, in one of their events, they found that a substorm expansion was in progress when wave power returning from the ionosphere was observed at the CRRES satellite. However, the reflected Alfven waves were out of phase with the magnetospheric electric field oscillation, with the result that the substorm electrojet turned off momentarily until the wave power and the electric field oscillations retuned to the in-phase condition. Figure 4.15 shows that, during the second auroral activation interval, patch 3 (~225^0) temporarily faded at 0742:01 UT but was reactivated at 0742:42 UT, while at the same time the original patch 2 totally disappeared. We believe such sequences are similar to the observations of *Maynard et al.* [1996] and have the same physical explanation, that is, unfavorable (destructive) interference between the returning Alfven waves and the "trigger waves", leading to quenching of the latter waves.

An interesting feature shown in Figures 4.14 to 4.16 is that the discrete intensified patches are separated by greater and greater azimuthal distances as the event sequence proceeds. If we assume that the azimuthal distance between two adjacent discrete patches roughly equals the wavelength of the drift wave, then the wavelength seemed to become larger, as did the distances between each succeeding activation interval. The possible reason for such an increase is as follows. Since in our event the substorm development evolved in a multi-step fashion and there were successive dipolarizations of the NGOPS magnetic field after 0732 UT, which can be deduced from the GOES-8 observations in Figure 4.19, the particles became more and more energized at the NGOPS. Simple linear theory for drift waves predicates a wavelength between $v_{di}T/2$ and $v_{\mathrm{di}}T$, where v_{di} is the gradient-drift speed of ions and T is the wave period. If we assume the wave period was constant, the rise of the ion energy and thus the rise of

gradient-drift ion speed would cause the wavelength of the drift wave to increase, which would be seen in the ionosphere as an increasing azimuthal distance between the discrete intensified patches.

Due to the negative and positive charges in the dipole structure of the drift waves, the FACs associated with the DAB mode should be filamentary. *Hoffman et al*. [1994] found that, during the substorm EP, while there is sufficient net upward FAC for electrojet closure, the FACs are indeed very filamentary. Either sign of FAC can be encountered locally. Evidence showing these filamentary FAC structures and the increasing wavelength of the drift wave can be found from the delay time between the red-line (630 nm) and H_β blue-line (486.1 nm) peaks measured by the Gillam MSP in our event. Bin 7 of 630.0 nm and bin 6 of the 486.1 nm emission are chosen because they approximately measure the same latitude ($\sim 1^0$ poleward of the Gillam station). We shall associate the red-line and H_β blue-line emission with upward and downward FAC filaments, respectively, in the dipole structure of the drift waves. The red-line arises from the electron precipitation and is generally associated with upward FACs, and the blue-line from the proton emissions and downward FACs. Figure 4.21 shows, in the top panel, the intensity versus time of the two emission lines. The bottom panel is obtained by matching the five peaks in the red-line with the increasingly retarded peaks in the H_β blue-line. The fourth peak of each line is broad, and in particular it is difficult to assign a precise time to the 486.1 nm line, so the center of the flat-topped peak was chosen. It is clear that the red- and blue- line peaks occurred alternatively, with the red-line peaks preceding. Such a signature is consistent with the scenario of the passage of a series of eastward-propagating "trigger waves" over a fixed observation position on the ground. It is also interesting to note that there is almost a linear increase with time in the delay of the blue-line peaks with respect to the red-line peaks (the dotted line at 45° slope would be the line along which the peaks would occur if they were simultaneous), which implies that the negative and positive charges within the drift wave were becoming separated by greater and greater distances. The possible reason for such an increase is exactly the same one we used to explain the increasing azimuthal separation of the discrete intensified patches observed during each auroral activation, that is, the successive dipolarizations of the NGOPS magnetic field led to the particles becoming

more and more energized in the NGOPS. This may have two consequences: first, the negative and positive charges within the drift wave would be separated by increasingly greater distances; second, the eastward propagation of drift wave would be retarded by the enhanced westward ion gradient-drift speed. These two effects combine to cause the progressively greater time delay over the ground observation point between the passage of the upward FAC leg and the downward FAC leg within a "trig ger wave", or equivalently, an increasing delay between the red-line emissions and the H_β emissions.

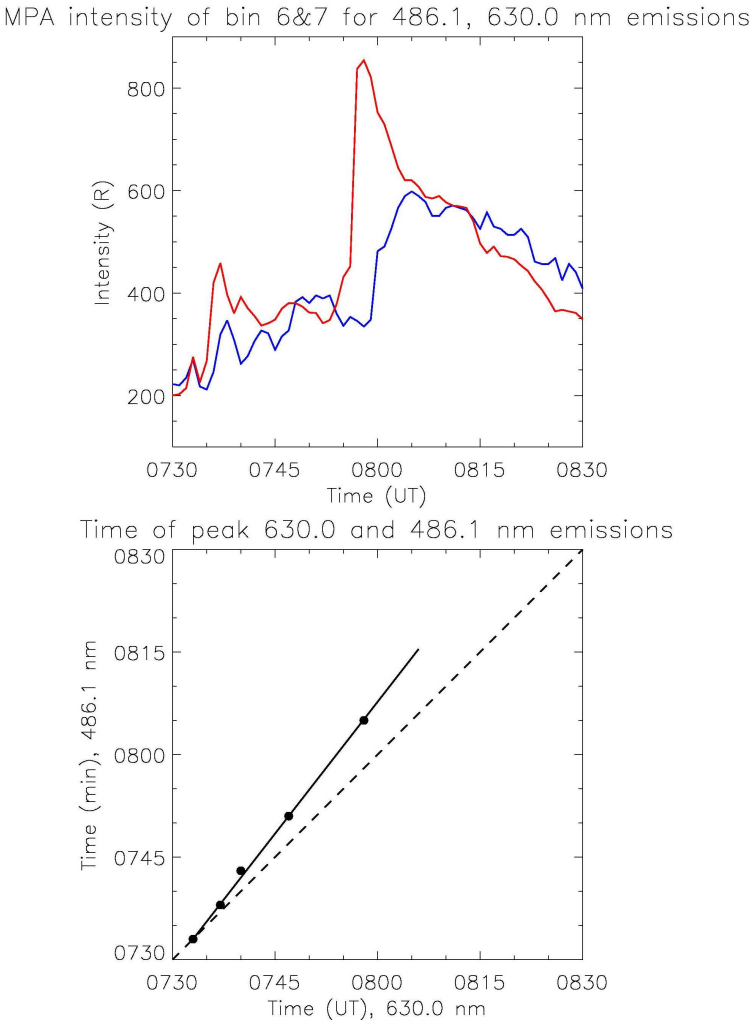

Figure 4.21 Top panel shows a plot of the Gillam MSP observations of red-line emissions (bin 7) and H emissions (bin 6) versus time, while the bottom panel shows the time delays between the red-line and H emission maxima.

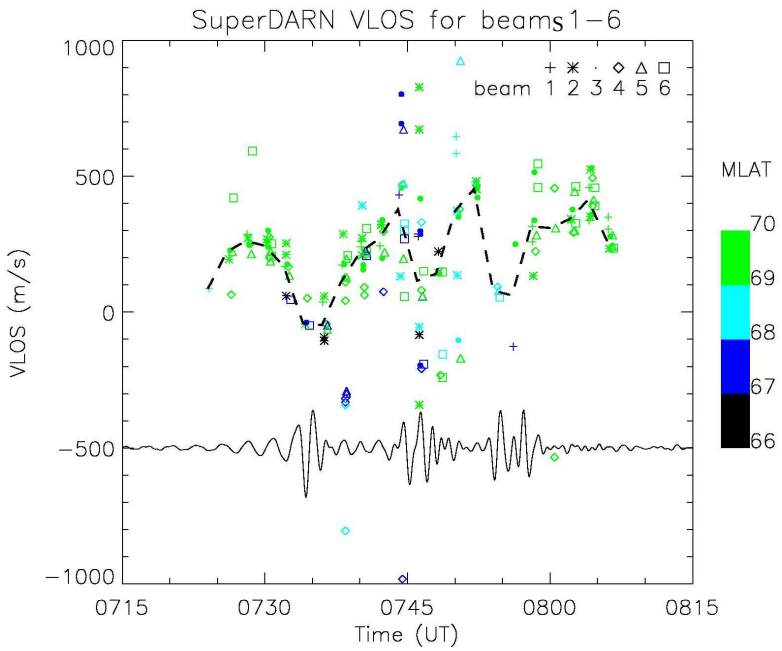

Figure 4.22 A plot of the Saskatoon radar VLOS on beams 1 to 6 and the Pi2 activity. The dashed line joins the median value (over the 6 beams) of the velocities observed during each 2-minute scan, in the magnetic latitude range 66 - 70°. Positive velocities denote westward electric field, while negative velocities denote eastward field.

Hints of the existence of the "trigger waves" can also be found in the radar observations. By its definition the trigger wave should contain an eastward polarization electric field which may overwhelm the background westward electric field in the plasma sheet. The eastward electric field should also map to the ionosphere and lead to convective plasma flows. However, the oscillating polarization electric field $\delta\mathbf{E}$ associated with the drift waves was found to have a typical oscillation period of 60-90 seconds and was spatially confined, according to the CRRES observations [*Maynard et al.*, 1996; *Erickson et al.*, 2000]. This electric field would produce very little effect on the fitted convection maps (such as in Figures 4.9 to Figure 4.12), which are averaged both in time and space in a 2-minute scan by the FIT procedure (see the description in Chapter 2.1). Therefore the convection map should show mainly the ambient electric field. However, the VLOS observations from individual beams may be useful for achieving more time resolution, because the time interval between adjacent beams is 7 seconds. The SuperDARN VLOS values for the Saskatoon radar were plotted in Figure

4.22 for beams 1 through 6. Magnetic north is about midway between beams 3 and 4, so the 6 beam directions are no more than ~10^0 from magnetic north (recall that the beams are ~3.24° apart) at latitudes <70^0 MLAT. Care was taken to exclude *E* region echoes by using the Saskatoon radar elevation angle observations obtained from the interferometer mode. The Rabbit Lake magnetometer is selected for the plot of Pi2 bursts because it is located near the center of the chosen radar beams. Different symbols are used for data from each of the beams. In effect, the Doppler VLOS so measured is roughly the magnetic north-south component of the convection velocity. A positive VLOS value indicates that the flow is towards the radar and thus associated with westward electric field, while a negative VLOS value indicates that the flow is away from the radar and thus associated with an eastward electric field. For this analysis, the data were deliberately limited to the range cells at the lower latitudes roughly where the Pi2 pulsations occurred. There were not many radar echoes in this region and there is some spread in the data, but a clear trend can be seen. While the overall VLOS was dominantly positive, implying a westward electric field, some negative VLOS appeared within the development of each Pi2 burst. In order to better illustrate this trend, the median value of all the Doppler velocities for each two-minute scan was determined, and these median values were joined by a dashed line. The plot shows that, the median VLOS values exhibit three clear minima which exactly correspond to the three maxima of the Pi2 wave trains. There is an obvious tendency toward eastward electric fields at the time of each Pi2 pulsations. Since the Pi2s were the manifestation of the bouncing Alfven waves, we can conclude that such bouncing Alfven waves and the related energy transfer between the magnetosphere and the ionosphere are closely associated with an eastward turning of the magnetospheric electric field. This result is totally consistent with the CRRES observations that eastward electric field excursions inside the "trigger waves" lead to substorm expansions [*Erickson et al*., 2000].

4.3.3 Stage-2 EP

As mentioned previously, about 10 minutes after the onset of auroral breakup at 0752 UT, there was a second-stage auroral brightening. As one may notice from the third panel of Figure 4.13, there was a second rise of emission intensity staring at 0802

UT, although this second maximum did not quite reach the values of the main maximum. It should be noted that this second optical auroral brightening occurred at the same time as the second magnetometer negative X bay and Pi2 burst at Eskimo Point. The 10-minute delay between the first and second intense auroral brightenings, as well as the magnetic bays and Pi2s at Eskimo Point, are strongly suggestive of two expansive phases of the substorm.

The Stage-2 EP, however, is significantly different from the previous three intensifications. As seen in Figure 4.13, the maximum auroral activation of the Stage-2 EP remains located at -33^0 MLON, which is roughly the same longitude where the Stage-1 auroral brightening maximized and finally settled. This stable location is in contrast to the near-midnight origin and eastward evolution shown in the previous three intensifications. The other interesting feature is that, for the convection enhancement associated with the Stage-2 EP, no corresponding intensification could be found in either the PCN index or the solar wind. The convection enhancement was restricted to the nightside as shown in Figure 4.17f, and occurred almost simultaneously with the Stage-2 auroral brightening as shown in Figure 4.18. Thus the Stage-2 EP is very likely to have been associated with an internal magnetotail process only. On the other hand, Figure 4.12 shows that just before and during the Stage-2 auroral brightening, the flow pattern through the bright patch is nearly equatorward. The equatorward flow extends well poleward of the bright patch. All these features are very consistent with the Stage-2 EP mechanism suggested by *Erickson et al*. [2000]. Their suggestion is that, after the Stage-1 EP, the cross-tail current disruption in the near-Earth plasma sheet produces a tailward-traveling rarefaction wave. The rarefaction wave may induce a collapse of the stretched field lines in the mid-tail plasma sheet, and reconnection is the natural consequence of that collapse. That reconnection would generate the earthward flow bursts that showed up as the observed extended band of equatorward ionospheric flow enhancement, and resulted in the second stage of substorm expansion (see Chapter 3). As the successor to the Stage-1 EP, the second activation resumed roughly at the latitudes that the previous expansion had already reached. Thus the magnetic effect of the Stage-2 EP was clearly seen at Eskimo Point (71.2° MLAT) but was not clear at lower latitude stations. Also, since both the tailward-propagating rarefaction wave and

the enhanced earthward flows propagate mainly radially, it is also reasonable that the Stage-2 auroral brightening would occur at nearly the same azimuthal region where the Stage-1 brightening maximized.

4.4 Conclusion

In this chapter, the two-dimensional ionospheric structure of an October 9, 2000 substorm has been studied using optical images and radar maps, and associated magnetometer, riometer and MSP data. Although this substorm was not a strong one, with the IMF being dominantly northward, the sequence of events was clearly defined and quite comprehensive in terms of the processes involved. We advocate that there is a definite advantage to the study of a weaker substorm, namely that the signatures from the observations are clear and clean, unlike some of the very complex optical and flow patterns that occur during the more energetic substorms.

The two-dimensional auroral and convection dynamics that emerges in this event can be summarized as follows.

(a) A sequence of three magnetic perturbations, Pi2 bursts and accompanying optical intensifications was found during the event. The first two activations were characteristic of pseudobreakups, while the last and strongest activation corresponded to a substorm EP. All three activations originated close to midnight, but evolved progressively eastward. Most of the dynamic auroral and convection signatures were observed in the postmidnight sector.

(b) We found the enhancement of nightside convection and the appearance of a near-midnight counterclockwise convection vortex after first pseudobreakup as the signature of the tail "unloading" process [*Kamide and Kokubun*, 1996], but also indicated that the evolution of nightside convection and the previous auroral activations might have so preconditioned the magnetosphere/ionosphere as to result in a "directly driven" substorm EP.

(c) We showed that the auroral activations could be related directly to the development of drift waves and DAB instabilities in the NGOPS. The azimuthally-spaced auroral patches observed by the NASI during each of the auroral activation were the manifestation of the drift wave structures in the NGOPS. The SuperDARN line-of-

sight velocity (VLOS) measurements revealed the development of eastward electric fields within each Pi2 burst interval, which is consistent with the CRRES observations that the growing eastward electric field inside a "trig ger wave" leads to a substorm EP [*Erickson et al*., 2000].

(d) There is a second-stage magnetic bay and optical auroral brightening observed about 10 minutes after the substorm EP onset. This second-stage auroral brightening, as well as the accompanying convection enhancement characterized by dominantly southward flows across the bright aurora region, is consistent with the Stage-2 EP process suggested by *Erickson et al*. [2000].

Chapter 5

Comparison between ionospheric convection vortices and the associated equivalent currents

In this chapter we present a study comparing ionospheric convection patterns and the associated equivalent current patterns. The ionospheric equivalent current is derived by the spherical cap harmonic analysis (SCHA) method [*Haines*, 1985], using as input the magnetic data from the CANOPUS, MACCS, and NRCAN/GSC magnetometer stations. The equivalent current is the effective Hall current, which is directed in the opposite direction to the "effective" $\mathbf{E}\times\mathbf{B}$ convection. The equivalent convection (EQC) pattern can be derived and then compared with the SuperDARN convection (SDC) map obtained from the HF radar measurements. In particular, we have selected for this comparison an important particular type of convection structure, namely a convection vortex. There are two main reasons for studying these vortices. First of all, such vortex structures, either counterclockwise or clockwise, are directly related with the FAC and thus the magnetosphere-ionosphere coupling process. Secondly, such a vortex structure can occur in a spatially localized observation region which is within the FoV of a SuperDARN radar pair and for which there is good data from both radars, allowing for a detailed comparison of the magnetometer and radar results. Four SDC vortex events are studied in this chapter. The first is a clockwise convection vortex in the dusk sector; the second and third events are clockwise vortexes in the dawn sector; the fourth is a near-noon event containing both clockwise and counterclockwise vortices. Some possible mechanisms causing differences between the EQC and SDC patterns are

discussed. In particular, we have found that the disagreement between the EQC and SDC patterns can be substantial for a counterclockwise convection vortex, and that there is a consistent pattern for the discrepancy. We suggest that such a discrepancy may result from the relationship between the downward FAC and the ionospheric Pedersen conductance.

5.1 Review of some previous studies

High-latitude ionospheric plasma convection and electric fields can be monitored directly by a coherent or incoherent radar, while the ionospheric equivalent current pattern can be derived from ground-based magnetometer observations by either simply rotating the magnetic field perturbations 90^{o} clockwise, or by a more complicated upward continuation procedure such as SCHA algorithm [*Haines*, 1985; 1988]. During and after the International Magnetospheric Study (IMS, 1976-1979), several methods were developed to obtain the ionospheric electrodynamic parameters over the entire high-latitude region through the utilization of ground-based magnetic field observations (comprehensive reviews can be found in *Glassmeier* [1987] and *Untiedt and Baumjohann* [1993]). Those methods can be roughly distinguished into two categories.

The first approach, such as the Kamide-Richmond-Matsushita (KRM) algorithm [*Kamide et al.*, 1981] and its improved version, the Assimilative Mapping of Ionospheric Electrodynamics (AMIE) technique [*Richmond and Kamide*, 1988; *Richmond*, 1992], applies a statistical model of ionospheric conductance to estimate the true three-dimensional ionospheric current system and the convection pattern from the equivalent current. The AMIE technique is advantageous because it uses other measurements, e. g., satellite observations of the energy fluxes of precipitating particles, and/or auroral image data, to calibrate the conductance model. The AMIE technique has been successfully applied to the study of the large-scale steady ionospheric convection pattern [*Ridley et al.*, 1998] as well as to substorm-related dynamic processes [*Kamide et al.*, 1994; *Lu et al.*, 1998]. However, because the supplementary data sets are sometimes sparse and their use can be somewhat indirect (for example, the empirical formulas in *Robinson et al.* [1987] are required to relate the conductance to the

precipitating energy flux), uncertainties in the specification of the ionospheric conductances may persist and affect the accuracy of the solutions.

The second approach combines the two-dimensional electric field measurements from radars and the equivalent currents from magnetometers to derive both the true ionospheric current system and the conductance distribution [*Baumjohann et al*., 1981; *Untiedt and Baumjohann*, 1993; *Amm*, 1998]. As we will prove in section 5.4, even though one can measure both the two-dimensional equivalent currents and the electric fields, it nevertheless is still impossible to solve the true ionospheric current system unambiguously. Some other assumptions are required. For example, in the Untiedt algorithm [*Untiedt and Baumjohann*, 1993] and the method of characteristics [*Amm*, 1998], the ratio between the Hall and Pedersen conductances ($\alpha = \Sigma_H / \Sigma_P$) is assumed to be known over the region of interest. A second example applies in the "trial and error" approach, in which a parameterized model for the Hall and Pedersen conductances is used [*Baumjohann et al*., 1981].

Another direction of research, which is also the objective of the study in this chapter, is to compare the radar-measured convection and the magnetometer-derived EQC pattern, and to explore the possible reasons for the discrepancies between them. *Huang et al*. [2000] showed that the agreement between the SDC and the EQC pattern is fairly good between 1200-1500 MLT but becomes worse near 1800 MLT, when large conductivity gradients due to the day-night differences in photoionization rates are expected. One work of particular relevance to the study in this chapter was done by *Lyatsky et al*. [1999], who studied several clockwise SDC vortex events and their associated EQC patterns in the dayside winter ionosphere. Some general agreement between the SDC and EQC patterns was found. At the very least, the vortex structures are usually maintained in the equivalent current pattern. However, the EQC vortices were found to be shifted equatorward compared to the convection vortices. Such a shift was explained in terms of the effect of secondary interhemispheric FACs near the "terminator" that separates regions of sunlit, highly conducting ionosphere from dark, poorly conducting ionosphere [*Benkevitch and Lyatsky*, 2000a; *Benkevitch et al*., 2000b]. No counterclockwise convection vortex event was presented in *Lyatsky et al*. [1999].

5.2 Magnetic data processing procedures

To derive the equivalent current pattern from the ground-based magnetic observations, several data preprocessing procedures must be applied. These include: (a) the separation of current sources that contribute to the observed magnetic field; (b) the interpolation/extrapolation of data; (c) the upward continuation which relates the ground magnetic deviation to the currents at ionospheric height. Each of the above three procedures is discussed below.

5.2.1 Separation of the current sources

The magnetic fields observed on the ground result from many different sources, both internal and external to the earth, with the latter including ionospheric and magnetospheric sources. Roughly, the major contributions to the overall magnetic field are from: (1) the main geomagnetic field $\mathbf{B}_m$, which has a long-term variation; (2) fields $\mathbf{B}_e$ generated by the ionospheric currents, the main system required for our derivation of the equivalent current; (3) fields $\mathbf{B}_{ring}$ generated by the ring currents; (4) the fields $\mathbf{B}_{pul}$ arising from magnetic pulsations and other short-period disturbances; (5) the fields $\mathbf{B}_i$ generated by the induced currents in the Earth's crust and the upper mantle in response to external sources. The total field can thus be written as the following sum:

$$\mathbf{B}(r,t)=\mathbf{B}_m + \mathbf{B}_{eq} + \mathbf{B}_{ring} + \mathbf{B}_{pul} + \mathbf{B}_i \quad . \tag{5.1}$$

The main field (baseline) removal is vital for the study of the magnetic perturbations caused by auroral ionospheric currents. Usually the baseline is determined as the mean value of a selected extremely quiet nighttime interval which occurred close to the observation time. Magnetic pulsations usually have periods less than several minutes and hence can be removed numerically by a low pass filter or an averaging process. The ring current fields generally vary slowly and their symmetrical part can be modelled by the single zonal spherical harmonics $P_1^0(\cos\theta)$ [*Banks*, 1981]. Assuming the induced field is ~28% of the total disturbance, the horizontal and vertical magnetic field components, in magnetic dipole coordinates associated with the ring currents, are estimated as [*Walker et al*., 1997]

$$X(\theta) \approx Dst \cdot \sin\theta$$
$$Z(\theta) \approx -0.15 \cdot Dst \cdot \cos\theta \qquad (5.2)$$

where θ is the eccentric dipole colatitude of the observation point, and *Dst* is the magnetic index describing the ring current field on the Earth's magnetic equator.

In equation (5.1) the *Sq* (solar quiet mean) current system, which is driven by thermospheric winds, does not appear explicitly. Its effect, however, actually does appear in both the magnetometer measurements and in the radar measurements of the electric field. The *Sq* current system is usually smaller and more slow-varying than the auroral and polar cap current systems. Since the *Sq* current flows at exactly the same heights where the auroral and polar cap currents flow, the *Sq* system simply becomes a part of the equivalent current system. On the other hand, the electric fields generated by the motion of thermospheric neutral wind at ionospheric *E* region heights (the so-called "atmospheric motor effect") will also map to the *F* region and combine with the electric fields of magnetospheric origin. Therefore, the *Sq* effect is effectively included in the convection measurements of SuperDARN. Hence, for the purpose of comparing the equivalent convection and the true plasma convection, the contribution of the *Sq* current system is implicitly contained in both measurements.

The ionospheric (external) current will also produce induced current inside the Earth. The separation of such induced (internal) current is not easy. The SCHA method, which will be introduced in the following section, can be used to implement such a separation of external and internal sources, as well as the interpolation/ extrapolation and upward continuation for the ground-based magnetic observations.

5.2.2 SCHA method

The magnetometer distribution is often sparse and confined to several particular regions, so that proper interpolation/extrapolation procedures are required at intermediate locations. On the other hand, the relationship between the equivalent currents at ionospheric *E* region heights and the magnetic deviations on the ground must be found (the so-called "upward continuation"), which is not simple in a spherical geometry. A method for dealing with these difficulties is provided by the spherical cap harmonics

analysis (SCHA) technique [*Haines*, 1985; 1988]. We now give a brief introduction to the method in this section.

The magnetic field between the Earth's surface and the ionosphere is essentially curl-free and can be represented by a scalar potential function. In SCHA the magnetic potential V is modelled as follows:

$$\begin{aligned} V(r,\theta,\varphi) = R_e \sum_{k=1}^{K_e}\sum_{m=0}^{m_e}\left(\frac{r}{R_e}\right)^{n_k(m)} P^m_{n_k(m)}(\cos\theta)\left[g_k^{m,e}\cos(m\varphi) + h_k^{m,e}\sin(m\varphi)\right] \\ + R_e \sum_{k=1}^{K_i}\sum_{m=0}^{m_i}\left(\frac{R_e}{r}\right)^{n_k(m)+1} P^m_{n_k(m)}(\cos\theta)\left[g_k^{m,i}\cos(m\varphi) + h_k^{m,i}\sin(m\varphi)\right] \quad , \end{aligned} \tag{5.3}$$

where $K_{e,i}$, $M_{e,i}$ are the maximum external/internal order and degree of the SCHA method, respectively, and where m_e=min(k,M_e) and m$_i$=min(k,M_i) permit different order and degree for the anisotropic modeling (usually $K_{e,i} > M_{e,i}$ since the auroral current systems are known to extend zonally several times more than latitudinally). Note that the superscripts/subscripts *e* and *i* are added solely to distinguish between the external and internal sources. The noticeable feature of the SCHA is that its basis function is the associated Legendre function of nonintegral degree $n_k(m)$, instead of the integer degree used in ordinary spherical harmonic analysis (SHA). The definition of the associated Legendre functions which may have a nonintegral degree n is given by *Hobson* [1931] and *Haines* [1985],

$$P_n^m(\cos\theta) = K_n^m \cdot \sin^m\theta \; {}_2F_1\left(m-n, m+n+1; m+1; \frac{1-\cos\theta}{2}\right) \quad , \tag{5.4}$$

where ${}_2F_1(a,b;c;z)$ is the Gauss hypergeometric function and K_n^m is the normalization factor. When equation (5.4) was first proposed by *Hobson* [1931], the Neuman-normalization was used. However, in geophysics the Schmidt-normalization is usually applied, so that:

$$K_n^m = \begin{cases} 1 & m = 0 \\ \dfrac{\sqrt{2}}{2^m \Gamma(m+1)} \left[\dfrac{\Gamma(n+m+1)}{\Gamma(n-m+1)} \right]^{1/2} & m \neq 0 \end{cases} , \tag{5.5}$$

where $\Gamma(x)$ is the Gamma function. The degrees $n_k(m)$ in equation (5.3) are determined by the boundary conditions,

$$\begin{aligned} & P^m_{n_k(m)}(\cos\theta_0) = 0 && \text{for } k\text{-}m \text{ odd} \\ & \left. \frac{dP^m_{n_k(m)}(\cos\theta)}{d\theta} \right|_{\theta=\theta_0} = 0 && \text{for } k\text{-}m \text{ even} \end{aligned} , \tag{5.6}$$

where θ_0 is the colatitude half-angle, which defines the boundary of the spherical cap. Note that the SCHA analysis can be performed on any localized data set by rotation of the pole and selection of the colatitude half-angle. Table 3.1 gives the $n_k(m)$ calculated from equation (5.6) for different sets of k and m. The coefficients in equation (5.3) are determined by fitting $\mathbf{B} = -\nabla V$ to the observed magnetic field components X, Y and Z, where:

$$\begin{aligned} X(r,\theta,\varphi) = & \sum_{k=1}^{K_e} \sum_{M=0}^{m_e} \left(\frac{r}{R_e} \right)^{n_k(m)-1} \frac{dP^m_{n_k(m)}(\cos\theta)}{d\theta} \cdot \left[g_k^{m_e} \cos(m\varphi) + h_k^{m_e} \sin(m\varphi) \right] + \\ & \sum_{k=1}^{K_i} \sum_{M=0}^{m_i} \left(\frac{R_e}{r} \right)^{n_k(m)+2} \frac{dP^m_{n_k(m)}(\cos\theta)}{d\theta} \cdot \left[g_k^{m_i} \cos(m\varphi) + h_k^{m_e} \sin(m\varphi) \right] , \end{aligned} \tag{5.7}$$

$$\begin{aligned} Y(r,\theta,\varphi) = & \sum_{k=1}^{K_e} \sum_{M=0}^{m_e} \left(\frac{r}{R_e} \right)^{n_k(m)-1} \frac{mP^m_{n_k(m)}(\cos\theta)}{\sin\theta} \cdot \left[g_k^{m_e} \sin(m\varphi) - h_k^{m_e} \cos(m\varphi) \right] + \\ & \sum_{k=1}^{K_i} \sum_{M=0}^{m_i} \left(\frac{R_e}{r} \right)^{n_k(m)+2} \frac{mP^m_{n_k(m)}(\cos\theta)}{\sin\theta} \cdot \left[g_k^{m_i} \sin(m\varphi) - h_k^{m_e} \cos(m\varphi) \right] , \end{aligned} \tag{5.8}$$

$$\begin{aligned} Z(r,\theta,\varphi) = & \sum_{k=1}^{K_e} \sum_{M=0}^{m_e} \left(\frac{r}{R_e} \right)^{n_k(m)-1} n_k(m) P^m_{n_k(m)}(\cos\theta) \cdot \left[g_k^{m_e} \cos(m\varphi) + h_k^{m_e} \sin(m\varphi) \right] - \\ & \sum_{k=0}^{K_i} \sum_{M=0}^{m_i} \left(\frac{R_e}{r} \right)^{n_k(m)+2} \left[n_k(m)+1 \right] \cdot P^m_{n_k(m)}(\cos\theta) \left[g_k^{m_i} \cos(m\varphi) + h_k^{m_e} \sin(m\varphi) \right] . \end{aligned} \tag{5.9}$$

Table 5.1 Nonintegral degree $n_k(m)$ for colatitude half-angle $\theta_0 = 14^0$

k\m	0	1	2	3	4	5	6	7	8	9	10
0	0.00										
1	9.34	7.08									
2	15.19	15.19	12.07								
3	22.09	21.33	20.55	16.80							
4	28.22	28.22	26.97	25.67	21.40						
5	34.91	34.44	33.97	32.35	30.64	25.93					
6	41.14	41.14	40.32	39.48	37.56	35.51	30.41				
7	47.76	47.41	47.07	45.97	44.84	42.65	40.31	34.85			
8	54.03	54.03	53.42	52.79	51.46	50.08	47.66	45.05	39.27		
9	60.60	60.33	60.06	59.22	58.37	56.82	55.22	52.59	49.75	43.66	
10	66.91	66.91	66.42	65.92	64.88	63.82	62.08	60.29	57.46	54.40	48.03

The best spatial wavelength resolution for SCHA is determined by the highest degree $n_k(m)$, because $\lambda \sim 2\pi R_e / n_k(m)$. For example, to investigate a structure with scale size ~6^0 in latitude, the highest degree $n_k(m)$ of the spherical harmonics should be at least ~60. In accordance with Table 5.1, the maximum order and degree of the SCHA procedure can be chosen as K_e=10 and M_e=7. One important fact to note is that $n_k(m)$ is always much larger than k, which results in higher spatial resolution for small-scale structures than the resolution of the ordinary SHA technique with the same number of coefficients. Another advantage is that no other unsampled data outside the spherical cap is needed so it is good enough to select the half-angle θ_0 to be 1-2^0 larger than demanded by the data point coverage or the desired region of interest.

We can also obtain the ionospheric equivalent current potential ψ_{eq} (see the definition in Appendix B.3) and the equivalent current vectors from equation (5.3) [*Haines and Torta*, 1994],

$$\psi_{eq}(\theta,\varphi) = -\frac{R_e}{\mu_0}\sum_{k=1}^{K_e}\sum_{m=0}^{m_e}\frac{2n_k(m)+1}{n_k(m)+1}\left(\frac{R_I}{R_e}\right)^{n_k(m)} P^m_{n_k(m)}(\cos\theta)\left[g_k^{m,e}\cos(m\varphi) + h_k^{m,e}\sin(m\varphi)\right], \quad (5.10)$$

$$J^X_{eq}(\theta,\varphi) = \frac{1}{\mu_0}\sum_{k=1}^{K_e}\sum_{m=0}^{m_e}\frac{2n_k(m)+1}{n_k(m)+1}\left(\frac{R_I}{R_e}\right)^{n_k(m)-1}\cdot\frac{mP^m_{n_k(m)}(\cos\theta)}{\sin\theta}\left[h_k^{m,e}\cos(m\varphi) - g_k^{m,e}\sin(m\varphi)\right],$$

$$J_{eq}^{Y}(\theta,\varphi)=\frac{1}{\mu_0}\sum_{k=1}^{K_e}\sum_{m=0}^{m_e}\frac{2n_k(m)+1}{n_k(m)+1}\left(\frac{R_I}{R_e}\right)^{n_k(m)-1}\cdot\frac{dP_{n_k(m)}^{m}(\cos\theta)}{d\theta}\left[g_k^{m,e}\cos(m\varphi)+h_k^{m,e}\sin(m\varphi)\right], \tag{5.11}$$

where $R_I = R_E$ + 110 km is the assumed height at which the current shell is located and the Hall conductivity typically peaks. In case of large $n_k(m)$, neglecting the contribution of induced current sources, we have the simple form,

$$\mathbf{J}_{eq}\approx\frac{2}{\mu_0}\mathbf{B}_{\perp}\times\hat{\mathbf{e}}_{\mathbf{r}} \quad , \tag{5.12}$$

where $\mathbf{B}_{\perp}$ is the horizontal component of the ground magnetic deviations associated with the equivalent current. Some simplified approaches just use the 90^0 clockwise rotation of the horizontal magnetic vector as the equivalent current, i. e., they skip the upward continuation procedure. However, we see from equation (5.11) that those approaches will introduce considerable error, for smaller $n_k(m)$, which corresponds to a long wavelength structure. On the other hand, although the contribution of induced current sources is generally less than one-quarter of the total magnetic deviation, it is still not quite negligible.

Though SCHA requires substantially fewer coefficients to obtain a satisfactory spatial resolution than SHA, we still often encounter the conflict between a sparse magnetometer distribution and the high spatial resolution that is desired. According to Equations (5.7)-(5.9), we know that the number of coefficients needed is

$$\begin{aligned} N_{coff} &= (M_e+1)(M_e+2)-K_e-2+2\cdot(K_e-M_e)(M_e+1)+ \\ &\quad (M_i+1)(M_i+2)-K_i-1+2\cdot(K_i-M_i)(M_i+1) \quad , \end{aligned} \tag{5.13}$$

whereas the actual number of available observations N_{obs} is just triple the number of stations. The difficulty can be solved partly by optimizing the degree and the order of the models for the external and for the internal sources. For example, the induced current sources generally flow in the crust and upper mantle and are probably not as

structured as the external currents, so they may be modelled with somewhat lower degree and order. On the other hand, the standard SCHA routines generally use a stepwise multiple regression analysis which has the facility for both entering and removing variables at each step according to given different *F*-levels of statistical significance [*Haines*, 1988]. The regression can be done by the numerical order of the variables or by the order of the variables that contribute most to the regression. In the following analysis the latter method is used. We stop the regression when N_{coff} is less than half of N_{obs} so that we have enough degrees of freedom for the subsequent least-squares fitting. We have found that such an algorithm provides a good compromise between the spatial resolution and the reliability of the modelling (which is related to the number of observations), and that the modelling solution does not seem to be very sensitive to the selection of model order $K_{e,i}$ and $M_{e,i}$.

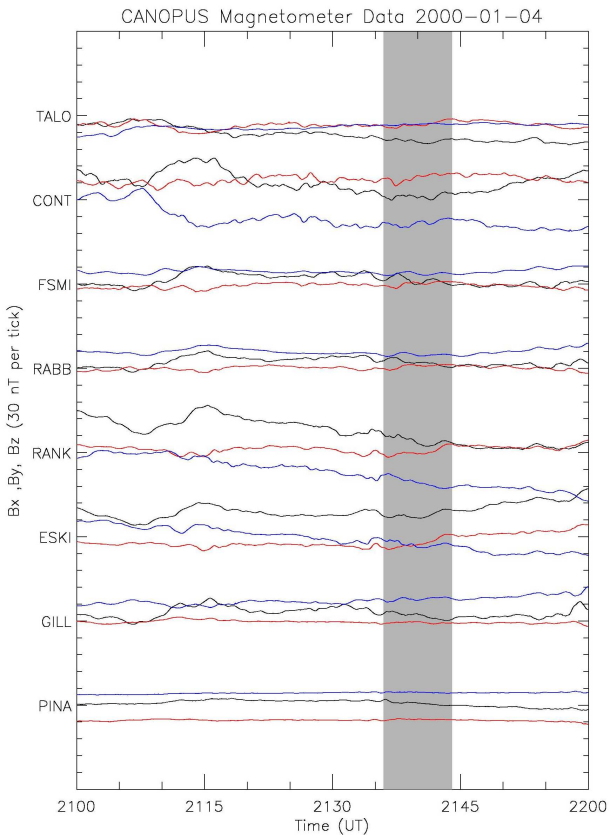

Figure 5.1 Stackplot of CANOPUS magnetometer data from 2100 to 2200 UT on January 4, 2000. Black, red and blue lines denote the X, Y, and Z components of the magnetic field. The gray band indicates the time interval of interest.

5.3 Four case studies

5.3.1 Event on January 4, 2000

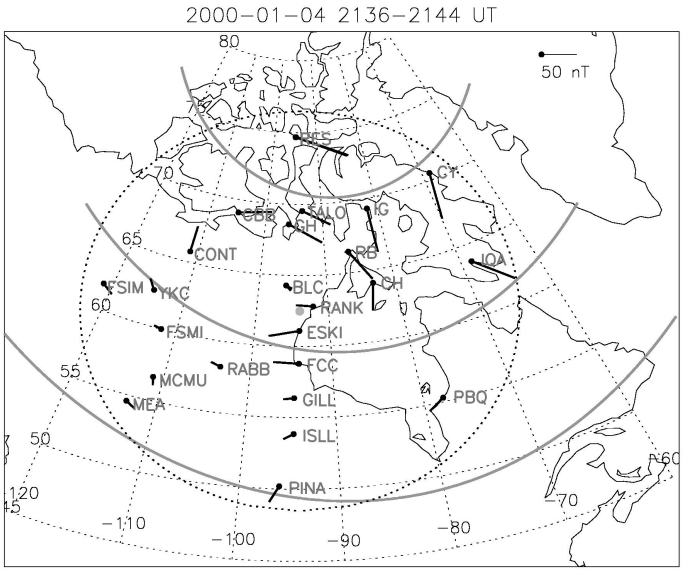

Figure 5.2 Geographical map showing all the available magnetometer observations during the interval 2136-2144 UT, January 4, 2000. The magnetic deviation observed at each station is averaged during the event interval and rotated by 90^0 counterclockwise. The gray dot and the dotted circle indicate the center point and the colatitude half-angle of the SCHA procedure. AACGM latitudes 60º , 70º, and 80º are shown in gray lines.

The first event we analyze occurred during the interval 2136-2144 UT, January, 04, 2000. Figure 5.1 gives the raw magnetometer data from several CANOPUS stations during the interval 2100-2200 UT. Figure 5.2 shows all the available magnetometers used in the analysis of the event (see section 2.2 and Tables 2.2 to 2.4 in Chapter 2). The magnetic deviation from each station is averaged during the event interval. The horizontal component of the magnetic field deviation is rotated by 90^0 counterclockwise to represent the convection vector. First, notice that this is only a weak geomagnetic disturbance interval, since the magnetic deviations at all stations are less than 100 nT. The data coverage is from stations approximately extending from 50^0 N to 75^0 N in latitude and from 65^0 W to 115^0 W in longitude in geographic coordinates. Therefore we choose the midpoint for the SCHA to be located at 62.5^0 N latitude, 94^0 W longitude

(shown in Figure 5.2 as a gray dot), and we choose the colatitude half-angle θ_0 to be 14^0 (shown in Figure 5.2 as a dotted circle).

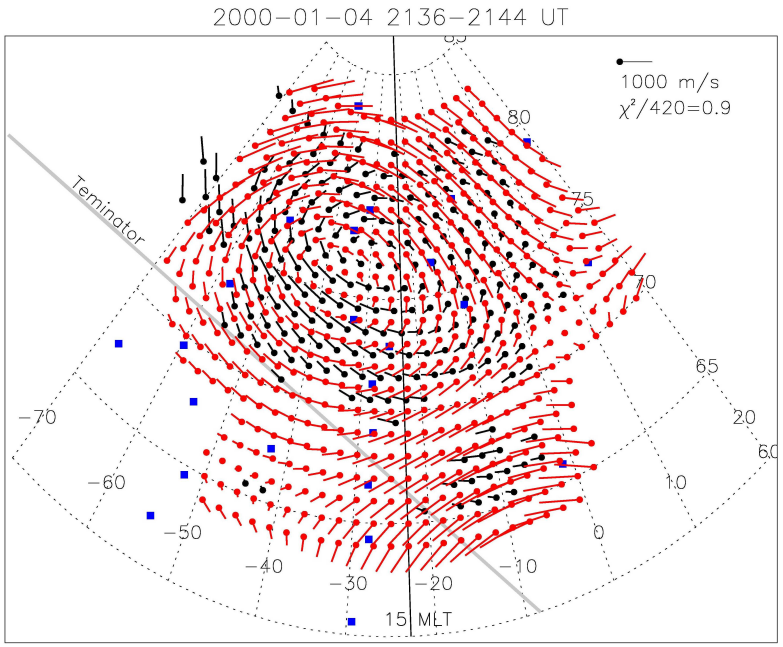

Figure 5.3 Equivalent convection (EQC, shown in red) and SuperDARN-observed convection (SDC, shown in black). The blue squares indicate the position of magnetometers. The gray line indicates the "terminator". An equivalent Hall conductance of 1.8 S was used.

The equivalent convection derived from the above magnetometer observations and the SCHA method is shown in Figure 5.3 by the red arrows, while the SuperDARN-observed convection (SDC) obtained from Saskatoon-Kapuskasing radar pair measurements and the map_potential procedure [*Ruohoniemi and* Baker, 1998] is shown by the black arrows. This event is an afternoon event, and the 15 MLT meridional line is given in Figure 5.3. The blue squares indicate the sites of the magnetometer observations. The gray line in the map indicates the "terminator", which is defined as the line where the solar zenith angle is 90^0 and thus separates the "dark" (northeastern side) and the "sunlit" (southwestern side) regions. The EQC shown in Figure 5.3 is defined as

$$\mathbf{V}_{eq} = -\frac{\mathbf{J}_{eq}}{\tilde{\Sigma}_H B} \quad , \tag{5.14}$$

where $\mathbf{J}_{eq}$ the equivalent current vector derived from equation (5.11), and B is the local vertical magnetic field strength. The so called an "equivalent Hall conductance" $\tilde{\Sigma}_H$ is a constant scale factor. Equation (5.14) is based upon the fact that, in the case of homogeneous conductance, the equivalent current is just the Hall current which is proportional, but in the opposite direction, to the convection velocity. For Figure 5.3 $\tilde{\Sigma}_H$ was taken to be 1.8 S which is a reasonable value for the "dark" ionosphere.

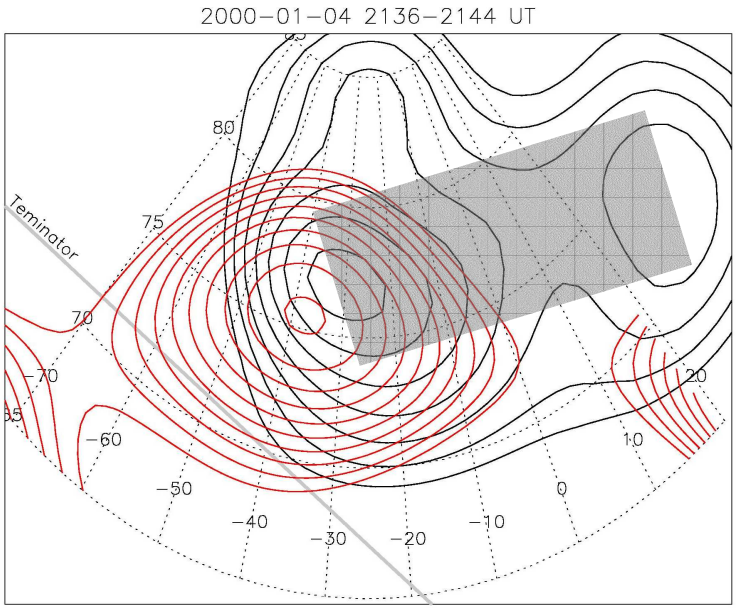

Figure 5.4 Equivalent current potential contours (red lines, separated by 3.6 kA/m) and the SuperDARN-observed electric potential contours (black lines, separated by 2 kV). The SDC and the EQC vectors are along the two contour streamlines in a clockwise rotation sense. The gray bar shows the region where upward FACs should be expected.

Figure 5.3 shows that an overall reasonable agreement between the EQC and SDC is achieved. In particular, both EQC and SDC show the existence of well-defined clockwise vortices. There are some large discrepancies on the western edge of the map, but they are likely due to a modelling extrapolation error because of the lack of magnetometer observations there. However, on investigating in detail the location of the EQC and SDC vortices, we found that the position of the EQC vortex is shifted considerably southwestward of the SDC vortex. The relative shift of the EQC vortex relative to the SDC vortex can be seen more clearly in Figure 5.4, which gives the

contours of electric potential (black lines) and the contours of the equivalent current potential (red lines, see equation 5.10). The convection velocity and the equivalent current vectors are along the two contour streamlines, respectively. It is seen that the focus of the SDC vortex was located at 77^0 MLAT and -40^0 MLON, while the focus of the SDC vortex was at 75.5^0 MLAT, -37^0 MLON. Compared to the SDC vortex, the EQC vortex is shifted considerably toward the "terminator".

On the other hand, in the northeastern portion of the EQC, the contours of the equivalent current potential are nearly tangential to the contours of electric potential but are much more dense, indicating a large ratio between the EQC magnitude and SDC magnitude. A Hall conductance of ~6 S was expected there.

5.3.2 Event on November 28, 1999

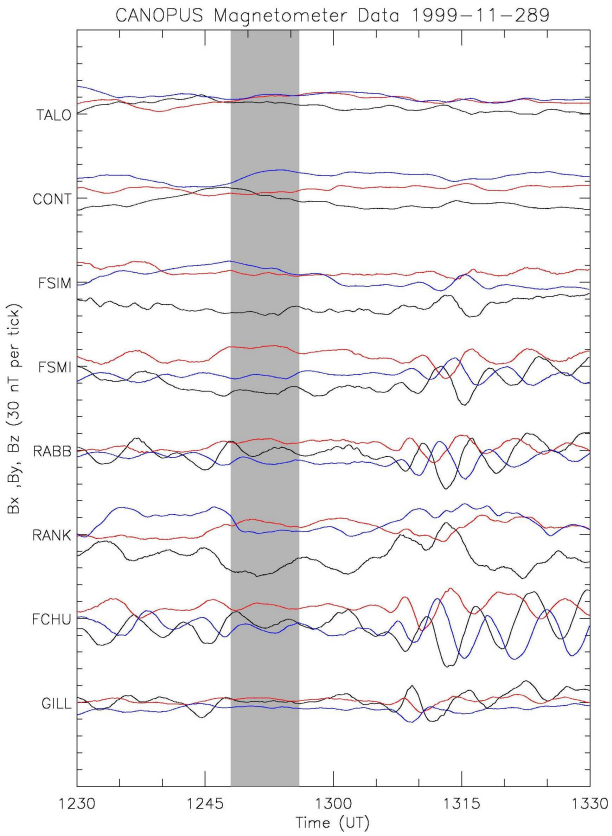

Figure 5.5 Stackplot of CANOPUS magnetometer data from 1230 to 1330 UT on November 28, 1999. Black, red and blue lines denote the X, Y, and Z components of the magnetic field. The gray band indicates the time interval of interest.

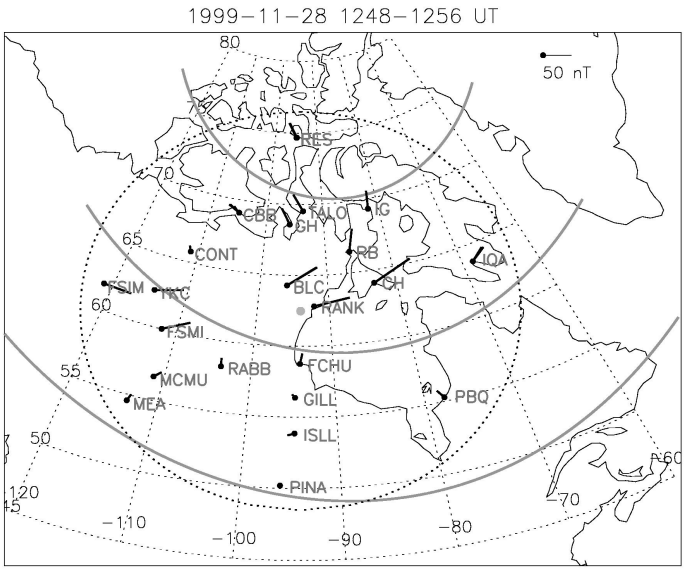

Figure 5.6 Geographical map showing all the available magnetometer observations during the interval 1248-1256 UT, November 28, 1999.

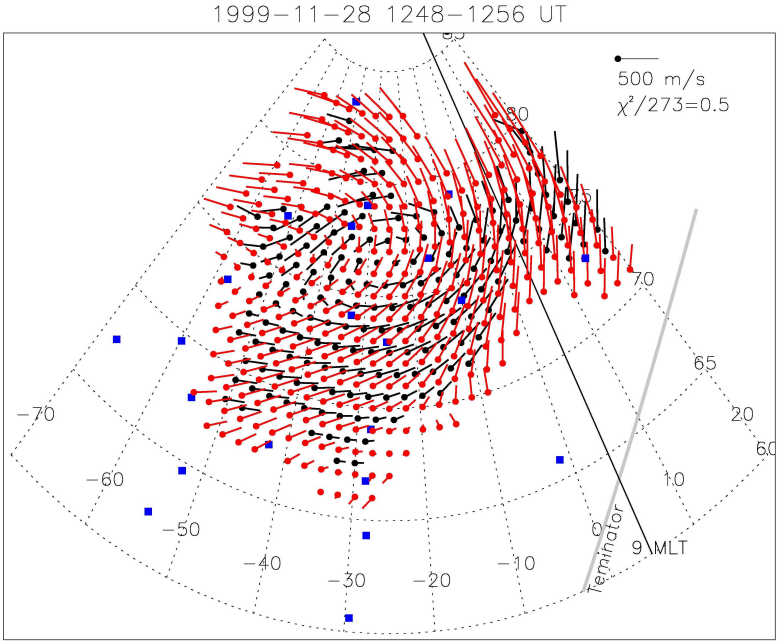

Figure 5.7 EQC and SDC map for 1248-1256 UT, November 28, 1999. All symbols and denotations are similar to Figure 5.2, except that an equivalent Hall conductance of 2.5 S was used here.

Next we will describe an event for the period 1248-1256 UT on November 28, 1999. Figure 5.5 gives the raw magnetometer data from several CANOPUS stations during the interval 1230-1330 UT. Figure 5.6, which is similar to Figure 5.2, shows all the available magnetometer observations, while Figure 5.7 gives the EQC and SDC maps during this event interval. This is also a weak geomagnetic disturbance interval. During this time interval the entire region of interest was in darkness, and an equivalent Hall conductance of 2.5 S is used in Figure 5.7. The SuperDARN observations show a well-defined counterclockwise convection vortex centered at 76.5^0 MLAT, -28^0 MLON. In the equatorward and eastern part of the vortex, there is some agreement between the SDC and EQC directions. However, obvious discrepancies between the EQC and SDC maps are found in the poleward part of the SDC vortex. In particular, where the SDC turns westward at ~78º MLAT and then southwestward, the EQC directions deviate significantly northward with respect to the SDC directions. A vortex structure is not clearly seen in the EQC pattern.

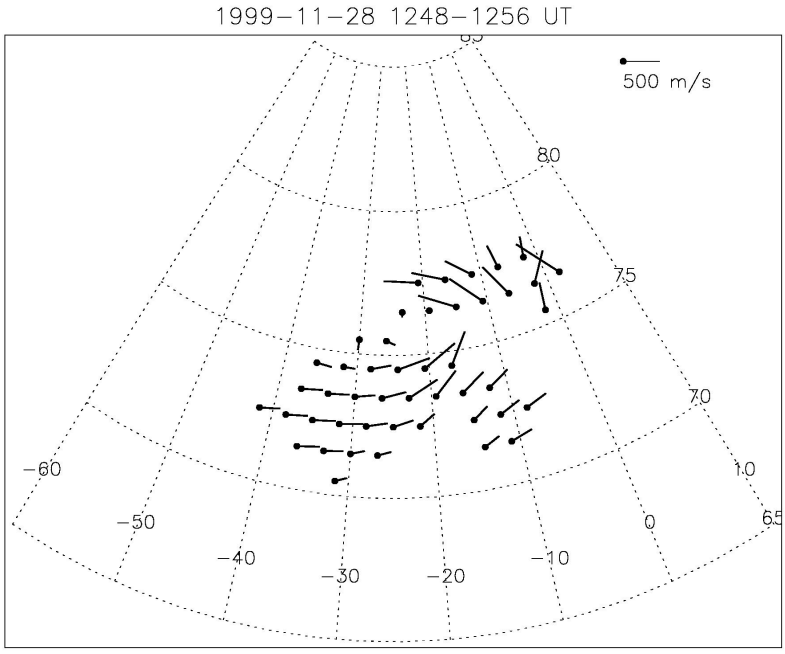

Figure 5.8 SuperDARN merged velocities for 1248-1256 UT, November 28, 1999.

To further illustrate that such a discrepancy between the SDC and EQC patterns was not due to the errors which might be introduced by the SuperDARN FIT technique

(see Chapter 2.1), we present the SuperDARN velocity map during the interval of interest based on the merge technique in Figure 5.8. Though the merged convection map contained much fewer data points than the fitted convection map, the agreement between them at the locations of the available merged data points is obvious. A counterclockwise vortex structure can be inferred in both cases. In particular, where the most preeminent discrepancies between the SDC and EQC patterns are found in Figure 5.7, namely at ~78º MLAT and ~ -20º MLON, the merged convection velocities are dominantly westward, which is consistent with the fitted convection velocities but significantly different from the dominantly northward EQC direction shown in Figure 5.7. Therefore we conclude that the above-mentioned discrepancy does not arise because of convection velocity errors caused by the SuperDARN FIT technique.

5.3.3 Event on February 11, 1999

Next we will describe an event for the period 1408 to 1416 UT on February 11, 1999. Figure 5.9 gives the raw magnetometer data from several CANOPUS stations during the interval 1345-1445 UT. Figure 5.10 gives all the available magnetometer observations of the magnetic deviations during the event interval (1408-1416 UT). This is a moderate geomagnetic disturbance interval. The magnetic deviations at all stations are mostly between 100-250 nT. Figure 5.11 gives the EQC and SDC map for this time interval, which are of the same form as those in Figure 5.3, with the exception that an equivalent Hall conductance of 9 S is used here. The "terminator", which is shown in Figure 5.11 as a gray line, separates the dark region to the west from the sunlit region to the east. Though some agreements between the EQC and SDC patterns could be found in the southeastern corner of the map, the overall discrepancies are substantial. In particular, the SDC pattern contained a clear counterclockwise vortex centered at 70.5^0 MLAT and -17^0 MLON, but such a vortex is not seen in the EQC pattern. In particular, the EQC pattern is roughly perpendicular, or even in the opposite direction to the SDC in the poleward part of the SDC vortex, between 70º to 76º MLAT and -40º to -8º MLON, where the SDC direction was westward and/or southward while the EQC direction was dominantly eastward and/or northward. It should be noticed that such a discrepancy was definitely not caused by SCHA model error because in the region of

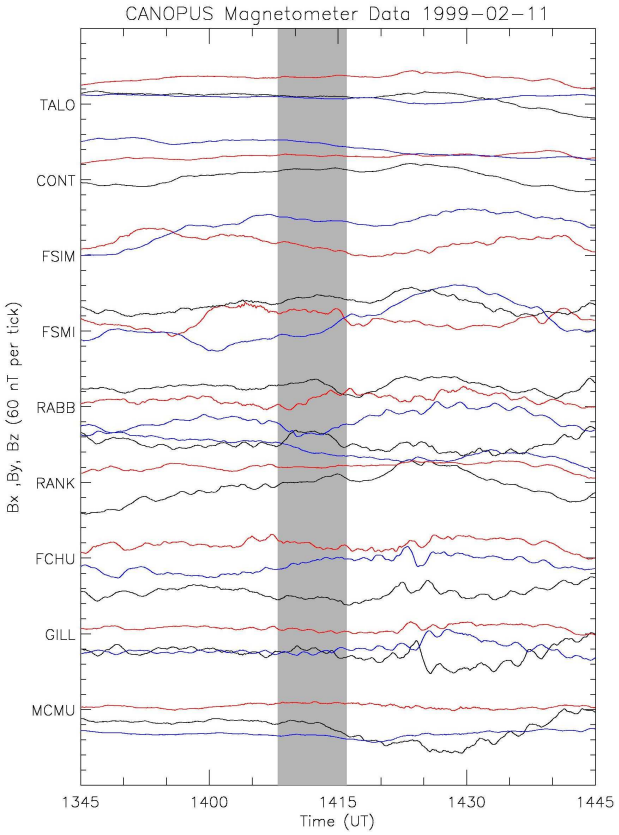

Figure 5.9 Stackplot of CANOPUS magnetometer data from 1345 to 1445 UT on February 11, 1999. Black, red and blue lines denote the X, Y, and Z components of the magnetic field. The gray band indicates the time interval of interest.

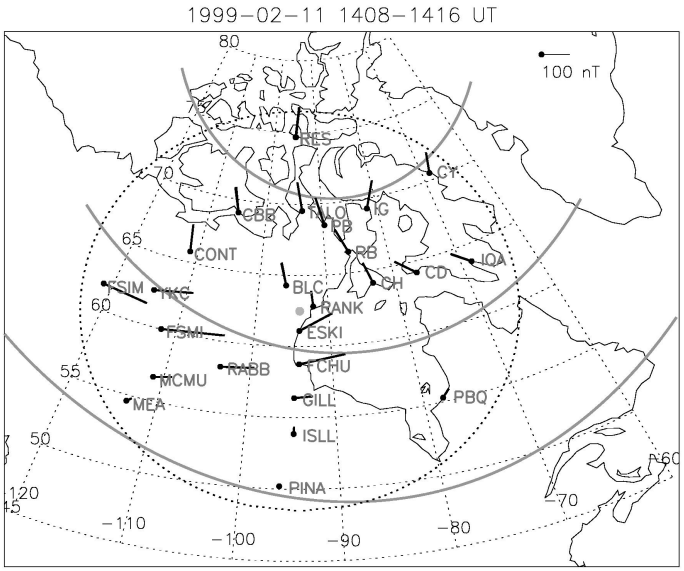

Figure 5.10 Geographical map showing all the available magnetometer observations during the interval 1408-1416 UT, February 11, 1999.

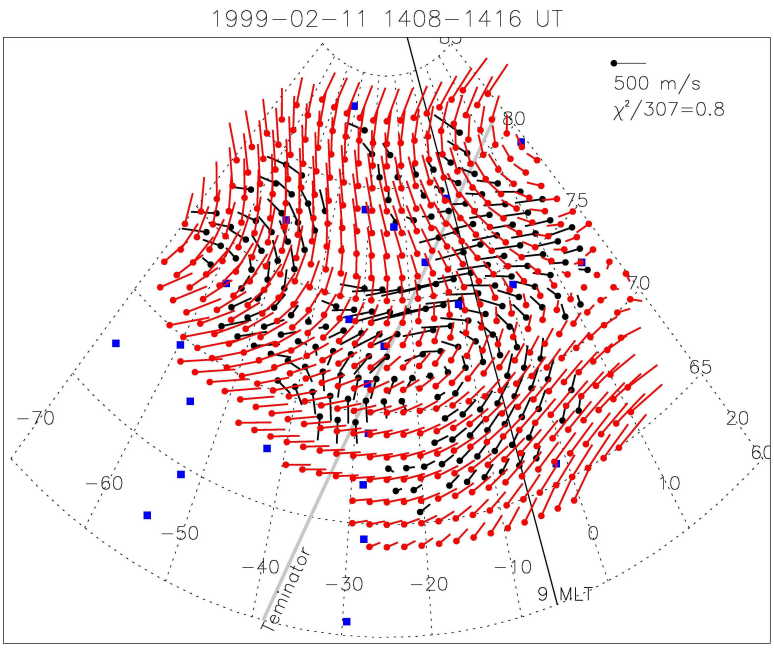

Figure 5.11 EQC and SDC map for 1408-1416 UT, February 11, 1999. All symbols and denotations are similar to Figure 5.3, except that an equivalent Hall conductance of 9 S was used here.

discrepancy there are a number of magnetometer observations (shown as blue squares in Figure 5.11) that were collocated with the positions of radar observations. Near the western edge of the map there is another hint of a counterclockwise SDC vortex, though the contours are incomplete on its western edge. Again, we notice some large discrepancies between the EQC and SDC patterns in the poleward part of that vortex, where the SDC turned westward but the EQC was mostly northward. This discrepancy thus has the same trend as that for the vortex centered at ~-17^0 MLON. However, since there was lack of actual magnetometer observations on the western edge of the SDC map, we cannot exclude the possibility of a modelling error there.

5.3.4 Event on April 6, 2000

In the above events, we described the comparisons between the EQC and SDC patterns for a clockwise vortex in the dusk sector (Event 1) and for counterclockwise vortices in the dawn sector (Events 2 and 3). In the April 6 event, the observations were made near noon. Figure 5.12 gives the raw magnetometer data from several CANOPUS

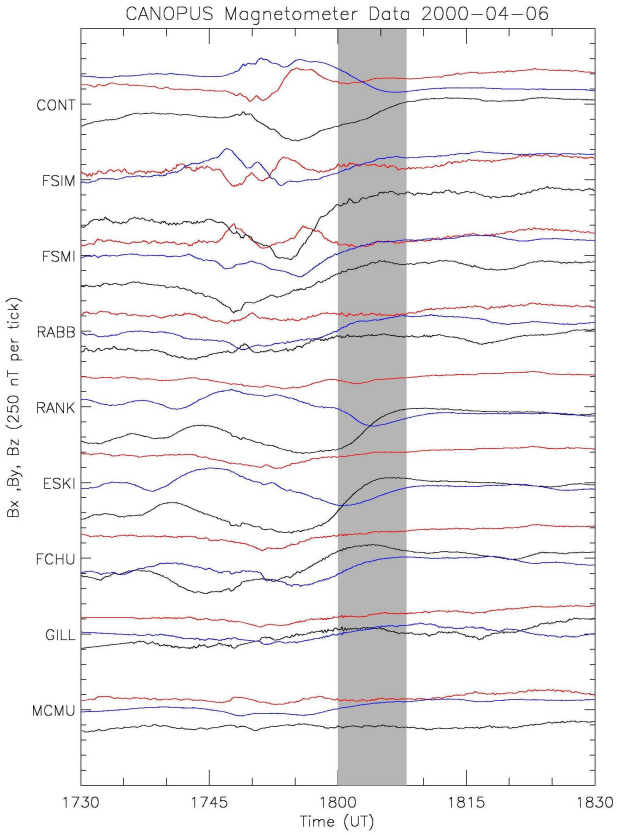

Figure 5.12 Stackplot of CANOPUS magnetometer data from 1730 to 1830 UT on April 6, 2000. Black, red and blue lines denote the X, Y, and Z components of the magnetic field. The gray band indicates the time interval of interest.

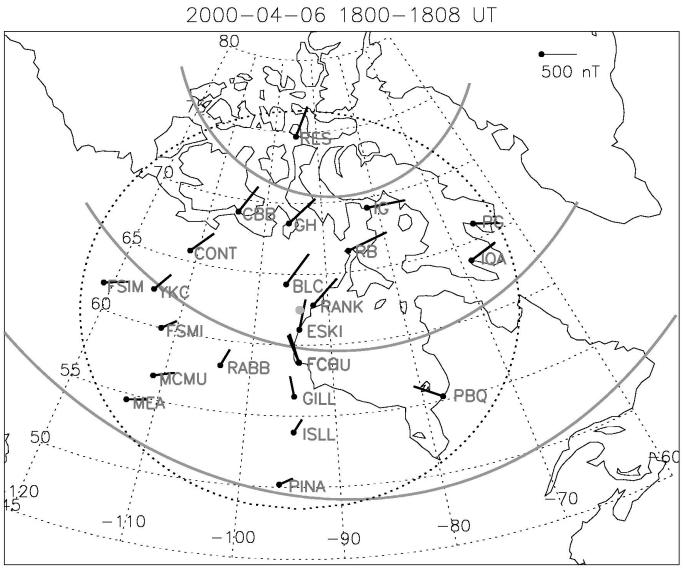

Figure 5.13 Geographical map showing all the available magnetometer observations for the period 1800-1808 UT, April 6, 2000.

stations during the interval 1730-1830 UT. Figure 5.13 shows all the available magnetometer observations of the magnetic deviations during 1800 to 1810 UT on April 6, 2000, which was a strongly geomagnetically disturbed period. The magnetic deviations at all stations are several hundreds nT. Figure 5.14 gives the calculated EQC and SDC maps. Since this was an equinox near-noon event the entire region of interest shown in the map was sunlit. An equivalent Hall conductance of 12 S is used on Figure 5.14. Despite the rather localized observations, a clear hint of both cells of the usual two-cell pattern, namely a counterclockwise cell in the pre-noon sector and a clockwise cell in the afternoon sector, can be identified in Figure 5.14. For the available part of the afternoon clockwise cell, a reasonable agreement in direction, between the EQC and SDC patterns was found. However, for the available part of the pre-noon counterclockwise cell, there were obviously large discrepancies. On the poleward part of the SDC pre-noon vortex, the flow direction turned westward while the EQC direction was mostly northeastward. The vortex structure was significantly deformed in the pre-noon EQC pattern. Such a trend is quite similar to that we have shown above for both the November 28, 1999 event and the February 11, 1999 event.

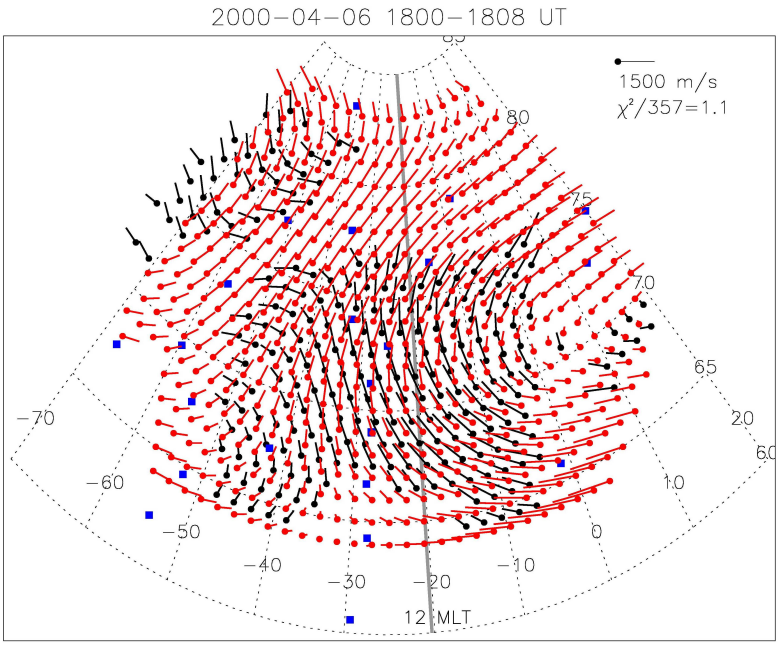

Figure 5.14 EQC and SDC map for the event of 1800-1808 UT, April 6, 2000. All symbols and denotations are similar to Figure 5.3 except that an equivalent Hall conductance of 12 S was used here.

5.4 Discussion

The basic equations relating the equivalent currents, FACs, conductances, and electric fields are the following (see Appendix B.3),

$$j_{//} = -\Sigma_P \nabla \cdot \mathbf{E} - (\nabla \Sigma_P + \nabla \Sigma_H \times \hat{\mathbf{b}}) \cdot \mathbf{E} \quad , \tag{5.15}$$

$$\nabla \cdot (\hat{\mathbf{b}} \times \mathbf{J}_{eq}) = -\Sigma \ \nabla \cdot \mathbf{E} + (\nabla \Sigma_P \times \hat{\mathbf{b}} - \nabla \Sigma_H) \cdot \mathbf{E} \quad , \tag{5.16}$$

where $\mathbf{J}_{eq,}$ **E,** and **v** are the ionospheric equivalent current, electric field and convection velocity, respectively, and $j_{//}$ is the FAC. The symbols $\sum_P$ and $\sum_H$ are the height-integrated Pedersen and Hall conductivities, or conductances, respectively, and the unit vector $\hat{\mathbf{b}}$ is along the magnetic field. It is important to note that, even if we knew the distribution of both the equivalent current and the electric field, it would still be impossible to solve the true ionospheric current system unambiguously because we have only two equations but three unknown variables, Σ_P, Σ_H and $J_{//}$.

If the conductance is homogeneous, the equivalent current is just the Hall current; this is known as the Fukushima's theorem [*Fukushima*, 1976]. In this case, the EQC is proportional to the plasma convection, the proportionality constant being determined by the Hall conductance. Obviously such homogeneity is never realized in the ionosphere. Conceptually, a major difference between the EQC and the plasma convection is caused by the inhomogeneity in the conductance. The total ionospheric conductance can be represented by [*Blomberg and Markland*, 1988],

$$\Sigma = \sqrt{\Sigma_0^2 + \Sigma_{abg}^2 + \Sigma_{EUV}^2 + \Sigma_{j//}^2} \quad , \tag{5.17}$$

where Σ_0 is a background term having a constant low value representing the contribution from cosmic radiation and galactic extreme ultraviolet (EUV) radiation; Σ_{abg} represents an average auroral oval background conductance, which usually maximizes at the latitude of the diffuse auroral oval (~70^0 MLAT on the dayside) and decreases towards both higher and lower latitudes; Σ_{EUV} describes the photoionization conductance that caused by the solar EUV radiation, which is strongly dependent on the

solar radio flux at 2.8 GHz (λ=10.7 cm) and the solar zenith angle; finally, $\Sigma_{j//}$ represents the contribution associated with the field-aligned currents (FACs), e. g., electron precipitation from the magnetosphere (upward FAC). Note that every term in equation (5.17) has two values, one for the Hall conductance and one for the Pedersen conductance. The root-sum-square relationship is applied in equation (5.17) instead of a direct summation because the photoionization and particle-ionization processes that give rise to the conductivity take place almost within the same altitude range (*E* region), and the ionization rate is proportional to n_e^2 when recombination is the main loss process. As discussed by *Wallis and Budzinski* [1981], the quadratic sum of the ionization rates gives a far more accurate estimate of the total conductance, which is proportional to n_e , than a mere direct summation would give.

First we will show the effect of the photoionization conductance inhomogeneity. In the January, 4, 2000 event, the SDC and EQC patterns show reasonable agreement; in particular, the clockwise structures are well-defined in both SDC and EQC, except that the EQC vortex was found to be shifted toward the terminator compared to the SDC vortex. The result is quite consistent with the study of *Lyatsky et al*. [1999] on SDC clockwise vortex events in the dayside winter ionosphere. Such a shift was explained in terms of the effect of a secondary interhemispheric FAC system arising at the boundary where a sharp change in the ionosphere conductance occurs, for example, near the "terminator" [*Benkevitch and Lyatsky*, 2000a; *Benkevitch et al*., 2000b]. However, we notice that in *Benkevitch and Lyatsky*'s [2000a] model, the Hall and Pedersen conductance profiles were assumed to be uniform in the dark region but abruptly switched to *Hardy et al*. [1987] conductance model in the sunlit region, which contains a discontinuity at the "te rminator". If we assume a more physically realistically smooth transition of Hall and Pedersen conductances from dark to sunlit region across the terminator, the conductance gradient in the dark region will provide another alternate mechanism that would also cause the shift of the EQC vortex relative to the convection vortex. This will be illustrated as follows.

Equation (5.16) can be rewritten in another form which gives the curl of the equivalent current,

$$(\nabla \times \mathbf{J}_{eq}) \cdot \hat{\mathbf{b}} = \Sigma_H \nabla \cdot \mathbf{E} + \nabla \Sigma_H \cdot \mathbf{E} + B \nabla \Sigma_p \cdot \mathbf{v} \quad , \tag{5.18}$$

where $\mathbf{v} = \mathbf{E} \times \hat{\mathbf{b}} / B$ is the convection velocity. Let us assume a clockwise convection cell ($\nabla \cdot \mathbf{E} < 0$) in the X-Y plane, as shown in the left panel of Figure 5.15. The Hall and Pedersen conductances both have gradients toward the –Y direction. The convection cell is divided into four quadrants where the electric fields **E** and convection velocity **v** make different angles with the gradients of Hall and Pedersen conductance. Consider the three terms on the right side of equation (5.18). In the first quadrant, the second and third terms containing the Hall and Pedersen conductance gradients, respectively, both have the opposite sign to the first term $\Sigma_H \nabla \cdot \mathbf{E}$, and thus act to reduce the curl of the equivalent current, while in the third quadrant, the two conductance gradients both act to enhance the curl of the equivalent current. In the second and the fourth quadrants, the Hall and Pedersen conductance gradient terms have different signs and will tend to cancel each other. Therefore the location of maximum curl, which is usually the location of the "focus" of the convection cell or of the equivalent current, is shifted southwestward, to the third quadrant. Because the Hall conductance is usually higher than the Pedersen conductance, the southward shift will be more pronounced than the westward shift. If the conductance gradient is associated with the day-night difference of photoionization near the "terminator", the EQC cell on the dark region should shift toward the high-conductance sunlit region and also shift slightly left along the direction of the "terminator", which is exactly what we have seen in Figures 5.3 and 5.4.

Note that *Lyatsky et al.*'s mechanism [1999] (which involves a secondary interhemispheric FAC system) and the mechanism presented above both require a large day-night photoionization conductance gradient. Both mechanisms are viable near the "terminator". However, it is not the purpose of this study to distinguish their relative importance in causing the shift of EQC vortex relative to SDC vortex in a specific event. On the other hand, there is also another conductance gradient related to the Σ_{abg} term in equation (5.17), pointing equatorward toward the location of the diffuse auroral oval.

According to the above analysis, this conductance gradient might also produce a southwest shift of the vortex.

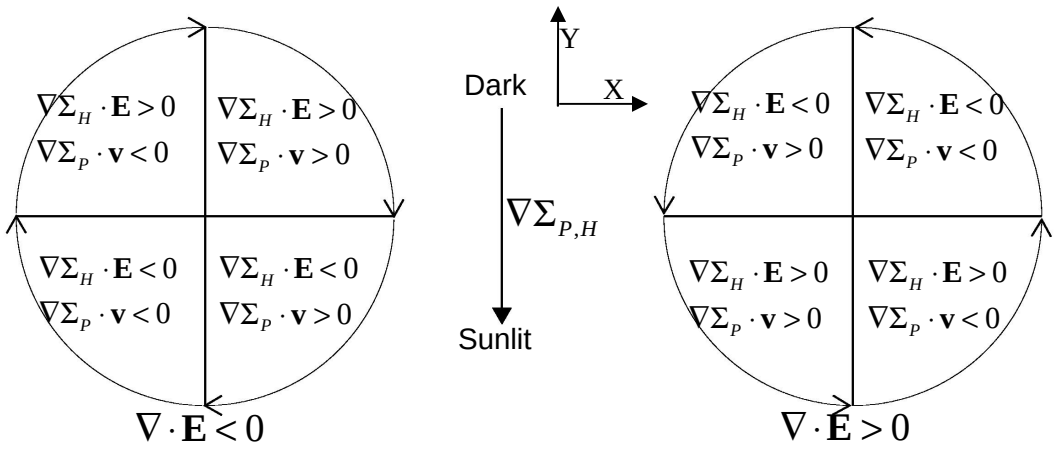

Figure 5.15 A schematic diagram showing the effects of the conductance gradient terms in the right side of equation (5.18) on a clockwise convection cell (left panel) and a counterclockwise convection cell (right panel).

Another important source of conductance inhomogeneity comes from the effect of a localized FAC structure. In particular, the association of the conductance with the upward FAC carried by the downward field-aligned electron flux is an obvious one. The effect of an upward FAC-conductance coupling process can be easily identified in the January 4, 2000, event. Figure 5.4 shows that this SDC vortex is embedded in an azimuthally-spread clockwise convection cell. Such a cell extended to east of 20^0 MLON, where another localized clockwise vortex was observed by the Goose Bay-Stokkseyri SuperDARN radar pair. It is reasonable to assume that, embedded in the large convection cell, there was an azimuthally extended upward FAC region (shown in Figure 5.4 as a gray band). Inside the upward FAC region, the ionospheric conductance was significantly enhanced. Electric fields tend to decrease in an enhanced conductance region [*Yeoman et al*., 2000a; *Parkinson*, 2004]. Figure 5.3 shows that in the northeast portion of the SDC vortex, the convection became rather small, and the equivalent current was similar in direction to the SDC but was much larger in magnitude. A Hall conductance of 6 S was found there, which is several times larger than the usual level of

"dark" ionosphere. Obviously this represents the effect of a strong Hall conductance enhancement associated with the upward FAC.

A conductance inhomogeneity which is not related to a FAC should cause a similar effect on both a clockwise convection vortex and a counterclockwise vortex. As one can see from the right panel of Figure 5.15, a similar analysis for a counterclockwise cell undergoing a conductance gradient will lead to the conclusion that the curl of the EQC will also increase in the third quadrant but decrease in the first quadrant, so the EQC cell will move towards the high conductance region. Also, in *Benkevitch and Lyatsky* 's [2000a] model calculation, the EQC vortex associated with a counterclockwise convection vortex will move in the same sense as that for a clockwise vortex, though no counterclockwise vortex event was presented in *Lyatsky et al*. [1999]. However, on investigation of our event database for SDC vortices and their associated EQC patterns, we frequently found that the agreement between the EQC and SDC patterns is reasonably good for a clockwise convection vortex. In this case, the EQC usually shows a clearly identifiable vortex structure, except for some shift and distortion relative to the SDC vortex structure due to the above-mentioned mechanisms. However, for a counterclockwise convection vortex, the agreement between the EQC and SDC usually is poor; at many times a vortex structure may not even be identified in the EQC pattern. Such an asymmetry between the clockwise and counterclockwise vortex cases can be seen in the April, 6 event. Though the full extent of the two vortices was not fully observed, in the portions that were obtained from the measurements, it is clear that the agreement between the EQC and SDC patterns is much worse for the pre-noon clockwise vortex than for the afternoon clockwise vortex. Reviewing the November 28, 1999, February 11, 1999, and April 6, 2000, events, a consistent pattern for the discrepancy between the EQC and SDC patterns, for a counterclockwise SDC vortex, was found, and is summarized in Figure 5.16. Though the EQC pattern also showed a positive curl, the vortex structure is significantly deformed. The agreement between the EQC and SDC becomes particularly poor, since where the SDC velocity direction turns westward and equatorward, the EQC is usually more northward-directed.

In all three counterclockwise SDC vortex events the positions of the vortex are quite different with respect to the "terminator". In the November 28, 1999 event, the

SDC vortex is totally immersed in the dark region, while in the February 11, 1999 event, the "terminator" cuts across the SDC vortex. Especially in the April 6, 2000 event, the region of interest is near noon thus the photoionization should be rather smooth there. Since the pattern discrepancy shown in Figure 5.16 persisted in every event, we believe that the photoionization conductance gradient is not the main reason for the discrepancy. Instead, we suggest that the discrepancy is most likely associated with the downward FAC-conductance coupling process.

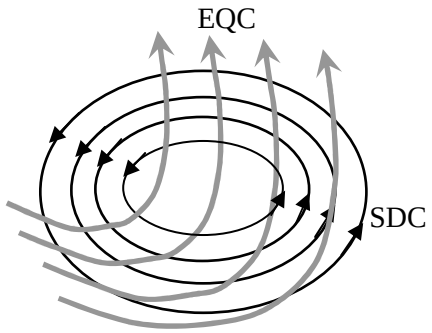

Figure 5.16 A general pattern of the discrepancy between the EQC and SDC for a counterclockwise SDC vortex.

It is well known that an upward FAC is dominantly carried by the field-aligned precipitating electron flux [*Lyons et al*., 1979]. The energy spectrum of the downgoing electrons can be split into two characteristic parts. One is the high energy (>>1kev) precipitation, responsible for the aurora and ionization production at ionospheric *E* region heights. The other is the lower energy component (<1kev), which produces ionization at higher altitudes. As we have discussed in Chapter 1.2, the ionospheric Hall conductivity usually peaks at ~100 km but decreases quickly with increasing altitude; the major contribution to the Hall conductance comes from altitudes <120 km [*Aksnes et al*., 2004]. The Pedersen conductivity peaks at a slightly greater height (~130 km) and the maximum is smaller than that of the Hall conductivity, but the Pedersen conductivity decreases more slowly than the Hall conductivity with increasing altitude. Therefore, the high energy electron precipitation contributes considerably to both the Hall and Pedersen conductances, while the soft precipitation contributes primarily to the

Pedersen conductance only. The energy spectrum of precipitating electrons is usually complex. Nevertheless, an enhancement of the upward FAC is usually accompanied by a simultaneous enhancement of the ionization, leading to a positive correlation between the FAC and ionospheric conductance, and the resulting Hall conductance is usually several times larger than the Pedersen conductance at auroral latitudes [*Aksnes et al*., 2004]. For downward FAC, the correlation between the FAC and the conductance is less obvious. A downward FAC usually consists of upflowing suprathermal electrons which tend to deplete rather than enhance the ionospheric ionization; this depletion leads to the formation of the so-called "auro ral ionospheric cavities" (AIC) [*Doe et al*. 1993; 1995; *Aikio et al*. 2002]. *Doe et al*. [1993] showed that, in a typical AIC, more than 40% of the *F* region plasma density could be depleted on a time scale as short as 4 minutes. A numerical model for the temporal development of an AIC by *Doe et al*. [1995] showed that the plasma depletion rate due to the effect of a downward FAC is negligibly small in the lower ionospheric *E* region (<120 km altitude), but quickly rises to a maximum at the top of the *E* region (~140 km), and retains throughout all the *F* region (see Figure 9 in their paper). Thus one should expect that the coupling of downward FAC and the ionospheric conductance would primarily affect the Pedersen conductance but would have only a small effect on the Hall conductance. This is probably the reason that the effect of a downward FAC has usually been neglected in FAC-conductance coupling models [*Blomberg and Markland*, 1988; *Zhu et al*., 1997].

We now can make the argument that reduction of Pedersen conductance caused by downward FACs probably accounts for the large discrepancy between the EQC and SDC patterns, for a counterclockwise vortex. Again we rewrite equation (5.16) in another form,

$$\nabla \cdot (\mathbf{J}_{eq} \times \hat{\mathbf{b}} - \Sigma_H \mathbf{E}) = \nabla \Sigma_P \cdot (\mathbf{E} \times \hat{\mathbf{b}}) \qquad . \tag{5.19}$$

It is interesting to note in equation (5.19) the roles of the Hall conductance Σ_H and the Pedersen conductance Σ_P. The Hall conductance Σ_H behaves more as a multiplier; a strong local enhancement of Σ_H, which could arise because of an upward FAC, may lead to a large magnitude change in the ratio between the equivalent current and the

convection velocity, but would not cause a significant difference in their directions. This has been demonstrated for the January 04, 2000, event (Figure 5.3 and 5.4) in the northeastern portion of the map. On the other hand, the Pedersen conductance gradient can produce a significant deviation between the directions of the equivalent current and the convection velocity.

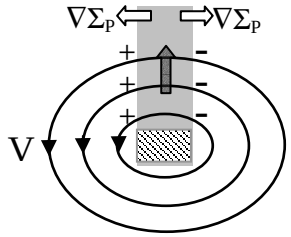

Figure 5.17 A schematic diagram showing the effect of a reduction of Pedersen conductance with a cavity structure shown in a gray band. At the equatorward edge of the cavity there is a downward FAC region shown in a hatched box. The associated convection pattern is shown in solid lines with arrows. The Pedersen conductance gradients (shown in white heavy arrows) lead to a southward deviation of equivalent current with respect to the Hall current, or a northward deviation of EQC (shown in dark heavy arrow) with respect to the plasma convection.

Let us consider the effect of the reduction of Pedersen conductance associated with a downward FAC and an AIC structure. A numerical model for the temporal development of an AIC [*Doe et al*., 1995] revealed that the plasma depletion cavity appeared to form initially at the location of the downward FAC. However, after the cavity has grown for ~20 seconds, the downward FAC region migrates to the equatorward edge of the cavity (see Figure 8 in their paper). The geometry is shown in Figure 5.17. A downward FAC located at the south edge of a cavity structure can produce a counterclockwise convection cell. Inside the cavity the plasma density and thus the Pedersen conductance are considerably reduced. We further assume the Hall conductance is not affected for the reasons we discussed above. Therefore equation (5.19) takes the form of a Poisson equation. As we see from Figure 5.17, at the west edge of the cavity, the right side term of equation (5.19) would have a positive sign,

while at the east edge of the cavity the term is negative. The geometry is similar to a "capacitor" in which an eastward "electric field" is developed within the cavity. Such an eastward "electric field" corresponds to a southward deviation of the equivalent current with respect to the Hall current, or a northward deviation of equivalent convection with respect to the plasma convection, in the upper part of the convection vortex, which is consistent with the discrepancy pattern shown in Figure 5.16.

Another possible charge carrier of the downward FAC is precipitating protons from the magnetosphere. The proton precipitation may contribute to the ionization and thus increase the ionospheric conductance. However, the contribution of proton precipitation is usually only ~15% of the total auroral particle energy [*Galand et al*., 2001], except in certain special regions, such as the equatorward edge of the auroral oval in the evening sector [*Hardy et al*., 1989].

Finally, we note that counterclockwise vortices and clockwise vortices are dominantly found in the dawn sector and dusk sector, respectively, in accordance with the usual 2-cell global convection pattern. The asymmetry between the EQC and SDC patterns for counterclockwise vortices and clockwise vortices would naturally lead to a dawn-dusk asymmetry as well, which is supported by a global statistical study of the deviation of direction between the magnetic disturbances and the SuperDARN-observed convection velocity in all time sectors [*L. Benkevitch*, unpublished result]. The agreement is much worse in the dawn sector than in the dusk sector. Such a dawn-dusk asymmetry may raise some questions about the validity of inversion techniques which use the magnetic observations to estimate the global ionospheric convection patterns, particularly in the dawn sector.

5.5 Summary

The equivalent convection pattern derived from CANOPUS, NRCAN/GSC and MACCS magnetometers by the SCHA procedure [*Haines*, 1985] has been compared with the ionospheric convection pattern observed by SuperDARN HF radars. We have found that a large day-night photoionoziation conductance gradient near the "terminator" may cause a shift of the focus of the EQC vortex relative to the SDC vortex. Within the region of upward FACs, the ratio between the EQC magnitude and

the SDC magnitude significantly increases due to the conductance enhancement associated with the upward FAC. The agreement between the EQC and SDC patterns is usually worse for a counterclockwise convection vortex than for a clockwise cell, but a consistent pattern of discrepancy for counterclockwise convection vortices has been found. We suggest that such a discrepancy is caused by the coupling between the downward FAC and the Pedersen conductance. A conceptual model to explain the deviation of EQC pattern with respect to a counterclockwise SDC vortex is proposed. The study in this chapter is ongoing. For the future extension of this study, a quantitative model of the relationship between the downward FAC and the ionospheric conductance must be developed.

Chapter 6

Conclusions

This thesis is devoted to a multi-instrument study of convection, auroral emissions, and currents in the high-latitude ionosphere. The major instruments involved are the SuperDARN HF radars, CANOPUS ground-based magnetometers and MSPs, the NASI, and particle and magnetic detectors on some satellites. In this Chapter we will summarize the main results of the thesis and recommend some future projects to extend the work.

From an investigation of observations from the Saskatoon-Kapuskasing SuperDARN radar pair, a data set of NRFE events has been compiled. The NRFEs are distinguished into two classes, those on open field lines and those on closed field lines. The NRFEs on open field lines usually have very little accompanying auroral and magnetic activity. The NRFE on closed field lines may be associated with two types of auroral activities. The first is high-latitude auroras, such as auroral streamers, located or initiated near the poleward boundary of the auroral oval. The other is auroral intensifications inside the main auroral oval, which are generally associated with the substorm/pseudosubstorm process. However, there is not a well-defined one-to-one correspondence between NRFEs and auroral intensifications. A detailed analysis was made of an NRFE during a pseudosubstorm event on December 26, 1998. The HF radar observations showed that the high-latitude part of the NRFE structure was located just equatorward of the OCFLB determined from the poleward edge of 630 nm emissions. The structure extended downward in magnetic latitude to 68.5 ± 0.4^0, which is roughly estimated to be the boundary between the BPS and the CPS, based upon Doppler spectral width transition observed by the radar during the event time. The ionospheric optical auroral intensifications were located at $64.5\text{-}66.5^0$ MLAT, inside the CPS. A

zonal flow shear region characteristic of the Harang discontinuity was inferred from the radar observations. The Harang discontinuity was closely associated with upward FACs and auroral intensifications. Both the statistical investigation and event study showed that the NRFE may occur nearly simultaneously with the auroral intensification. This temporal relationship cannot easily be explained by the existing models that associate the tail reconnection process and the near-geosynchronous onset of substorms. We suggest a new model which fills a gap that two existing models could not explain, namely the near-simultaneous occurrence of the NRFEs and the auroral activations, as follows. A fast mode wave is generated at the tail reconnection site and propagates earthward. When the wave penetrates into the IPS, it assists in the activation of NGOPS instabilities and the onset of the pseudosubstorm. On the other hand, the electric fields associated with the reconnection first lead to earthward flows, and the signature of these is conveyed from the equatorial tail to the ionosphere with a time delay equal to the Alfven wave travel time along the rather long OPS field lines. The result of these Alfven waves is the NRFE signature in the ionosphere. Although these are two different sets of processes, one leading to the auroral activation and one to the NRFE, the time delay between the reconnection and the subsequent appearance both of the auroral intensifications and of the NRFEs is about the same, so the radar (NRFE) and optical auroral signatures would appear in the ionosphere almost simultaneously.

The two-dimensional ionospheric structure of a small substorm event on October 9, 2000 was studied using optical and radar images, and associated magnetometer and meridian scanning photometer data. Solar wind observations on GEOTAIL revealed a prolonged dominant Bz+ and steady By+ IMF prior to the substorm onset, except for a southward excursion at 0645-0655 UT, and a "square-wave" IMF Bx-By structure at 0727-0735 UT. A sequence of three Pi2 bursts and associated optical intensifications was found. The last and strongest Pi2 burst was associated with an substorm EP onset, characterized by a 100 nT magnetic bay at Fort Churchill and an auroral breakup in which the 630 nm emissions moved poleward about 2.5 degrees. All three activations originated close to midnight, but evolved progressively eastward. Most of the dynamic auroral and convection signatures were observed in the postmidnight sector. Within each of the three optical intensifications, discrete azimuthal auroral structures that

appeared successively from midnight toward the morning sector were identified, giving evidence for drift wave activity in the NGOPS. The SuperDARN VLOS measurements reveal the development of eastward electric fields within each Pi2 burst interval, which is consistent with the CRRES observations that the growing eastward electric field inside the dipole structure of the drift wave leads to a substorm EP [*Erickson et al*., 2000]. About 10 minutes after the initial substorm onset, there is a second stage of auroral brightening with the expected characteristics of a "Stage-2 EP" [*Erickson et al*., 2000]. In examining the solar wind parameters, the polar cap magnetic activity index, and the global ionospheric convection measurements from eight SuperDARN radars in the northern hemisphere, we find that the IMF southward excursion led to the convection enhancement and energy transport into the magnetosphere, where the energy is stored mainly in the magnetotail. When the dayside convection decreased, two pseudobreakups occurred as the consequence of the release of the stored energy into the ionosphere. The evolution of nightside convection and the previous auroral activity had preconditioned the magnetosphere/ionosphere, with the result that the IMF Bx-By structure possibly led to a substorm EP in "directly driven" fashion. The Stage-2 expansion was probably internally driven within the magnetotail, namely a reconnection process at mid-tail as the consequence of the initial Stage-1 EP current disruption at NGOPS and its generation of a tailward-propagating rarefaction wave.

The EQC derived from CANOPUS, GSC and MACCS magnetometers by the SCHA procedure [*Haines*, 1985] is compared to the ionospheric plasma convection pattern observed by the SuperDARN HF radars. We found that a large day-night photo-ionization conductance gradient near the "terminator" may cause the focus of the EQC vortex to shift relative to that for the SDC vortex. Within the region of upward FACs, the ratio between the EQC magnitude and the SDC magnitudes significantly increases due to the Hall conductance enhancement associated with the upward FAC. The agreement between the EQC and SDC patterns is usually much worse for a counterclockwise convection vortex than for a clockwise vortex. However, we have found that there is a consistent pattern of discrepancy between EQC and SDC for a counterclockwise convection vortex. We suggest the coupling between the downward FAC and the Pedersen conductance is the possible reason for such a discrepancy.

SUGGESTIONS FOR FUTURE RESEARCH

We would like to recommend two potential research projects which are related to, and will be a good extension of, this thesis work.

1. Joint observation of NRFEs and auroral poleward boundary intensifications by NASI and SuperDARN

The auroral poleward boundary intensifications (PBI), especially the N-S auroras or "auror al streamer" structure, have long been though to be associated with BBFs in the tail [*Hendersen et al*., 1998; *Zesta et al.*, 2000]. In Chapter 3 we described a NRFE event on March, 21, 1999, in which the auroral streamer structures were found from the MSP observations at Fort Smith, which was west of the NRFE region, but no auroral activations were found from the MSP observations at Gillam, which is east of the NRFE region. The auroral streamer structure is very likely to be associated with the NRFE as suggested by the model of *Nakamura et al*. [2001b], that is, the flow shear on the westside of the flow enhancement region in the tail generates upward FACs which leads to the intensified auroras. However, as can be seen from Figure 3.1, the scan line of the MSP at Fort Smith has considerable longitudinal separation from the radar observation area. In that region, there is no coverage from any of the SuperDARN radars, so no actual observations of the flow shear are available. On the other hand, the auroral PBI may have quite different alignment, either equatorward-extending or non-equatorward-extending; equatorward-extending structures are either north-south aligned structures (such as auroral streamers) or east-west arcs propagating equatorward [*Zesta et al*., 2002]. As we have mentioned in Chapter 3, the MSP observational geometry results in some limitations for the observation of PBIs whose extension has a considerable

azimuthual component. Those deficiencies make the quantitative study on the relationship between the NRFEs and the PBIs very difficult, if not impossible.

Nowadays the NASI instrument makes high-resolution, two dimensional optical auroral observations. In particular, the NASI at Rankin Inlet provides excellent overlapping coverage with both the Saskatoon-Kapuskasing radar FoV and the poleward portion of the auroral oval, at most times. With the ongoing CGSM program, additional NASIs are to be built. These will overlap the FoV of Prince George-Kodiak radar pair as well. It is quite possible that, through joint observations with NASI and SuperDARN, the relative position and alignment of auroral PBIs, such as auroral streamer structures, with respect to the NRFE, and the temporal relationship between them, can de determined. Together with some well-positioned satellites in the magnetotail, if available, a detailed understanding and improved model of the physical association between the PBIs and flow bursts in the tail could be found. Some research in this direction has been done and reported by *Lam et al*. [2004], but there remains much more to explore. One could also combine this work with the study of the relationship between the NRFEs and substorms/pseudosubstorms that was pursued in Chapter 3 of this thesis. It would be interesting to investigate whether and how magnetospheric processes related to the NRFE can produce different types of aurora under different conditions in the magnetosphere/ionosphere. This would be of particular importance in helping to settle the long-standing debate about the importance of the two main substorm EP onset mechanisms; namely, the MTI and the NEI scenarios (see Chapter 1.4, and *Lui* [2001])

2. Combination of SuperDARN, magnetometer, and NASI observations to obtain the three-dimensional ionospheric current systems

The basic equations relating the equivalent currents, FACs, conductances, and electric fields are given in equations (B.18) and (B.23) in Appendix B. If we know only one of the ionospheric equivalent current and the electric field (or plasma convection velocity, equivalently), then the ionospheric conductivity distribution, either statistically

or from some other experiments, is required to obtain the other quantity as well as the FAC. For example, the KRM method and its improved version, the AMIE technique, both can be used to derive the plasma convection and FAC from the magnetic observations. The SuperDARN FAC analysis technique [*Sofko* et al., 1995; *McWillams*, 1997] derives the FAC component due to the curl of convection velocity, but usually does not take conductivity gradients into account (they can be approximated by an assumed model, but the exact gradients are not known). The uncertainties in the specification of ionospheric conductivities can greatly affect the solutions. Those statistical models may describe the photo-ionization part of the conductances, for example, *Moen and Brekke* [1993]. But the part of the conductances resulting from the precipitating particles is very hard to model accurately because the precipitations are usually highly sporadic and variable both spatially and temporally. *Hardy et al*. [1987] analyzed a great deal of satellite data to derive a statistical model of the contribution of auroral precipitation to the conductances. In the AMIE technique, the satellite observations of the energy fluxes of precipitating particles at the time of the event being analyzed, together with auroral image data, are used to calibrate the conductance model [*Richmond and Kamide*, 1988; *Richmond*, 1992]. Even if the distributions of both the equivalent current and the electric field are known, it is still impossible to solve for the true ionospheric current system unambiguously because in equations (B.18) and (B.23), we have only two equations but three unknown variables, the Pedersen conductance Σ_P, the Hall conductance Σ_H and the FAC $j_{//}$. Some other assumptions are required. For example, in the Untiedt algorithm [*Untiedt and Baumjohann*, 1993] and the method of characteristics [*Amm*, 1998], the ratio between the Hall and Pedersen conductance $\alpha = \Sigma_H / \Sigma_P$ is assumed to be known over the region of interest, or in the "trial and error" approach, a parameterized model for the Hall and Pedersen conductance is used [*Baumjohann et al*., 1981].

With some uncertainties, the conductances can be estimated from the auroral optical emissions at the time of the event. This has been done using data from the auroral imager on the DE-1 satellite [*Lummerzheim et al*., 1991], and the X-ray imager and Ultraviolet imager (UVI) on POLAR satellite [*Aksnes et al*., 2002; *Bristow and Lummerzheim*, 2001]. The model used to invert the brightness of auroral features to

obtain conductances depends on knowledge of the composition of the neutral atmosphere and cross section for ionization and excitation of neutrals by electron impact. It is usually assumed that the auroral precipitation causing the optical emissions is composed only of electrons with a Maxwellian energy distribution. The limitations of such a technique have been discussed by *Germany et al*. [2001]. Despite the uncertainties, the NASI optical observations may also be used to yield useful information about ionospheric conductances. If this optical data are combined with the electric field measurements from the Saskatoon-Kapuskasing radar pair and the magnetic measurements from the CANOPUS (now CGSM), MACCS, and NRCAN/GSC magnetometer arrays (the geometry of observations can be found in Figure .5 and Figure 4.2), a study of three-dimensional ionospheric current systems can be done. In particular, with the construction and deployment of a new ASI at Fort Churchill, the Rankin Inlet-Fort Churchill-Gillam NASI chain will provide coverage from the equatorward edge of the auroral oval to deep inside the polar cap, in conjunction with the observations of Saskatoon-Kapuskasing radar pair. Some other new NASIs are also designed to have overlapping FoVs with the Prince George-Kodiak radar pair. In addition, another set of imagers is being installed in conjunction with the US THEMIS satellite program. The ionospheric conductance estimated from the NORSTAR imager observations can be further calibrated by direct ionization density measurements from the Canadian Advanced Digital Ionosondes (CADI, also a part of CGSM) at several stations. In summary, CGSM and THEMIS ground-based observations will provide the most advanced view of the spatial-temporal evolution of the ionospheric and magnetospheric electrodynamics. A three-dimensional ionospheric current system in the auroral zone and polar cap region over western Canada can be derived with a time resolution as short as one minute. Such a study would be extremely important in improving our understanding of the ionospheric current dynamics and the magnetosphere/ionosphere coupling processes. The prerequisite for this research is the development of some empirical and/or theoretical formulas associating the ground-based auroral emission intensity with the ionospheric conductance; this may not be easy. However, it should be noticed that, for our research purposes, we do not ultimately need definitive conductance estimates from the auroral emission intensity,

because we require only one more or even two (which would provide some redundancy in the degrees of freedom) empirical relationships between Σ_H, Σ_P, and $j_{//}$ to complete the equation set that we have mentioned above. For example, since the green-line (557.7 nm) and red-line (630.0 nm) emission lines are characteristic of high energy (>> 1 keV) and low energy (< 1 keV) electron precipitation respectively, it is possible that, judging from their relative importance, the ratio $\alpha = \Sigma_H / \Sigma_P$ between the ionospheric Hall and Pedersen conductances can be estimated (see Chapter 5.4 for a discussion about the dependence of the Hall and Pedersen conductances on the energy of the precipitating electrons). Thus a method similar to *Untiedt and Baumjohann* [1993] or to *Amm* [1998] can be developed to solve for the ionospheric current with little ambiguity.

References

Aikio, A. T., T. Lakkala, A. Kozlovsky, and P. J. S. Williams, Electric fields and currents of stable drifting auroral arcs in the evening sector, *J. Geophys. Res. 107(A12)*, 1424, doi:10.1029/2001JA009172, 2002.

Aikio, A. T., V. A. Sergeev, M. A. Shukhtina, L. I. Vagina, V. Angelopoulos, and G. D. Reeves, Characteristics of pseudobreakups and substorms observed in the ionosphere, at the geosynchronous orbit, and in the midtail, *J. Geophys. Res*, *104*, 12,263-12,286, 1999.

Akasofu, S.-I., A source of auroral electrons and the magnetospheric substorm current systems, *J. Geophys. Res*, *108(A4)*, 8086, doi:10.1029/2002JA009547, 2003.

Akasofu, S.-I., The development of the auroral substorm, *Planet. Space Sci.*, *12*, 273-282, 1964.

Aksnes, A., J. Stadsnes, G. Lu, N. Østgaard, R. R. Vondrak, D. L. Detrick, T. J. Rosenberg, G. A. Germany, and M. Schulz, Effects of energetic electrons on the electrodynamics in the ionosphere, *Ann. Geophysicae*, *22*, 475-496, 2004.

Aksnes, A., J. Stadsnes, J. Bjordal, N. Østgaard, R. R. Vondrak, D. L. Detrick, T. J. Rosenberg, G. A. Germany, and D. Chenette, Instantaneous ionospheric global conductance maps during an isolated substorm, *Ann. Geophysicae, 20*, 1181-1191, 2002.

Amm, O., Ionospheric elementary current system in spherical coordinates and their application, *J. Geomagn. Geoelectr., 49*, 947-956, 1997.

Amm, O., Method of characteristics in spherical geometry applied to a Harang-discontinuity situation, *Ann. Geophysicae*, *16*, 413-424, 1998.

Andre, R., M. Pinnock, J.-P. Villain, and C. Hanuise, Influence of magnetospheric processes on winter HF radar spectra characteristics, *Ann. Geophysicae*, *20*, 1783-1793, 2002.

Andre, R., M. Pinnock, J.-P. Villain, and C. Hanuise, On the factors conditioning the Doppler spectral width determined from SuperDARN HF radars, *Int. J. Geomag. Aeronomy*., *2*, 77-86, 2000.

Angelopoulos, V., C. F. Kennel, F. V. Coronti, R. Pellat, M.G. Kivelson, R. J. Walker, C. T. Russel, W. Baumjohann, W. C. Fredman, and J. T. Gosling, Statistical characteristics of bursty bulk flow events, *J. Geophys. Res*., *99*, 21,257-21,280, 1994.

Angelopoulos, V., W. Baumjohann, C. F. Kennel, F. V. Coronti, M. G. Kivelson, R. Pellat, R. J. Walker, H. Luhr, and G. Paschmann, Bursty bulk flows in the inner central plasma sheet, *J. Geophys. Res*., *97*, 4027-4039, 1992.

Axford, W. I., and C. O. Hines A unifying theory of high-latitude geophysical phenomena and geomagnetic storms, *Can. J. Phys.*, *39*, 1433-1464, 1961.

Baker, D. N., A. J. Klimas, D. Vassiliadis, T. I. Pulkkinen, and R. L. McPherron, Reexamination of driven and unloading aspects of magnetospheric substorms, *J. Geophys. Res*., *102*, 7169-7177, 1997.

Baker, D. N., T. I. Pulkkinen, V. Angelopoulos, W. Baumjohann, and R. L. McPherron, Neutral line model of substorms: Past results and present view, *J. Geophys. Res.*, *101*, 12,975-13,010, 1996.

Baker, K. B., and S. Wing, A new magnetic coordinate system for conjugate studies at high latitudes, *J. Geophys. Res*., *94*, 9139-9143, 1989.

Baker, K. B., J. R. Dudeney, R. A. Greenwald, M. Pinnock, P. T. Newell, A. S. Rodger, N. Mattin, and C.-I. Meng, HF radar signatures of the cusp and low-latitude boundary layer, *J. Geophys. Res*., *100*, 7671-7695, 1995.

Banks, P. M., and G. Kockarts, *Aeronomy: Part A*, pp. 430, Academic Press, 1973.

Banks, R. J., Strategies for improved global electromagnetic response estimates, *J. Geomagn.. Geoelect*., *33*, 569-586, 1981.

Bargatze, L. F., D. N. Baker, R. L., Mcpherron, and E. W. Hones, Magnetospheric impulse response for many levels of geomagnetic activity, *J. Geophys. Res*., *90*, 6387-6394, 1985.

Baumjohann, W., G. Paschmann, and H. Lühr, Characteristics of high-speed ion flows in the plasma sheet, *J. Geophys. Res.*, *95*, 3801-3809, 1990.

Baumjohann, W., R. J. Pellinen, H. J. Opgenoorth, and E. Nielsen, Joint two-dimensional observations of ground magnetic and ionospheric electric fields associated with auroral zone currents: Current systems associated with local auroral break-ups. *Planet. Space Sci*., *29*, 431-447, 1981.

Baumjohann, W., Y. Kamide, and R. Nakamura, Substorms, storms, and the near-Earth tail, *J. Geomag. Geoelec.*, *48*, 177–185, 1996.

Belehaki, A., I. Tsagouri, and H. Mavromichalaki, Study of the longitudinal expansion velocity of the substorm current wedge, *Ann. Geophysicae, 16*, 1423-1433, 1998.

Benkevitch, L., and W. Lyatsky, Detached vortices in equivalent ionospheric currents in the winter dayside ionosphere, *Geophys. Res. Lett*., *27*, 1375-1378, 2000a.

Benkevitch, L., W. Lyatsky, and L. L. Cogger, Field-aligned currents between conjugate hemispheres, *J. Geophys. Res*., *105*, 27,727- 27,738, 2000b.

Bilitza D., International Reference Ionosphere 2000, *Radio Sci*. *36*, 261-275, 2001.

Birkeland, K., On the cause of magnetic storms and the origin of terrestrial magnetism, *The Norwegian Auroral Polaris Expedition* 1902-1903, Vol. 1, 1st section, pp. 1-315, Christiana(Oslo): H. Aschehoug & Co., 1908.

Birn, J., F. Thomsen, J. E. Borovsky, G. D. Reeves, D. J. McComas, and R. D. Belian, Characteristic plasma properties during dispersionless substorm injections at geosynchronous orbit, *J. Geophys. Res*., *102*, 2309-2324, 1997.

Birn, J., M. Hesse, G. Haerendel, W. Baumjohann, and K. Shiokawa, Flow braking and substorm current wedge, *J. Geophys. Res*., *104*, 19,895-19,904, 1999.

Blanchard G. T., L. R. Lyons, and J. C. Samson, Accuracy of using 6300 A auroral emission to identify the separatrix on the nightside of Earth, *J. Geophys. Res*., *102*, 9697-9703, 1997.

Blanchard, G. T., L. R. Lyons, O. de la Beaujardière, R. A. Doe, and M. Mendillo, Measurement of the magnetotail reconnection rate, *J. Geophys. Res*., *101*, 15,265-15,276, 1996.

Blomberg L. G., and G. T. Marklund, The influence of conductivities consistent with field-aligned currents on high-latitude convection patterns, *J. Geophys, Res*., *93*, 14,493-14,499, 1988.

Boralv, E., P. Eglitis, H. J. Opgenoorth, E. Donovan, G. Reeves, and P. Stauning, The dawn and dusk electrojet response to substorm onset, *Ann. Geophysicae, 18*, 1097-1107, 2000.

Bristow, W. A., A. Otto, and D. Lummerzheim, Substorm convection patterns observed by the Super Dual Auroral Radar Network, *J. Geophys. Res.*, *106*, 24,593-24,609, 2001.

Bristow, W. A., and D. Lummerzheim, Determination of filed-aligned currents using the Super Dual Auroal Radar Network and the UVI ultraviolet imager, *J. Geophys. Res.*, *106*, 18,577-18,588, 2001.

Bristow, W. A., G. J. Sofko, H. C. Stenbaek-Nielsen, S. Wei, D. Lummerzheim, and A. Otto, Detailed analysis of substorm observations using SuperDARN, UVI, ground-based magnetometers, and all-sky imagers, *J. Geophys. Res, 108(A3)*, doi:10.1029 /2002JA009242, 2003.

Burg, J. P., Maximum Entropy Spectral Analysis, Ph.D. thesis, Stanford University, 1975.

Cowley, S. W. H., and M. Lockwood, Excitation and decay of solar wind-driven flows in the magnetosphere-ionosphere system, *Ann. Geophysicae*, *10*, 103-115, 1992.

Cowley, S. W. H., Interpretation of observed relations between solar wind characteristics and effects at ionospheric altitudes, in *High Latitude Space Plasma Physics*, edited by B. Hultquist and T. Hagfors, pp. 225-249, Plenum, New York, 1983.

Cravens, T. E., *Physics of solar system plasmas*, Cambridge University Press, New York, 1997.

Danskin, D. W., A.V. Koustov, R. Makarevitch, and M. Lester, Observations of double-peaked E-region coherent spectra with the CUTLASS Finland HF radar. Radio Science, *39*, RS2006, doi:10.1029/2003RS0029032, 2004.

De la Beaujardière, L. R. Lyons, J. M. Ruohonmiemi, E. FriisChristensen, C. Danielsen, F. J. Rich, and P. T. Newell, Quite-time intensifications along the poleward auroral boundary near midnight, *J. Geophys. Res*., *99*, 287-298, 1994.

Doe, R. A., J. F. Vickrey, and M. Mendillo, Electrodynamic model for the formation of auroral ionospheric cavities, *J. Geophys. Res. Vol. 100*, 9683-9696, 1995.

Doe, R. A., M. Mendillo, J. F. Vickrey, L. J. Zanetti, and R. W. Eastes, Observations of nightside auroral cavities, *J. Geophys. Res.*, *98*, 293-310, 1993.

Donovan, E. F., B. J. Jackel, I. Voronkov, T. Sotirelis, F. Creutzberg, and N. A. Nicholson, Ground-based optical determination of the b2i boundary: A basis for an optical MT-index, *J. Geophys. Res.*, *108*(A3), 1115, doi:10.1029/2001JA009198, 2003.

Dudeney, J. R., A. S. Rodger, M. P. Freeman, J. Pickett, Scuder, G. J. Sofko, and M. Lester, The nightside ionospheric response to IMF By changes, *Geophys. Res. Lett*., *25*, 2601-2604, 1998.

Dungey, J. W., Interplanetary magnetic field and the auroral zones, *Phys. Rev. Lett.*, *6*, 47-48, 1961.

Eastman, T. E., and E.W. Hones, Characteristics of the magnetospheric boundary layer and magnetopause layer as observed by IMP 6, *J. Geophys. Res*., *84*, 2019-2028, 1979.

Elphinstone, R. D., D. J. Hearn, L. L. Cogger, J. S. Murphree, H. Singer, V. Sergeev, K. Mursula, D. M. Klumpar, G. D. Reeves, M. Johnson, S. Ohtani, T. A. Potemra, I. Sandahl, E. Nielsen, M. Persson, H. Opgenoorth, P. T. Newell, and Y. I. Feldstein, Observations in the vicinity of substorm onset: Implications for the substorm process, *J. Geophys. Res*., *100*, 7937-7969, 1995.

Erickson, G. M., N. C. Maynard, W. J. Burke, G. R. Wilson, and M. A. Heinemann, Electromagnetics of substorm onsets in the near-geosynchronous plasma sheet, *J. Geophys. Res*., *105*, 25265-25290, 2000.

Fairfield, D. H., T. Mukai, M. Brittnacher, G. D. Reeves, S. Kokubun, G. K. Parks, T. Nagai, H. Matsumoto, K. Hashimoto, D. A. Gurnett, and T. Yamamoto, Earthward flow bursts in the inner magnetotail and their relation to auroral brightenings, AKR

intensifications, geosynchronous particle injections magnetic activity, *J. Geophys. Res*., *104*, 355-370, 1999.

Friedrich, E., J.C. Samson, I. Voronkov, and G. Rostoker, Dynamics of the substorm expansive phase, *J. Geophys. Res*., 106, 13,145-13,163, 2001.

Fukushima, N., Generalized theorem of no ground magnetic effect of vertical current connected with Pedersen currents in the uniform conductivity ionosphere, *Rep. Ionos. Space. Res. Jap*., *30*, 35-40, 1976.

Fuselier S. A., D. M. Klumpar, W. K. Peterson, and E. G. Shelley, Direct injection of ionospheric O+ into the dayside low latitude boundary layer, *Geophys. Res. Lett*., *16*, 1121-1124, 1989.

Galand, M., T. J. Fuller-Rowell, and M. V. Codrescu, Response of the upper atmosphere to auroral protons, *J. Geophys. Res., 106*, 127-139, 2001.

Gauld, J. K., T. K. Yeoman, J. A. Davies, S. E. Milan, and F. Honary, SuperDARN radar HF propagation and absorption response to the substorm expansion phase, *Ann. Geophysicae, 20*, 1631-1645, 2002.

Germany, G. A., D. Lummerzheim, and P. G. Richards, Impact of model differences on quantitative analysis of FUV auroral emissions: total ionization cross sections, *J. Geophys*. *Res*., *106*, 12,837-12,843, 2001.

Glassmeier, K. H., Ground-based observations of field-aligned currents in the auroral zone: Methods and results, *Ann. Geophysicae*, *5*, 115-125, 1987.

Greenwald, R. A., K. B. Baker, J. R. Dudeney, M. Pinnock, T. B. Jones, C. Thomas, J.-P. Villain, J.-C. Cerisier, C. Hanuise, R. D. Hunsucker. G. J. Sofko, J. Koehler, E. Nielsen, and R. Pellinen, DARN/SUPERDARN, A Global View of the Dynamics of High-Latitude Convection, *Space Sci. Rev*., *71*, 761-796, 1995.

Grocott, A., S. W. H. Cowley, J. B. Sigwarth, J. F. Watermann, and T. K. Yeoman, Excitation of twin-vortex flow in the nightside high-latitude ionosphere during an isolated substorm, *Ann. Geophysicae, 20*, 1577-1601, 2002.

Haines, G. V., and M. J. Torta, Determination of equivalent current sources from spherical cap harmonic models of geomagnetic field variations, *Geophys. J. Intl*., *118*, 499-514, 1994.

Haines, G. V., Computer programs for spherical cap harmonic analysis of potential and general fields. *Computers and Geosci*., *14*, 413-447, 1988.

Haines, G. V., Spherical cap harmonic analysis, *J. Geophys. Res*., *90*, 2583-2591, 1985.

Hairston, M. R., and R. A. Heelis, Response time of the polar ionospheric convection pattern to changes in the north-south direction of the IMF, *Geophys. Res. Lett*., 22, 631-634, 1995.

Hapgood, M. A., Space Physics Coordinate Transformations: A User Guide, *Planet. Space. Sci*., *40*, 711-717, 1992.

Harang, L., The mean field of disturbance of polar geomagnetic storms, *Terr., Magn., Atmos. Electr*., *51*, 353-380, 1946.

Hardy, D. A, M. S. Gussenhoven, R. Raistrick, and W. J. McNeil, Statistical and functional representations of the pattern of auroral energy flux, number flux, and conductivity, *J. Geophys. Res., 92*, 12,275-12,294, 1987.

Hardy, D. A., M. S. Gussenhoven, and D. Brautigam, A statistical model of auroral ion precipitation, *J. Geophys. Res.*, *94*, 370-392, 1989.

Hashimoto, K., L. Lyons, T. Kokuchi, and E. Sagawa, Case study of the evolution of global ionospheric convection during substorms, *SuperDARN Workshop*, Saskatoon, Canada, 2004.

Henderson, M. G., G. D. Reeves, and J. S. Murphree, Are north-south structures an ionospheric manifestation of bursty bulky flows? *Geophys. Res. Lett., 25*, 3737-3740, 1998.

Heppner, J. P., and N. C. Maynard, Empirical high-latitude electric field models, *J. Geophys. Res.*, *92*, 4467-4489, 1987.

Hobson, E. W., *The Theory of Spherical and Ellipsodal Harmonics*, Cambridge University Press, New York, 1931.

Hoffman, R. A., R. Fujii, and M. Sugiura, Characteristics of the field-aligned current system in the nighttime sector during auroral substorms, *J. Geophys. Res*., *99*, 21,303-21,325, 1994.

Huang, C. S., D. Murr, G. J. Sofko, W. J. Hughes, and T. Moretto, Ionospheric convection response to changes of interplanetary magnetic field Bz component during strong By component, *J. Geophys. Res., 105*, 5231-5243, 2000.

Huber, M., and G. J. Sofko, Small-scale vortices in the high-latitude F region, *J. Geophys. Res. 105*, 20,885-20,897, 2000.

Iijima T., and T. A. Potemra, Large-scale characteristics of field-aligned currents associated with substorms, *J. Geophys. Res., 83*, 599-615, 1978.

Ivanov, V. N., and O. A. Pokhotelov, Flute instability in the plasma sheath of the Earth' s magnetosphere, *Sov. J. Plasma Phys., 13*, 833-842, 1987.

Ivanov, V. N., O. P. Pokhotelov, F. Z. Feygin, A. Roux, S. Perraut, and D. Leko, Balloon instability in a terrestrial magnetosphere with irregular pressure and a finite β, *Geomagn. Aeron., 32*, 211-216, 1992.

Jackel, B. J., F. Creutzberg, E. F. Donovan, and L. L. Cogger, Triangulation of auroral red-line emission heights, *Proc. Atoms. Studies by Optical Methods*, pp. 1-4, 2003.

Jayachandran P. T., E. F. Donovan, J. W. MacDougall, D. R. Moorcroft, J.-P. St. Maurice, and P. Prikryl, SuperDARN E-region backscatter boundary in the dusk-midnight sector – tracer of equatorward boundary of the auroral oval, *Ann. Geophysicae, 20*, 1899-1904, 2002.

Jayachandran, P. T., J. W. MacDougall , E. F. Donovan , J. M. Ruohoniemi , K. Liou, D. R. Moorcroft and J.-P. St-Maurice, Substorm Associated Changes in High-latitude Ionospheric Convection, *Geophys. Res. Lett., 30*, 2064-2067, doi:10.1029/2003GL017497, 2003.

Jones, A. V., *Aurora*, edited by Geophysics and Astrophysics Monographs, pp. 83-84, D. Reidel Publishing Company, Dordrecht, Holland, 1974.

Kadokura, A., A. S. Yukimatu, M. Ejiri, T. Oguti, M. Pinnock, and M. R. Hairston, Detailed analysis of a substorm event on 6 and 7 June 1989, 1. Growth phase evolution of nightside auroral activities and ionospheric convection toward expansion phase onset, *J. Geophys. Res., 107*, doi:10.1029/2001JA009127, 2002a.

Kadokura, A., S. S. Yukimatu, M. Ejiri, T. Oguti, M. Pinnock, and P. R. Sutcliffe, Detailed analysis of a substorm event on June 6-7, 1989: 2, Stepwise auroral bulge evolution during expansion phase, *J. Geophys. Res., 107(A12)*, doi:10.1029/2001JA009129,2002b.

Kamide, Y., A. D. Richmond, and S. Matsushita, Estimation of ionospheric electric fields, ionospheric currents, and field-aligned currents from ground magnetic records, *J. Geophys. Res.*, *86*, 801-813, 1981.

Kamide, Y., A. D. Richmond, B. A. Emery, C. F. Hutchins, B.-H. Ahn, O. de la Beaujardiere, J. C. Foster, R. A. Heelis, H. W. Kroehl, F. J. Rich, and J. A. Slavin, Ground-based studies of ionospheric convection associated with substorm expansion, *J. Geophys. Res*., *99*, 19,451-19466, 1994.

Kamide, Y., and S. Kokubun, Two-component auroral electrojet: Importance for substorm studies, *J. Geophys. Res., 101*, 13,027-13,046, 1996.

Kamide, Y., The substorm current system: Predicting specific features, *Proc. ICS-3, ESA, SP-389*, pp. 5–10, 1996.

Kan, J. R. and L. C. Lee, Energy coupling function and solar wind-magnetosphere dynamo, *Geophys. Res. Lett*., *6*, 577-580, 1979.

Kan, J. R., A global magnetosphere-ionosphere coupling model of substorms, *J. Geophys. Res.*, *98*, 17,263-17,276, 1993

Kavanagh, A.J., F. Honary, I.W. McCrea, E. Donovan, E. E. Woodfield, J. Manninen, and P.C. Anderson, Substorm related changes in precipitation in the dayside auroral zone: a multi-instrument case study, *Ann. Geophysicae, 20*, 1321-1334, 2002.

Kelley, M. C., J. F. Vickrey, C. W. Carlson, and R. Torbert, On the origin and spatial extent of high-latitude F region irregularities, *J. Geophys. Res.*, *87*, 4469-4475, 1982.

Kelley, M. C., *The earth's ionosphere: Plasma physics and electrodynamics*, pp. 15, Academic Press, San Diego, 1989.

Kennel, C. F., *Convection and Substorms: Paradigms of magnetospheric Phenomenology*, pp. 116-120, Oxford Univ. Press, New York, 1995.

Kepko, L., and M. Kivelson, Generation of Pi2 pulsations by bursty bulk flows, *J. Geophys. Res*. *104*, 25,021-25,034, 1999.

Kepko, L., M. Kivelson, and K. Yumoto, Flow bursts, braking, and Pi2 pulsations, *J. Geophys. Res*. *106*, 1903-1915, 2001.

Khan, H., and S. W. H. Cowley, Observations of the response time of high-latitude ionospheric convection to variations in the interplanetary magnetic field using EISCAT and IMP-8 data, *Ann. Geophysicae, 17*, 1305-1335, 1999.

Khan, H., S. W. H. Cowley, E. Kolesnikova, M. Lester, M. J. Brittnacher, T. J. Hughes, W. J. Hughes, W. S. Kurth, D.J. McComas, L. Newitt, C. J. Owen, G.D. Reeves, H. J. Singer, C. W.Smith, D. J. Southwood, and J. F. Waterman, Observations of two complete substorm cycles during the Cassini Earth swing-by: Cassini magnetometer data in a global context, *J. Geophys. Res., 106*, 30,141-30,175, 2001.

Kikuchi, T., H. Luhr, T. Kitamura, O. Saka, and K. Schlegel, Direct penetration of the polar electric field to the equator during a DP2 event as detected by the auroral and equatorial magnetometer chains and the EISCAT radar, *J. Geophys. Res., 101*, 17,161-17,173, 1996.

Kikuchi, T., M. Pinnock, A. Rodger, H. Luehr, T. Kitamura, H. Tachihara, M., Watanabe, N. Sato and M. Ruohoniemi, Global evolution of a substorm-associated DP2 current system observed by SuperDARN and magnetometers, *Adv. Space Res., 26*, 121-124, 2000.

Kivelson, M. G., and C. T. Russel, *Introduction to space physics*, pp. 268, Cambridge University Press, New York, 1995.

Kokubun, S., and R. L. McPherron, Substorm signatures at synchronous altitude, *J. Geophys. Res., 86*, 11,265-11,277, 1981

Koskinen H. E. J., R. E. Lopez, R. J. Pellinen, T. I. Pulkkinen, D. N. Baker, and T. Bosinger, Pseudobreakup and substorm growth phase in the ionosphere and magnetosphere, *J. Geophys. Res, 98*, 5801-5813 1993.

Koskinen, H. E. J., and T. I. Pulkkinen, Midnight velocity shear zone and the concept of Harang discontinuity, *J. Geophys. Res., 100*, 9539-9547, 1995.

Lam, M. M., M. Pinock, and E. F. Donovan, Relating observations of nightside reconnection to substorms and auroral poleward boundary intensifications, *SuperDARN Workshop*, Saskatoon, Canada, 2004.

Lester, M, HF coherent scatter observations of ionospheric condition during magnetospheric substorms, *Adv. Polar Upper Atmos. Res., 14*, 179-201, 2000.

Lester, M, Ionospheric Convection during magnetospheric substorms, *Proceedings of ICS-6*, pp. 85-92, 2002.

Lester, M., S. Milan, V. Besser, and R. Smith, A case study of HF radar spectra and 630.0 nm auroral emission in the pre-midnight sector, *Ann. Geophysicae*, *19*, 327-339, 2001.

Lewis, R. V., M. P. Freeman, A. S. Rodger, G. D. Reeves, and D. K. Milling, The electric field response to the growth phase and expansion phase onset of a small isolated substorm, *Ann. Geophysicae*, *15*, 289-299, 1997.

Lewis, R. V., P. J. S. Williams, T. S. Virdi, T. K. Yeoman, and M. Lester, EISCAT measurements of flow bursts in plasma velocity during substorm activity, in *Proc. ICS-1*, pp. 125-129, *Eur. Space Agency Spec. Publ., ESA SP-335*, 1992.

Liang, J., G. J. Sofko, and E. F. Donovan, On the spatial and temporal relationship between auroral intensification and flow enhancement in a pesudosubstorm event, *J. Geophys. Res.*, *109(A6)*, A06213, doi:10.1029/2003JA010200, 2004a.

Liang, J., G. J. Sofko, E. F. Donovan, M. Watanabe, and R. A. Greenwald, Convection dynamics and driving mechanism of a small substorm during dominantly IMF By+, Bz+ conditions, *Geophys. Res. Lett.*, *31*, L08803, doi:10.1029/2003GL018878, 2004b.

Liou, K., C.-I. Meng, A. T. Y. Lui, P. T. Newell, and S. Wing, Magnetic depolarization with substorm expansion onset, *J. Geophys. Res.*, *107*(A7), doi:10.1029 /2001JA000179, 2002.

Liu, W. W., Physics of the explosive growth phase: Ballooning instability revisited, *J. Geophys. Res*., *102*, 4927-4931, 1997.

Lockwood, M., and S. W. H. Cowley, Comment on "A statistical study of the ionospheric convection response to changing interplanetary magnetic field conditions using the assimilative mapping of ionospheric electro-dynamics technique" by A. J. Ridley et al., *J. Geophys. Res*., *104*, 4387-4391, 1999.

Lopez, R. E., and A. T. Y. Lui, A multisatellite case study of the expansion of a substorm current wedge in the near-Earth magnetotail, *J. Geophys. Res.*, *95*, 8009-8017, 1990.

Lopez, R. E., H. Lühr, B. J. Anderson, P. T. Newell, and R. W. McEntire, Multipoint observations of a small substorm, *J. Geophys. Res*., *95*, 18,897-18,912, 1990.

Lu, G., A. D. Richmond, Y. Kamide, D. Lummerzheim, M. Brittnacher, and G. Parks, Global ionospheric convection during substorm expansion, in *Proc. ICS-4*, edited by S. Kokubun and Y. Kamide, pp. 617-622, Kluwer Academic, Norwell, 1998.

Lu, G., M. Brittnacher, G. Parks, and D. Lummerzheim, On the magnetospheric source regions of substorm-related field-aligned currents and auroral precipitation, *J. Geophys. Res*., *105*, 18,483-18493, 2000.

Lui, A. T. Y., A synthesis of magnetospheric substorm models, *J. Geophys. Res*. *96*, 1849-1856, 1991.

Lui, A. T. Y., and Y. Kamide, A fresh perspective of the substorm current system and its dynamo, *Geophys. Res. Lett*., *30(18)*, 1958, doi:10.1029/2003GL017835, 2003.

Lui, A. T. Y., C.-L. Chang, A. Mankofsky, H.-K.Wong, and D. Winske, A cross-field current instability for substorm expansions, *J. Geophys. Res*. *96*, 11,389-11,401, 1991.

Lui, A. T. Y., Current controversies in magnetospheric physics, *Rev. Geophys*., *39*, 533-563, 2001.

Lui, A. T. Y., Current disruption in the Earth' smagnetosphere: Observations and models, *J. Geophys. Res*., *101*, 13,067-13,088, 1996.

Lui, A. T. Y., K. Liou, M. Nose, S. Ohtani, D. J. Williams, T. Mukai, K. Tsuruda, and S. Kokubun, Near-Earth dipolarization: Evidence for a non-MHD process, *Geophys. Res. Lett*., *26*, 2905-2908, 1999.

Lui, A. T. Y., T. E. Eastman, D. J. Williams, and L. A. Frank, Observations of ion streaming during substorms, *J. Geophys. Res.*, *88*, 7753-7764, 1983

Lummerzheim, D., M. H. Rees, D. J. Craven, and L. A. Frank, Ionospheric Conductances Derived from DE-1 Auroral Images, *J. Atm. Terr. Phys*., *53*, 281-292, 1991.

Lyatsky, W., A. V. Kustov, G. J. Sofko, B. Jacobsen, D. Andre, and L. L. Cogger, Ionospheric convection and equivalent ionospheric currents in the dayside high-latitude winter ionosphere, *J. Geophys. Res*., *104*, 22,525-22,534, 1999.

Lyons L. R., G. Lu, O. de la Beaujardière, and F. J. Rich, Synoptic maps of polar caps for stable interplanetary magnetic field intervals during January 1992 geospace environment modeling campaign, *J. Geophys. Res*., *101*, 27,283-27,298, 1996.

Lyons, L. R., D. S. Evans, and R. Lundin, An observed relationship between magnetic field-aligned electric fields and downward electron energy fluxes in the vicinity of auroral forms, *J. Geophys. Res*., *84*, 457-461, 1979.

Lyons, L. R., J. M. Ruohoniemi, and G. Lu, Substorm-associated changes in large-scale convection during the November 24, 1996 Geospace Environment Modeling event, *J. Geophys. Res., 106*, 397-405, 2001.

Lyons, L. R., S. Liu, J. M. Ruohoniemi, S. I. Solovyev, and J. C. Samson, Observations of dayside convection reduction leading to substorm onset, *J. Geophys. Res*., *108*(A3), 1119-, doi:10.1029/ 2002JA009670, 2003

Lyons, L. R., T. Nagai, G. T. Blanchard, J. C. Samson, T. Yamamoto, T. Mukai, A. Nishida, and S. Kokubun, Association between Geotail plasma flows and auroral poleward boundary intensifications observed by CANOPUS photometers, *J. Geophys. Res*, *104*, 4485-4500, 1999.

Machida, S., Y. Miyashita, A. Ieda, A. Nishida, T. Mukai, Y. Saito, and S. Kokubun, Geotail observations of flow velocity and north-south magnetic field variations in the near and mid-distant tail associated with substorm onsets, G*eophys. Res. Lett., 26*, 635-638, 1999.

Maynard, N. C., W. J. Burke, E. M Basinska, G. M Reickson, W. J. Hughes, H. J. Singer, A. G. Yahnin, D. A. Hardy, and F. S. Moser, Dynamics of the inner magnetosphere near times of substorm onsets, *J. Geophys. Res*., *101*, 7705-7736, 1996.

McPherron, R. L., C. T. Russell, and M. Aubry, Satellite studies of magnetospheric substorms on August 15, 1978, 9, Phenomenological model for substorms, *J. Geophys. Res.*, *78*, 3131-3149, 1973.

McWilliams, K. A., A SuperDARN Study of Dayside Field-aligned Current Regions, M. Sc. Thesis, Dept. of Physics and Engineering Physics, Univ. of Saskatchewan, Saskatoon, Canada, 1997.

McWilliams, K. A., Multi-Pulse Sequence Optimization and Testing: A Tutorial, *SuperDARN Workshop*, Kiljava, Finland, 2003

Milan, S. E., and M. Lester, Interhemispheric differences in the HF radar signature of the cusp region: A review through the study of a case example, *Adv. In Polr Upper Atmos. Res*., *15*, 159-177, 2001.

Milan, S. E., M. Lester, S. W. H. Cowley, K. Oksavik, M. Brittnacher, R. A. Greenwald, G. Sofko, and J.-P. Villain, Variations in polar cap area during two substorm cycles, *Ann. Geophysicae, 21*, 1121-1140, 2002.

Moen, J., and A. Brekke, The solar flux influence on quiet time conductivities in the auroral ionosphere, *Geophys, Res. Lett*., *20*, 971-974, 1993.

Moldwin, M. B., and W. J. Hughes, Geomagnetic substorm association of plasmoids, *J. Geophys. Res.*, 98, 81-88, 1993.

Murr, D. L., and W. J. Hughes, Reconfiguration timescales of ionospheric convection, *Geophys. Res. Lett*., *28*, 2145-2149, 2001.

Nagai, T., Field-aligned currents associated with substorms in the vicinity of synchronous orbit, 2. GOES 2 and GOES 3 observations, *J. Geophys. Res*., *92*, 2432-2446, 1987.

Nagai, T., K. Takahashi, H. Kawano, T. Yamamoto, S. Kokubun, and A. Nishida, Initial Geotail survey of magnetic substorm signatures in the magnetotail, *Geophys. Res. Lett., 21*, 2991-2994, 1994.

Nagai, T., M. Fujimoto, Y.Saito, S. Machida, T. Terasawa, R. Nakamura, T. Yamamoto, T. mukai, A. Nishida, and S. Kokubun, Structure and dynamics of magnetic reconnection for substorm onsets with GEOTAIL observations, *J. Geophys. Res*, *103*, 4419-4440, 1998.

Nakamura, R., D. N. Baker, T. Yamamoto, R. D. Belian, E. A. Bering III, J. R. Benrook, and J. R. Theall, Particle and field signatures during pseudobreakup and major expansive onset, *J. Geophys. Res*, *99*, 207-222, 1994.

Nakamura, R., L. F. Bargatze, T. Mukai, T. Nagai, K. B. Baker, M. R. Hairston, P. H. Reiff, A. A. Petrukovich, M. Nozdrachev, and O. A. Troshichev, Response of the midtail electric field to enhanced solar wind energy input, *J. Geophys. Res., 104*, 17,299-17,310, 1999.

Nakamura, R., W. Baumjohann, M. Brittnacher, V. A. Sergeev, M. Kubyshkina, T. Mukai, and K. Liou, Flow bursts and auroral activations: Onset timing and foot point location, *J. Geophys. Res*., *106*, 10,777-10,789, 2001a.

Nakamura, R., W. Baumjohann, R. Schodel, M. Brittnacher, V. A. Sergeev., M. Kubyshkina, T. Mukai, and K. Liou, Earthward flow bursts, auroral streamers, and small expansions, *J. Geophys. Res*., *106*, 10,791-10,802, 2001b.

Nemecek, Z., and J. Safrankova, The Earth's bow shock and magnetopause position as a result of the solar wind-magnetosphere interaction, *J. Atmos. Terr. Phys*., *53*, 1049-1054, 1991.

Newell, P. T., Y. I. Feldstein, Y. I. Galperin, and C.-I. Meng, Morphology of nightside precipitation, *J. Geophys. Res*., *101*, 10,737-10,748, 1996.

Nishida, A., T. Mukai, T. Yamamoto, S. Kokubun, and K. Maezawa, A unified model of the magnetotail convection in geomagnetically quiet and active times. *J. Geophys. Res. 103*, 4409-4418, 1998.

Ohtani, S., and S. Tamao, Does the ballooning instability trigger substorms in the near-Earth magnetotail? *J. Geophys. Res.*, *98*, 19,369-19,379, 1993a.

Ohtani, S., B. J. Anderson, D. G. Sibeck, P. T. Newell, L. J. Zanetti, T. A. Potemra, K. Takahashi, R. E. Lopez, V. Angelopoulos, R. Nakamura, D. M. Klumpar, and C. T. Russell, A multisatellite study of a pseudo-substorm onset in the near-Earth magnetotail, *J. Geophys. Res.*, *98*, 19355-19367, 1993b.

Ohtani, S., On the tailward expansion of current disruption during substorms, *Adv. Space. Res*., *13*, 265-268, 1993c.

Ohtani, S., R. Yamaguchi, M. Nosé, H. Kawano, M. Engebretson, and K. Yumoto, Quiet time magnetotail dynamics and their implications for the substorm trigger, *J. Geophys. Res.*, *107(A2)*, 1030, doi:10.1029/2001JA000116, 2002.

Olson, J. V., and G. Rostoker, Pi2 pulsations and the auroral electrojet, *Planet. Space. Sci*., *23*, 1129-1139, 1975.

Olson, J. V., Pi2 pulsations and substorm onsets: A review, *J. Geophys. Res*., *104*, 17,499-17,520, 1999.

Parker, E. N., Extension of the solar corona into interplanetary space, *J. Geophys. Res.*, *64*, 1675-1681, 1959.

Parkinson M. L., The importance of ionospheric Pedersen conductivity in the control of ionospheric irregularities and their Doppler characteristics, *SuperDARN Workshop*, Saskatoon, Canada, 2004.

Parkinson, M. L., M. Pinnock, H. Ye, M. R. Hairston, J. C. Devlin, P. L. Dyson, R. J. Morris and P. Ponomarenko . On the lifetime and extent of an auroral westward flow channel (AWFC) observed during a magnetospheric substorm, *Ann. Geophysicae, 21*, 893-913, 2003.

Penman, J. M., J. K. Hargreaves, and C. E. McIlwain, The relation between 10 to 80 keV electron precipitation observed at geosynchronous orbit and auroral radio absorption observed with riometers, *Planet. Space Sci., 27*, 445-451, 1979.

Pu, Z. Y., A. Korth, Z. X. Chen, R. H. W. Friedel, Q. G. Zong, X. M. Wang, M. H. Wong, S. Y. Fu, and T. I. Pulkkinen, MHD drift ballooning instability near the inner edge of the near-Eearth plasma sheet. *J. Geophys. Res., 102*, 14,397-14406, 1997.

Pu, Z. Y., K. B. Kang, A. Korth, S. Y. Fu, Q. G. Zong, Z. X. Chen, M. H. Hong, Z. X. Liu, C. G. Mouikis, R. H. W. Friedel, and T. Pulkkinen. Ballooning instability in the presence of a plasma flow: A syntheses of tail reconnection and current disruption models for the initiation of substorms. *J. Geophys. Res., 104*, 10,235-10248, 1999.

Rees, D., Cosper International Reference Atmosphere: 1986 Part I:Thermosphere Models, *Advances in Space Research Vol.8 No 5-6*, Pergamon Press,1988.

Reiff, P. H., and J. L. Burch, IMF By-dependent plasma flow and Birkeland currents in the dayside magnetopause. 2. A global model for northward and southward IMF, *J. Geophys. Res., 90*, 1595-1609, 1985.

Richmond A. D., and Y. Kamide, Mapping electrodynamic features of the high-latitude ionosphere from localized observations: Technique, *J. Geophys. Res., 93*, 5741-5759, 1988.

Richmond, A. D., Assimilative mapping of ionospheric electrodynamics, *Adv. Space Res., 12*, 59-68, 1992.

Ridley, A. J., Estimations of the uncertainty in timing the relationship between magnetospheric and solar wind processes, *J. Atmos. Sol. Terr. Phys., 62*, 757-771, 2000.

Ridley, A. J., G. Lu, C. R. Clauer, and V. O. Papitashvili, A statistical study of the ionospheric convection response to changing interplanetary magnetic field conditions using the assimilative mapping of ionospheric electrodynamics technique, *J. Geophys. Res*., *103*, 4023-4039, 1998.

Ridley, A. J., G. Lu, C. R. Clauer, and V. O. Papitashvili, Reply, *J. Geophys. Res*., *104*, 4393-4396, 1999.

Robinson, R. M., R. R. Vondrak, K. Miller, T. Dabbs, and D. Hardy, On calculating ionospheric conductances from the flux and energy of precipitating electrons, *J. Geophys. Res*., *92*, 2565-2569, 1987.

Rostoker, G., J.C. Samson, F. Creutzberg, T.J. Hughes, D.R. McDiarmid, A.G. McNamara, A. Vallance Jones, D.D. Wallis and L.L. Cogger, CANOPUS- a ground-based instrument array for remote sensing the high latitude ionosphere during the ISTP/GGS program, *Space Sci. Rev., 71* , 743-760, 1995.

Rostoker, G., On the place of the pseudo-breakup in a magnetospheric substorm, *Geophys. Res. Lett*., *25*, 217-220, 1998.

Rostoker, G., S.-I. Akasofu, J. Foster, R. A. Greenwald, Y. Kamide, K. Kawasaki, A. T. Y. Lui, R. L. McPherron, and C. T. Russell, Magnetospheric substorms - Definition and signatures, *J. Geophys. Res.*, 85, 1663-1668, 1980.

Rostoker, G., S.-I. Akasofu, W. Baumjohann, Y. Kamide, and R. L. McPherron, The roles of direct input of energy from the solar wind and unloading of stored magnetotail energy in driven magnetospheric substorms, *Space Sci. Rev., 46*, 93-111, 1987.

Rostoker, G., The macrostructure of geomagnetic bays, *J. Geophys. Res*., *73*, 4217-4229, 1968.

Roux, A., S. Perraut, P. Robert, A. Morane, A. Pedersen, A. Korth, G. Kremser, B. Aparicio, D. Rodgers, and R. Pellinen, Plasma sheet instability related to the Westward Traveling Surge, *J. Geophys. Re*s., *96*, 17,697-17,714, 1991.

Ruohoniemi, J. M, and R. A. Greenwald, The response of high-latitude convection to a sudden southward IMF turning, *Geophys. Res. Lett*., *25*, 2913-2916, 1998.

Ruohoniemi, J. M., and K. B. Baker, Large-scale imaging of high-latitude convection with Super Dual Auroral Radar Network HF radar observations, *J. Geophys. Res*., *103*, 20,797-20,811, 1998.

Ruohoniemi, J. M., and R. A. Greenwald, Rates of scattering occurrence in routine HF radar observations during solar cycle maximum, *Radio Sci., 32*, 1051-1070, 1997.

Ruohoniemi, J. M., and R. A. Greenwald, Statistical patterns of high-latitude convection obtained from Goose Bay HF radar observations, *J. Geophys. Res.*, *101*, 21,743-21,763, 1996.

Saka, O., T. Kitamura, H. Tachihara, M. Shinohara, N. B. Trivedi, N. Sato, J. M. Ruohoniemi, and R. A. Greenwald, A substorm onset signature at auroral zone as observed with SuperDARN and equatorial magnetometers, *J. Geophys. Res, 106*, 29037-29050, 2001.

Samson, J. C., A. K. MacAulay, R. Rankin, R., P. Frycz, I. Voronkov, and L. L. Cogger, Substorm Intensifications and Resistive Shear Flow Ballooning Instabilities, in *Proc. ICS-3*, edited by E. J. Rolfe and B. Kaldeich, pp. 399-404, ESA SP-389, Versailles, 1996.

Sandholt, P. E., C. J. Farrugia, M. Lester, S. W. H. Cowley, S.E. Milan, W.F. Denig, B. Lybekk, E. Trondsen, and V. Vorobjev, Multi-stage substorm expansion: Auroral dynamics in relation to plasma sheet particle injection, precipitation, and plasma convection, *J. Geophys. Res, 107*, doi:10.1029/2001JA90016, 2003.

Saunders, M. A., M. P. Freeman, D. J. Southwood, S. W. H. Cowley, M. Lockwood, J. C. Samson, C. J. Farrugia, and T. J. Hughes, Dayside ionospheric convection changes in response to long-period interplanetary magnetic field oscillations: Determination of the ionospheric phase velocity, *J. Geophys. Res*., 97, 19,373-19,380, 1992.

Schiffler, A, SuperDARN measurements of double-peaked velocity spectra, M. Sc. These, Univ. of Saskatchewan, Saskatoon, Canada, 1996.

Schlegel, K., and J.-P. St-Maurice, Anomalous heating of the polar E-region by unstable plasma waves, *J. Geophys. Res., 86*, 1447-1452, 1981.

Sergeev, V. A, M. A. Shukhtina, R. Rasinkangas, A. Korth, G. D. Reeves, H. J. Singer, M. F. Thomsen, and L. I. Vagina, Event study of deep energetic particle injections during substorm, *J. Geophys. Res*., *103*, 9217-9234, 1998a.

Sergeev, V. A., A. G. Yahnin, R. A. Rakhmatulin, S. I. Solovjev, F. S. Mozer, D. J. Williams, and C. T. Russell, Permanent flare activity in the auroral zone, *Planet. Space Sci.*, *34*, 1169-1188, 1986.

Sergeev, V. A., M. Kubyshkina, K. Liou, P. Newell, G. Parks, R. Nakamura, and T. Mukai, Substorm and convection bay compared: Auroral and magnetotail dynamics during convection bay, *J. Geophys. Res.*, *106*, 18,843-18,855, 2001

Sergeev, V. A., Y. Kamide, S. Kokubun, R. Nakamura, C. S. Deehr, T. J. Hughes, R. P. Lepping, T. Mukai, A. A. Petrukovich, J.-H. Shue, K. Shiokawa, O. A. Troshichev, and K. Yumoto, Short-duration convection bays and localized interplanetary magnetic field structures on November 28, 1995, *J. Geophys. Res.*, *103*, 23,593-23,609, 1998b.

Shiokawa, K., W. Baumjohann, and G. Haerendel, Braking of high-speed flows in the near-earth tail, *Geophys. Res. Lett*., *24*, 1179-1182, 1997.

Shiokawa, K., W.Baumjohann, G. Haerendel, G. Paschmann, J. G. Fenell, E. Friis-Christensen, H. Luhr, G. D. Reeves, C. T. Russell, P. R. Sutcliffe, and K. Takahashi, High-speed ion flow, substrom current wedge, and multiple Pi2 pulsations, *J. Geophys. Res*., *103*, 4491-4507, 1998.

Shirai, H., K. Maezawa, M. Fujimoto, T. Mukai, T. Yamamoto, Y. Saito, and S. Kokubun, Entry process of low-energy electrons into the magnetosphere along open field lines: Polar rain electrons as field line tracers, *J. Geophys. Res.*, *103*, 4379-4390, 1998.

Sibeck, D. G., R. E. Lopez, and E. C. Roelof, Solar wind control of the magnetopause shape, location, and motion, *J. Geophys. Res.*, *96*, 5489-5495, 1991.

Sofko, G. J., R. A. Greenwald, and W. Bristow, Direct determination of large-scale magnetospheric field-aligned currents with SuperDARN, *Geophys. Res. Lett.*, *22*, 2041-2044, 1995.

Southwood, D. J., and M. G. Kivelson, Charged particle behavior inlow-frequency geomagnetic pulsations, 2. Graphical approach, *J. Geophys. Res*., *87*, 1707-1710, 1982.

Stoker, P. H., M. J. Mathews, and M. W. J. Scourfield, Coordinated measurements of auroral light intensities and riometric radio-wave absorption, *Geophys. Res*. *Lett.*, *23*, 641-644, 1996.

Stoker, P. H., M. J. Mathews, and M. W. J. Scourfield, cosmic radio noise absorption related to structures in auroral luminosity, *J. Geophys. Res*., *102*, 7439-7447, 1997.

Troshichev, O. A., V. G. Andrezen, S. Vennerstroem, and E. Friis-Christensen, Magnetic activity in the Polar Cap - a new index, *Planet. Space Sci*., *36*, 1095-1102, 1988.

Tsyganenko, N. A., and D. P. Stern, Modeling the global magnetic field of the large-scale Birkeland current systems, *J. Geophys. Res.*, 101, 27,187-27,198, 1996.

Untiedt, A. J., and W. Baumjohann, Studies of polar current systems using the IMS Scandinavian Magnetometer Array, *Space Sci. Rev*., *63*, 245-390, 1993.

Vetoulis G., and L. Chen. Global structure of Alfvén-ballooning modes in magnetospheric plasma. *Geophys. Res. Lett*., *21*, 2091-2094, 1994.

Villain, J.-P., R. A. Greenwald, K. B. Baker, and J. M. Ruohoniemi, HF radar observations of E region plasma irregularities produced by oblique electron streaming, *J. Geophys. Res*., *92*, 12,327-12,342, 1987.

Voronkov, I., E. Friedrich, and J. C. Samson, Dynamics of the substorm growth phase as observed using CANOPUS and SuperDARN instruments, *J. Geophys. Res, 104*, 28,491-28505, 1999.

Walker, J. K., Spherical cap harmonic modelling of high latitude magnetic activity and equivalent sources with sparse observations, *J. Atmos. Terr. Phys*., *51*, 67-79, 1989.

Walker, J. K., V. Yu. Semenov, and T. L. Hansen, Synopic models of high latitude magnetic activity and equivalent ionospheric and induced currents, *J. Atmos. Solar-Terr. Phys*, *59*, 1435-1452, 1997.

Wallis, D. D., and E. E. Budzinski, Empirical models of height-integrated conductivities, *J. Geophys. Res*., *86*, 125-137, 1981.

Watanabe, M., M. Pinnock, A. S. Rodger, N. Sato, H. Yamagishi, A. S. Yukimatu, R. A. Greenwald, J-P. Villain, and M. R. Hairston, Localized activation of the distant tail neutral line just prior to substorm onsets, *J. Geophys. Res.*, *103*, 17,651-17,669, 1998.

Watanabe, M., N. Sato, R. A. Greenwald, M. Pinnock, M. R. Hairston, R. L. Rairden, and D. J. McEwen, The ionospheric response to interplanetary magnetic field variations: Evidence for rapid global change and the role of preconditioning in the magnetosphere, *J. Geophys. Res.*, *105*, 22,955–22,977, 2000.

Weimer, D. R., D. Ober, N. C. Maynard, W. J. Burke, M. R. Collier, D. J. McComas, N. F. Ness, and C. W. Smith, Variable Time Delays in the Propagation of the Interplanetary Magnetic Field**,** *J. Geophys. Res*, 107(A8), doi:10.1029/ 2001JA009102, 2002.

Wild, J. A., and T. K. Yeoman, CUTLASS HF radar observations of high latitude azimuthally propagating vortical currents in the nightside ionosphere during magnetosphere substorms, *Ann. Geophysicae, 18*, 640-652, 2000.

Winnigham, J. D., and W. J. Heikkila, Polar cap auroral electron fluxes observed with ISIS 1, *J. Geophys. Res.*, *79*, 949-957, 1974.

Winningham, J. D., F. Yasuhara, S.-I. Akasofu, and W. J. Heikkila, The latitudinal morphology of 10-eV to 10-keV electron fluxes during magnetically quiet and disturbed times in the 2100--0300 MLT sector, *J. Geophys. Res., 80*, 3148-3171, 1975.

Woodfield, E. E., J. A., Davies, M. Lester, T. K. Yeoman, P. Eglitis, and M. Lockwood, Nightside studies of coherent HF radar spectral width behaviour, *Ann. Geophysicae, 20*, 1399-1413, 2002.

Wu C.-C., K. Liou, G. Le, R. P. Lepping, and C.-I. Meng, Observations of substorms during prolonged northward IMF conditions, in *Proc. ICS-6*, pp. 410-414, 2002.

Xu, L., SuperDARN-derived plasma convection: Comparison with other observation methods, and the application to field-aligned current studies, Ph. D. thesis, Univ. of Saskatchewan, Saskatoon, Canada, 2003.

Yeoman T. K., and D. M. Wright, ULF waves with drift resonance and drift-bounce resonance energy sources as observed in artificially-induced HF radar backscatter, *Ann. Geophysicae*, *19*, 159-170, 2001.

Yeoman, T. K., J. A. Davies, N. M. Wade, G. Provan, and S. E. Milan, Combined CUTLASS, EISCAT and ESR observations of ionospheric plasma flows at the onset of an isolated substorm, *Ann. Geophysicae*, *18*, 1073-1087, 2000a.

Yeoman, T. K., R. V. Lewis, H. Khan, S. W. H. Cowley, and J. M. Ruohoniemi, Interhemispheric observations of nightside ionospheric electric fields in response to IMF Bz and By changes and substorm pseudobreakup, *Ann. Geophysicae*, *18*, 897-907, 2000b.

Yumoto, K., K. Takahashi, T. Saito, F. W. Menk, B. J. Fraser, T. A. Potemra, and L. J. Zanetti, Some aspects of the relation between Pi 1-2 magnetic pulsations observed at L = 1.3-2.1 on the ground and substorm-associated magnetic field variations in the near-Earth magnetotail observed by AMPTE CCE, *J. Geophys. Res*., *94*, 3611-3618, 1989.

Zesta, E., E. F. Donovan, L. R. Lyons, G. Enno, J. Murphree, and L. L. Cogger, The two-dimensional structure of auroral poleward boundary intensifications, *J. Geophys. Res.*, *107*(A11), doi: 10.1029/2002JA000260, 2002.

Zesta, E., L. R. Lyons, and E. F. Donovan, The auroral signature of earthward flow bursts observed in the magnetotail, *Geophys. Res. Lett*, *27*, 3241-3244, 2000.

Zhu L., P. Gifford, J. J. Sokja, and R. W. Schunk, Model study of ground magnetic signatures of traveling convection vortices, *J. Geophys. Res*., *102*, 7449-7460, 1997

Zmuda, A. J., and J. C. Armstrong, The diurnal flow pattern of field-aligned currents, *J. Geophys. Res*., *79*, 4611-4619, 1974.

Appendix A

Geophysical coordinate systems

A number of different coordinate systems are used within space physics. The need for multiple coordinate systems arises from the factors such as the difference between the solar equatorial plane and the Earth's orbital plane, the changing direction of Earth's spin axis during the year, and the magnetic dipole orientation. Space research analyses can be more ordered, or calculations performed more easily, in one coordinate system than in the others. The following materials describe the main coordinate systems used in this thesis. For a detailed description of geophysics coordinate systems and how to make transformation between them, see *Hapgood* [1992].

Geocentric Solar Ecliptic (GSE) coordinate system

The GSE coordinate is a geocentric coordinate system which uses the center of the Earth as the origin. The X axis points from the Earth towards the Sun, the Z axis is perpendicular to the ecliptic plane and towards the ecliptic north pole, and the Y axis completes the right-hand orthogonal system.

Geocentric Solar Magnetospheric (GSM) coordinate system

The GSM system, like the GSE system, has its x-axis pointing from the center of the Earth toward the center of the Sun. The difference between the GSM and GSE systems is simply a rotation about the common X-axis. In the GSM coordinate system the Y axis is perpendicular both to the Earth's dipole axis and the X-axis, and that the Z-axis completes the right-hand orthogonal system and is positive in the northern hemisphere. The X-Z plane contains the dipole axis.

Geographic coordinate system

The geographical coordinate is also a geocentric coordinate system but corotates with the Earth. Its X-axis is defined as the intersection of the Earth's equatorial plane and the Greenwich meridian (0 longitude), with the positive X-axis being in the direction such that the angle between it and the vertical line through Greenwich is an acute angle. The Z-axis is parallel to the rotation axis of the Earth and is positive toward the north pole, and the Y-axis completes the right-hand coordinate system.

VDH coordinate system for spacecraft

The VDH coordinate system is defined as a local coordinate system which is dependent on the position of the observation point. Its H axis is antiparallel to the Earth's dipole axis, the V axis is radially outwards and is parallel to the magnetic equator, and the D axis completes the right-hand orthogonal system.

XYZ coordinate system for magnetometer observation

Throughout this thesis, when a XYZ component of magnetic vector observed by ground-based magnetometers is mentioned, it is defined as follows. The X axis is horizontal (tangential to the Earth's surface) and pointing toward magnetic north, the Z axis is vertical downward, and the Y axis is horizontal and positive eastward.

DGRF/IGRF, Corrected GeoMagnetic (CGM) and Altitude-Adjusted Corrected GeoMagnetic (AACGM) Coordinate System

The International Geomagnetic Reference field (IGRF) model is the empirical representation of the Earth's main (core) magnetic field without external sources. It is modeled in terms of a spherical harmonics expansion of the scalar potential in geocentric coordinates. The IGRF model coefficients are based on all available data sources including geomagnetic measurements from observatories, ships, aircraft and satellites. The latest IGRF-2000 model consists of coefficient sets for the epochs 1945 to 2000 in steps of 5 years and the first time derivative of the coefficients for the time period 2000 to 2005. During the 5-year intervals between consecutive models, linear

interpolation is recommended. The coefficients for years before 1990 are definitive coefficient sets (DGRF90), meaning that no further revisions are anticipated.

The CGM coordinate of a point in space is computed on the basis of this DGRF/IGRF model. By definition, the CGM coordinates (latitude, longitude) of a point in space are computed by tracing the non-dipole DGRF/IGRF magnetic field line through the specified point to the dipole geomagnetic equator, then returning to the same altitude as the original specified point along the pure dipole field line, and assigning the obtained dipole latitude and longitude as the CGM coordinates to the starting point. Thus the CGM coordinates have been proven to be useful for geophysical phenomena controlled by the Earth's magnetic field, like auroras, high-latitude ionospheric currents, etc.

In 1988 a new magnetic coordinate system, the AACGM coordinate system, was defined for use with the Polar Anglo-American Conjugate Experiment (PACE) radar [*Baker and Wing*, 1989]. The AACGM coordinates of any point in the space is computed by tracing the DGRF/IGRF magnetic field line through the specified point to the dipole geomagnetic equator, then using the pure magnetic dipole model to trace the magnetic field line back to the Earth's surface. The dipole latitude and longitude of that final point at the Earth's surface yield the AACGM coordinates of the original specified point. The AACGM coordinates are identical to the standard CGM coordinates at the Earth's surface. The important feature of AACGM system that is different from CGM is that all points along a DGRF/IGRF magnetic field line have the same AACGM coordinates (except for a change in the sign of the latitude when going from the northern to the southern hemisphere). Thus measurements from different ionospheric heights, e.g., ~110 km for optical auroral instruments, ~300 km for radars, and ~800 km for satellites, can be better organized and conjunctively studied. Nowadays AACGM is the standard system used by the international SuperDARN science team. The AACGM is the default system throughout this thesis; AACGM are thus implied whenever "magnetic latitude/longitude" (MLAT/MLON) coordinates are used.

Appendix B

Equations for high-latitude ionospheric currents

In this appendix we will derive several basic equations for the currents in the high-latitude ionosphere. We will start from the momentum equation and analyze the validity of each assumption and simplification in the derivations.

B.1 Ohm's Law of ionospheric currents

Let us consider the motion of ions and electrons in the ionosphere. For simplicity we consider a singly-ionized ion species of mass m_i, and use the plasma approximation $n_i = n_e = n$, the plasma density. The basic equation is,

$$nm_i \, d\mathbf{V}_i / dt = -\nabla p_i + nm_i \mathbf{g} + ne(\mathbf{E} + \mathbf{V}_i \times \mathbf{B}) - nm_i \nu_{in}(\mathbf{V}_i - \mathbf{U}) - nm_e \nu_{ei}(\mathbf{V}_i - \mathbf{V}_e) \qquad \text{(B.1a)}$$

$$nm_e \, d\mathbf{V}_e / dt = -\nabla p_e + nm_e \mathbf{g} - ne(\mathbf{E} + \mathbf{V}_e \times \mathbf{B}) - nm_e \nu_{en}(\mathbf{V}_e - \mathbf{U}) - nm_e \nu_{ei}(\mathbf{V}_e - \mathbf{V}_i) \ , \quad \text{(B.1b)}$$

where **g** is the gravitational acceleration, **E** is the electric field, **B** is the magnetic field, **V**, and *p* are the velocity and pressure, subscripts '*i*' and '*e*' denote ions and electrons, respectively, ν_{in}, ν_{en}, and ν_{ei} are the collision frequencies between ions and neutrals, electrons and neutrals, electrons and ions, respectively, and **U** is the neutral wind velocity.

To simplify the algebra we examine the relative importance of each item of equation (B.1) in different regions. The acceleration terms on the left side of equation (B.1) contain the time-derivative term and convective term implicitly, namely,

$$d\mathbf{V}/dt = \partial \mathbf{V}/\partial t + (\mathbf{V} \cdot \nabla)\mathbf{V} \qquad \text{(B.2)}$$

The two terms on the right side of equation (B.2) are of order $V_{i,e}/\tau$ and $V_{i,e}^2/L$, respectively, where τ is the response time to a new set of forces and L is the distance scale for velocity change. Comparing these two terms to the Lorentz force term (in the third term on the right side) or the friction item (the fourth item on the right side) we find that as long as $\tau >> 1/\Omega_i$ or $\tau >> 1/\nu_{in}$, where $\Omega_i = q_i B/m_i$ is the ion gyro-frequency, we can make the approximation that the time-derivative term can be neglected. Also, if L is greater than the gyro radius and the mean free path of ions and electrons, we can make the approximation that the convective term is negligibly small. If we consider only macroscopic ionospheric dynamics, the above two approximations are usually satisfied so that the acceleration term is generally ignored, which is the so-called "steady-state" approach. The first two terms of the right sides of equation (B.1a) and (B.1b) represents the contribution of pressure gradient and gravity force, respectively. It can be estimated that the pressure gradient force and the gravity are normally at least one or two orders less than the electric field force in the high-latitude ionosphere. Therefore we will also ignore the first two terms in equation (B.1).

Finally, equation (B.1) can be simplified to,

$$e(\mathbf{E} + \mathbf{V}_i \times \mathbf{B}) - m_i \nu_{in}(\mathbf{V}_i - \mathbf{U}) - m_e \nu_{ei}(\mathbf{V}_i - \mathbf{V}_e) = 0 \quad , \tag{B.3a}$$

$$-e(\mathbf{E} + \mathbf{V}_e \times \mathbf{B}) - m_e \nu_{en}(\mathbf{V}_{ei} - \mathbf{U}) - m_e \nu_{ei}(\mathbf{V}_e - \mathbf{V}_i) = 0 \quad . \tag{B.3b}$$

After some vector manipulations, the final expressions for the ion and electron velocity derived form (B.3) are,

$$\begin{aligned}
\mathbf{V}_i &= \mathbf{V}_E + \mathbf{U}_{//} + \frac{(\alpha_{in}\alpha_{en} - \alpha_{en}^2 - \alpha - \alpha^2)\cdot(\mathbf{V}_E - \mathbf{U}_\perp) + (\alpha_{en}\alpha + \alpha_{in})\mathbf{E}'_\perp}{(1+\alpha)^2 + (\alpha_{in} - \alpha_{en})^2} + \frac{\alpha_{en}}{\alpha}\cdot\frac{\mathbf{E}_{//}}{B} \\
\mathbf{V}_e &= \mathbf{V}_E + \mathbf{U}_{//} + \frac{(\alpha_{in}\alpha_{en} - \alpha_{in}^2 - \alpha - \alpha^2)\cdot(\mathbf{V}_E - \mathbf{U}_\perp) - (\alpha_{in}\alpha + \alpha_{en})\mathbf{E}'_\perp}{(1+\alpha)^2 + (\alpha_{in} - \alpha_{en})^2} - \frac{\alpha_{in}}{\alpha}\cdot\frac{\mathbf{E}_{//}}{B}
\end{aligned} \quad , \tag{B.4}$$

where $\alpha = \alpha_{in}\alpha_{en} + \alpha_{in}\alpha_{ei} + \alpha_{ei}\alpha_{en}$. α_{en}, α_{ei}, α_{in} denote the ratio between the electron-neutral collision frequency to the electron gyro-frequency, the ratio between the

electron-ion collision frequency to the electron gyro-frequency, and the ratio between the ion-neutral collision frequency to the ion gyro-frequency, respectively. $\mathbf{V}_E = \mathbf{E}\times\mathbf{B}/B^2$, and $\mathbf{E}'_\perp = \mathbf{E}_\perp + \mathbf{U}\times\mathbf{B}$. The subscript '//' and '⊥' of a vector denote the component of that vector along and normal to the magnetic field direction, respectively.

Note that the first two terms on the right side of equations (B.4) are independent of the properties (charge and/or mass) of the particle species, and thus represent the co-motion of both electrons and ions. In particular, the first term $\mathbf{V}_E$ gives the **E** × **B** drift, also called Hall drift, or the convective drift, of the plasma. The second term indicates that the plasma moves along the magnetic field line with the parallel neutral wind velocity $\mathbf{U}_{//}$. The neutral wind is dominantly horizontal and of the order of 100 m/s at ionospheric altitude. Since the magnetic field direction at high-latitude is nearly vertical, the effect of the neutral wind on plasma convection is sufficiently negligible at these latitudes. The rest terms on the right side of equations (B.4) are dependent on the properties of the particle species, and thus cause the difference of velocities between the ions and electrons, which results in current flowing in the ionosphere,

$$\mathbf{j} = \sum_{j=i,e} n_j q_j \mathbf{V}_j = \sigma_P \mathbf{E}'_\perp + \sigma_H \hat{\mathbf{b}}\times\mathbf{E}'_\perp + \sigma_{//}\mathbf{E}_{//} \quad , \tag{B.5}$$

where $\hat{\mathbf{b}}$ is the unit vector along the magnetic field. Equation (B.5) has the general form of Ohm's Law, in which the Pedersen conductivity σ_P, Hall conductivity σ_H, and parallel conductivity $\sigma_{//}$ are given by:

$$\sigma_P = \frac{(\alpha_{in} + \alpha_{en})(1+\alpha)}{(1+\alpha)^2 + (\alpha_{in} - \alpha_{en})^2}\cdot\frac{ne}{B} \quad , \tag{B.6a}$$

$$\sigma_H = \frac{\alpha_{in}^2 - \alpha_{en}^2}{(1+\alpha)^2 + (\alpha_{in} - \alpha_{en})^2}\cdot\frac{ne}{B} \quad , \tag{B.6b}$$

$$\sigma_{//} = \frac{\alpha_{in} + \alpha_{en}}{\alpha}\cdot\frac{ne}{B} \quad , \tag{B.6c}$$

respectively. Typical height profiles and properties of three conductivities are given in Figure 1.5b. Note that equations (B.6a) to (B.6c) are different from the usual expressions of three conductivities (e.g., see *Kivelson and Russell* [1995]) because the electron-ion collision term is fully taken into account here, but was ignored in *Kivelson and Russell* [1995] and many other similar works. However, the effect of electron-ion collision term is of little importance to σ_P and σ_H . Note in equations (B.6) the electron-ion collision term characterized by α_{ei} only appears in the parameter $\alpha = \alpha_{in}\alpha_{en} + \alpha_{in}\alpha_{ei} + \alpha_{ei}\alpha_{en}$. In the ionospheric *E* region, the electron-neutral collision dominates over the electron-ion collision thus the latter can be neglected. In the *F* region, the electron-ion collision gradually becomes important with increasing height. However, it should be noted that in *F* region we have $\alpha_{ei}, \alpha_{en} << \alpha_{in} << 1$, thus α is always several orders smaller than 1, and plays little role in equation (B.6a) and (B.6b). In conclusion, the electron-ion collision is always negligible in calculating σ_P and σ_H at all ionospheric altitude ranges of interest.

B.1 Field-aligned currents

In this section we will study the relationship between the FAC and the ionospheric convection and electric fields. According to the current continuity equation we have,

$$\begin{aligned}\nabla\cdot\mathbf{j} &= \nabla\cdot(-j_{//}\hat{\mathbf{b}}+\mathbf{j}_\perp) = -j_{//}\nabla\cdot\hat{\mathbf{b}} - (\hat{\mathbf{b}}\cdot\nabla)j_{//} + \nabla\cdot\mathbf{j}_\perp \\ &= -j_{//}\nabla\cdot\left(\frac{\mathbf{B}}{B}\right) - \frac{\partial j_{//}}{\partial s} + \nabla\cdot\mathbf{j}_\perp = \frac{j_{//}\nabla B}{B}\cdot\hat{\mathbf{b}} - \frac{\partial j_{//}}{\partial s} + \nabla\cdot\mathbf{j}_\perp \\ &= \frac{j_{//}}{B}\frac{\partial B}{\partial s} - \frac{\partial j_{//}}{\partial s} + \nabla\cdot\mathbf{j}_\perp = -B\frac{\partial}{\partial s}\left(\frac{j_{//}}{B}\right) + \nabla\cdot\mathbf{j}_\perp = 0 \quad ,\end{aligned} \tag{B.7}$$

where *s* is the distance along the magnetic field line. Here we define the sign of $j_{//}$ to be positive for FAC antiparallel to $\hat{\mathbf{b}}$ (upward FAC in northern hemisphere) and negative for FAC parallel to $\hat{\mathbf{b}}$ (downward FAC in northern hemisphere), in accordance with the

SuperDARN FAC analysis convention. From equation (B.5), neglecting the neutral wind effect, we have,

$$\begin{aligned}\nabla\cdot\mathbf{j}_\perp &= \nabla\cdot\left(\sigma_p\mathbf{E}_\perp - \sigma_H\mathbf{E}_\perp\times\hat{\mathbf{b}}\right)\\ &= \sigma_p\nabla\cdot\mathbf{E}_\perp + \nabla\sigma_p\cdot\mathbf{E}_\perp - \sigma_H\nabla\cdot(\mathbf{E}_\perp\times\hat{\mathbf{b}}) - \nabla\sigma_H\cdot(\mathbf{E}_\perp\times\hat{\mathbf{b}}) \qquad \text{(B.8)}\\ &= \sigma_p\nabla\cdot\mathbf{E}_\perp + \nabla\sigma_p\cdot\mathbf{E}_\perp - \sigma_H\hat{\mathbf{b}}\cdot\nabla\times\mathbf{E}_\perp - \nabla\sigma_H\cdot(\mathbf{E}_\perp\times\hat{\mathbf{b}}) - \sigma_H\mathbf{E}_\perp\cdot\frac{\mathbf{R}\times\hat{\mathbf{b}}}{R^2} \quad ,\end{aligned}$$

where the curvature radius vector **R** of magnetic field lines is defined by,

$$-(\hat{\mathbf{b}}\cdot\nabla)\hat{\mathbf{b}} = \frac{\mathbf{R}}{R^2} \quad . \qquad \text{(B.9)}$$

In terms of convection velocity, the electric field and the plasma drift velocity is associated with $\mathbf{E}_\perp = \mathbf{B}\times\mathbf{v}$, so,

$$\begin{aligned}\nabla\cdot\mathbf{j}_\perp &= \sigma_p(\mathbf{v}\cdot\nabla\times\mathbf{B} - \mathbf{B}\cdot\nabla\times\mathbf{v}) + \nabla\sigma_p\cdot\mathbf{B}\times\mathbf{v} - \sigma_H\nabla\cdot(B\mathbf{v}) - B\nabla\sigma_H\cdot\mathbf{v}\\ &= \sigma_p(\mathbf{v}\cdot\mu_0\mathbf{j} - \mathbf{B}\cdot\nabla\times\mathbf{v}) + \nabla\sigma_p\cdot\mathbf{B}\times\mathbf{v} - \sigma_H\nabla(B\cdot\mathbf{v}) - B\nabla\sigma_H\cdot\mathbf{v}\\ &= \sigma_p(-\mu_0\sigma_H Bv^2 - \mathbf{B}\cdot\nabla\times\mathbf{v}) + \nabla\sigma_p\cdot\mathbf{B}\times\mathbf{v} - \sigma_H\nabla\cdot(B\mathbf{v}) - B\nabla\sigma_H\cdot\mathbf{v} \quad .\end{aligned} \qquad \text{(B.10)}$$

We notice that,

$$\begin{aligned}\mathbf{B}\cdot\nabla\times\mathbf{E} &= \nabla\cdot(\mathbf{E}\times\mathbf{B}) + \mathbf{E}\cdot\nabla\times\mathbf{B} = \nabla\cdot(B^2\mathbf{v}) + \mu_0\mathbf{E}\cdot\mathbf{j}\\ &= B\nabla\cdot(B\mathbf{v}) + B\nabla B\cdot\mathbf{v} + \mu_0\sigma_p B^2v^2 \quad .\end{aligned} \qquad \text{(B.11)}$$

Hence, by combining (B.10) and (B.11) we have,

$$\nabla\cdot\mathbf{j}_\perp = -\sigma_p\mathbf{B}\cdot\nabla\times\mathbf{v} + \nabla\sigma_p\cdot(\mathbf{B}\times\mathbf{v}) - \sigma_H\hat{\mathbf{b}}\cdot\nabla\times\mathbf{E}_\perp - B\nabla\sigma_H\cdot\mathbf{v} + \sigma_H\nabla B\cdot\mathbf{v}. \qquad \text{(B.12)}$$

We will introduce the following approximations to simplify (B.12). First we assume,

$$\hat{\mathbf{b}} \cdot (\nabla \times \mathbf{E}_{\perp}) = -\hat{\mathbf{b}} \cdot \frac{\partial \mathbf{B}}{\partial t} = 0 \quad . \tag{B.13}$$

The electric field induced by the temporal variation of Earth's magnetic field is generally negligible in the high-latitude ionosphere except during geomagnetic storms and intense substorms. Thus the perpendicular electric fields are usually assumed to be electrostatic. Equation (B.13) is satisfied naturally.

Secondly, comparing the last two items in the right hand of equation (B.8), we see that their relative magnitudes depend on the ratio of the horizontal scale of Hall conductance to the radius of curvature of the Earth's magnetic field line. To the first order the Earth's magnetic field is dipolar, in which case the radius of curvature of the field line is given by,

$$R = \frac{r(1+3\sin^2\Lambda)^{3/2}}{3\cos\Lambda(1+\sin^2\Lambda)} \quad , \tag{B.14}$$

where Λ is the magnetic latitude. Similarly, the importance of the last item in equation (B.12) depends on the horizontal scale of the magnitude of Earth's magnetic fields. For a dipolar field,

$$\left|\frac{(\nabla B)_{\perp}}{B}\right| = \left|(\hat{\mathbf{b}} \cdot \nabla) \cdot \hat{\mathbf{b}}\right| = \frac{1}{R} \quad , \tag{B.15}$$

R is about 24000 km at 300 km height and $\Lambda = 70^0$, and greater than 50000 km at $\Lambda = 80^0$, much greater than any scale size of interest for ionospheric Hall conductance. Hence the last items in equations (B.8) and (B.12) are negligible.

Finally, equations (B.8) and (B.12) are simplified to,

$$\begin{aligned} \nabla \cdot \mathbf{j}_{\perp} &= \sigma_p \nabla \cdot \mathbf{E}_{\perp} + \nabla \sigma_p \cdot \mathbf{E}_{\perp} - \nabla \sigma_H \cdot (\mathbf{E}_{\perp} \times \hat{\mathbf{b}}) \\ &= -\sigma_p \mathbf{B} \cdot \nabla \times \mathbf{v} + \nabla \sigma_p \cdot (\mathbf{B} \times \mathbf{v}) - B \nabla \sigma_H \cdot \mathbf{v} \quad . \end{aligned} \tag{B.16}$$

Returning to (B.7) we get,

$$\frac{\partial}{\partial s}\left(\frac{j_{//}}{B}\right)=\frac{1}{B}\left[\sigma_p\nabla\cdot\mathbf{E}_\perp+\nabla\sigma_p\cdot\mathbf{E}_\perp-\nabla\sigma_H\cdot(\mathbf{E}_\perp\times\hat{\mathbf{b}})-\sigma_H\hat{\mathbf{b}}\cdot\nabla\times\mathbf{E}_\perp\right]$$
$$=-\sigma_p\hat{\mathbf{b}}\cdot\nabla\times\mathbf{v}+\nabla\sigma_p\cdot(\hat{\mathbf{b}}\times\mathbf{v})-\nabla\sigma_H\cdot\mathbf{v}\quad . \tag{B.17}$$

If we choose the lower limit of the integral at the lower ionospheric *E* region where the parallel current vanishes because the *D* region is highly resistive, the upper limit of integral correspond to the observation point, we have,

$$j_{//}=B\int\left[\sigma_p\hat{\mathbf{b}}\cdot\nabla\times\mathbf{v}-\nabla\sigma_p\cdot(\hat{\mathbf{b}}\times\mathbf{v})+\nabla\sigma_H\cdot\mathbf{v}\right]\cdot ds$$
$$\approx B\left(\Sigma_p\hat{\mathbf{b}}\cdot\nabla\times\mathbf{v}+\nabla\Sigma_p\cdot\mathbf{v}\times\hat{\mathbf{b}}+\nabla\Sigma_H\cdot\mathbf{v}\right) \tag{B.18}$$
$$=-\Sigma_P\nabla\cdot\mathbf{E}-\nabla\Sigma_p\cdot\mathbf{E}-\nabla\Sigma_H\cdot\hat{\mathbf{b}}\times\mathbf{E}\quad ,$$

where Σ_P and Σ_H are known as the Pedersen and Hall height-integrated (more exactly, field-line-integrated) conductivities, or conductance, respectively. We have used the fact that the convection velocity changes less than 5% from lower E-region up to 300 km altitude. Beyond that height the Pedersen conductivity decreases rapidly and Hall conductivity vanishes.

B.3 Ionospheric equivalent currents

Both the Pedersen and Hall conductivity strongly peak in the lower *E* region (see Figure 1.5b). Thus the height-integrated perpendicular currents can be roughly treated as sheet current at a height of about 110 km,

$$\mathbf{J}_\perp=\Sigma_P\mathbf{E}+\Sigma_H\hat{\mathbf{b}}\times\mathbf{E}\quad , \tag{B.19}$$

According to the Helmholtz theorem, any vector can be divided into a divergence-free part $\mathbf{J}_{df}$ and a curl-free part $\mathbf{J}_{cf}$,

$$\mathbf{J}_{\perp} = \mathbf{J}_{cf} + \mathbf{J}_{df} \quad . \tag{B.20}$$

The curl-free part $\mathbf{J}_{cf}$ is the closure current of FAC,

$$\nabla \cdot \mathbf{J}_{cf} = j_{//} \quad . \tag{B.21}$$

$\mathbf{J}_{cf}$ and $j_{//}$ combine to produce no magnetic field below the ionosphere [*Uniedit and Baumjohann*, 1993; *Amm*, 1997]. The "equivalent current" $\mathbf{J}_{eq}$ is just the divergence-free part of the horizontal current. It is the current component which produces the magnetic effects measured by magnetometers on the ground. Since $\mathbf{J}_{eq}$ is divergence free we can express it into the following format,

$$\mathbf{J}_{eq} = \mathbf{J}_{df} = \nabla \psi_{eq} \times \hat{\mathbf{b}} \quad , \tag{B.22}$$

where ψ_{eq} is defined as the equivalent current potential, if we neglect the curvature of geomagnetic field lines, as we have justified before. We may derive from Equations (B.19) and (B.22) the following results,

$$\begin{aligned} \nabla^2 \psi_{eq} &= \nabla \cdot (\hat{\mathbf{b}} \times \mathbf{J}_{eq}) = \nabla \cdot (\hat{\mathbf{b}} \times \mathbf{J}_{\perp}) \\ &= \nabla \cdot (\Sigma_p \hat{\mathbf{b}} \times \mathbf{E} - \Sigma_H \mathbf{E}) \\ &= -\Sigma_H \nabla \cdot \mathbf{E} + (\nabla \Sigma_p \times \hat{\mathbf{b}} - \nabla \Sigma_H) \cdot \mathbf{E} \quad . \end{aligned} \tag{B.23}$$

Equations (B.23) and (B.18) give the relationships between the equivalent current, electric field and FAC and are the basic equation set for almost all magnetometer-related inversion or forward methods. In case of uniform conductance, equations (B.23) and (B.18) lead to,

$$\mathbf{J}_{eq} = \Sigma_H \hat{\mathbf{b}} \times \mathbf{E} = -\Sigma_H B \mathbf{v} \quad , \tag{B.24}$$

$$\nabla \cdot \mathbf{E} = -\mathbf{B} \cdot \nabla \times \mathbf{v} = -j_{//} / \Sigma_p \quad . \tag{B.25}$$

Equation (B.24) shows that, for this case of uniform conductance, the equivalent current is exactly the Hall current. In other words, the FACs and the Pedersen currents produce magnetic field that exactly cancel each other so that only magnetic effects of the Hall current can be observed on the ground, this is known as Fukushima's theorem [*Fukushima*, 1976].

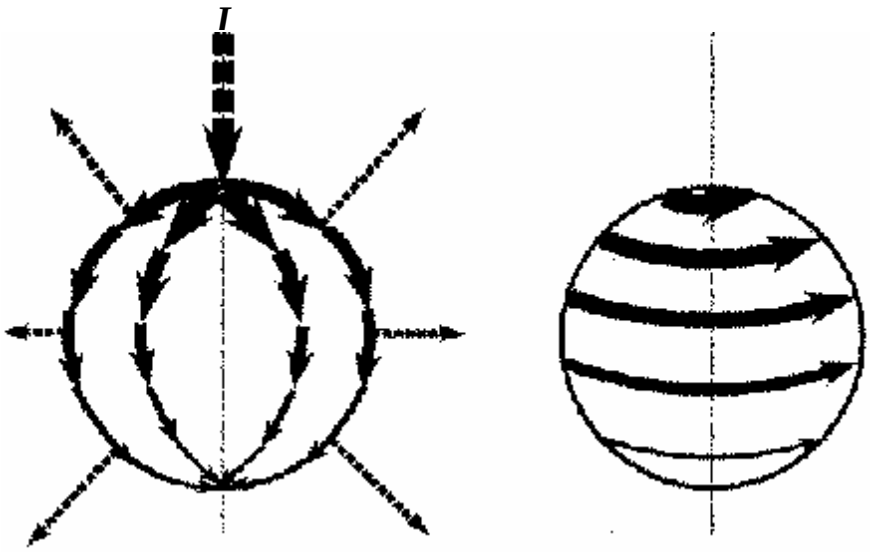

(a) (b)

Figure B.1 Sketch of an elementary current system. (a) FACs and their resulting ionospheric electric fields. The curl-free (Pedersen) current is along the direction of electric field and act as closure current for FACs. (b) The resulting **E x B** drift in the ionosphere. The divergence-free (Hall) current is in the opposite direction to the plasma drift (from *Amm*, 1997).

An instructive understanding of the Fukushima's theorem can be obtained as follows. The ionospheric current system is simplified as shown in Figure B.1. A downward FAC of current density I into the pole is balanced by upward FACs uniformly distributed over the sphere. Assuming uniform Hall and Pedersen conductances all over the ionosphere, the electric field is meridional at the ionosphere height ($r = R_i$). The Pedersen current is along the electric field direction and acts as the closure current for the FACs, while the Hall currents flow azimuthally in the

ionosphere. Also, the Pedersen and Hall current are exactly the curl-free part and divergence-free parts, respectively, of the horizontal currents shown in equation B.20. The current system shown in the Figure B.1 is called an "elementary current system" [*Amm*, 1997], because any realistic ionospheric current can be expressed as a superimposition of such elementary current systems.

The magnetic field generated by the current system shown in Figure B.1a, in spherical coordinates, is [*Fukushima*, 1976],

$$\mathbf{B}(r,\theta,\varphi)=\begin{cases}-\dfrac{\mu_0 I}{4\pi r}\cot(\theta/2)\hat{\mathbf{e}}_{\varphi} & r>R_i\\ 0 & r<R_i\end{cases} \quad . \tag{B.26}$$

Thus the combined magnetic effects of FACs and the Pedersen current on the ground is zero. Ground-based magnetometers will measure only the effect of the Hall current in Figure B.1b, whose resulting magnetic field is given by [*Amm*, 1997],

$$\mathbf{B}(r,\theta,\varphi)=\begin{cases}-\dfrac{\mu_0 I}{4\pi r}\left[\dfrac{R_i}{r}\left(\dfrac{1}{\sqrt{1-2R_i\cos\theta/r+(R_i/r)^2}}-1\right)\hat{\mathbf{e}}_r-\dfrac{1}{\sin\theta}\left(\dfrac{1-R_i\cos\theta/r}{\sqrt{1-2R_i\cos\theta/r+(R_i/r)^2}}-1\right)\hat{\mathbf{e}}_{\theta}\right] & r>R_i\\ -\dfrac{\mu_0 I}{4\pi r}\left[\left(\dfrac{1}{\sqrt{1-2r\cos\theta/R_i+(r/R_i)^2}}-1\right)\hat{\mathbf{e}}_r-\dfrac{1}{\sin\theta}\left(\dfrac{r/R_i-\cos\theta}{\sqrt{1-2r\cos\theta/R_i+(r/R_i)^2}}+\cos\theta\right)\hat{\mathbf{e}}_{\theta}\right] & r<R_i\end{cases} \tag{B.27}$$

Equation (B.27) indicates that for an elementary current system, the resulting ground magnetic field has a vertical component in the same sense as the input FAC at the "pole", and a meridional component parallel to the electric field.

Appendix C

Two common procedures

In this Appendix we will describe two common procedures repeatedly applied throughout this thesis. The first procedure is estimating the propagation time delay of the solar wind between a satellite and the subsolar magnetopause. The second is estimating the position of the OCFLB using the MSP observations of 630 nm optical auroral emissions.

C.1 How to estimate the solar wind propagation time between satellite and subsolar magnetopause

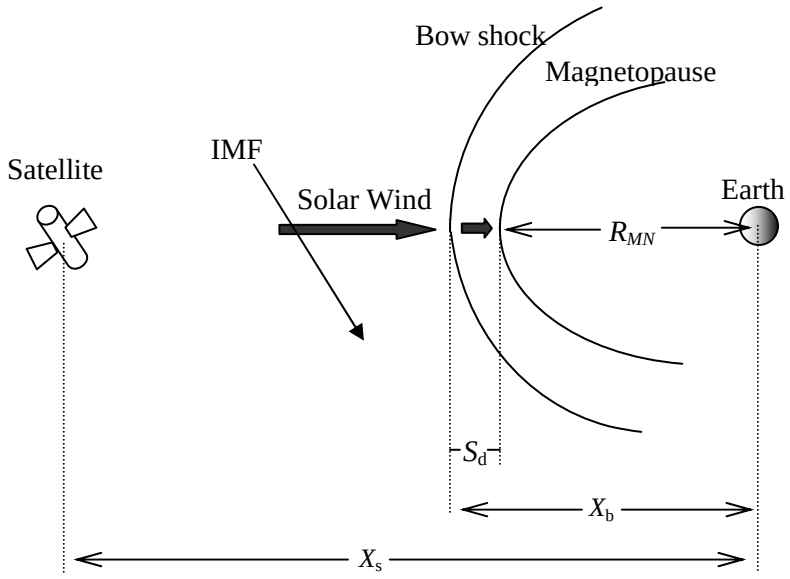

Figure C.1 Geometry of the solar wind propagation from satellite to subsolar magnetopause

In this thesis (and almost always in space physics research) the upstream solar wind parameters are taken from the satellite/spacecraft measurements. For an accurate timing of the effect of the solar wind on the magnetosphere and ionosphere, an estimate of the solar wind propagation time delay between the satellite and the subsolar magnetopause is required. First we will introduce the simplest one-dimensional method which assumes that the solar wind structure propagates only along the sun-Earth line. In this case, the transit time between the satellite and the bow shock is,

$$T_{s-b} = (X_s - X_b)/V_{sw} \quad , \tag{C.1}$$

where X_s and X_b are the X distance of the satellite and the nose of bock shock, respectively, and V_{sw} is the solar wind speed. As soon as the solar wind has passed through the bow shock, the velocity decelerated significantly, roughly by a factor of 4. Inside the magnetosheath the solar wind velocity drops to nearly zero at the subsolar magnetopause. Thus the mean velocity in the magnetosheath is about 1/8 of the unshocked solar wind speed, and the transit time between he bow shock and the subsolar magnetopause is,

$$T_{b-m} = S_d/V_{sw} * 8 \quad , \tag{C.2}$$

where S_d is the X distance between the bow shock and the magnetopause, also known as the standoff distance. The standoff distance can be calculated using the empirical formula given by *Nemecek and Safrankova* [1991]

$$S_d = R_{MN} \cdot \left[\left(1 + \frac{B}{2B_0} \right) \cdot \frac{(\gamma - 1)M_{MS}^2 + 2}{(\gamma + 1)M_{MS}^2} \right] \quad , \tag{C.3}$$

where B_0=5.5 nT , γ=1.8, B is the IMF magnitude in nT. M_{MS} is the fast magnetosonic Mach number of the solar wind, and R_{MN} is the magnetopause nose position in Earth radii (R_E). *Sibeck* [1991] gave the following empirical formula for R_{MN} as a function of IMF Bz in nT,

$$R_{MN} = 11.3 + B_z / 4 \quad . \tag{C.4}$$

Equations (C.2) to (C.4) are used in this thesis to estimate the solar wind propagation time from bow shock to the subsolar magnetopause.

In the case that solar wind monitoring is available by only one satellite, the above X-distance method is applied. However, it has been recognized that the variations in the IMF may be treated by using an approximately planar structure tilted with respect to the Sun-Earth line [*Ridley*, 2000; *Weimer et al.*, 2002]. The X-distance method may cause large errors in estimating the solar wind propagation delay. If the solar wind parameters can be measured from two or more satellites, an improved method can be applied to determine the orientation of solar wind plasma phase front. We will give the following example to illustrate that method in the following.

Figure C.2 shows the solar wind observation form ACE and WIND during the interval 0200-0530 UT on December, 26, 1998. In this event, the ACE satellite was located at 224 R_E upstream and ~36 R_E off the Sun-Earth line in the GSE-Y direction, while WIND was located at X = 51 R_E upstream and Y = -54 R_E (GSE). The solar wind observations on WIND are found to agree quite well with those on ACE but with a lag of ~51 minutes. Such a transition delay indicates that the orientations of the phase front normal of solar wind plasma is somewhat tilted from the Sun-Earth line; otherwise a delay of ~39 minute would be expected from the X-distance between the two satellites and the observed solar wind speed. As shown in Figure C.3, the "equivalent" propagation path of the solar wind along the X line is from A^* to W^*. According to the additional delay (~12 minutes) and the Y coordinates of the WIND and ACE satellites, the orientation of the plasma phase front in the solar wind can be determined. Adding the propagation delay from W^* to the bow shock nose and the extra delay due to the deceleration of the solar wind through the magnetosheath, the actual time delay of the solar wind from WIND to the subsolar magnetopause was thus estimated to be about 6 minutes.

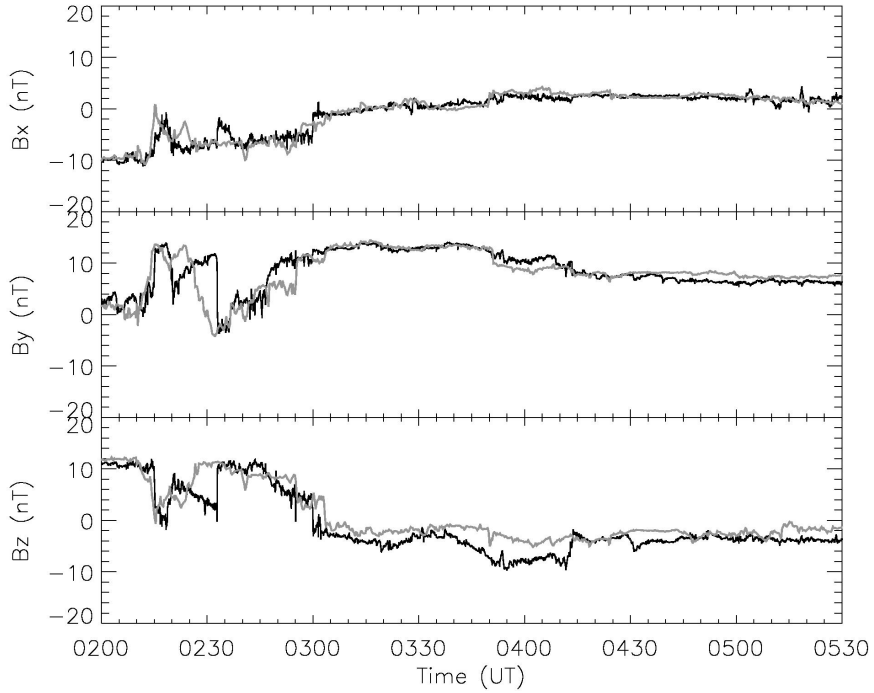

Figure C.2 Solar wind parameters observed by WIND (black lines) and ACE (gray lines) on December 26, 1998. The ACE data are shifted 51 minutes to match the observations on WIND.

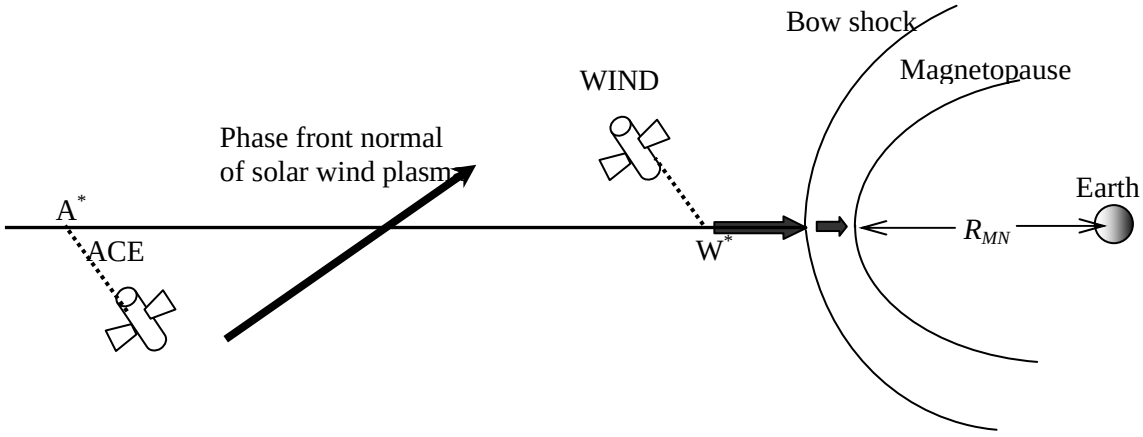

Figure C.3 Geometry of using two-satellite joint observation to determine the phase front of solar wind plasma.

C.2 How to estimate the OCFLB from 630 nm emissions

Inside the polar cap there is spatially relatively homogenous precipitation of a few hundred eV electrons, called the polar rain [*Winningham and Heikkila*, 1974]. It was found that the 630 nm emission inside polar cap is fairly uniform at about 60 R, while in the poleward part of auroral oval the average emission is about 170 R. Therefore, an intermediate value, namely 110 R was used as the threshold to identify the location of polar cap boundary (PCB), or OCFLB, to an accuracy of ~1^0 on the basis of the comparison with the DMSP observations [*Blanchard et al*, 1997]. However, it should be noticed that the OCFLB identification using precipitating particles and the resulting optical emission usually does not work well near the dawnside and the duskside, because the so-called soft zone precipitation at high latitudes exhibits spectral characteristics intermediate between mantle and cleft (closed boundary layer) signatures [*Lyons et al*., 1996].

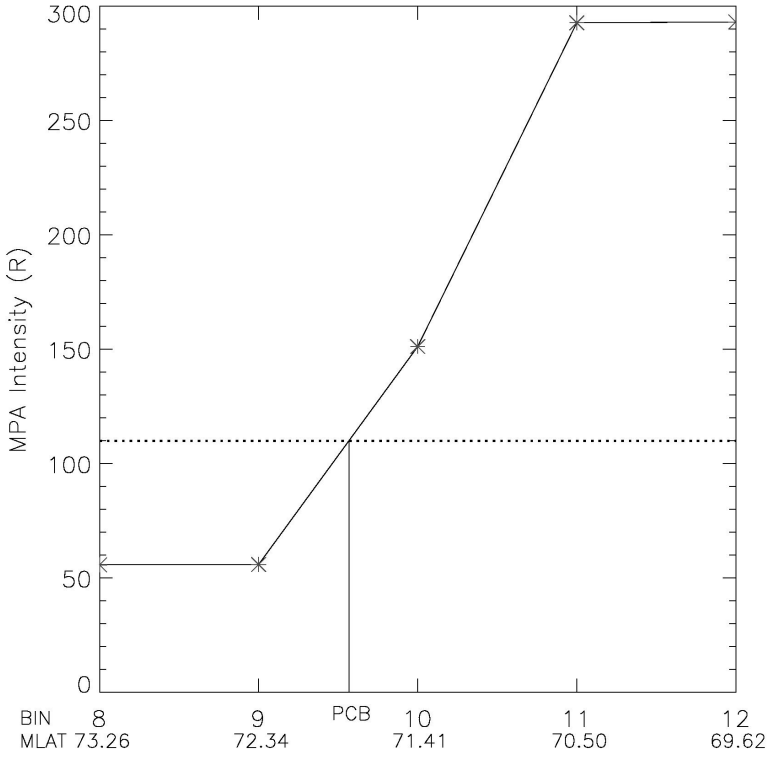

Figure C.4 Example of the OCFLB determination using the 630 nm MSP observations at Rankin Inlet.

In this thesis, the following procedures are applied to estimate the OCFLB from the 630 nm MSP observations at Rankin inlet: We usually start from bin 12 (69.6^0 MLAT) and scan poleward (decreasing bin number) to find the last bin with emission greater than 150 R. Beyond that bin, the intensity then drops to less than 75 R in the next one or two bins. Linear interpolation is applied between the two adjacent bins with emissions above 110 R and below 110 R, respectively. The intersection between the linear interpolation and the 110 R threshold determines the latitude of the PCB or OCFLB. The above procedure guarantees that the 110 R threshold occurs within the regions of steep intensity decrease. If the emission intensity decrease is not sharp enough, the poleward border of the 630 nm emission is not well defined, so the OCFLB information cannot be determined.